Massive Passive Galaxies at $z \sim 1.6$

by

Liz Maria Arcila-Osejo

A Thesis Submitted to Saint Mary's University, Halifax, Nova Scotia in Partial Fulfillment
of the Requirements for the Degree of PhD in Astronomy
(Department of Astronomy and Physics)

March 29 2018

Approved: Dr. Marcin Sawicki
Supervisor

Approved: Dr. Ivana Damjanov
Examiner

Approved: Dr. Laura Parker
Examiner

Approved: Dr. Rob Thacker
Examiner

Date: March 29 2018.

Acknowledgements

I would like to thank my supervisor Dr. Marcin Sawicki for his support, patience and ensuring the completeness of this project. To my committee members, for their time and their suggestions to improve this work. To Bobby, Anneya, Diego, Gurpreet, Nathalie and Thibaud for their moral support and constant help; I could not have done this without you. To my hermana del alma Paola for always being there for me, your support is invaluable to me. To my amazing family, for always believing in me, even when I did not. Finally this thesis is dedicated to my mom and my husband, my pillars, for making me want to be a better person every day, for giving me courage and for never letting me give up.

This work is based on observations obtained with MegaPrime/MegaCam, a joint project of CFHT and CEA/IRFU, at the Canada-France-Hawaii Telescope (CFHT) which is operated by the National Research Council (NRC) of Canada, the Institut National des Science de l'Univers of the Centre National de la Recherché Scientifique (CNRS) of France, and the University of Hawaii. This work is based in part on data products produced at Terapix available at the Canadian Astronomy Data Centre as part of the Canada-France-Hawaii Telescope Legacy Survey, a collaborative project of NRC and CNRS.

Contents

List of Figures

List of Tables

Abstract

Massive Passive Galaxies at $z \sim 1.6$

by Liz Arcila-Osejo

March 29 2018

We build a K-selected catalog of $z \sim 1.6$ gzK_s galaxies in the Deep and Wide fields of the Canada-France-Hawaii Legacy Survey, with a final effective area of 27.6 deg^2. This catalog allows us to recover a representative sample of rare massive passive galaxies ($log\left(M_*/M_\odot\right) > 11.14$) and very rare ultra-massive passive galaxies ($log\left(M_*/M_\odot\right) > 11.49$). The latter is an important population of galaxies, with significant build-up of stellar mass when the universe was only $\sim$ 4 Gyr old. This sample of ultra-massive passive galaxies (or UMPEGs) allows us to constrain the bright end of the stellar mass function. Once corrected for Eddington Bias, we find that passive galaxies at this redshift are well described by a Schechter function, as expected in a mass quenching scenario (Peng et al. 2010). Next, we find a lack of massive companions (star-forming or passive) to these UMPEGs and only a handful of lower mass (50% or less the mass of the UMPEG) companions. Using a simple dynamical friction estimate, we find that through merging these companions can at most contribute a $\sim$ 25% mass growth of these galaxies from $z \sim 1.6$ to $z \sim 1$. Finally, we recover regions with an over-density of massive passive galaxies as sample environments for proto-clusters with an evolved population. These proto-clusters have an under-density of bright star-forming galaxies, hinting at them being proto-clusters where quenching is largely done.

Chapter 1

Introduction

In a late universe dominated by dark matter, gravitational collapse is the leading force of structure formation in the universe. Dark matter halos form from an initial field of density perturbations and grow in a bottom-up scenario. Galaxies form inside these structures where cold streams provide fuel to allow the formation of new stars (Katz et al. 2003). In contrast, external and internal processes (e.g., feedback, galaxy interactions) can cause quenching (i.e., cessation of star-formation) to produce passive galaxies.

Galaxies grow in mass through different processes: star-formation, and galaxy interactions (mainly minor and major mergers). Star-formation is an estimate of the efficiency in the process of converting gas into stars (in an interplay between gas cooling and feedback mechanisms, such as star, super nova or active-galactic nucleus winds). Statistical samples have allowed the identification of a star-forming main sequence (Daddi et al. 2007; Salim et al. 2007; Santini et al. 2009) where star-formation can be parameterized as a power law, dependent on the stellar mass of the galaxy at low ($z < 1$, Salim et al. 2007) and high

redshifts ($z \geq 1$, Daddi et al. 2007):

$$log\,(SFR) = \alpha \times log(M_*) + \beta, \tag{1.1}$$

which implies that star-formation processes are regular or quasi-static (Noeske et al. 2007). After taking into account model dependencies (choice of initial mass-function and conversion from luminosity to SFR), Speagle et al. (2014) finds that the slope of the star-formation main sequence is likely to be time-dependent, and Whitaker et al. (2012, 2014) finds the slope to be dependent on stellar mass.

The stellar mass function, or number density of galaxies per unit of mass, is an indicator of the physical evolution of galaxies as they assemble in mass (due to star-formation or mergers) and evolve through different feedback mechanisms. The Schechter function (Schechter 1976), shown in Figure 1.1 and Equation 1.2, typically used to describe this number density of galaxies, is characterized by a combination of a power law (to describe faint galaxies) truncated (at a characteristic mass) by an exponentially declining function. In terms of stellar mass (M_*), this implies that this function is defined by three parameters: (1) a normalization factor Φ^*, (2) a characteristic mass M^* (or knee, the most common mass), and (3) a faint end slope α. Mathematically, this is written as:

$$\Phi(M) = ln\,(10)\,\Phi^* \left[10^{(M_* - M^*)(1+\alpha)}\right] exp\left[-10^{(M_* - M^*)}\right]. \tag{1.2}$$

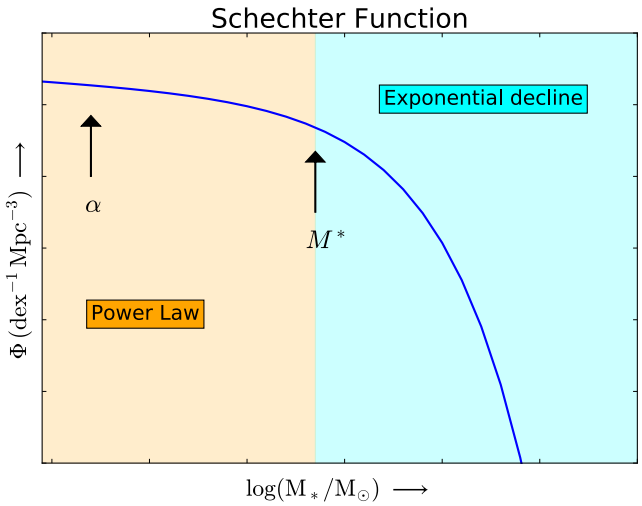

Figure 1.1: Schechter function (Schechter 1976). Used to describe the number density of galaxies (# per Mpc^3), is characterized by a power law behaviour at the low mass end (defined by its slope: α), and an exponential decline at the high-mass end (and a 'knee' or characteristic mass between the two defined by M^*). These two parameters and a normalization factor (Φ^*) are used to parameterize this function, as seen in Equation 1.2.

An important connection between the Schechter function and the evolution of galaxies comes into play when understanding the possible quenching channels of a galaxy: Peng et al. (2010) developed a simple empirical approach to explain how mass, star-formation rates and environments correlate with the cessation of star-formation in galaxies. They found that the effects of mass and environment are fully separable and independent to at least $z \sim 1$. These processes are labelled environmental and mass quenching.

The former, environmental quenching, seems to be independent of mass and cosmic time at a fixed over-density. It appears as an excess of low-mass galaxies (or an upturn at the faint end of the SMF) as large-scale structure develops and galaxies tend to live in higher-density regions (Peng et al. 2010; Peng et al. 2012; Muzzin et al. 2013a; Papovich et al. 2018). This shift causes an apparent acceleration of environmental effects, such as

ram pressure stripping (removal of gas as a satellite galaxy falls into a larger halo), strangulation (supply of cold gas to the galaxy is halted), major merging and galaxy harrassment (high velocity encounters can remove stars and gas from the interacting galaxies). Moutard et al. (2016a) showed that these environmentally quenched galaxies are young quiescent galaxies, expected to have experienced rapid quenching. Low-mass passive galaxies ($log\left(M_*/M_\odot\right) \leq 9.7$) are characterized by denser environments at $0.2 < z < 0.5$, confirming the role the environment (i.e., environmental quenching) has in the observed increase of low-mass quenched galaxies at lower redshifts (Moutard et al. 2018).

The latter, mass quenching, dominates the quenching of massive galaxies. Starting from the assumption that as the stellar mass function of star-forming galaxies evolves (increasing their normalization Φ^*), their characteristic mass (M^*) remains constant. This quenching mechanism is dependent on epoch and leads to the conclusion that the rate at which these massive galaxies quench is proportional to their individual star-formation rates (SFR).

This mechanism will produce a stellar mass function well described by a Schechter function, whose M^* remains the same as the SF population and a faint end slope difference between SF and PEGs of $\Delta\alpha = 1.0$. Even though there is no single physical mechanism that has been found responsible for mass quenching, suggested mechanisms are: virial-shock heating (as gas infalls into a dark-matter halo it will be heated to the halo virial temperature, Dekel & Birnboim 2006) or radio mode active galactic nucleus (AGN) feedback (also known as kinetic-jet feedback, in which the energy released by the jet re-heats the cooling atmosphere impeding further star-formation, Fabian 2012). Following Moutard et al. 2016a, unlike environment quenching, mass quenching is expected to happen over long

timescales (slow quenching: 1-to-a few Gyrs).

The combination of both processes (environmental and mass quenching) generates a double Schechter function for passive galaxies, with its high mass end produced by a mass quenching mechanism (described by the same M^* and a faint end slope that differs by $\Delta\alpha_s = +1$ from that of the original SF population). And a second component, produced by environmental quenching, resulting in a M^* and α equal to the original SF stellar mass function, but an amplitude dependent on the density of the environment.

Constraining a Schechter fit at high-redshifts demands a complete sample, especially of low-number density massive passive galaxies (their low numbers have a high impact on the exponential decline of the number densities). They are important to understand the physical processes in the evolution of galaxies and represent an upper limit on growth and efficiency of feedback mechanisms (e.g. AGN, SN winds). Nevertheless, obtaining a representative sample of these galaxies is observationally challenging as they are extremely rare, specially at high-redshift.

At high redshifts, near-infrared observations are critical to obtain rest-frame optical information. Previous work has been done in trying to constrain the stellar mass function of galaxies at high redshifts (e.g., Ilbert et al. 2013; Muzzin et al. 2013b; Tomczak et al. 2014; Moutard et al. 2016a). However, some of these surveys are performed over a single field (Ilbert et al. 2013; Muzzin et al. 2013b; Tomczak et al. 2014) and are too small ($\sim 1.52\,deg^2$) to recover a large sample of massive passive galaxies. Others are not K-band selected, potentially missing a population of red galaxies (Moutard et al. 2016b). In this work, we build a large ($\sim 27\,deg^2$) catalog of K-selected galaxies over six different fields in order to

obtain a complete sample of high-redshift ($z \sim 1.6$) passive and star-forming galaxies.

In order to build our K-selected catalog, we use optical data from the Canada-France-Hawaii Telescope Legacy Survey (CFTHLS) for both their Deep and Wide fields, in combination with infra-red data from the WIRCam Deep Survey (WIRDS, Bielby et al. 2012) for the Deep fields and the Visible Multi-Object Spectrograph (VIMOS) Public Extragalactic Multi-Lambda Survey (VIPERS-MLS, Moutard et al. 2016b) for the Wide fields.

1.1 Near-infrared surveys

As seen in Figure 1.1, since massive passive galaxies have low-number densities (~ 2 per deg^2, Tomczak et al. 2014; Huertas-Company et al. 2016), it is necessary to obtain deep and wide near-infrared observations. At high-redshifts, a K-selected sample corresponds more closely to a stellar-mass selected sample, where we are observing the light from near-solar, long-lived population of stars with lifetimes similar to that of the host galaxy.

Moreover, at $z > 1$ near-infrared observations are essential to properly identify the 4000 $\AA$ or Balmer break. These two features are representative of intermediate and old stellar populations in the galaxy. Separately, the Balmer break corresponds to the absorption of photons by a free proton to form an excited Hydrogen atom (hence $n = \infty \rightarrow 2$), while the 4000 $\AA$ break is due to blanket absorption in atmospheres of old stars with ionized metals. As can be seen in figure 1.2, at $z = 1.6$, this 4000 $\AA$/Balmer break redshifts past the z band and depending on redshift will lie somewhere between z, H, or K_s bands. Without this near-infrared information, due to the degeneracy between age, metallicity and extinction,

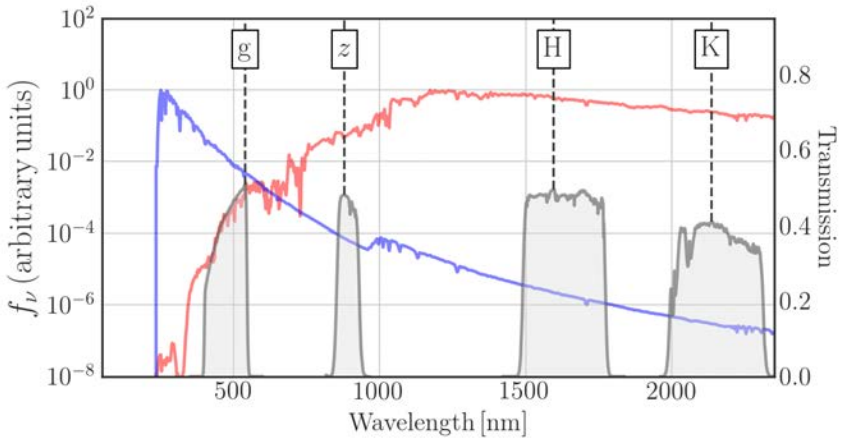

Figure 1.2: Spectral energy distribution for star-forming (blue) and passive (red) galaxies at $z \sim 1.6$. As can be seen from the transmission curves, the 4000 $\AA$/Balmer break in passive galaxies has red-shifted to $\lambda \sim 1040$ nm and lies in the near-infrared region between z and K_s filters.

stellar masses will be uncertain (Moutard et al. 2016b).

Hence, building a representative sample of K-selected high-redshift galaxies will allow us to build a more complete stellar mass function. This is fundamental to understand the physical processes of mass assembly in the evolution of galaxies (Peng et al. 2010; Ilbert et al. 2013) and the evolutionary history of the most-massive passive galaxies.

Improving our understanding of the evolution of galaxies is made possible by advances in large ground-based near-infrared surveys, where early works made significant progress in the identification of massive high-redshift galaxies (Franx et al. 2003; Daddi et al. 2005; van Dokkum et al. 2006). Samples of these surveys are FIRES (0.002 deg^2; Labbé et al. 2003), GOODS (0.04 deg^2; Wuyts et al. 2008), MUSYC (0.12 deg^2; Quadri et al. 2007), NEWFIRM Medium Band Survey (NMBS 0.44 deg^2; van Dokkum et al. 2009), UKIDSS-UDS (0.7 deg^2; Lawrence et al. 2007), WIRDS (2.1 deg^2; McCracken et al. 2010; Bielby et al. 2012), UltraV-

ISTA (1.8 deg^2, McCracken et al. 2012), COSMOS (2 deg^2; Scoville et al. 2007) and VIKING (1500 deg^2; VISTA Kilo-degree Infrared Galaxy Survey, Edge et al. 2013). At high redshifts, limited sizes and the use of a single field makes most of these surveys sensitive to cosmic variance, specially for the red-clustered galaxy population. Large samples of galaxies allow for an improved study of the overall properties of the population of galaxies, and their evolution.

For this work, in Chapters 2 and 3 we built a representative sample of K-selected, high redshift galaxies ($z \sim 1.6$) in an effective area of ~ 27 deg^2 using six independent fields in the sky. In order to do so, we employ an adaptation of the BzK_s colour-colour selection technique, to match the Canada France Hawaii Telescope filters (g, z, and K_s) to build a catalog of star-forming and passive galaxies at high redshift.

1.2 Ultra-Massive Passive Galaxies

In the local universe, the most massive galaxies ($log\,(M_*/M_\odot) > 11.5$) are in general terms a uniform population: they have low specific star-formation rates, tend to live in dense environments and have early-type morphologies (Thomas et al. 2005; Cappellari et al. 2011).

Marchesini et al. (2014), using the K_s-selected COSMOS/UltraVISTA catalog (~ 1.62 deg^2), proposed an evolutionary track for the progenitors of these massive galaxies (local ultra-massive galaxies, $log\,(M_*/M_\odot) > 11.8$, or UMGs). Using a semi-empirical abundance matching method to identify these progenitors, Marchesini et al. (2014) found that the progenitors of UMGs have not lived on the blue cloud since $z = 3$ (albeit SF, their

star-formation rates are significantly higher than the regular blue cloud), in fact, most of the stellar mass has already been assembled at this point via short and intense dusty star-formation, which makes these progenitors dusty, red, massive star-forming galaxies. Once they quench, these progenitors continue to age and grow via minor dry mergers. At $z \sim 1.6$, $\sim 60\%$ of the progenitors of local UMGs are already passive galaxies , and by $z \leq 1$ this number increases to 100%.

Other works also show evidence of the existence of massive passive galaxies when the universe was only 1.5 Gyr old (i.e., $z \sim 4$) (Marchesini et al. 2009; Ilbert et al. 2010; Muzzin et al. 2013a), however, none of these works have large effective areas to recover a representative sample of these rare objects), and some estimates suggest that $20 - 24\%$ of the local population was already in place by $z \sim 2$ (Daddi et al. 2005; Ilbert et al. 2010). This is in apparent agreement with the downsizing paradigm of galaxy evolution (Cowie et al. 1999) where high-mass galaxies form first while less massive galaxies grow more gradually, assembling at later times (Marchesini et al. 2009).

To obtain these high masses $(log\,(M_*/M_\odot) > 11.5)$ in such short amount of times (3-4 Gyr after the Big Bang), these galaxies must have gone through either major mergers or intense burst of star-formation (before quenching, at $z > 2$ these galaxies could have presented star-formation rates $\sim 1000\, M_\odot/yr$; Santini et al. 2017). Given these high star-formation rates, submillimeter galaxies (or SMGs) are the most likely candidates for the progenitors of UMGs. SMGs are a class of ultra-luminous infrared galaxy identified at $z \sim 2 - 4$, their sub-millimeter emission dominated by dust heated from star-formation activity (Pope et al. 2008). Other high-redshift star-forming galaxies, such as Lyman-break galaxies

(LGBs, identified due to a break in their spectral energy distribution at the Lyman limit, Steidel & Hamilton 1993), or Lyman-alpha emitters (LAEs, identified due to the presence of the Lyman alpha emission line, Partridge & Peebles 1967) lack these high star-formation rates at early times.

Building a representative sample of these ultra-massive passive galaxies (UMPEGs) will allow us to constrain the bright end of the stellar-mass function and their best-fit function. As explained in the previous section, if mass quenching is already in place, we expect the Schechter function to describe the number density of galaxies, specifically, its exponential cut-off at the high-mass end. A best fit to our stellar mass function is presented in Chapter 4.

1.3 Evolution of Ultra-Massive Passive Galaxies

Once these UMPEGs are quenched it is also important to understand how they evolve from high-redshifts to the local universe. Specifically, assuming they no longer form stars, how can their environments affect their evolution and change their masses?

Based on that assumption (low star formation), mergers are the main channel through which these galaxies can experience the most change as they evolve to the present. Previous research favors an evolution in which these galaxies evolve mainly through dry mergers while still evolving on as a passive galaxy, possibly increasing the stellar build up in the outer regions of the galaxy and potentially triggering star-forming events (Naab et al. 2009; Hilz et al. 2013). By studying the environment in which these high-redshift passive

galaxies reside we estimate their mass evolution due to mergers.

We can study these interactions through the dynamical friction between the halo of a central galaxy and its satellite galaxies. Chandrasekhar (1943) developed an idealized case of dynamical friction for a rigid object moving in a uniform sea of collision-less matter particles to explain the dynamical friction that stars experience in the field due to near neighbours. Shown in equation 1.3 is Chandrasekhar's original formula:

$$\eta = 4\pi m_1(m_1 + m_2)\frac{G^2}{v^3} log_e \left[\frac{D_0|\ \bar{u}\ |^2}{G(m_1 + m_2)}\right] \int_0^v N(v_1)\, dv_1, \tag{1.3}$$

where m_1 and m_2 are the masses of a given field star and the star under consideration, G is the gravitational constant, $|\ \bar{u}\ |^2$ is the mean square velocity of the stars, D_0 the average distance between the stars, $N(v_1)\, dv_1$is the number of field stars whose velocities are distributed within $v_1$and $v_1 + dv_1$ and v is the velocity of the star.

This concept of dynamical friction can be applied to a satellite orbiting a more massive central galaxy. Its orbit deflects as it moves in the central galaxy dark matter halo, suffering a steady deceleration and eventually merging with the central galaxy. This type of interaction is more complicated than the simple movement of a solid object in a uniform sea for a couple of reasons: there is a change in density as the satellite is stripped of its material due to the interaction and this material will trail such satellite creating an external drag force (Jiang et al. 2008).

Using two adaptations of dynamical friction time, and the statistical nature of satellite galaxies around UMPEGs, we can estimate in Chapter 5 an approximate evolution of these

galaxies from $z \sim 1.6$ to $z \sim 1$. The first of these adaptations, presented in Jiang et al. (2008) is shown in equation 1.4:

$$T_{merge} = \frac{0.94\varepsilon^{0.60} + 0.60}{0.86} \frac{M_{cent}}{M_{sat}} \frac{1}{ln\left(\Lambda\right)} \frac{r}{v}, \tag{1.4}$$

where,

$$ln\left(\Lambda\right) = ln\left(1 + \frac{m_{cent}}{m_{sat}}\right),$$

m_{sat} is the mass of the satellite, m_{cent} the mass of the central UMPEG, r is the radius of the satellite orbit, v is the velocity of the satellite around the central UMPEG, and ϵ is the eccentricity of the satellite's orbit. The second equation, presented in Kitzbichler & White (2008) is shown in equation 1.5:

$$T_{merge} = 3.2Gyr \frac{r_p}{50kpc} \left[\frac{M_*}{4 \times 10^{10} h^{-1} M_\odot}\right]^{-0.3} \left(1 + \frac{z}{20}\right), \tag{1.5}$$

where r_p is the projected separation between a pair of close galaxies, M_* is the mass of the satellite and z is the redshift at which the interaction is taking place.

1.4 Groups with Passive Massive Galaxies

Of equal interest is the study of environments with an over-density of relatively massive passive galaxies ($log\left(M_*/M_\odot\right) \sim 11.14$). In the argument between nature vs nurture, it is clear that galaxies are influenced by external events: their evolution will be impacted by a

higher probability of galaxy interactions (e.g., galaxy harassment Moore et al. 1996, strangulation Peng et al. 2015, ram-pressure stripping Gunn & Gott 1972, dynamical friction Boylan-Kolchin & Ma 2007, minor and major mergers Schawinski et al. 2014) during their formative years.

For instance, galaxies that live in dense environments have been found to have different morphologies, colours, symmetries and metallicities than isolated galaxies (e.g., Dressler 1980; Visvanathan & Sandage 1977; Oemler 1974). The well known halo assembly bias (Miyatake et al. 2016) suggests that the properties of galaxies that reside in dense environments are dependent on the mass of the halo and its formation time. However, it is often difficult to understand the underlying cause of many of these effects, and to fully understand the importance environment plays in shaping them.

Clusters constitute an over-density of gravitationally bound (but not necessarily virialized) galaxies. Following a Oemler (1974) classification, they are divided into 3 kinds:

- cD clusters: These kind of clusters have a dominant (or two) cD galaxy (elliptical galaxies with a large diffuse envelope, Matthews et al. 1964) and are characterized by a high number of elliptical and S0 galaxies.

- Spiral rich clusters: As explained by their name are dominated by spiral galaxies ($\sim 50\%$) similar to the distribution of galaxies found in the field.

- Spiral poor clusters: Have no dominant cD galaxy and their most common population are S0 galaxies.

In the local universe, morphology is strongly correlated with environment (morphology-

density relation, Dressler 1980; Oemler 1974), where elliptical and S0 galaxies are more commonly found in dense environments. In addition, clusters contain a large number of passively evolving galaxies. This relation is still present at relatively large redshifts ($z < 1.5$), where the dominant population of galaxies are still elliptical and S0s (Hilton et al. 2009; van Dokkum & Franx 2001). However, at higher redshifts ($z > 2$), star-forming galaxies start to become the dominant population (Noirot et al. 2016), such that clusters are identified by detecting high concentrations of Lyman break galaxies or radio sources (Daddi et al. 2017; Toshikawa et al. 2016).

High-redshift progenitors of clusters are labelled proto-clusters. Although there is no consistent definition to distinguish between the two (i.e., proto-cluster and cluster) often, clusters are defined as massive, virialized structures ($M/M_{\odot} \geq 10^{14}$, Bowler et al. 2014; Overzier 2016), while a proto-cluster is an over-density (compared with its surroundings) at any redshift, that will become a virialized, massive structure before $z \sim 0$ (other more conservative approaches can also include the detection of thermal intra-cluster medium, ICM).

The redshift range $1.4 < z < 2.0$ is an important epoch in the evolution of clusters (and proto-clusters, if we assume their members will be part of the same halo by z=0, Diener et al. 2013) since this is the time when elliptical galaxies start to become the dominant population and star-formation is being quenched in spiral-type galaxies (Nantais et al. 2013; Stanford et al. 2012; Strazzullo et al. 2010). This is not unexpected, given that on average, galaxies in high-density environments tend to form earlier than galaxies in the field and formation redshifts of clusters are high. Hence passive galaxies up to this redshift are a

good tracer of high density peaks in galactic structure (Strazzullo et al. 2015; Nantais et al. 2016).

There are several techniques to identify clusters at different redshifts: looking for concentrations of red-sequence galaxies (such as the Spitzer Adaptation of the Red-sequence Cluster Survey or SpARCS, Muzzin et al. 2009), search of over-densities in redshift space (Chiang et al. 2014), the presence of an ICM (due to inverse Compton scattering between the hot plasma and microwave background photons, causing an apparent change in their brightness, Andreon et al. 2014; Bleem et al. 2015), or by searching the environment around galaxies known to be good tracers of clusters (such as high-redshift radio galaxies, or AGNs, Overzier 2016, Collet et al. 2015, Noirot et al. 2018). Regardless, proto-clusters allow us to investigate this red-sequence formation and understand the transition from a cold flow to a hot regime in clusters (below a given critical halo mass, star-formation is not interrupted by virial shock heating, whereas at higher masses, all accreted gas is shock heated and requires longer cooling times, Dekel & Birnboim 2006).

This is why, in Chapter 6, we perform a search of over-dense massive passive galaxies at $z \sim 1.6$ and perform a statistical analysis of galaxies residing in these environments by kind (star-forming vs. passive).

Chapter 2

Data

In order to assemble a representative sample of passive galaxies at high redshift, we require observations that fulfill two important characteristics: first, images need to be deep enough to sample low mass galaxies and second, cover large effective areas to obtain a significant number of rare massive passive galaxies.

In Arcila-Osejo & Sawicki (2013), as a follow up to my M.Sc. Thesis, we used the Deep T0006 release (refer to section 2.1 and Goranova et al. 2010) to build the stellar mass function of passive, high redshift galaxies selected using a modified BzK_s selection criteria (defined in Section 3.1 as ($z-K_s$) vs. (B-z) colors; Daddi et al. 2004). With this sample, we were able to constrain the faint end of the stellar mass function, and probe the existence of a mass-dependent quenching scenario. Nevertheless, due to small areas, we were unable to recover a representative sample of massive passive galaxies at high redshift. In order to obtain a sizable sample of this rare population, we complemented our catalog with photometry from 47 pointings from the T0007 release of the Wide survey (Hudelot et al. 2012).

Due to the large areas of the Wide survey, we are now able to reach a better understanding of the number statistics of these rare massive passive galaxies.

In this Chapter, we build a K_s-selected catalog, since the infrared light from these high-redshift 'dead' galaxies will be dominated by low-mass, long-lived stars, an infrared-selected sample will closely match a stellar mass-selected sample. Moreover, we complement the infrared data, with optical information to classify them (using a (z-K_s) vs. (g-z) colour-colour technique. Refer to section 3.1).

2.1 Data

2.1.1 Optical Data: The Canada-France-Hawaii Telescope Legacy Survey

The Canada-France-Hawaii Telescope Legacy Survey (CFHTLS) is a large collaborative project composed of two main surveys: Deep and Wide. The Deep survey consists of four independent, ultra deep, one square degree pointings labeled D1, D2, D3 and D4: this survey was developed to detect type Ia supernovae and study galaxy distribution. On the other hand, the Wide survey consists of 171 pointings (when discussing pointings, we refer to approximately one square degree telescope pointings that follow the field of view of the optical imager at CFHT) that combine into four main fields: W1, W2, W3 and W4. Due to an overlap between contiguous pointings, the survey covers a total of 155 square degrees. The purpose of this survey is to study matter distribution, large scale structure and clusters of galaxies. For this work, we used all four Deep fields in combination with two Wide fields: W1 and W4.

The optical survey was carried out using MegaCam, the wide-field optical imager at MegaPrime. MegaCam CCD pointings cover (1 x 1) deg^2 field of view with a sampling of 0.186 arc seconds per pixel. Each of our four Deep (D1-4) and two Wide (W1, W4) fields was observed in five broad-band filters (u*, g′, r′, i′, i2′ -the release contains data from two similar i filters: the original i′ and a replacement i2′ (also called y′) installed in 2007- and z′. See Figure 2.1). For the Deep fields, the 80% completeness limit for extended objects in g band is 25.29, 25.30, 25.29 and 25.26 and for the z band is 23.83, 23.90, 23.71, 23.76 AB mags respectively for D1, D2, D3 and D4 (Goranova et al. 2010). Likewise, for the Wide fields, W1 and W4, in the g band completeness limit is 24.67 and 24.71, and in the z band is 22.91 and 22.90 respectively (Hudelot et al. 2012). For the filters used in our analysis (g and z, refer to section 3.1) the full width at half maximum (FWHM) of the point spread function (PSF) was determined using bright, random, non-saturated stars to be approximately ~ 3.7 pixels in the Deep fields and 5 pixels in Wide for both filters (i.e., g and z).

Terapix[1], dedicated to the data reduction and processing of large data from different surveys, was involved in the process of data acquisition and pre-processing. Pre-processing involves image quality checking, flat fielding, stacking of dithered images, identification of bad pixels, removal of cosmic rays and saturated pixels, background estimation and astrometric and photometric calibration. Finally, Terapix is also involved in archiving and providing data products to the scientific community.

As previously mentioned, for the Deep fields, we used optical photometry from the T0006 release, while for the Wide fields, we use the T0007 release. One of the key dif-

[1]http://terapix.iap.fr/

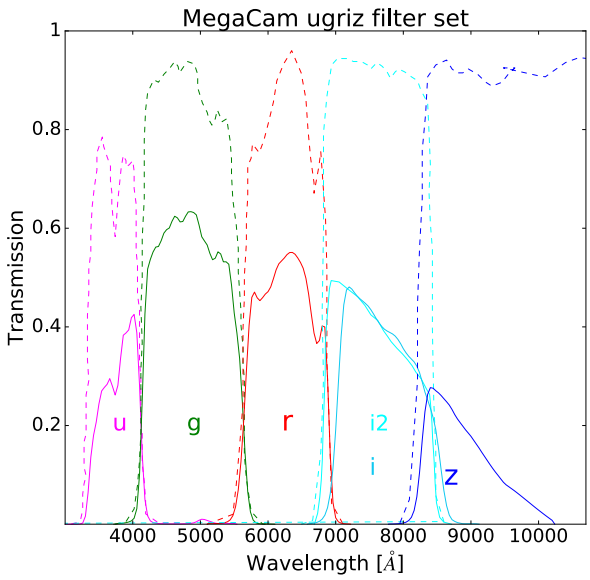

Figure 2.1: MegaCam Filter set transmission curves. Dashed lines represent transmission curves, while solid lines represent the total response of the system once the filter transmission has been multiplied by the telescope response. Information taken from the MegaPipe image stacking pipeline at http://www.cadc-ccda.hia-iha.nrc-cnrc.gc.ca/en/megapipe/docs/filt.html.

ferences between these two releases is a different photometric calibration: For the T0006 release, Terapix used the Two Micron All Sky Survey (2MASS) reference sources to perform field-to-field flux rescaling of each image and was later verified by comparing them with bright Sloan Digital Sky Survey (SDSS) sources available in overlapping regions. On the other hand, for the T0007 release, Terapix used standard field stars from the Supernova Legacy Survey (SNLS) as calibrators. Due to this different calibration, we have noticed a shift in the z band between the two releases.

In order to investigate this shift we downloaded images in all filters for the pointing in W1 labeled as 020241-050800 for both the T0006 and the T0007 releases. We performed

object extraction and photometry in the same pointing in the sky but for different releases (T0006 and T0007) while maintaining the same SExtractor's (Source Extractor, Bertin & Arnouts 1996, version 2.19.5) parameters for both procedures.

The main outcome from performing this photometry for both releases can be seen in Figure 2.2 . As can be seen from the orthogonal regression fit there seems to be a systematic magnitude shift in the z magnitudes of 0.107 ± 0.001 between the T0006 and T0007 releases (no other significant shifts were found for other bands). This systematic shift was already presented in Moutard et al. (2016b), where they reported a systematic shift of 0.148 ± 0.054 the difference in this range of uncertainties does not significantly affect our results. We take into account this difference between the two surveys when constructing our combined catalog to ensure that our new sample from the Wide survey matches the T0006 calibration of our Deep sample, hence converting the T0007 to the T0006 calibration. As presented in Moutard et al. (2016b), there is no other systematic shift in the other optical photometric bands.

2.1.2 Infrared Data: WIRDS and VIPERS-MLS

To complement the Deep and Wide optical observations, we added infrared observations from the Wide-field Infrared Camera imager (WIRCam) at the Canada-France-Hawaii Telescope (CFHT), WIRCam consists of four detectors in a 2×2 array with 2048×2048 active pixels, which covers 20×20 arcmin field of view with a sampling of 0.3 arc seconds per pixel. It has four broad-band filters, Y, J, H and K_s (filter transmission curves shown in Figure 2.3) , and seven narrow-band filters.

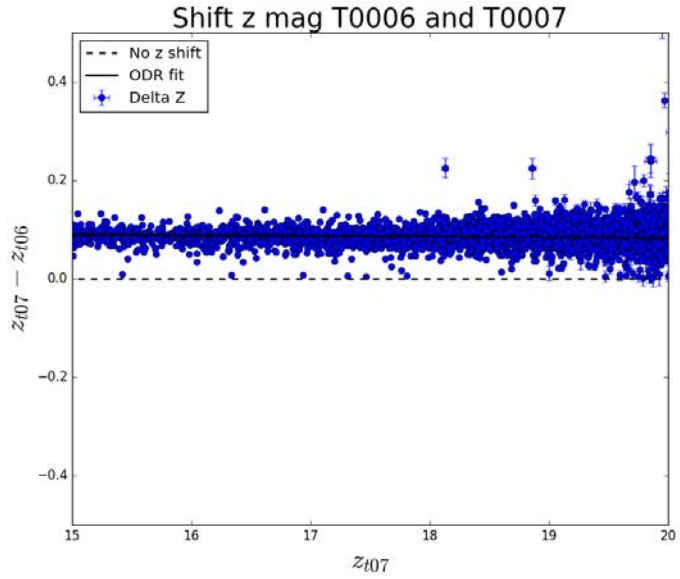

Figure 2.2: Systematic shift in z magnitudes between the T06 and T07 CFHTLS Releases . To account for this shift, we subtracted from all z magnitudes in the T0007 release a value of 0.1 magnitudes so that it matches the calibration of the T0006 release.

To complement the Deep survey optical observations, we used the WIRCam Deep Survey (or WIRDS) (Bielby et al. 2012) . WIRDS was a large project carried out during 2006 to 2008 to obtain near infrared, broad band photometry for the four Deep fields. The results for this survey included images from the J, H and K_s filters that have been re-sampled to match the pixel scale of MegaCam. Nevertheless, since the field of view of WIRCam is smaller than that of MegaCam, most of the effective areas for the Deep fields are less than one square degree (with the exception of D2 which is part of the COSMOS field). Our data were obtained through the Terapix T0002 WIRDS release. For the WIRCam Deep Survey, a 50% completeness limits for point-like objects is reached at 24.5 AB mags (except for D2, which corresponds to a limit of 24.0 AB mags) (Bielby et al. 2012). For this release, Bielby et al. (2010) reports a PSF FWHM of $\sim 3.2 - 3.7$ pixels.

Through private communications (Arnouts S.), we obtained K_s observations for 47 pointings (one square degree telescope pointings that match their optical observations) of the Wide survey from the Visible Multi-Object Spectrograph (VIMOS) Public Extragalactic Multi-Lambda Survey or VIPERS-MLS[2]. The VIPERS-MLS incentive was to conduct a follow-up of the CFHTLS Wide fields using WIRCam K_s observations (Moutard et al. 2016b) with a 80% completeness limit of $K_s \leq 22.0$. The K_s band calibration matches that of the WIRDS Survey used for the T0006 release (As stated in Moutard et al. (2016b) K band calibration matches well the VIDEO and UKIDSS data in the overlapping regions). The PSF in all K_s images from VIPERS-MLS are uniform, with a FWHM of $\sim$3 pixels.

In Figure 2.4 we show the layout of our g, z and K_s coverage in W1 (represented in blue), W4 (cyan). As well as g, z, H and K_s coverage in D1 to D4 (in different shades of purple). As can be seen in the figure, the two Wide fields cover a significantly larger area than those sampled by the Deep fields (the largest of the Deep fields is D2, which covers one square degree in the sky).

2.2 K_S-selected Catalogs

We used Source Extractor, or SExtractor (Bertin & Arnouts 1996, version 2.19.5) to perform source detection and photometry in each pointing. SExtractor is a software developed to detect, measure, classify, and perform photometry from astronomical images.

Before running SExtractor, we either created or downloaded previously constructed external masks to identify spurious regions in the images. It is important to create masks

[2]http://cesam.lam.fr/vipers-mls/

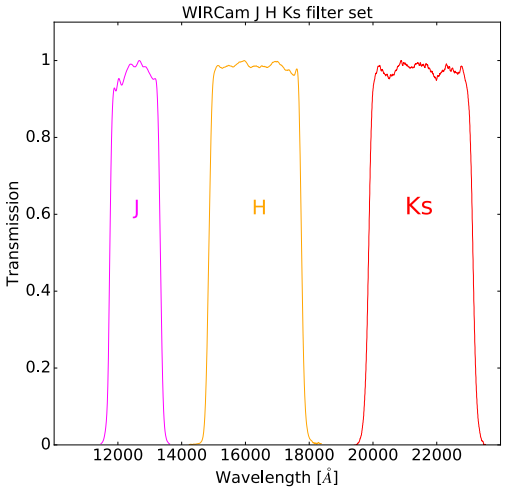

Figure 2.3: WIRCam Transmission for the broad-band filters. Information taken from CFHT Instruments and Manuals found at http://www.cfht.hawaii.edu/ Instruments/ Filters/wircam.html.

of areas where detection and photometry may be compromised. For instance, sources that overlap with the reflective halo or blooming from a bright star (see Figure 2.5), a cosmic ray trail, or a dead pixel. Starting with the image associated with each filter, if available, we downloaded and visually inspected a catalogue of masked regions (only available for the Wide optical images [3]). Otherwise, by visual inspection in each filter, we created region files that include all these spurious pixels. Subsequently, we transformed these region files into fits files that assign a value of 1 to any pixel inside these regions and 0 elsewhere. These flag images are different from SExtractor's internal flags, which are a default output of SExtractor (see table 2.1), hence, we refer to them as external flags. External flags are normally created by the user in order to identify detected sources in 'bad' or compromised pixels (for the full explanation on how this was done see Section 2.2.1).

[3]http://www.cadc-ccda.hia-iha.nrc-cnrc.gc.ca/en/megapipe/cfhtls/uc.html

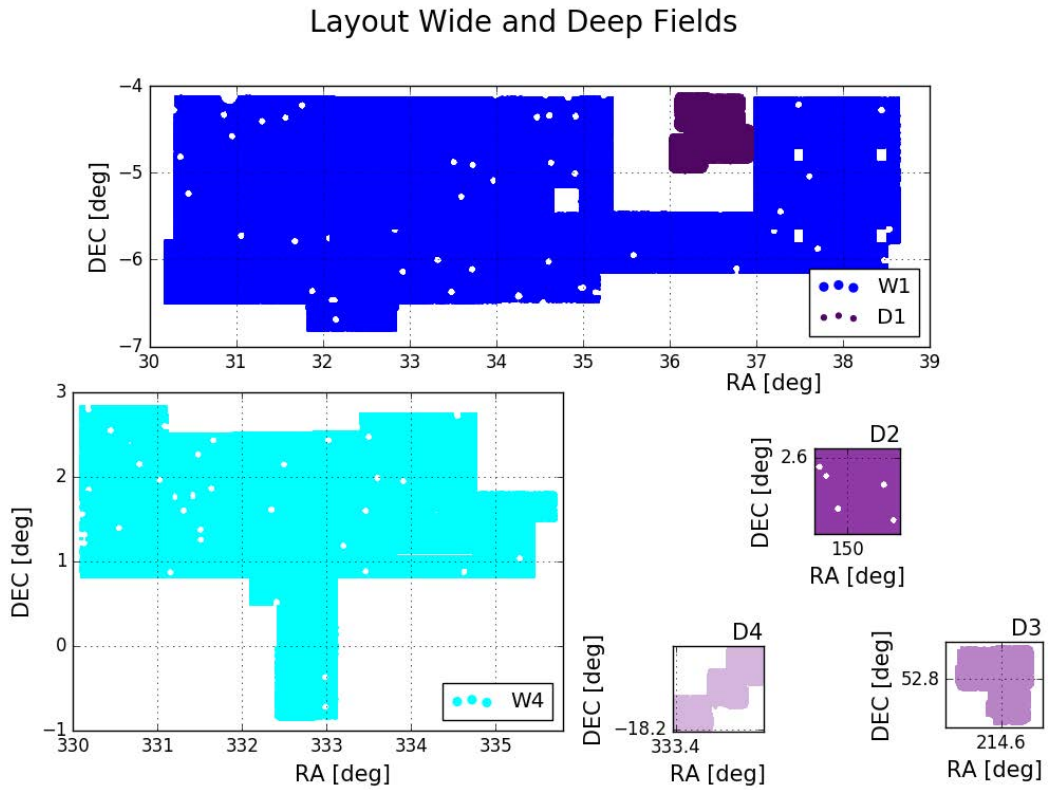

Figure 2.4: Layout of W1 and W4. For our catalog, W1and W4 are comprised of 28 and 19 overlapped pointings respectively. Gaps in each plot represent either areas where there is no K_s observations available or where the area has been masked due to the presence of bright stars or spurious objects . Each field is scaled with size (e.g., for reference, D2 covers $\sim 1\, deg^2$ in the sky).

SExtractor was run in dual image mode. This means that objects were detected in the K_s band images, followed up by their magnitudes determined from all given bandpasses. It is important to perform detection of sources in the K_s band because our desired population of dead passive galaxies are most likely devoid of short-lived blue stars. Hence their spectral energy distribution will be dominated by long-lived, less bright stars, making them significantly fainter in the optical bands. Therefore, if we were to make our selection based on an optical band, we could face incompleteness due to non-detections.

A given source was identified in the K_s image based on it having a signal that was at least five contiguous pixels above a detection threshold. Due to the different science objectives between the Wide and Deep surveys, exposure times for the Deep survey were considerably larger than for the Wide. Empirically, by visual inspection, the determined detection threshold for the Deep fields was 1.2σ, whereas for the Wide fields it was 1.5σ above the sky level (in order to avoid correlated noise in the Wide fields). Photometry is then performed at the K_s band positions in g, z, H (if available), and K_s.

For the Deep and Wide fields, total fluxes were calculated using auto mags (total magnitudes from a Kron-like aperture). Additionally, since in the Deep fields we probe to fainter magnitudes, to determine colours we used circular magnitudes (within a 10 pix aperture, or 1.86") from point-spread-function matched images performed by Dr. Taro Sato (Sato et al. 2014). Obtaining colours for the Deep fields in this way, ensures that our ten pixel apertures sample the same flux fraction in the various bandpasses. For the Wide sample, since we are only recovering the brightest sources in these fields, their signal-to-noise ratio is higher than in the Deep fields. This is why we employed total magnitudes to determine

their colours.

Since we needed to obtain images, generate and stack masks (see Section 2.2.1), and perform photometry on 51 square degrees (one for each of the four bands) this required a parallelization of the process: In order to achieve this, we used the Atlantic Computational Excellence Network (or ACENet[4]), a large scale high-performance computing facility that provides computing resources, training, software and visualization tools for research. Open message passing interface (an implementation of MPI) is specifically useful for this project, even though the communication between nodes was minimal, it allowed us to do the processing in each filter in parallel.

In the automatization process while the main node downloaded all necessary images, all other available nodes worked in parallel to transform region mask files into flexible image transport system (FITS) images and stacked them to create external flags. Later on, the same nodes performed source extraction on each filter, hence each node was assigned to work on an individual filter. This work was performed in a loop to work on all Wide and Deep pointings.

The products of this process are: flag images (identifying areas affected by bright stars, dead pixels, etc) a stacked image of all flags, a check output FITS file showing detected objects and a final merged detections catalog of all the sources in both the Wide and Deep fields ($\sim$ 2,000,000 extracted objects, before taking into account masking or completeness limit). Overall, our data is about 3 TB of information including sub products for all 51 square degree pointings.

[4]http://www.ace-net.ca/

Number	SExtractor internal flags and user's external flags
1	The object has neighbors, bright and close to bias the photometry,
	or bad pixels (more than 10% of the integrated area affected).
2	The object was originally blended with another.
4	At least one pixel of the object is saturated (or very close to).
8	The object is truncated (too close to an image boundary).
16	Object's aperture data are incomplete or corrupted.
32	Object's isophotal data are incomplete or corrupted.
64	A memory overflow occurred during deblending.
128	A memory overflow occurred during extraction.
256	Bright star, halos, cosmic rays or any other spurious object.
512	Dead pixel or outside of boundaries

Table 2.1: SExtractor's internal flags ($\leq$128) and our defined external flags (256 and 512). These are present as an output product during photometry.

2.2.1 External Flags

As mentioned in the previous section, one important input parameter when performing source extraction is external flags. In these, we store information about the quality of any given pixel in the image. They are a stacked result of our visual identification and removal of cosmic ray trails, bright halos from stars, diffraction spikes, and dead pixels. These external masks are used as input in our SExtractor runs.

For the Wide optical images, external flags of bright stars and cosmic ray trails were taken from Erben et al. 2012. We performed a visual inspection of each one of the 235 masks to ensure the masking was correct. In contrast, since the K_s band images are not public there are no available public external masks. Consequently, for the Wide infrared images (K_s band) we created our own external masks. Similarly, for the Deep Fields, both optical and infrared bands, we constructed our own external flags from visual inspection of the different bandpasses.

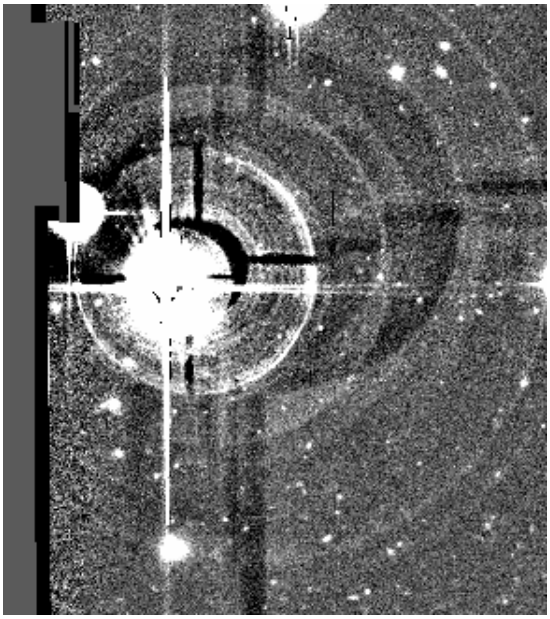

Figure 2.5: Diffraction spike and bright halo around a bright star in W1_020241-050800, the mask ensures that any source identified in these areas will be flagged as a potential artifact.

Internal flags are always an output from SExtractor. They inform the user if, for example, a source was truncated or if it is saturated (for a list of the possible outputs of this internal flag please refer to Table 2.1). If a source was identified as having an external flag in either g, z, H (in the Deep fields, refer to section 3.1.1) or K_s, or an internal flag larger than four, it was not included in the catalog since this will affect its classification. Sources with internal flags larger than four or with external flags, represent approximately 4 and 1 percent of our sample, respectively.

2.2.2 Building a combined catalog for both the Deep and Wide surveys

Once we obtained SExtractor's output catalogs, it was important to create a combined catalog of all sources. In order to build this catalog of the Deep and Wide surveys, first we

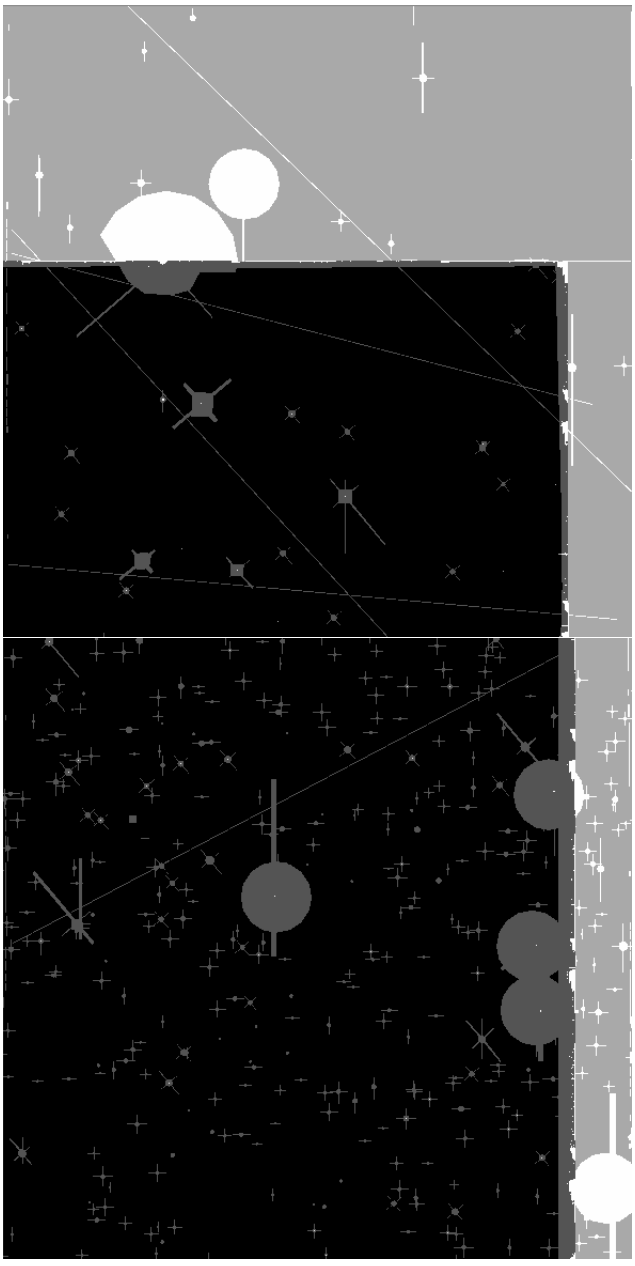

Figure 2.6: Sample stacked masks for two pointings: One in W1 (top) and another in W4 (bottom). The black areas represent good pixels, which means that detected objects will be considered as good only if they reside in a non-masked environment. Also visible is the masking of bright stars and cosmic rays, as well as the limits of our K_s images compared to the optical ones, and any other spurious object. Each one of these images represents a one square-degree pointing in the Wide fields.

needed to combine all the individual pointings that comprise both W1 and W4. Since all contiguous pointings in the Wide fields partially overlap (see Figure 2.7), when building a combined catalog for W1 and W4, it is important to identify these regions and make sure our final catalog does not have duplicate sources.

To account for overlapped contiguous areas, we could query for duplicates within the full catalog. This, however, is time consuming in catalogs with approximately 1 000 000 objects, especially since there could be more than one duplicate such as in the corner of an image.

To make things more efficient, we used KDTree (k-dimensional tree) algorithms, where the catalog matching was performed by assigning the first pointing in the field as a master catalog. Then, we cross matched this tree catalog with the next available pointing in the field; its adjacent neighbour (ensuring a radius of search larger than the average size of galaxies). Once these two adjacent pointings were cross matched and we identified that there were certain duplicate sources, based in position and magnitude, we take the inverse-variance weighted average of their fluxes (and their associated errors given by $\sigma^2 = 1/\sum(1/\sigma_i^2)$). Following the completion of the cross matching, the first and second pointings were added together taking into account repeated objects. These adjacent pointings were now defined as the master tree catalog, hence we are ready to add the next adjacent pointing. Figure 2.8 shows the K_s magnitude difference between matched objects in two adjacent pointings.

Whenever we would find an object that was determined to be a positive match based on position, but not on magnitude, we created a separate file of potentially problematic

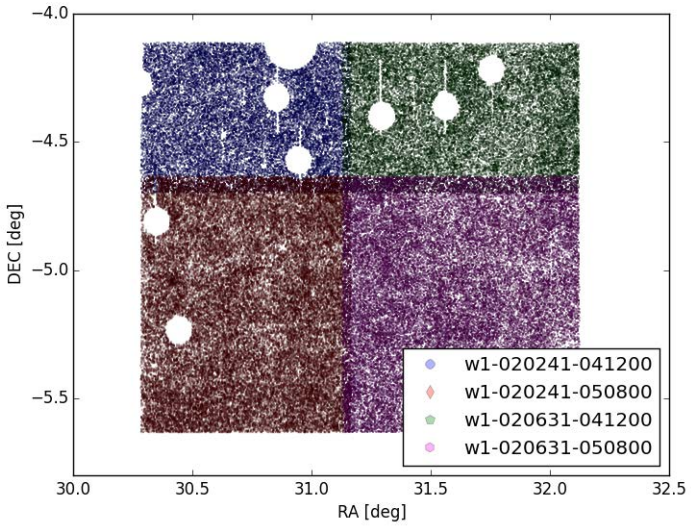

Figure 2.7: Overlap between four adjacent pointings in W1. Darker regions represent those areas in which these four pointings overlap, hence duplicate objects present in these areas need to be merged when creating a combined catalog. White empty spaces represent masked stars in the field.

sources. If any of these problematic sources were either classified as a passive or star-forming $gzK_{s,}$we carefully analyzed their differences in magnitudes. For the most part, these problematic sources were faint and close to the edges of the image, and although they represented the same object, their magnitudes were significantly different in adjacent pointings ($\Delta mag > 0.5$). Under other circumstances, we found that one source had a closely positioned companion within our search radius. Hence, this companion was discarded as a positive match. Consequently, only one of these 400 problematic objects was truly part of the population we want to further understand: passively evolving galaxies as classified by an adaptation to the BzK_s selection technique (section 3.1). Sources that were identified as too noisy and past the completeness limit of the sample (which will be further explained in Section 3.3) were catalogued by their first documented magnitude, and

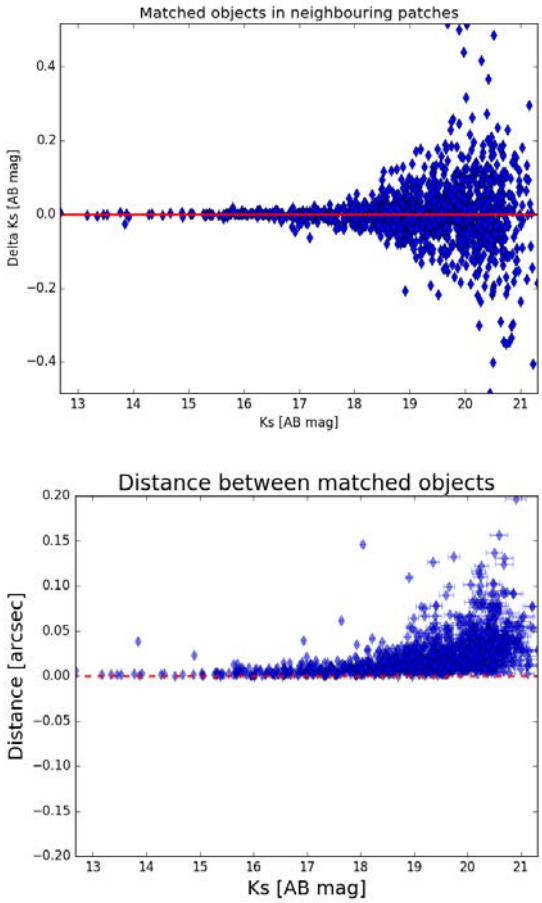

Figure 2.8: Top plot: K_s-band magnitude difference for a sample of matched objects in two neighboring pointings. Bottom plot: Distance between matched objects in neighboring pointings. For both plots, these objects have been matched based on the closest source found around a radius of 1.08 arc seconds (the center of this circle, whose radius is $\sim 40\%$ larger than the average size of galaxies in the image, is the position of the object we are analyzing for possible duplicates).

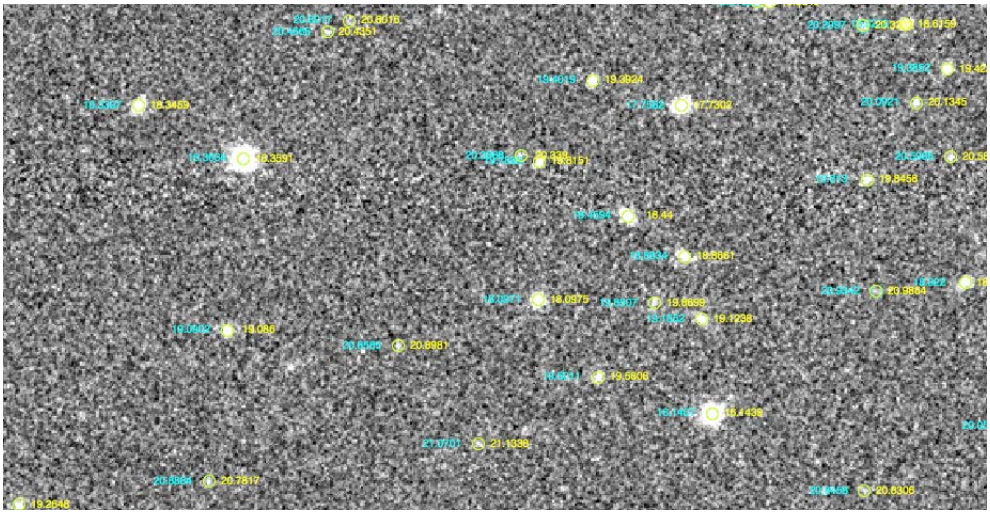

Figure 2.9: Sample region file of objects that were matched as duplicates in adjacent neighbors in W4. Shown in cyan are the magnitudes the object had in the original catalog and in yellow the magnitudes of the object that was matched as a positive duplicate of this object based on position and magnitude.

an average of their fluxes was not considered. This means the object is present in the catalog, but its duplicate data was not taken into account. Moreover, these objects are not part of the passive or star-forming gzK_s population, but for future use of the present catalog, specifically for fainter objects, a more suitable approach should be used.

Lastly, since none of the Deep fields overlap with the Wide fields, the Deep fields were treated independently and included in our master catalog.

2.3 Effective Areas

In order to determine the effective areas of both the Deep and Wide final catalogs we used our stacked flags. As mentioned during the process of extracting our objects from the images in Section 2.2, we generated external flags to mask regions that could present a

potential bad area: diffraction spikes from bright stars or cosmic rays. The output we obtained from these images was a FITS file with the same dimensions as each one of our individual pointings, with each pixel value being either 0, 256, 512 or a combination of these numbers (refer to table 2.1). The value zero represents a 'good' or usable pixel and everything else was a 'bad' or masked pixel. For more specific details refer to the section on source extracting 2.2.1. We took each individual pointing in our fields and added all the pixels that had a value of zero. Furthermore, we multiplied the number of 'good' pixels by the value of the area in degrees of each pixel. This procedure allowed us to obtain the effective area for each pointing in the Wide fields, and for each independent Deep field.

Nevertheless, as previously shown, the Wide fields, W1 and W4, are comprised of several individual pointings that overlap slightly both in RA and DEC by a few arcmins. Due to this, simply adding the area of each individual pointing could lead to overestimating the value of the area in each field, hence we need to account for these overlapping regions.

In order to overcome this, we individually added each individual pointing to our final grid, for instance W1 or W4, and once a new pointing was added into the grid, we analyzed if there was an overlapped area with the existing one. If there was, the overlapped area was removed in order to not overestimate the effective areas in our sample. Then, we added the next contiguous pointing until we filled the total grid. Through this method, we ensured that we accounted for small masked stars that could represent a significant number due to large numbers and also account for those areas that are overlapped between contiguous pointings.

2.4 Dust Correction

An important step in our data manipulation is to correct for dust present in our own Galaxy, which absorbs light and re emits it at longer wavelengths. The amount of reddening depends on the column density of the foreground dust and the wavelength of the incident photons.

In order to correct for this effect, we have used the Schlegel et al. (1998) galactic dust maps with the updated reddening correction by Schlafly & Finkbeiner (2011). Schlegel et al. created dust maps of the full sky by taking advantage of composite maps from COBE and IRAS and determined the dust distribution using a ratio of the 100 μm to 240 μm maps. Schlafly et al. introduced a new calibration of these maps by analyzing the spectra of multiple stars in the Sloan Digital Sky Survey (SDSS).

Given the position in the sky of each galaxy, using these dust maps along with the suggested calibration, we applied a correction to the photometry. A sample of the galactic extinction values within a patch of W1 is shown in Figure 2.10.

Summary

Up until this point we have created a full combined catalog of detected sources both in the Deep and Wide fields. In the following chapters we will use colour-colour diagrams to classify our sample as gzK_s passively evolving (PE) or star-forming (SF) galaxies (for a full definition please refer to Chapter 3). In total, we have recovered approximately 700,000 sources in a total effective area of 27.6 deg^2. A full summary for each field can be found in

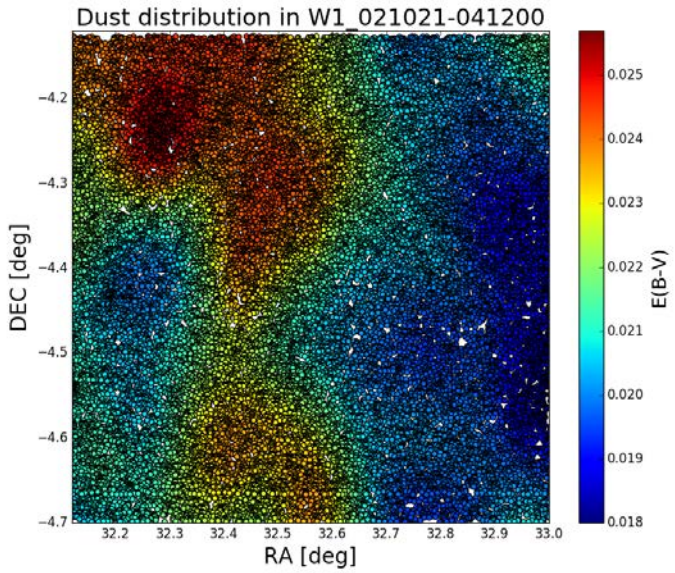

Figure 2.10: Sample of extinction values across one pointing in the Wide Fields. Each source in our combined catalog has a corresponding correction due to dust extinction based on their specific location on the sky.

Table 2.2.

Field	Area [deg^2]	Total Sources	gzK$_s$ galaxies	Depth SF sources	Completeness	Depth PE sources	Completeness
D1	0.69	71712	16517-18804	23.5	80%	23.5	67%
D2	0.91	109490	16821-22897	23.5	52%	23.0	55%
D3	0.45	48425	10490-11795	23.5	80%	23.5	67%
D4	0.46	48757	10160-12090	23.5	75%	23.5	55%
W1	15.53	236213	5502	20.5	100%	20.5	90%
W4	9.56	191570	3254	20.5	100%	20.5	90%

Table 2.2: Summary of detected sources in all Deep and Wide fields. The area represents the effective area once external flags have been taken into account. The total number of sources includes all galaxies (once they have been masked), irrespective of redshift and stars to a limiting magnitude of 23.5 for the Deep Fields and 20.5 for the Wide Fields (their different completeness limit is the reason why the number of galaxies does not scale directly with effectife area). gzK$_s$ sources are high-redshift objects (z$\sim$1.6) that have been identified either as star-forming or passive based on their location on a (g-z) vs. (z-K$_s$) colour-colour plot (see Section 3.1). The Depth in this table represents the completeness limit of our sample given the nature of our sources (star-forming or passive). If a range is given, the lower value indicates gzK$_s$ galaxies that are unambiguously selected as star-forming galaxies at $z \sim 1.6$, while the higher value includes possible low-redshift interlopers (i.e., it includes all SF-classified galaxies, even if they were not detected in g.). For more information please refer to Subsection 3.1.1.

Chapter 3

Results: Sample Selection and Number Counts

3.1 The BzK$_s$ and gzK$_s$ colour-colour selection

As part of my Master's Thesis, we developed an adaptation of the BzK$_s$ Selection Technique (Arcila-Osejo 2011, Arcila-Osejo & Sawicki (2013)) in order to classify and distinguish between passive and star-forming galaxies at high redshift, while using the CFHT, g, z and K$_s$ filter set.

Daddi et al. studied the evolution of BzK_s colors of galaxies by modeling colous of passive and star-forming galaxies using Bruzual & Charlot (2003) stellar population synthesis models with constant star-formation and instantaneous burst models, along with several reddenings and ages. This selection is based on the identification of the $4000\mathring{A}$/Balmer break in passive systems (refer to Introduction), using a color difference between the z

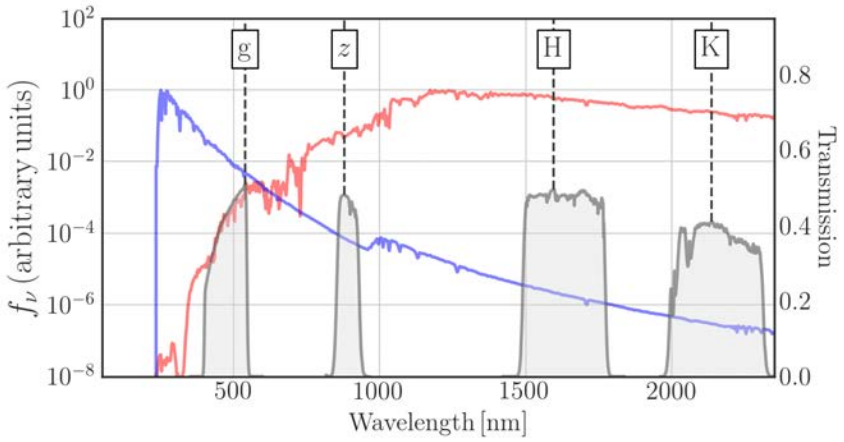

Figure 3.1: Mock SEDs of star-forming and passive galaxies at $z \sim 1.6$, shown with MegaCam's g and z and WIRCam's H and K_s filter transmission curves. As can be seen, the presence of an evolved stellar population in the SED of the passive galaxy is represented by the evolution of a break redshifted to $\lambda \sim 1100$ nm.

and K_s filters (shown in Figure 3.1, as in the introduction, shows SED models for SF and PE galaxies, for the latter, at $z \sim 1.6$ we can observe such break redshifted to $\sim$ 1100 nm). To distinguish between reddening in a galaxy due to this break or dust, the diagonal line shows the parallel evolution in colors for galaxies with constant star-formation and increasing reddening.

As can be seen in Figure 3.2 the z and K_s filters are somewhat similar to the original Daddi et al., filters, but the g filter is significantly different from Daddi's original B filter. With this motivation, we modified the BzK_s selection technique. [1]

In order to accomplish this, we used galaxy model magnitudes (defined with the same parameters as Daddi et al. 2004) and compared these models in a BzK_s colour-colour plot with the same models in a gzK_s colour-colour plots. With this comparison, we adapted the BzK_s selection criteria to a gzK_s selection criteria that selects the same models while using

[1] Sections of this text have been taken from Arcila-Osejo & Sawicki (2013).

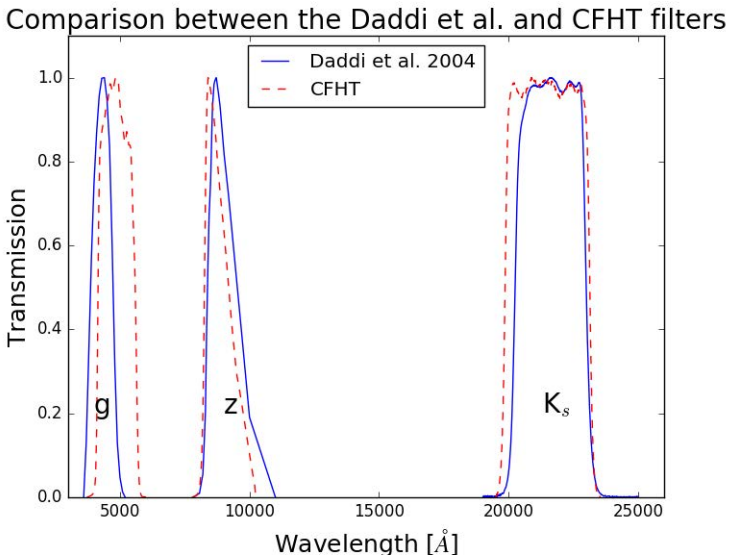

Figure 3.2: Transmission curves for the original BzK$_s$ Daddi et al. 2004 filters compared with our available CFHT filters.

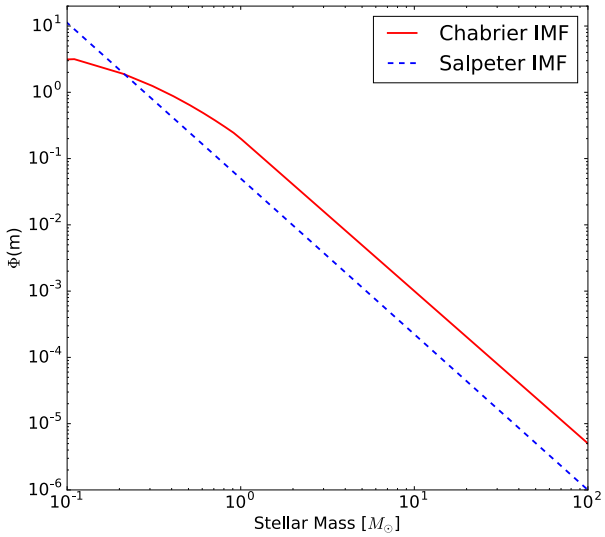

Figure 3.3: Comparison of Chabrier (2003a) and Salpeter (1955) IMFs. Information taken from Shimizu & Inoue (2013).

a different set of filters.

To model galaxy colours, we followed Daddi et al. (2004) and used rest-frame model spectra of constant-SFR and single-burst stellar populations (SSP) from the GALAXEV library (Bruzual & Charlot 2003). The models have solar metallicity and follow a Salpeter (1955) initial stellar mass function (IMF). This IMF defines an initial probability distribution of stellar masses and is most likely determined by gravitational fragmentation, accretion and feedback mechanisms. Their shape is usually represented as a series power laws. Two of the most famous prescriptions are given by Chabrier (2003a) and Salpeter (1955), as shown in Figure 3.3.

Starting from these models we apply attenuation by interstellar dust (Calzetti et al. 2000), redshifting to the observed frame, and integration through the filter transmission curves shown in Figure 3.2. This was all performed using the software for spectral energy distribution fitting of photometric data, SEDfit (Sawicki 2012).

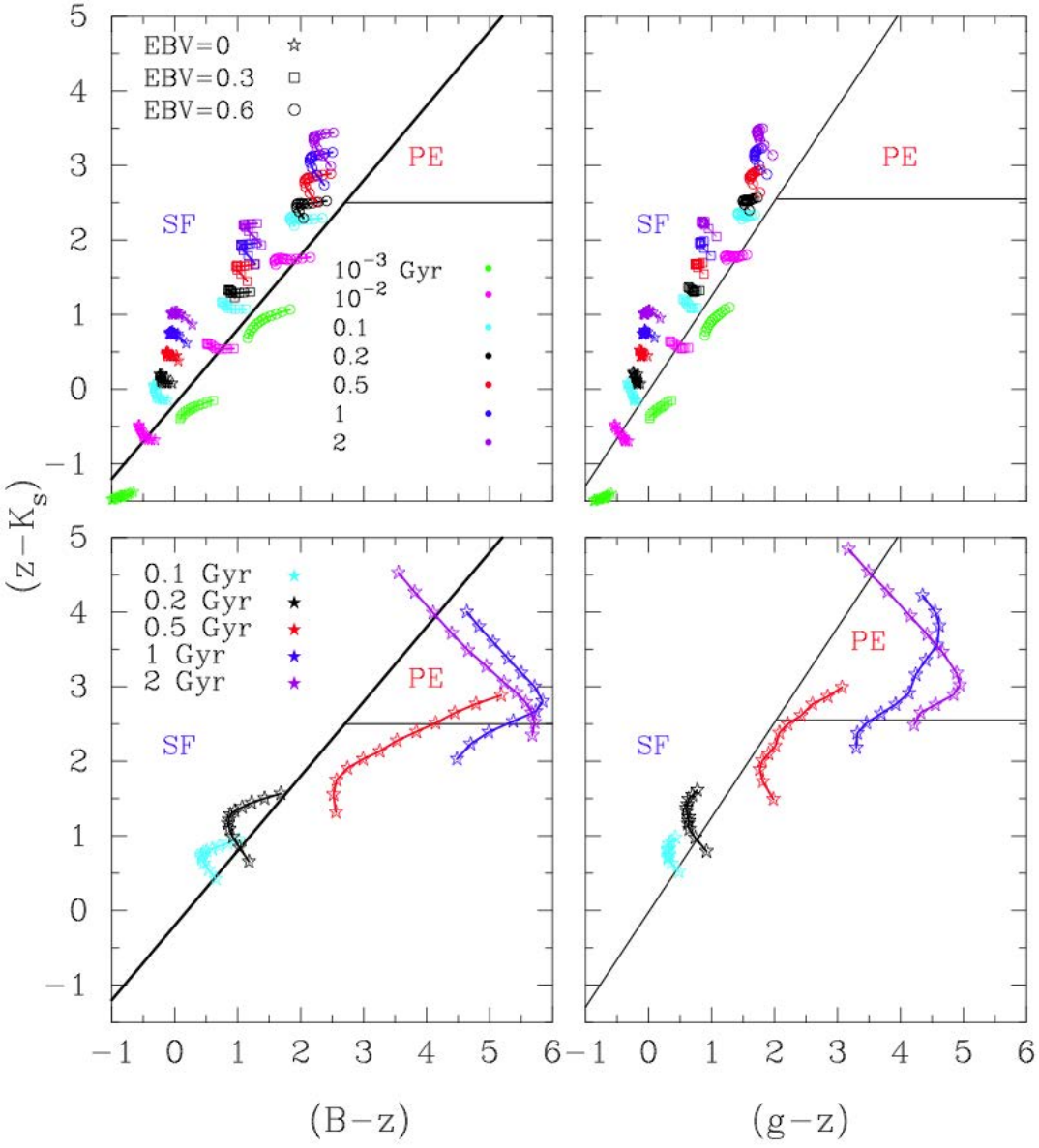

Figure 3.4: Bruzual and Charlot 2003 stellar population synthesis models for BzK_s and gzK_s colour-colour plots with $1.4 \leq z \leq 2.5$. Top-left panel : These models are intended to reproduce BzK_s colours of star-forming galaxies. Ages in Gyr are shown with different colours while different E(B-V) are represented with different symbols. Top-right panel: The same constant star-formation (CSF) models shown previously in the BzK_s plot, are shown in the CFHT gzK_s filters. Bottom-left panel: Instantaneous Burst (SSP) Models. These models are intended to reproduce BzK_s colours of passive galaxies with different ages and E(B-V)=0. Bottom-right panel: Shows the same SSP models shown in the bottom-left panel but in a gzK_s colour-colour plot. The solid black lines on the left-side plots are the same as given by Daddi et al. (2004). Solid black lines in the right-hand side plots are shifted from the original criteria to select the same BzK_s models. Figure and text taken from Arcila-Osejo & Sawicki (2013).

To reproduce the BzK_s selection diagram of Daddi et al. 2004, in the top panel of Figure 3.4 we plot star-forming constant-SFR (CSF) models with ages between 10^{-3} and 2 Gyr, solar metallicity, Salpeter stellar initial mass function (Salpeter 1955) , $0 \leq E(B-V) \leq 0.6$, and redshifts between $1.4 \leq z \leq 2.5$. Passive galaxies (as shown in the bottom panel of Figure 3.4), are represented using instantaneous burst models (SSP) with older stellar populations (ages between 0.1 and 2 Gyrs), and no dust (all these models were chosen to reproduce Daddi et al. original work). In the BzK_s colour-colour plot objects that lie to the left of the diagonal line are considered to be star-forming gzK_s selected galaxies (SF-gzK_s), while those to the right of the diagonal line but above the horizontal line are considered gzK_s selected passively-evolving galaxies (PE-gzK_s). Spectroscopy, along with morphological studies, support the validity of BzK_s selected passive and star-forming galaxies (Daddi et al. 2004, 2005; Ravindranath et al. 2007; Onodera et al. 2010; Mancini et al. 2010).

To modify the BzK_s technique for use with the CFHTLS+WIRDS gzK_s filters we considered the positions of the Daddi et al. 2004 models (left panels of Figure 3.4) in the gzK_s colour-colour diagram (right panels of Figure 3.4). While the gzK_s and BzK_s filter systems are different, they are similar enough that the main qualitative features of the colour-colour diagram are preserved, as can be seen by comparing the left and right panels of Figure 3.4. Even though the filters are somewhat different, we can adjust the original Daddi et al. (2004) BzK_s selection to develop a gzK_s colour-colour selection. We did this by locating the gzK_s models that correspond to the same colour-colour cuts as establish by Daddi et al., and, using a fit around the models close to the classification line, designed simple cuts shown as black lines in Figure 3.4.

Star-forming gzK$_s$ galaxies can be selected using equation 3.1:

$$(z - K_s) - 1.27(g - z) \geq -0.022 \tag{3.1}$$

And passive galaxies using equation 3.2:

$$(z - K_s) - 1.27(g - z) < -0.022 \bigcap (z - K_s) \geq 2.55 \tag{3.2}$$

Finally, in analogy with the BzK$_s$ technique, by visual inspection of the data we identified the stellar locus and distinguished between stars and galaxies using equation 3.3:

$$(z - K_s) - 0.45(g - z) \leq -0.57 \tag{3.3}$$

As an illustration, we have shown in Figure 3.5 how our different populations are selected. For the Wide fields, we employ a gzK$_s$ colour-colour plot to select and distinguish between star-forming and passive galaxies as defined by equations 3.1 and 3.2.

For the Deep Fields, we need to employ an additional selection criteria as described in the next section.

3.1.1 The gzHK$_s$ colour-colour selection

In principle, our gzK$_s$ selection criteria (equations 3.1 and 3.2) allow us to select and classify high redshift galaxies in a way that closely resembles the popular BzK$_s$ technique of Daddi et al. (2004) but is directly applicable to the gzK$_s$ CFHTLS+WIRDS filter set.

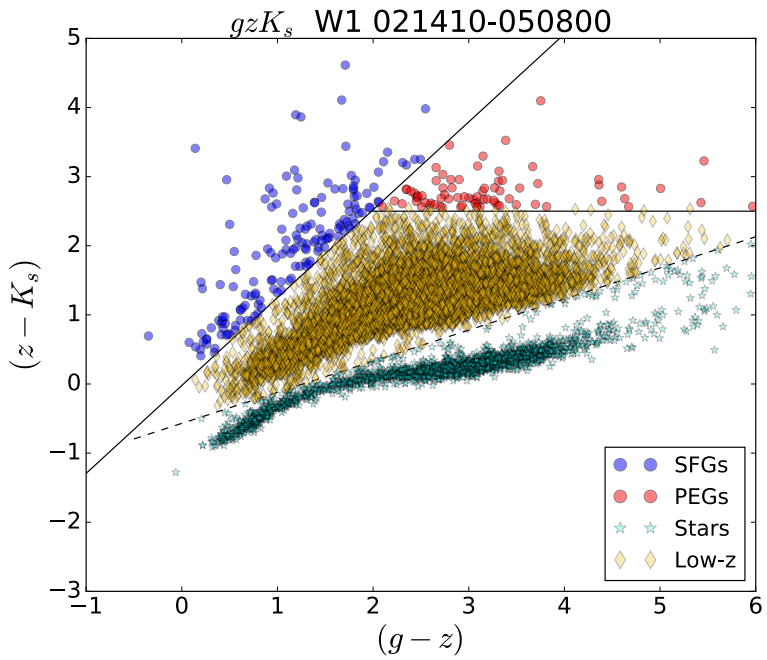

Figure 3.5: Selection of star-forming and passive galaxies in a (z-K_s) vs. (g-z) plot for one patch in the Wide fields (Each Wide field is composed of approximately 1 deg^2 patches. 28 of these patches compose W1 and 19 W4) down to $K_s < 20.5$. Blue symbols represent galaxies that were classified as star-forming, red symbols for passive, orange for low-redshift galaxies and cyan for stars as determined with Equations 3.1, 3.2 and 3.3.

Nevertheless, high-redshift galaxies are expected to have very red colours, so the use of gzK_s (or BzK_s) selection alone requires very deep g or B data (for $K_s \sim$ 23–24, we would require optical data reaching g $\sim$ 28–29 in order to discriminate between passive and star-forming high-redshift galaxies). The current CFHTLS data, for the Deep Fields as deep as they are for such a wide survey, are not deep enough. This limitation is illustrated in Figure 3.6.

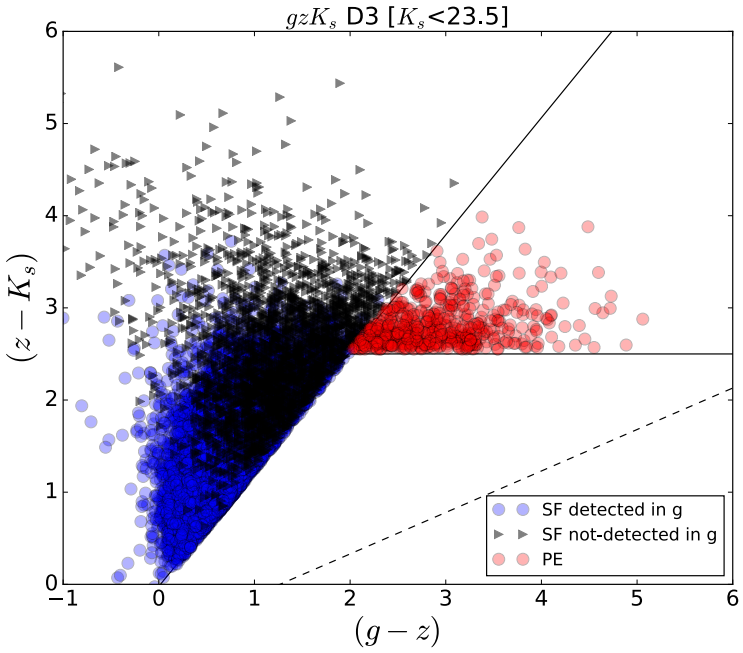

Figure 3.6: gzK_s colour-colour plot for Deep field 3 or D3. Classified according to their position in the colour-colour plot, we have represented star-forming galaxies with blue points and passive with red. Black triangles on the upper left part of the figure represent objects classified as star forming but were not detected in g. The solid lines represent the colour cuts defined previously in equations 3.1 and 3.2 and the dashed line shows the stellar cut defined in equation 3.3.

Although our data allow us to identify all objects with z–$K_s > 2.55$ as high-redshift, the majority of these galaxies are undetected in g and so we cannot tell whether they are passive or star-forming objects (these undetected in g objects are represented as black triangles in Figure 3.6). We also face a lesser, but related problem in that a fraction of the galaxies with z–$K_s < 2.55$ is undetected in g, making it unclear whether they are high-redshift or low-redshift objects. One solution to these problems would be to obtain much deeper g data than those already in hand, but this approach would be very costly in telescope time. Instead we took a different approach, as follows.

While unable to usefully distinguish between star-forming and passive galaxies, the present gzK_s data are deep enough to select high-redshift, $1.4 \leq z \leq 2.5$ galaxies (albeit with redshift ambiguity for the relatively small number of g-undetected objects below ($z - K_s$) = 2.55, i.e., $< 15\%$). In other words, the union of the regions defined by those objects to the left of the solid diagonal line, and above the horizontal line, represents high-redshift $1.4 \leq z \leq 2.5$ galaxies, as selected in equation 3.4:

$$(z - K_s) - 1.27(g - z) < -0.022 \quad \cup \quad (z - K_s) \geq 2.55 \tag{3.4}$$

The above approach does not give us information on the evolutionary states of our high-redshift galaxies. Consequently, to determine whether these galaxies are star-forming or passive we developed a new technique, which we defined as gzHK_s colour-colour selection.

To address the passive/star-forming ambiguity above $z - K_s = 2.55$, we developed and apply a follow-up selection technique based on (z–H) versus ($H - K_s$) colours. The red colour of ($z - K_s$) > 2.55 galaxies is caused either by dust (in the case of star-forming objects) or by the presence of the 4000 Å/Balmer break complex (for sufficiently old passive systems). Dust attenuation of star-forming spectra produces a continuous, tilted spectral slope, while, in contrast, the 4000 Å/Balmer break complex gives a sharp spectral discontinuity. Consequently, it should be possible to distinguish between the two phenomena, and therefore between dusty star-formers and passive systems, by adding a flux measurement between the z and K_s bandpasses. Specifically, past $z \sim 1.6$ the 4000 Å/Balmer break

complex is redshifted to ∼10,000–11,000 Å and so will fall between the z and H filters. Therefore, we should be able to identify this feature using the (z − H) versus (H − K_s) colour-colour diagram (Figure 3.7).

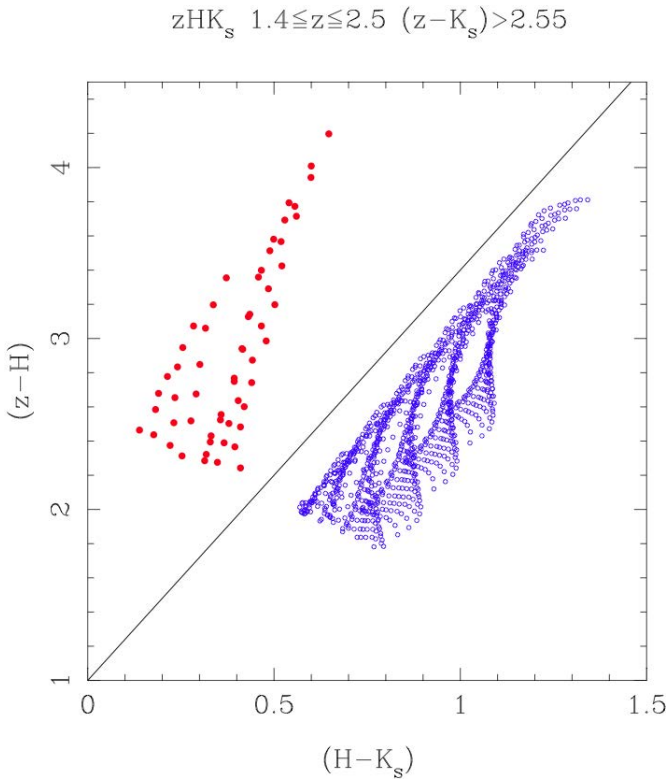

Figure 3.7: Model (z-H) versus (H-K_s) colours for those objects with (z − K_s) > 2.55 in the gzK_s diagram (see Figure 3.4). Blue points represent star-forming galaxies with $\log_{10}$(Age) between 7.28 and 9.36 (0.02 and 2 Gyr) and E(B-V)≥0. Red points represent passive galaxies with $\log_{10}$(Age) between 8.63 and 9.36 (0.4 and 2 Gyr) and E(B-V)=0. The solid line separates the star-forming and passive regions described by Equations 3.5 and 3.6 . Figure taken from Arcila-Osejo & Sawicki (2013).

The passive/star-forming ambiguity exists for (z − K_s) > 2.55 objects only, and so in Figure 3.7 we plot only those models from the gzK_s diagrams (Figure 3.4) that are above (z − K_s) = 2.55. As expected, the star-forming and passive models lie in different regions of Figure 3.7 and thus provide us with the means to distinguish the two populations. Note

that for a star-forming galaxy, as age, dust, and redshift are increased, the models shift parallel to the diagonal line shown in Figure 3.7. This linear shift occurs because increasing dust will affect both colours by roughly the same amount and, moreover, the fact that the star-forming spectrum is not expected to have a break also ensures smooth evolution with redshift. S tar-forming galaxy spectra, even in the presence of dust, are essentially power laws at these wavelengths, ensuring their position in the top of Figure 3.4. In contrast, for passively evolving models the presence of a spectral break results in a much stronger change between the (z-H) and (H-K_s) colours. As expected, models that represent passively evolving galaxies lie on a different locus in Figure 3.7, where they can be clearly separated from the constant star formation models. We adopted the solid black line in Figure 3.7 as the division between models of star-forming and passive gzK_s -selected galaxies that have $(z - K_s) > 2.55$.

We then used the following criteria to select and classify high-redshift galaxies in our Deep fields sample. First, as described before, we use equation 3.4 to select high redshift galaxies regardless of their spectral type. Below $(z - K_s) = 2.55$ all objects selected using equation 3.4 are classified as star-forming gzK_s galaxies. Above $(z - K_s) = 2.55$, all galaxies selected using equation 3.4 are also deemed to be at high redshift, and are the classified as star-forming if

$$(z - H) \leq 2.4(H - K_s) + 1 \tag{3.5}$$

and passively evolving if:

$$(z - H) > 2.4(H - K_s) + 1 \tag{3.6}$$

We call the star-forming objects thus selected "SF-gzHK$_s$" galaxies, and the passively evolving ones "PE-gzHK$_s$" galaxies. The models used in designing the above selection criteria are the same as those in the "classic" BzK$_s$ colour-colour cuts, and so we stress that the populations selected by our criteria are essentially the same as those selected using the "classic" BzK$_s$ technique. Application of the above criteria to our photometric catalogs yields samples of high-redshift star-forming and passively-evolving galaxies in the CFHTLS Deep Fields.

However, it is important to clarify that this problem is only present in the Deep fields, where the completeness of our sample goes to faint magnitudes (K$_s$ $<$ 23). On the other hand, since the completeness for passive galaxies in the Wide survey is brighter in comparison (K$_s$ $<$ 20.5), we find that up to this magnitude we do not suffer the same incompleteness. This is shown in Figure 3.8, where we reproduce Figure 3.6 with sources from our Wide Survey up to K$_s$ $<$ 20.5. As can be seen in Figure 3.8 only one source at a magnitude of K$_s$ $\sim$ 20.4 was undetected in g. Nevertheless, if we assess this effect down to K$_s$ $<$ 21.5 we find a considerable number of star-forming galaxies that could in fact be passively evolving. Consequently, for the Wide fields, we only work with galaxies (both star-forming and passive) down to K_s $<$ 20.5 and employ gzK$_s$ colour-colour cut to classify star-forming and passive galaxies at high-redshift.

In conclusion, the Deep fields not only require a gzK$_s$ colour selection, but a zHK$_s$

colour-colour selection as well to further distinguish star-forming and passive galaxies above (z-K_s) = 2.55 as shown in Figure 3.9. For simplicity, in the remainder of this document, we refer to our objects as gzK_s selected galaxies, regardless of whether they are gzK_s or gzHK_s colour-colour selected galaxies.

3.2 Inspection of Bright PE-gzK_s

Considering that we are trying to recover a rare population of galaxies, it is important to confirm that the low-number statistics of the brightest objects are not contaminated by spurious objects (objects on the halo of a star, mergers, AGNs, etc). Consequently, we inspected bright ($K_s < 20$) passive galaxies (PEGs) in the Deep and Wide fields in order to flag any false positives. In order to do this, we performed a visual inspection of approximately 600 bright PEGs, taking into account any significant event that could alter the g, z or K_s colours of the galaxy.

Most of the bright ($K_s < 20$) objects in our sample seem to be unaffected by edge effects or bright stars, except for six cases (less than one percent of our sample): Two sources were found on the halo and diffraction spike of a nearby star, one source was found close to a corrupted part of the image and three sources appear to be not real objects but artifacts (samples of these effects are shown in Figure 3.10).

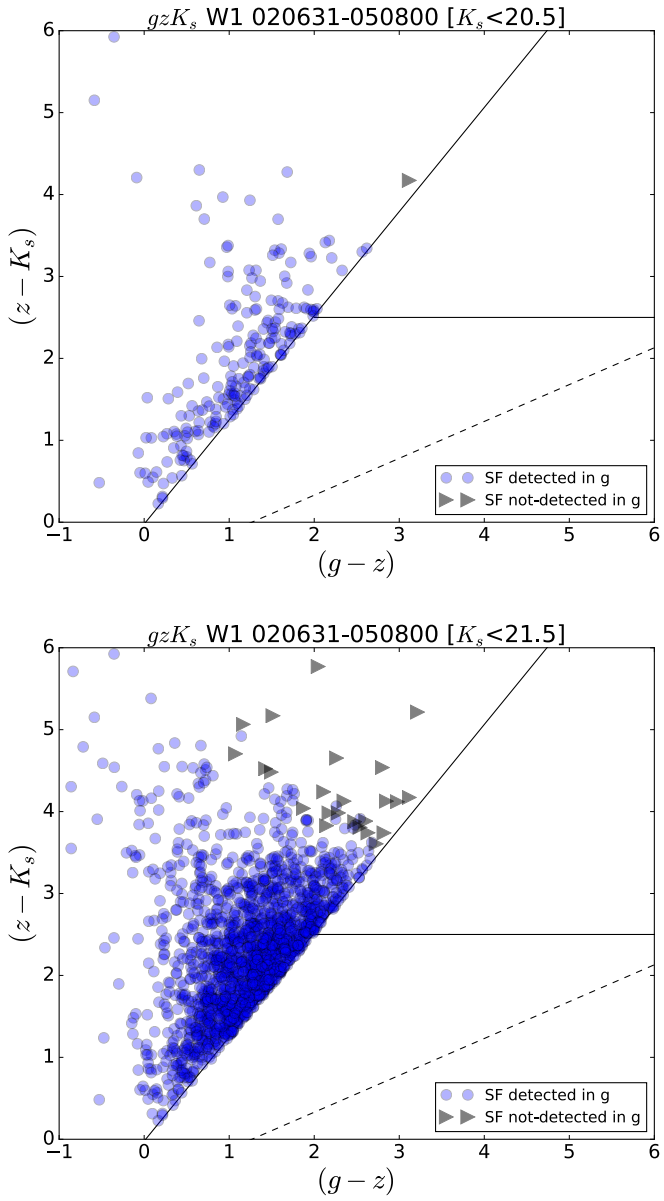

Figure 3.8: gzK_s colour-colour plot for one W1 pointing. Classified according to their position in the colour-colour plot, we have represented star-forming galaxies with blue points and passive with red. Black triangles in the upper left part of the figure represent objects classified as star forming but were not detected in g. The solid lines represent the colour cuts defined previously in equations 3.1 and 3.2. The top panel shows that down to $K_s \sim 20.5$, most of our high-redshift gzK_s galaxies will be classified as either star-forming or passive, nevertheless as an example, we show that if our sample was a magnitude fainter ($K_s < 21.5$) the classification of some non-detected in g star-forming galaxies would be ambiguous. Hence for the Wide fields, a simple gzK_s selection criteria is enough to distinguish between passive and star-forming galaxies for $K_s < 20.5$.

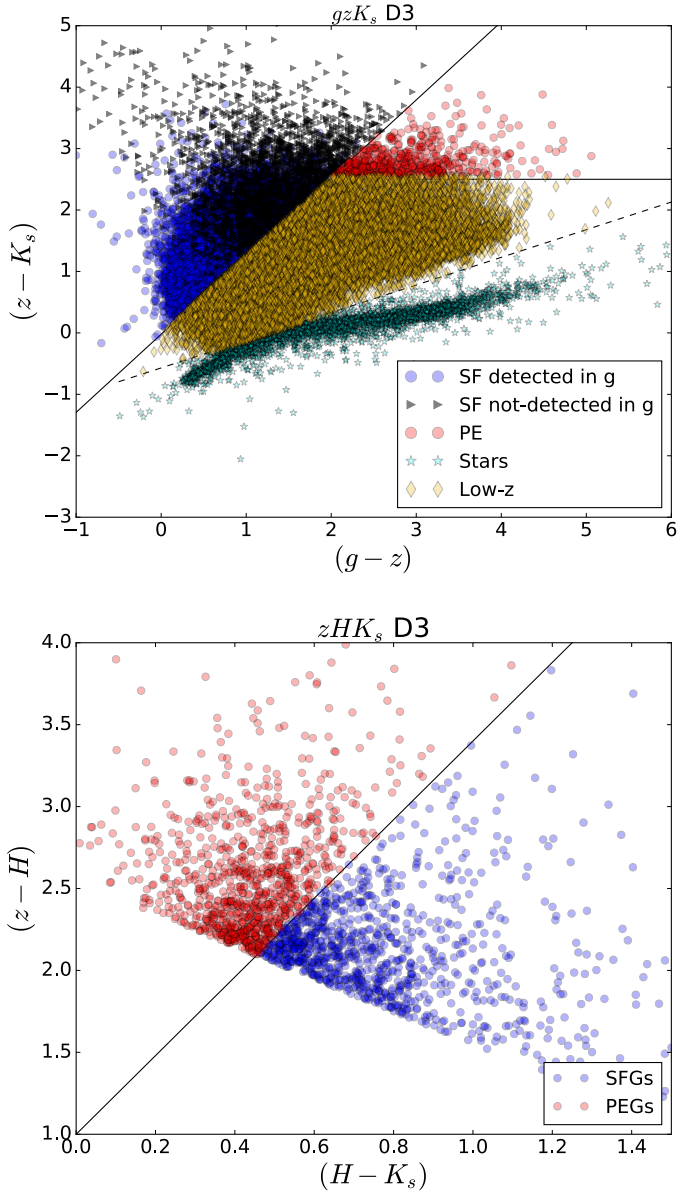

Figure 3.9: Selection of star-forming and passive galaxies in a (g-z) vs. (z-K_s) colour-colour plot, followed by a (z-H) vs (H-K_s) colour-colour plot for the Deep fields. The passive/star-forming ambiguity only exists for objects (z-K_s)>2.55. Consequently, we classified this sample as star-forming or passive based on their position on a (z-H) vs (H-K_s) colour-colour plot as defined in equations 3.5 and 3.6.

Additionally, a closer inspection of ultra-bright galaxies ($K_s < 19.5$) revealed the pres-

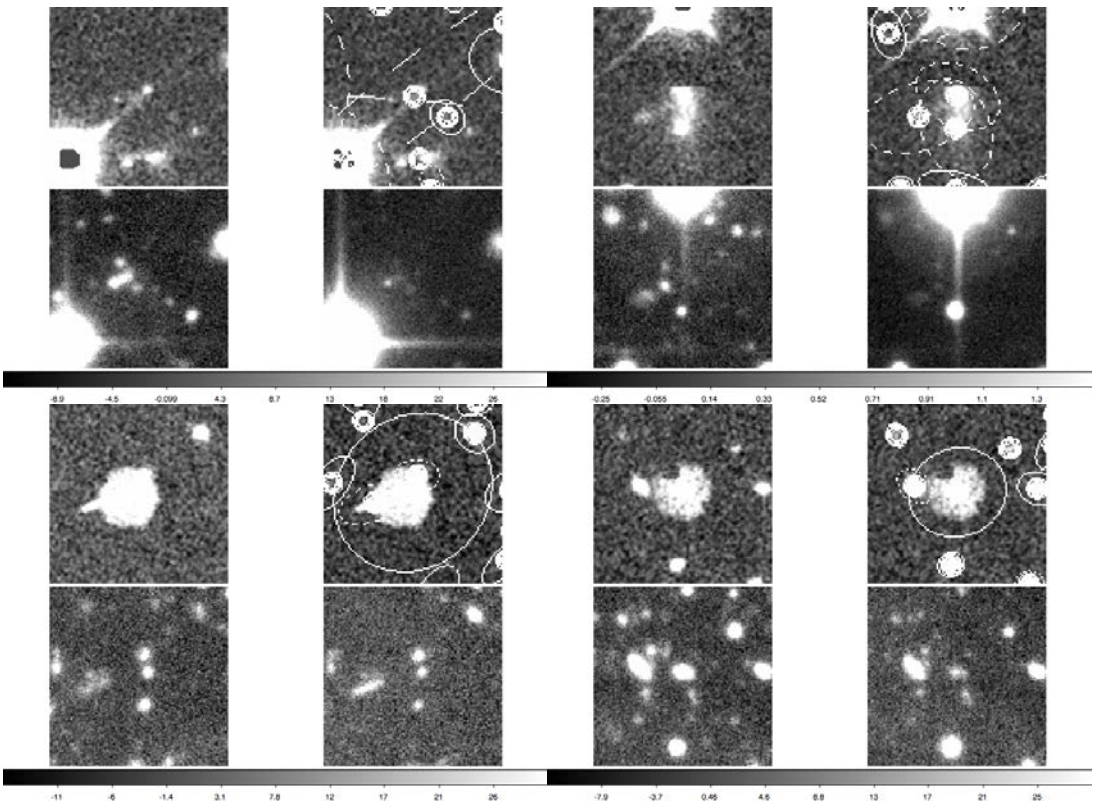

Figure 3.10: Top images: Sources in D3 and D4 whose photometry is contaminated by the diffraction spike from a nearby star. Bottom images: Sample of two spurious elements present in D4. Frames in each image show from top left to bottom right K_s band, SExtractor's aperture output (defined as CHECKIMAGE, it displays user-defined apertures, used for photometry), z and g band images for each source . These objects will be removed from any subsequent analysis.

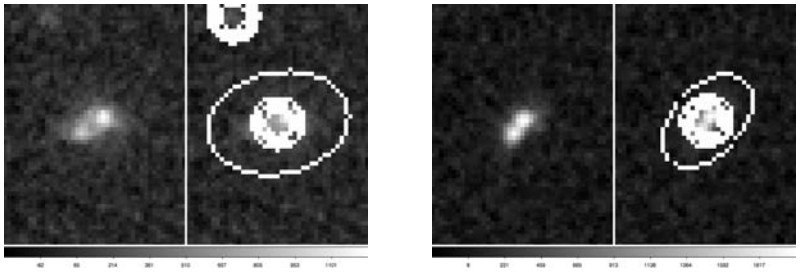

Figure 3.11: Sample of two bright, i.e., $K_s < 19.5$ double-cored passive galaxies not segmented by SExtractor, hence the output appears to be ultra-massive passive galaxies. On the left of each panel is the original K_s image and on the right SExtractor's output of found sources, for all cases SExtractor returned both cores as a single ultra-bright source.

ence of six possible major mergers ($\sim$ 10% of our sample): Galaxies with a double core feature that were not properly segmented by SExtractor. Figure 3.11 shows a sample of two of these galaxies. By visually identifying a boundary between the two sources, we recovered a separate background corrected flux for each source in the pair, confirming the fact that what appears to be an ultra-bright passive galaxy could in fact be an ongoing, major merger between two less bright sources ($K_s \sim 20$). This major merger could potentially result, with time, in an ultra-bright passive galaxy.

Furthermore, we cross-correlated all $K_s < 20$ objects with the Chandra[2], XMM[3], NED[4] and Simbad[5] databases in order to discard any possible AGN sources in our sample. In the Deep fields, no X-ray sources were found in the the XMM and Chandra databases but one object in D3 was identified in the Simbad catalog as an AGN source in the Extended Groth Strip, belonging to the AEGIS-X Deep Survey (Goulding et al. 2012). In addition, two X-ray sources were found in W1.

[2]http://cda.harvard.edu/chaser/
[3]http://nxsa.esac.esa.int/nxsa-web/
[4]https://ned.ipac.caltech.edu/forms/nnd.html
[5]http://simbad.u-strasbg.fr/simbad/sim-fbasic

Finally, we analyzed the surface brightness with respect to magnitude for all galaxies classified as passively evolving (PEGs) in the gzK$_s$ colour-colour plot, and compared them with those of all galaxies and stars in the same fields. As can be seen in Figure 3.12 most stars in any given patch lie on a straight line showing, as expected for point sources, a narrow linear correlation between surface brightness and magnitude. On the other hand, since galaxies are extended objects, their location on this relation is represented by an extended cloud. We found that all PEGs detected at magnitudes K$_s$ $<$ 18.5 lie on the compact-source sequence (a total of 5 sources). This implies that even though these objects were classified as passive based on their location on the (g-z) vs (z-K$_s$) colour plot, they might be either stars or AGNs. In comparison, approximately 7% of PEGs detected at $18.5 \leq K_s < 19.5$ and less than 0.5% of PEGs detected at $19.5 \leq K_s < 20.5$ lie on this compact source sequence. If, these compact sources were in fact passively evolving gzK_s their masses would be larger than $log\,(^{M_*}/_{M_\odot}) > 11.84$, but, following Daddi et al. (2005), a compact passive galaxy at this redshift should be resolved in our images (for comparison, we use Daddi et al. (2005) most massive PEG at z$\sim$1.55 to estimate an effective radius for these massive objects, which at these redshifts would place them at $\sim$ 5 pixels in our images). Artifacts, X-ray sources, double cores and compact PEGs with $K_s < 18.5$, have been flagged as potentially spurious objects and removed from any subsequent analysis.

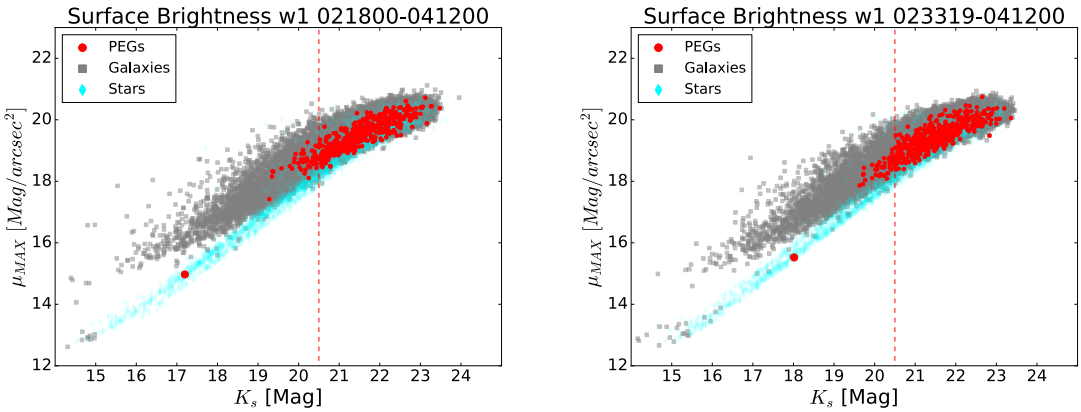

Figure 3.12: Surface Brightness of two sample patches in W1. Shown in cyan, grey and red are objects classified as stars, galaxies and passively evolving galaxies based on their gzK$_s$ colours. Shown with larger symbols are passively evolving galaxies that lie on the compact source sequence. Finally, a red-dashed line represents the completeness of our sample of PEGs.

3.3 Number Counts

In this section, we determined galaxy number counts for different populations of galaxies: star-forming and passive galaxies at high redshifts, as well as for all galaxies irrespective of redshift (see equation 3.3). To do this, we counted galaxies in 0.5 total K$_s$ magnitude bins. Since some faint galaxies can be undetected above night-sky fluctuations we applied incompleteness corrections to the Deep fields determined from simulations performed by Dr. Taro Sato (Arcila-Osejo & Sawicki 2013; Sato et al. 2014). These incompleteness corrections used artificial objects added at random locations into the science images with empirically motivated morphological parameters. Star-forming galaxies are assumed to be disk-like objects with effective radii between $1 \leq r_e \leq 3$ kpc (Yuma et al. 2011) while passive galaxies present a more compact morphology and effective radii between $3 \leq r_e \leq 6$ kpc (Mancini et al. 2010). The total (i.e., irrespective of redshift) galaxy number counts are

corrected using morphologies that mimic the observed CFHTLS galaxy population. Once artificial galaxies are added into an image, object-finding with SExtractor is used to determine the recovery rate as a function of apparent magnitude. These recovery rates are used to correct for incompleteness.

Incompleteness corrections for the Deep fields are typically of the order of $\sim$1.02 over K_s = 17 − 22 (AB) mag but become larger at fainter levels. We limited our analysis in magnitude bins where incompleteness corrections are smaller than a factor of two, namely $K_s < 23.5$ mag (except for D2, where our passive population is only complete to $K_s < 23.0$).

On the other hand, to determine the completeness of our Wide fields, we compared their number counts with the corrected Deep fields number counts, and determined the 90% completeness of our sample to be around $K_s \sim 21.5$ for the Star-Forming population (nevertheless, as mentioned in Section 3.1.1, due to g-limit incompleteness, our star-forming sample is selected down to $K_s < 20.5$), and $K_s \sim 20.5$ for the Passive population. Figures 3.13 and 3.14 show, as a dashed line, the detection completeness for each independent Deep fields and for the combined Wide fields as distinguished between star-forming and passive. For the star-forming population, we show an extra dotted line that represents a colour-completeness, or the limit to which we can fully separate between star-forming and passive galaxies due to g limiting detection in the Wide Fields. Table 3.1 lists our adopted completeness limits.

In Figure 3.15 we show how number counts are affected by incompleteness: Shown in orange triangles are the average number counts of gzK_s passive galaxies in the Deep fields without taking into account completeness corrections (dotted line), and orange cir-

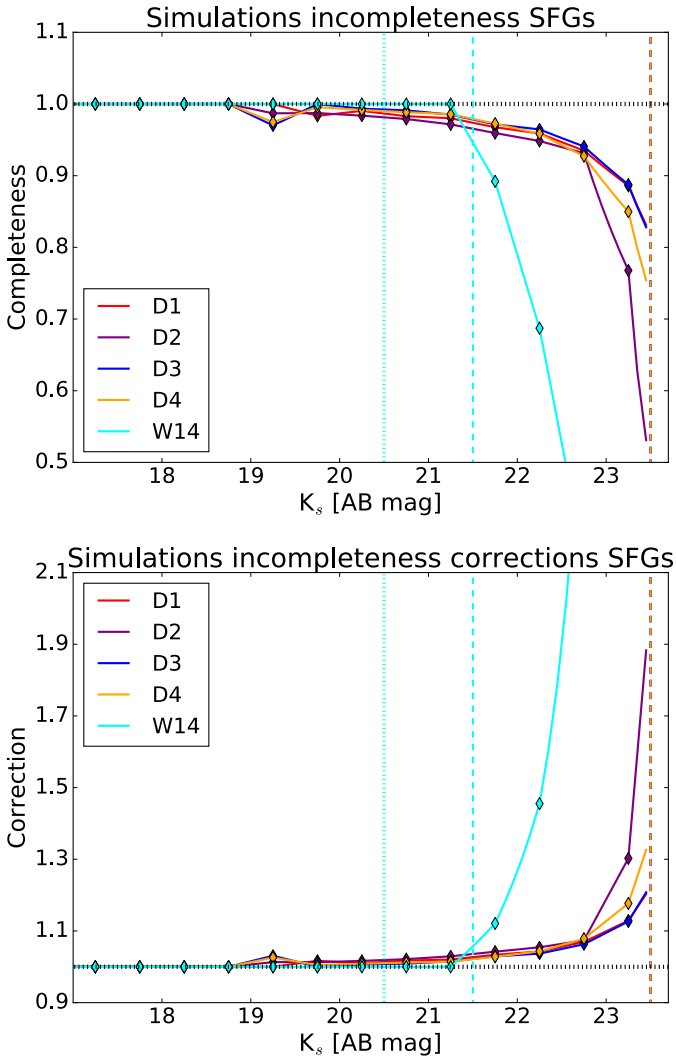

Figure 3.13: Top: Incompleteness for star-forming galaxies, determined from simulations for the Deep fields using artificial objects added at random locations to the science images, for the Wide fields we calculated the incompleteness of the sample using as a reference the completeness-corrected Deep sample. Star-forming galaxies in the Deep field simulations are modeled as disk-like objects with effective radii between 1 and 3 kpc. Bottom: Corrections applied to our number counts to account for these incompleteness. Dashed lines represent detection completeness and dotted lines represent our colour-completeness, as defined in Section 3.1.1.

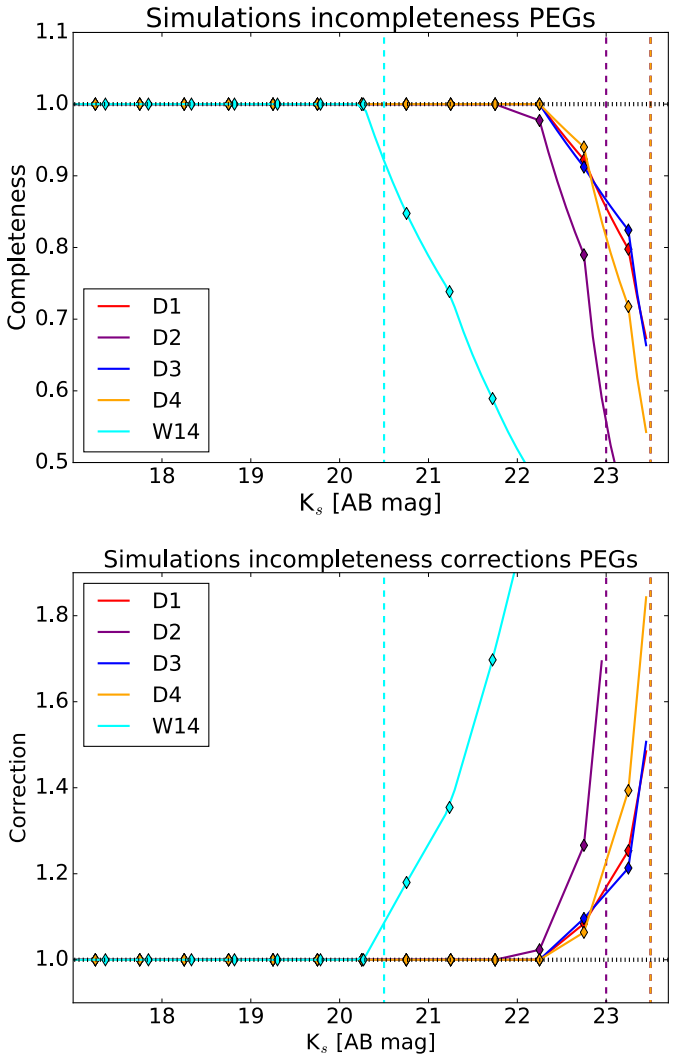

Figure 3.14: Top: Incompleteness for passive galaxies, determined from simulations for the Deep fields using artificial objects added at random locations to the science images, for the Wide fields we compared the incompleteness of the sample using as a reference the complete Deep sample. Passive galaxies in the Deep field simulations are modeled as elliptical objects with effective radii between 3 and 6 kpc. Bottom: Corrections applied to our number counts to account for these incompleteness.

Population	D1	D2	D3	D4	W1 & W4
All galaxies	23.5	23.5	23.5	23.5	21.5
Star-forming galaxies	23.5	23.5	23.5	23.5	20.5
Passive galaxies	23.5	23.0	23.5	23.5	20.5

Table 3.1: Adopted K_s band completeness limits for the Deep and Wide fields.

cles show the same number counts once they have been corrected for incompleteness (dashed line). Finally, shown for comparison in purple diamonds is the number counts of the Wide fields. From the purple points we can appreciate that the results are consistent with the Deep fields but they start to diverge for magnitudes fainter than $K_s \sim 20.5$. If our sample was to be homogeneously complete to 90% our number counts would stop at $K_s < 23$ (i.e., without the faintest point).

Using these completeness corrections we plotted the number counts for all the different populations in our fields. Number counts for all gzK_s galaxies in the fields are shown in Figure 3.16. In this figure, we show each independent field with a different symbol and different colours to represent the Deep and Wide fields (purple and cyan respectively). Error bars show Poissonian $\sqrt{N}$ uncertainties. We compared our results with those of McCracken et al. (2010), and as can be seen, our results seem to be in good agreement with these previously K_s-selecteded BzK_s galaxies. The small variations between our fields are most likely due to cosmic variance (i.e., variations in galaxy number density due to small-scale inhomogeneities in the universe).

Figure 3.17 shows galaxy number counts of gzK_s selected star-forming galaxies. Since many of our star-forming galaxies in the Deep survey ($gzHK_s$ candidates) are undetected in the g-band (refer to Figure 3.6), we need to deal with potential low-redshift interlopers

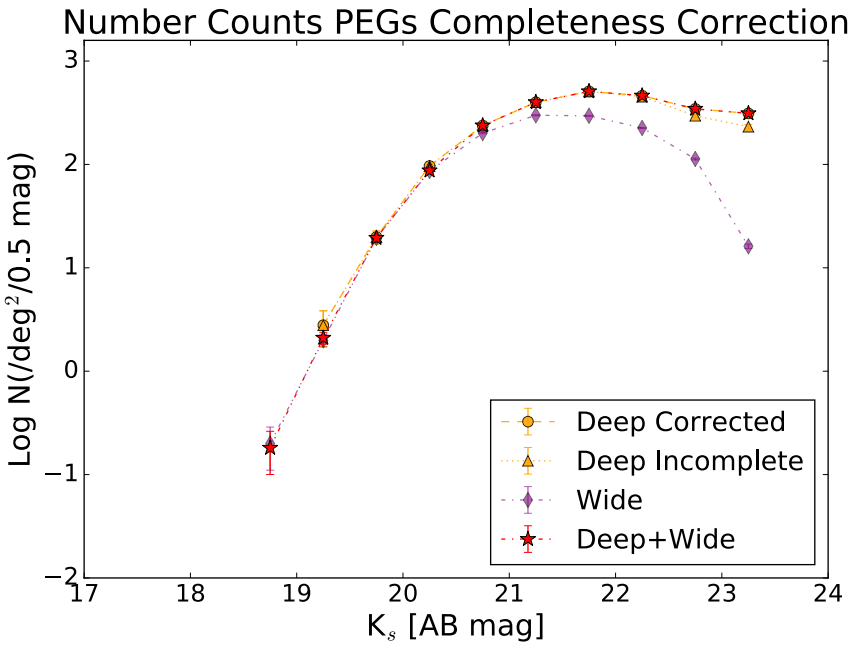

Figure 3.15: Number counts of passive gzK_s galaxies and their completeness correction. Shown in orange triangles with a dotted line is the number counts of passive galaxies in the Deep fields before correcting our number counts for incompleteness. As a complement to this line, we show with orange circles and a dashed line the same number counts once they have been corrected by incompleteness. Also shown, for comparison, in purple is the number counts of passive galaxies in the Wide fields. And finally, shown in red circles is the final number counts for passive galaxies once both samples have been taken into account (up to their completeness limits). As can be seen from this figure, both our number counts for the Deep and Wide surveys are in agreement up until $K_s < 20.5$. From this point, the Wide fields are incomplete as represented by the turn over in their number counts as compared from the Deep fields. This is the reason why the final red points are comprised of the Wide survey up to K_s <20.5 and the Deep survey up to $K_s < 23.5$ once it has been corrected for incompleteness.

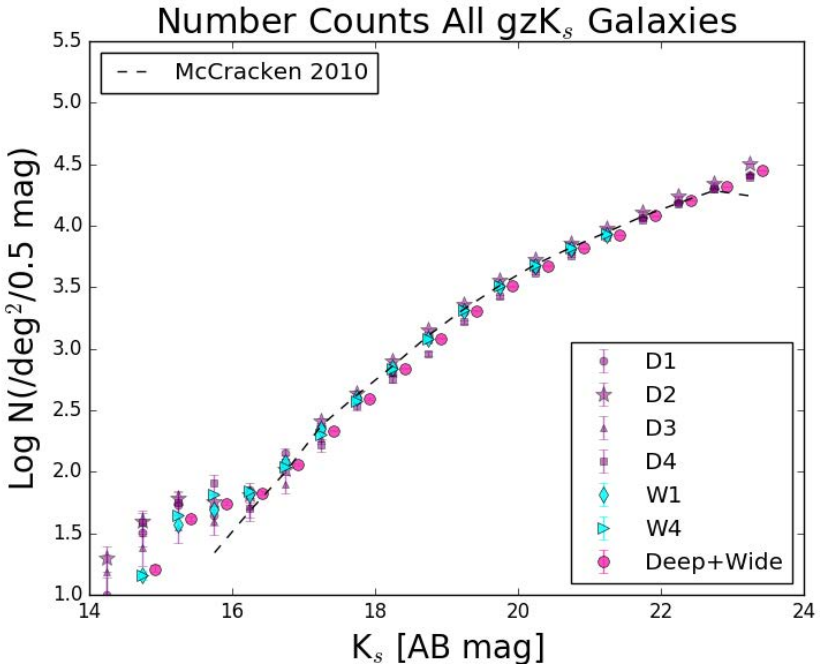

Figure 3.16: Number counts for K_s-selected galaxies irrespective of redshift. Our results are in good agreement with previous results of K_s-selected samples. Points for the combined Deep+Wide fields have been shifted to the right for clarity.

amongst the $z - K_s < 2.55$ objects (the $z - K_s > 2.55$ objects are all regarded as at high redshift and their SF/PE nature is resolved using zHK_s colours, refer to Figure 3.9). To address this interloper issue, Figure 3.17 shows two extreme number count cases. The points show the number counts of $z - K_s < 2.55$ galaxies that are detected in g-band and hence known to fulfill the high-z colour selection criteria (in this case we are rejecting from the sample any galaxy that was not detected in g). As such, the points represent a lower limit on the true number counts of star-forming galaxies. In particular, the cyan filled points represent the average of the lower limits set by our four deep fields. In contrast, the blue shaded region represents the full range of allowable number counts as it accounts for the g-band undetected objects, many of which could be low-redshift interlopers (Arcila-Osejo & Sawicki 2013). The upper and lower limits of the shaded regions thus represent the allowable range of SF galaxies. Note that this allowed range is quite narrow and thus we can claim to have constrained the number counts of faint SF-gzK_s galaxies quite well.

Our results for star-forming galaxies seem to be in good agreement with recent works (McCracken et al. 2010, Sommariva et al. 2014) but have significantly smaller statistical uncertainties because of larger areas of our data.

Galaxy number counts for passive gzK_s galaxies (PE-gzK_s) are shown in Figure 3.18. As before, we compared our results with those of several different authors that used the BzK_s selection technique.

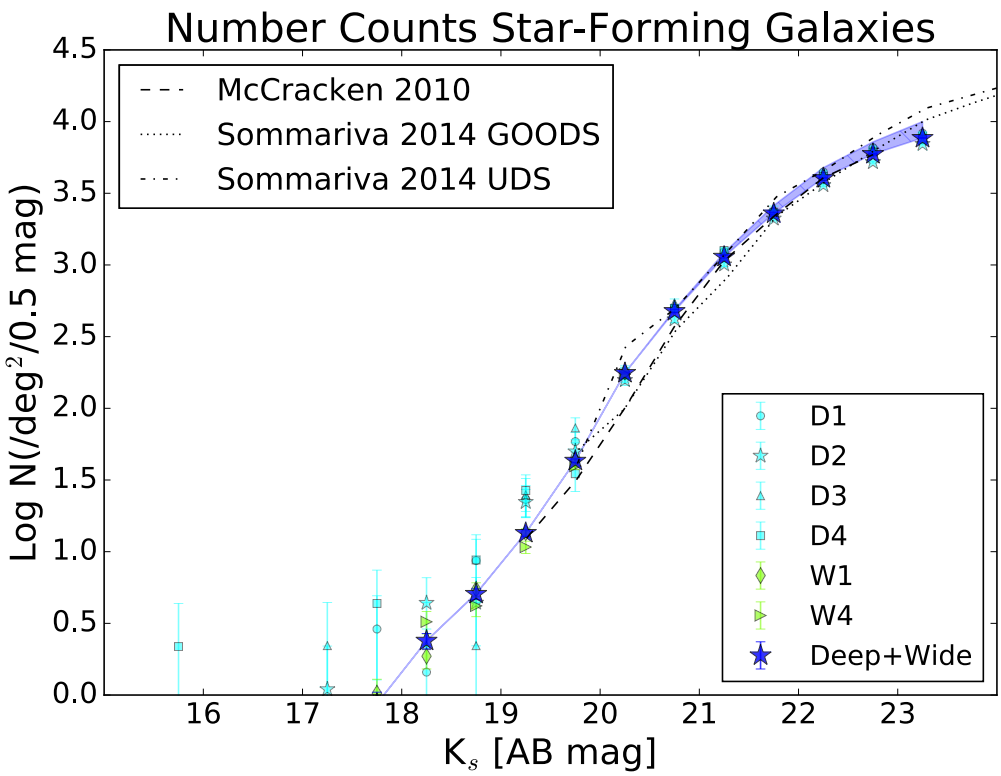

Figure 3.17: Number counts of star-forming gzK_s galaxies. Cyan symbols represent the Deep fields, and green symbols the Wide fields. Also shown with filled blue stars are galaxy number counts for the average of the Deep and Wide fields. Error bars were determined from Poissonian statistics. As explained in the text, the shaded blue area represents an upper and lower limit for those star-forming galaxies that were detected or undetected in g in the deep fields, in the wide fields g band incompleteness is negligible to K_s<20.5. Our results are in good agreement with other authors and their K_s selected BzK_s galaxies.

For McCracken et al. (2010), we included a shaded area that represents their upper and lower limits. The lower limit of their shaded region indicates galaxies that are unambiguously PE-BzK_s, while the upper limit also includes galaxies with ambiguous SF/PE classifications due to their lack of B-band detection. Even taking into account their worst case scenario, they observe a flattening of the number counts although within the limits the data are consistent with no turnover. Our results seem to be in good agreement with

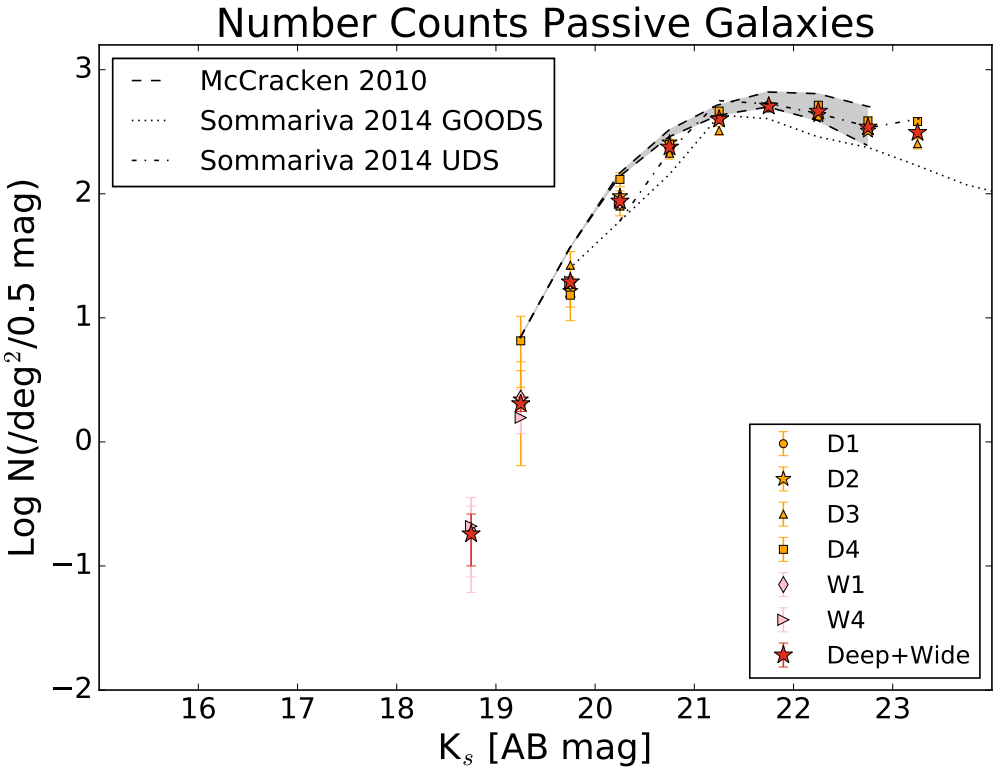

Figure 3.18: Number counts of passive gzK_s galaxies. Orange symbols represent the Deep fields, and pink symbols the Wide fields. Also shown with filled red stars are galaxy number counts of the average of both the Deep and Wide fields. Error bars were determined from Poissonian statistics. Our results are in good agreement with other authors and their K_s selected passive BzK_s galaxies. However, because of our much larger areas, our counts have smaller error bars.

most of the other studies, but with better statistics.

Table 3.2 shows the corrected number counts in units of $(N/deg^2/0.5mag)$ for the star-forming and passive populations. Figure 3.19 shows a comparison between the observed and predicted number counts from semi-analytical models of passive BzK_s galaxies. Shown in red points is this work and for comparison, we have selected three semi-analytical models, Kitzbichler & White (2007), Merson et al. (2013) and Somerville et al.

(2012).

Kitzbichler et al. compared observations of the high-redshift population with predictions from the Millennium simulation (Springel et al. 2005), which follows the hierarchical growth of dark matter structures from z=127 to the present, including several physical processes such as star-formation, gas cooling, growth of super-massive black holes, stellar population synthesis modeling for photometry and a new treatment for radio mode feedback only for galaxies at the center of groups or clusters (hence it is not applied uniformly to all massive galaxies). Sommerville et al. semi-analytical models, similar to those of Kitzbichler et al., include hierarchical dark matter growth, star-formation, gas cooling, star-formation, supernova and AGN feedback, and metal enrichment. Feedback processes are mainly driven by supernova at the faint end of the SMF and by AGN feedback at the massive end.

Finally, Merson et al. populates dark matter halos from the Millennium simulation with galaxies using the GALFORM semi-analytical prescription (Bower et al. 2006). This prescription includes gas cooling, supernova and AGN feedback (only effective in systems with quasi-hydrostatic cooling). In their semi-analytical models, Merson et al. recalculated their predicted number counts in two different ways: one representing model BzK$_s$ galaxies with a simple K-mag limit brighter than $K_s \leq 24$ and a second one which also takes into account a B-band detection limit of $B \leq 28$.

In Sommerville et al. and Kitzbichler et al., we can see that the number counts for analytical models over-predicts the number of faint passive galaxies. This is possibly due to two reasons: progenitors of these faint galaxies are characterized as having low virial

$K_s[AB\ mag]$	SF-gzK_s [(N/deg^2/0.5mag]	PE-gzK_s [(N/deg^2/0.5mag]
15.25	0.04±0.04 (0.04±0.04)	0
15.75	0.2±0.1 (0.2±0.1)	0
16.25	0 (0)	0
16.75	0.2±0.1 (0.2±0.1)	0
17.25	0.58±0.14 (0.58±0.14)	0
17.75	0.87±0.18 (0.87±0.18)	0
18.25	2.4±0.3 (2.4±0.3)	0
18.75	5.07±0.43 (5.11±0.43)	0.2±0.1
19.25	13.5±0.7 (13.5±0.7)	2.1±0.3
19.75	43.1±1.3 (43.1±1.3)	19.5±0.8
20.25	176±3 (177±3)	87.3±1.8
20.75	477±14 (488±14)	238±10
21.25	1140±21 (1217±22)	399±13
21.75	2288±30 (2596±32)	509±14
22.25	4034±40 (4765±44)	462±14
22.75	5934±49 (7211±54)	345±12
23.25	7688±55 (9998±63)	312±14

Table 3.2: Number counts per square degree per 0.5 magnitudes for our star-forming and passive gzK_s galaxies, once they have been corrected for incompleteness. For star-forming galaxies, numbers outside of the parenthesis represent number counts of only detected in g galaxies, whereas those inside the parenthesis represent an upper limit, including galaxies that were detected and not-detected in g.

temperatures and high densities, hence gas cooling is extremely efficient and the rapid star-formation in low-mass galaxies would result in over predicting their numbers. Secondly, for most of these models, when a galaxy merges with another and becomes a sub halo, it is stripped from its hot gas reservoir and consumes in short time-scales its cold gas reservoir, eventually becoming passive. Delaying the stripping of hot gas after merging can reduce the overestimation of faint passive galaxies (Sommariva et al. 2014; Merson et al. 2013).

On the other hand, most analytical models seem to under-predict the number of bright passive galaxies at this redshift. This is possibly due to the mode for suppressing gas cooling in massive halos in these simulations. This is normally implemented using specific models of AGN feedback. As can be seen in Figure 3.19, Sommerville et al. seems to be the best prescription to explain the number of bright objects (although their models do not extend bright than $K_s \sim 19.5$). Given their adopted prescriptions, it seems that radio-mode AGN feedback (also called kinetic feedback, where the jet-related energy re-heats the gas in the galaxy, stopping the necessary cooling for star-formation) is more efficient in producing bright passive galaxies than radiative feedback (or quasar mode, where the radiation generated by accretion removes available cold gas in the galaxy) Sommariva et al. 2014.

Summary

In this chapter, we presented the gzK_s and gzHK_s colour-colour selection technique, used to classify and distinguish between star-forming and passive galaxies at $z \sim 1.6$. We also

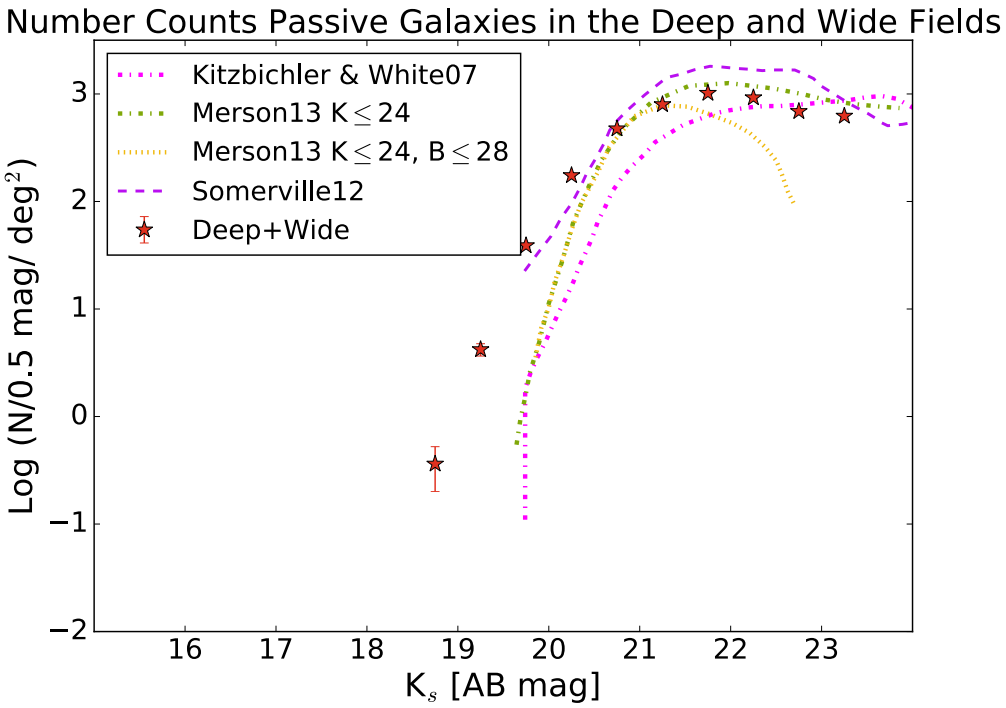

Figure 3.19: Comparison between the observed (this work) and predicted number counts of passive BzK$_s$ galaxies.

inspected the nature of the brightest passive galaxies in our sample and presented number counts for our sample as compared with other authors and their completeness corrections.

Chapter 4

Stellar Mass Function and Stellar Mass Density

The stellar mass function (SMF) is a fundamental statistical tool to characterize the mass assembly of galaxies at a given epoch. This chapter is devoted to explaining how we obtained our stellar mass functions for passively evolving galaxies at z $\sim$ 1.6.

4.1 Photometric Redshifts

In order to build our stellar mass function (SMF) we divided its construction into two steps: (1) determination of the survey's effective volumes (V_{eff}), and (2) conversion of apparent K_s-band magnitudes to stellar mass.

To obtain photometric redshifts for our sample of passive and star-forming galaxies, we do not use individual redshifts for each galaxy, instead we matched our D2 catalog with

that of Muzzin et al. (2013b) ($\sim$ 1400 matches) and our W1 and W4 catalogs with that of Moutard et al. (2016a) ($\sim$ 2200 matches) to obtain an overall redshift distribution.

Muzzin et al. determined photometric redshifts by spectral energy distribution (SED) fitting of the 30 available photometric bands in the COSMOS field (Our D2 field is a subset of the COSMOS field). All the galaxies in their catalog were fitted to galaxy model templates using EAZY (Easy and Accurate Zphot from Yale, Brammer et al. (2008)) until they converge on a model that determines a photometric redshift with an offset of less than 0.01 mag in every filter.

Similarly, Moutard et al. performed SED fitting using galaxy model templates, albeit they performed this fit with nine photometric bands (FUV, NUV, u, g, r, i, y, z, K_s) and with a different SED-fitting code (Le Phare, Arnouts et al. (2002)).

Figure 4.1 shows the redshift distribution found after we cross-correlated these two data sets with our sample: on the left we show star-forming galaxies for D2 in blue and the Wide fields in green, up to their respective completeness limit: $K_s < 23.5$ for D2 and $K_s < 20.5$ for W1 and W4, as mentioned in Section 3.3. On the right, we show the redshift distribution for passive galaxies in the Wide fields up to $K_s < 20.5$ in magenta and in orange, D2 up to $K_s < 23$. From the plot on the right the results for Muzzin et al in D2 seem to place these passive galaxies at higher redshifts compared with the distribution from Moutard et al. The reason for this discrepancy is probably because after z$\sim$1.4, the 4000 Å/Balmer break is redshifted past the z filter, and the lack of intermediate filters between z and K_s, like J and H in Moutard et al., when performing SED fitting can lead to a degenerate output, underestimating the true photometric redshift of the galaxy. This is why, for our

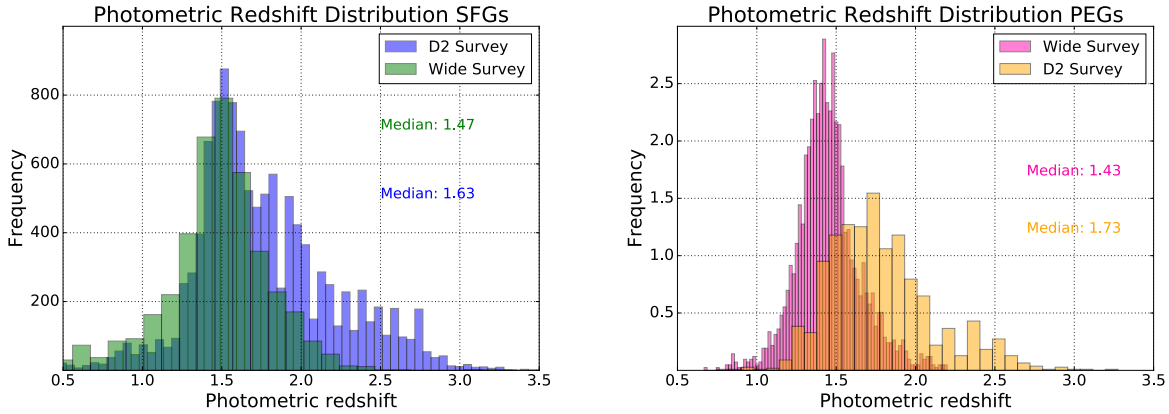

Figure 4.1: **Left:** Histogram of the photometric redshift distribution of star-forming galaxies in the Wide fields and in D2 (frequency = occurrences at that particular bin). **Right:** Redshift distribution of passive galaxies in the same fields. Photometric redshifts for D2 were obtained from Muzzin et al. (2013b) while redshifts for the wide fields were obtained from Moutard et al. (2016a).

final stellar mass function, we assumed that our PE-gzK$_s$ galaxies are characterized by the redshift distribution of Muzzin et al., as defined from the SEDfitting of 30 bands in the COSMOS field.

Also apparent from Figure 4.1, when comparing the redshift distribution for D2, is the fact that SF-gzK$_s$ peaks at lower redshifts than PE-gzK$_s$, and that even though there is seemingly a low-redshift ($z \leq 1.2$) tail for SF-gzK$_s$, PE-gzK$_s$ seem to be distributed at higher redshifts.

In addition, Figure 4.2 shows a 2D histogram of the redshift distribution of passive and star-forming galaxies as a function of their magnitudes. In this histogram we can see that the redshift distribution for our passive galaxies is $1.1 < z < 2.4$, with a lower mean than the originally $1.4 < z < 2.5$ redshift distribution proposed for BzK$_s$ galaxies by Daddi et al. (2004).

To assess the magnitude dependence for this redshift distribution, we smoothed our 2D histogram (at each magnitude bin) using a Gaussian kernel (with a $\sigma = 2$ for PEGs and a $\sigma = 3$ for SFGs), which extrapolates at both edges of the distribution, i.e, the brightest and faintest bins, and we normalized it by the area under the curve to obtain a redshift density distribution ($N(z, m)$), shown in Figure 4.3. We assume that this redshift density distribution is a good proxy for our probability density function, or $p(z, m)$. If instead, not all of our galaxies are detected with a gzK_s selection technique, our results at each magnitude will have a different normalization, mostly affected is the bright population ($log\,(^{M_*}/_{M_\odot}) < 19.5$), for which the new normalization would still be within uncertainties ($< 20\%$). Nonetheless, it is important to take into account the fact that as the catalog in D2 was selected using a gzHK_s selection technique, it might not have the exact redshift distribution as a gzK_s selected catalog (i.e., the wide fields). Similarly, given that we use the redshift distribution in a $\sim 1\,deg^2$ field and apply it to all of our survey $\sim 27\,deg^2$, our redshift distribution may suffer from effects of cosmic variance. From both figures we observe an apparent magnitude-dependent redshift distribution, i.e., brighter objects are found to be at lower redshifts than fainter ones.

The Daddi et al. initial assessment for the redshift distribution of BzK$_s$ galaxies was based on a smaller sample with a limited number of bright galaxies. Hence since most of their sample lies at fainter magnitudes, they recovered a redshift distribution of $1.4 < z < 2.5$, based on spectroscopic information for the K20 survey. With the advent of larger area surveys, we can see that for brighter galaxies, their redshift distribution peaks at lower values.

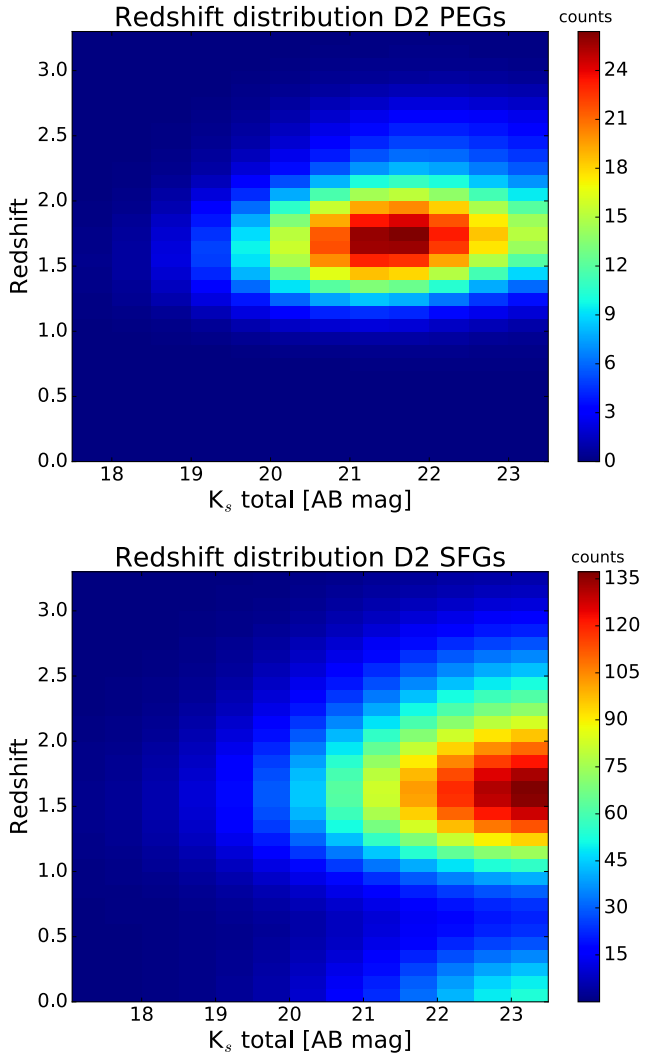

Figure 4.2: 2D Histogram of the redshift distribution for our passive galaxies (top) and star-forming galaxies (bottom) in D2. Based on photometric redshifts from Muzzin et al. (2013a). As can be seen our sample has a redshift distribution between $1.1 < z < 2.4$, lower than originally proposed by Daddi et al. 2004. Furthermore, this redshift distribution is dependent on magnitude as can be seen in our probability distribution in Figure 4.3

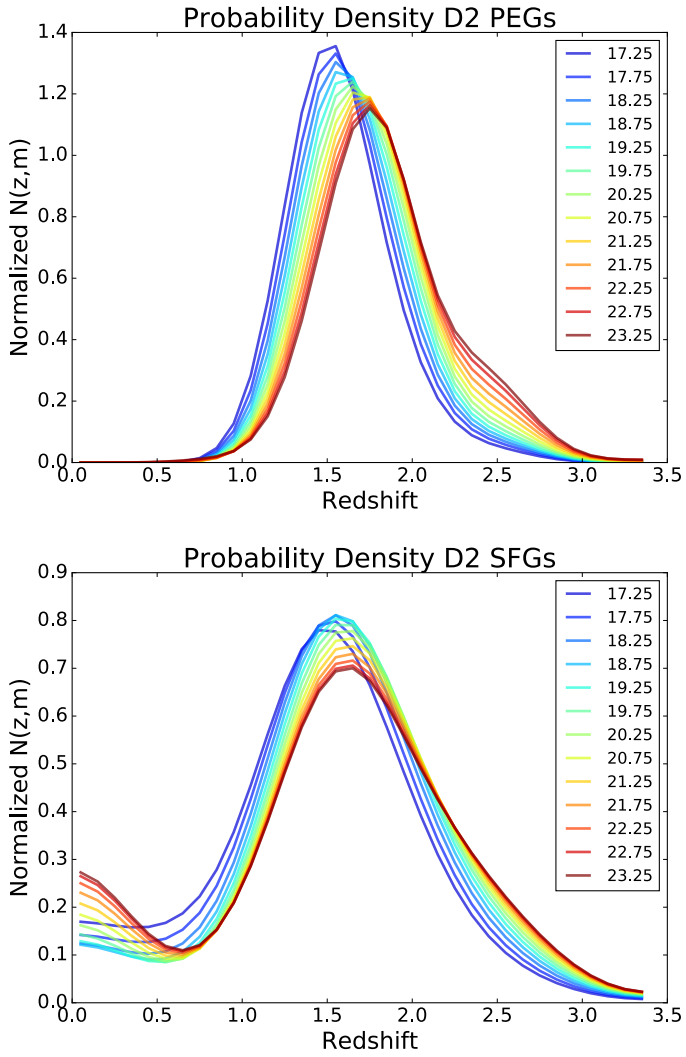

Figure 4.3: Magnitude dependent probability density distribution of redshift for our passive and star-forming galaxies. Photometric redshifts as in Figure 4.2. As can be seen as we move to brighter magnitudes, passive and star-forming galaxies are progressively found at lower redshifts. Also observed is a low-redshift contamination in the star-forming population. This has already been observed by previous authors Reddy et al. (2005), Merson et al. (2013).

Using the magnitude dependent redshift distribution that we observe in Figure 4.3, we compared the results obtained from our matched data with Muzzin et al, and Moutard et al. As can be seen in Figure 4.4 both redshift distributions seem to agree on the peak of the probability distribution for the brightest magnitudes. Nevertheless, Muzzin's photometric redshifts (top panel) have a probability tail that extends to higher redshifts compared to that of Moutard's (bottom panel) and the peak probability of $K_s < 20.5$ passive galaxies seems to be at $z \sim 1.6$ for Muzzin et al. while for Moutard et al. it seems to be at $z \sim 1.5$. This could be due to the fact that Moutard et al. constrain the 4000 Å/Balmer break using only the z and K_s bands. This implies that this break could be redshifted to anywhere between redshifts 1.3 to almost 4, but the lack of intermediate infrared bands (such as H, J and Y) could under-estimate their redshifts.

Starting from our probability density function, shown in Figure 4.3, we can estimate the effective volumes for our sample as a function of magnitude using equation 4.1:

$$V_{eff}(m) = A_f \int \frac{dV}{dz}\, p(m,z)\, dz\,, \tag{4.1}$$

where A_f is the effective area of our sample, $\frac{dV}{dz}$ is the comoving volume per square degree and $p(m,z)$ is the probability density function, dependent on magnitude and redshift.

4.2 Stellar Masses

We estimated galaxy masses for our passive galaxies from their K_s total magnitudes. At redshifts of $z \sim 1.6$ the observed K_s band light from galaxies is generated by the long-lived

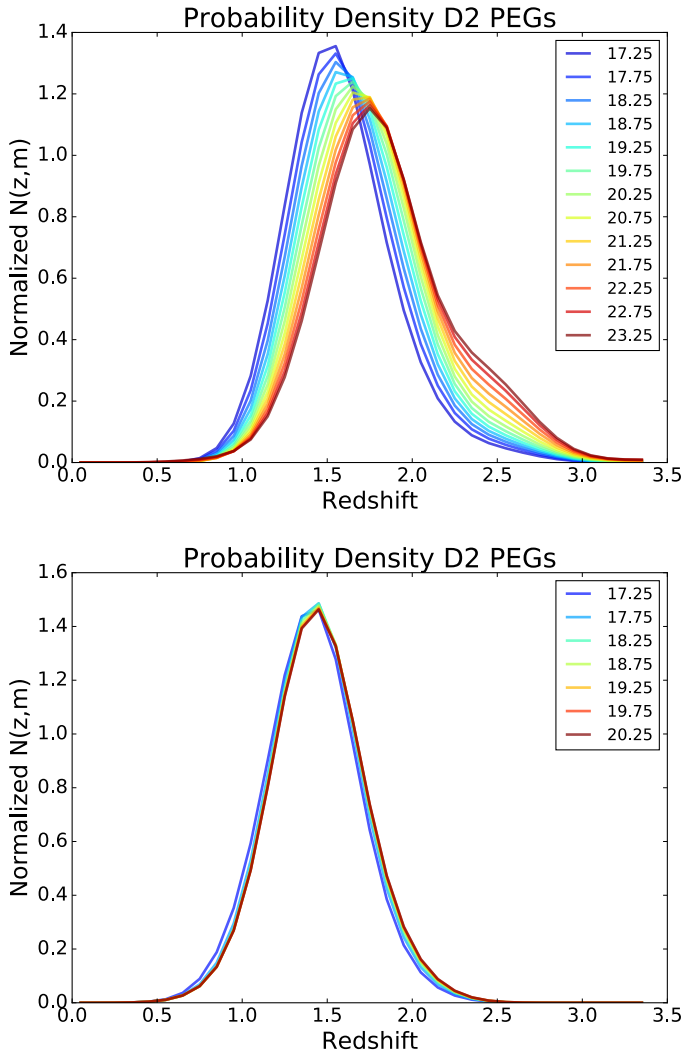

Figure 4.4: Magnitude dependent density distribution of redshifts for passive galaxies in Muzzin et al. (2013b) (Top panel) and Moutard et al. (2016b) (Bottom panel). As can be seen, both distributions sample similar limits for the distribution of passive galaxies (between redshifts of 0.5 and 2.5-3.0). However, the peak probability seems to be higher for Muzzin et al. and they spread to higher redshifts while for Moutard et al., all redshifts have a narrower distribution.

low-mass stars that are expected to contain most of the stellar mass of the galaxy. This is why the K_s band is a good proxy for a light-to-mass conversion, allowing us to build a stellar mass function.

The idea that infrared magnitudes are a good proxy for stellar masses is not new, Kauffmann & Charlot (1998) argue that the infrared light to mass ratio is fairly independent of the star-formation history and can be used to derive the stellar mass by applying a multiplicative factor to the K-band luminosity. Similarly, Longhetti & Saracco (2009) explored the dependence of the estimates of stellar masses of early type galaxies with different models and parameters used during the SED fitting procedure and proposed that a similar and suitable result can be found by a simple conversion to mass based on the redshift and observed K_s magnitude of the galaxy. In the same way, they claim that most of the optical/UV light from a galaxy is produced by short-lived bright stellar populations that only represent a few percent of the total stellar content of a galaxy.

In order to find a suitable conversion between magnitude and mass we used the same $\sim$ 1400 cross-correlated passive gzK_s in D2 that overlap with the COSMOS field in the Muzzin et al. 2013 catalog. To obtain stellar masses for their galaxies, Muzzin et al performed SEDfitting to a set of models with exponentially declining star-formation histories (SFH), solar metallicity, a Chabrier (2003a) initial mass function and allow visual attenuation (A_v) to vary between 0 and 4. Once we identified the corresponding galaxies for our D2 field, we were able to make a simple correlation of K_s total magnitudes and stellar masses as seen in Figure 4.5. The best-fit orthogonal distance correlation is shown as a solid line along with its 1σ scatter, represented with dashed lines.

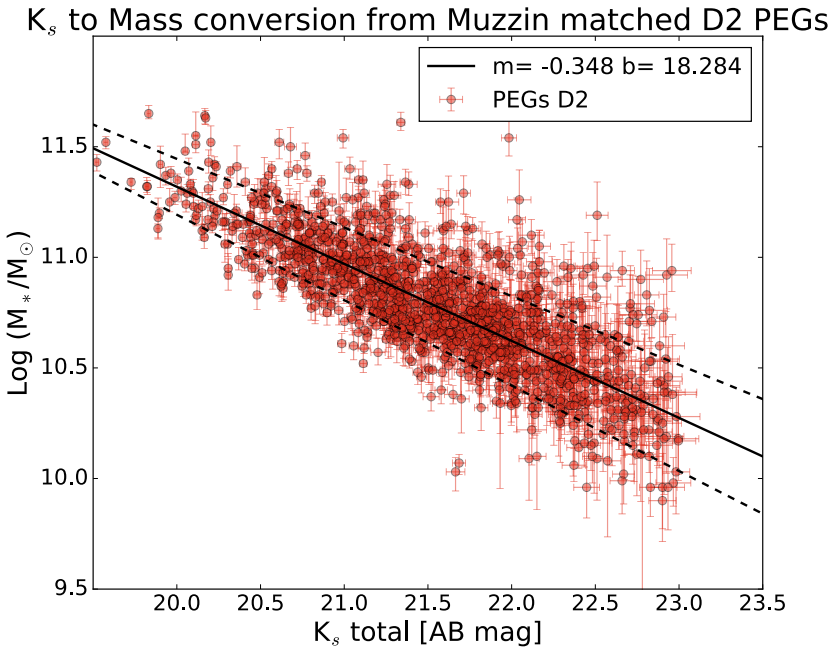

Figure 4.5: Correlation between K_s magnitudes and stellar mass. Stellar masses were obtained from Muzzin et al. after cross-matching $\sim$ 1400 objects in our sample that overlap with the COSMOS field. The best fit correlation is shown as a solid line and its 1σ scatter is represented with dashed lines. At $K_s \sim 20.5$ this 1σ scatter is approximately 0.12. As can be seen in this figure, there seems to be a good correlation between K_s band magnitudes and the stellar mass of a galaxy.

Hence, we used Equation 4.2 (the line of best fit to the data in Figure 4.5) to determine the masses of our galaxies based on their magnitude:

$$log[M_*/M_\odot] = (-0.348 \pm 0.007) \times K_s + (18.284 \pm 0.145) \tag{4.2}$$

For comparison, for early type galaxies and using a fixed IMF, Longhetti & Saracco (2009) find that the mass resulting from SED fitting is dependent on redshift. This is why, assuming a formation redshift of 4 they propose that for a given luminosity, and a Salpeter IMF, the stellar mass can be derived as a function of redshift by means of the following 4.3:

$$log[M^{Salp}(z)] = -0.4m_{k-vega} + 17.45 + 1.22z - 0.25z^2 \tag{4.3}$$

This mass can then be further calculated with a Chabrier IMF via:

$$[M^{Chab}] = 0.55 \times [M^{Salp}] \tag{4.4}$$

This conversion, between Salpeter (1955) and Chabrier (2003b) IMFs, independent of redshift, gives a conversion between IMFs that are within 10% in agreement when comparing them with results from stellar population models (Longhetti & Saracco 2009).

Using Equations 4.3 and 4.4 and assuming $z \sim 1.6$, we calculated the resulting masses for our population of PEGs. Then we found the line of best fit to this mass estimate, presented in Equation 4.5 and in Figure 4.6 as a dotted-dashed line.

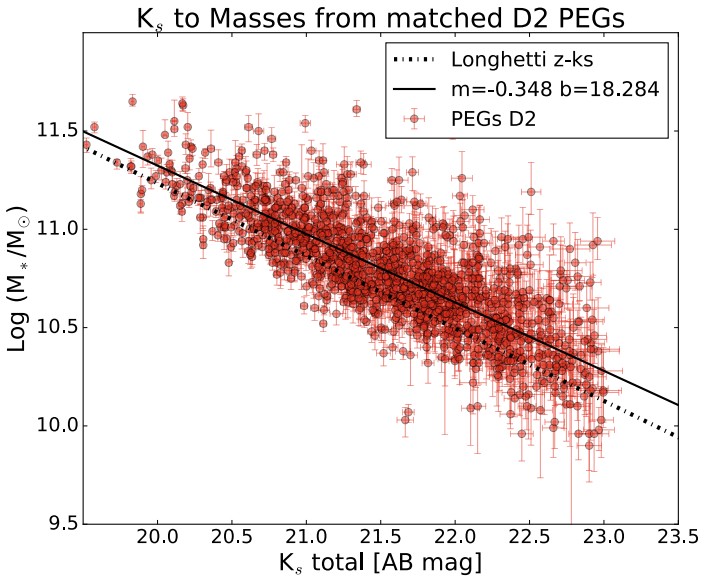

Figure 4.6: Best-fit correlation between K_s magnitudes and Muzzin et al., masses compared with Longhetti et al., redshift dependent masses. Even though the slopes are similar for both fits, there is a difference of $\sim$ 20% in their normalizations. This discrepancy could be attributed to Longhetti & Saracco (2009) initial assumptions.

$$log[M_*/M_\odot] = (-0.368 \pm 0.003) \times K_s + (18.612 \pm 0.071) \tag{4.5}$$

The slopes for both fits are similar (refer to Equations 4.2 and 4.5) but there is a difference of 20% in the normalization. As mentioned in Longhetti & Saracco (2009) their proposed relation between redshift and mass is probably not a reliable estimator due to the initial assumptions used to obtain it. Such assumptions include a fixed formation redshift of 4 and a simple star-formation history. This is why, we employ the best-fit correlation between K_s and $log\,(M_*/M_\odot)$ using Muzzin's et al. stellar masses (shown in equation 4.2) to obtain stellar masses for our sample.

Finally, using Muzzin's photometric redshifts along with the K_s to mass conversion

derived from their masses (i.e., Equation 4.2) we built a stellar mass function with our combined Deep and Wide catalogs for passive galaxies at z$\sim$ 1.6. We compare this result with that of previous authors who have also classified passively evolving galaxies at similar redshifts.

Figure 4.7 shows our result in red circles, along with those of Muzzin et al. (2013b), Ilbert et al. (2013) and Tomczak et al. (2014). As can be seen from this figure, our results seem to be in fair agreement with most of these surveys. Nevertheless, all surveys have a large scatter between each other, except at intermediate masses ($log\left(M_*/M_\odot\right) \sim 11.2$). This discrepancy is present even between surveys that use the same data, such as Muzzin et al. and Ilbert et al. A possible explanation for this effect could be cosmic variance between different surveys (our effective area is $\sim 27\, deg^2$, hence cosmic variance is not as prevalent, while Muzzin et al. and Ilbert et al. use a survey with an area of 1.62 deg^2 while Tomczak's survey effective area is 316 $arcmin^2$), or the different assumptions when performing SEDfitting to find the masses for each galaxy.

Finally, to assess the differences when considering just the photometric redshifts of Muzzin et al. or including as well those of Moutard et al. 2015, we plotted a comparison of our stellar mass function using both redshift distributions in Figure 4.8. The largest shift is 0.03 dex, which does not represent a considerable change in our results.

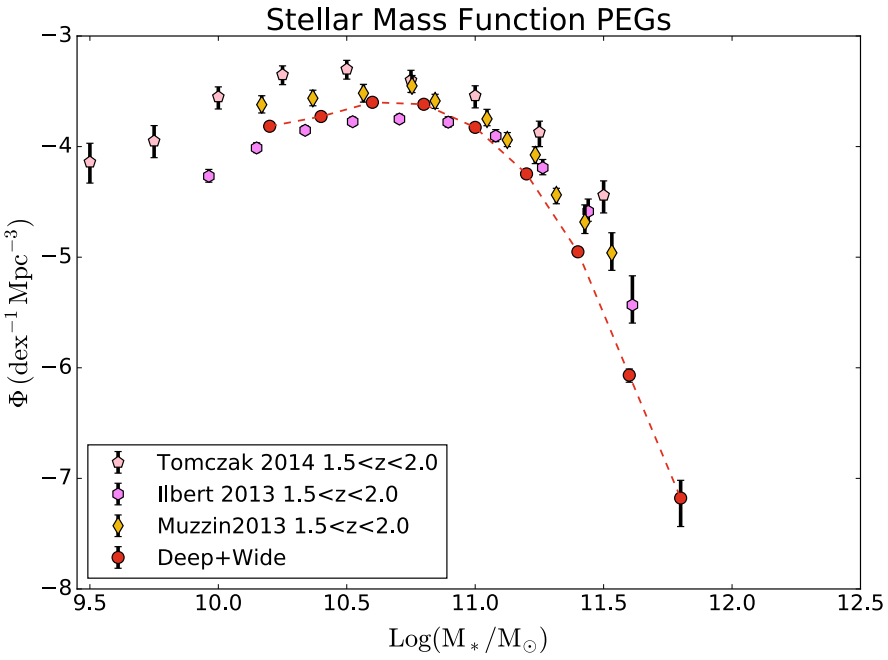

Figure 4.7: Stellar Mass Function of passive galaxies at z $\sim$ 1.6 selected with the gzK$_s$ colour-colour selection. Comparing with previous results, we can observe that our results are fairly consistent at the faint end but diverge at intermediate masses, possibly due to a lack of bright passive galaxies in D2, our K_s to $log\,(M_*/M_\odot)$ calibration could be underestimated. Nevertheless, due to the small areas of these previous results, the stellar mass function was not sampled past a mass of $Log\,(M_*/M_\odot) = 11.5$. Due to our large areas we are able to recover a significant population of ultra-massive passive galaxies at high redshift.

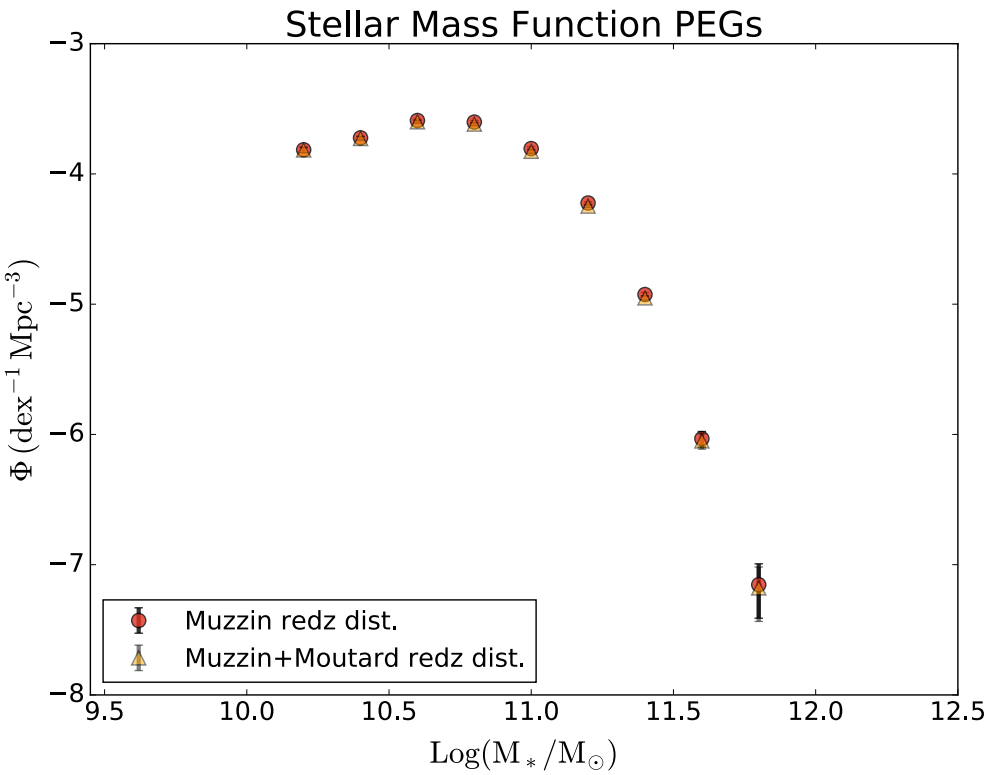

Figure 4.8: Stellar Mass Function of passive galaxies at z $\sim$ 1.6 selected with the gzK$_s$ colour-colour selection and two different redshift distributions: Shown in red circles is the redshift distribution of only Muzzin et al. (using a Chabrier IMF). On the other hand, orange triangles shows a combined redshift distribution of Muzzin et al. at all magnitudes and Moutard et al. (both assuming a Chabrier IMF) only for K$_s$ $<$ 20.5 galaxies (i.e., the completeness of our sample). As can be seen, using both redshifts distributions yield similar results in the building of our stellar mass function. Nevertheless, given the better constraint found with the 30 photometric bands of the COSMOS field, we continue our analysis with the stellar mass function built using the mentioned redshift distribution of Muzzin et al.

4.3 Fitting the Stellar Mass Function

In order to find the Schechter function that best describes our population of passively evolving gzK$_s$ galaxies, we performed a χ^2 minimization fit to our data. However, due

to uncertainties in our K_s to mass conversion and since galaxy density decreases exponentially towards brighter magnitudes, galaxies are more likely to scatter to higher mass bins than lower mass. This effect, called the Eddington Bias (Eddington 1913, Caputi et al. 2010 and Ilbert et al. 2013), can cause a steepening of the stellar mass function at the bright end. In order to assess this bias, we performed a χ^2 minimization fit on a convolved Schechter function.

To begin, we bootstrap our original sample, then perturb these bootstrapped masses using a normal distribution (its standard deviation is defined by the uncertainties in mass at each magnitude, previously shown as dashed black lines in Figure 4.5). By performing the bootstrap and mass perturbation on our sample, we are able to account for Poissonian errors and uncertainties in masses, respectively, when calculating the best-fit model.

Next, for each bootstrap, we bin our data and perform a χ^2 minimization using a Schechter function (Equation 4.6, Marchesini et al. 2009) that has been convolved with a Gaussian (as shown in Equations 4.7 and 4.8). As before, the standard deviation of this Gaussian is dependent on the uncertainties in the K_s to Mass conversion.

$$\Phi(M) = ln\,(10)\,\Phi^* \left[10^{(M-M^*)(1+\alpha)}\right] exp\left[-10^{(M-M^*)}\right] \tag{4.6}$$

$$\Phi_{convolved}(M) = \int_{-\infty}^{\infty} \phi(M')G(M-M',\sigma)dM', \tag{4.7}$$

$$G(M-M') = \tfrac{1}{\sigma\sqrt{2\pi}}\, exp\left(-\tfrac{M'-M}{2\sigma^2}\right)$$

$$\Phi_{convolved}\left(M\right) = \frac{1}{\sigma\sqrt{2\pi}} \int_{-\infty}^{\infty} \Phi\left(M'\right) exp\left(-\left(M' - M\right)/2\sigma^2\right) dM' \tag{4.8}$$

In equations 4.7 and 4.8, $\Phi(M)$ is the original Schechter function and $G(M - M', \sigma)$ is the Gaussian used in the convolution, integrated over stellar masses (M') with a given expected value, $\mu = M$ and a given associated error σ.

We performed this minimization along a parameter space for α, M^* and ϕ^* (the three parameters that define a Schechter function), until we find the best fit for this sample. We repeated this process 10000 times, and define our best-fit model to be the peak of our output model space (this model represents the most likely representation of our data when including uncertainties).

Figure 4.9 shows three best-fit lines. To begin with, red dashed lines represent the best-fit Schechter function for our passive gzK$_s$ galaxies once they have been corrected for Eddington Bias while the second best-fit line, shown as a dotted orange line, shows the result of a fit when Eddington Bias is not taken into account. Also shown in equivalent colours (red and orange) are the resulting best-fit parameters for these Schechter functions.

Considering the fact that the binned data also suffers from Eddington Bias, we use the fractional change between the biased and bias-corrected Schechter fit to correct the binned stellar mass function. This correction can be seen in Figure 4.9 as orange (biased) and red (unbiased) filled circles.

As can be seen from figure 4.9, given the uncertainty of our stellar masses, when Eddington bias is not taken into account, the number of galaxies at the bright end of the stellar

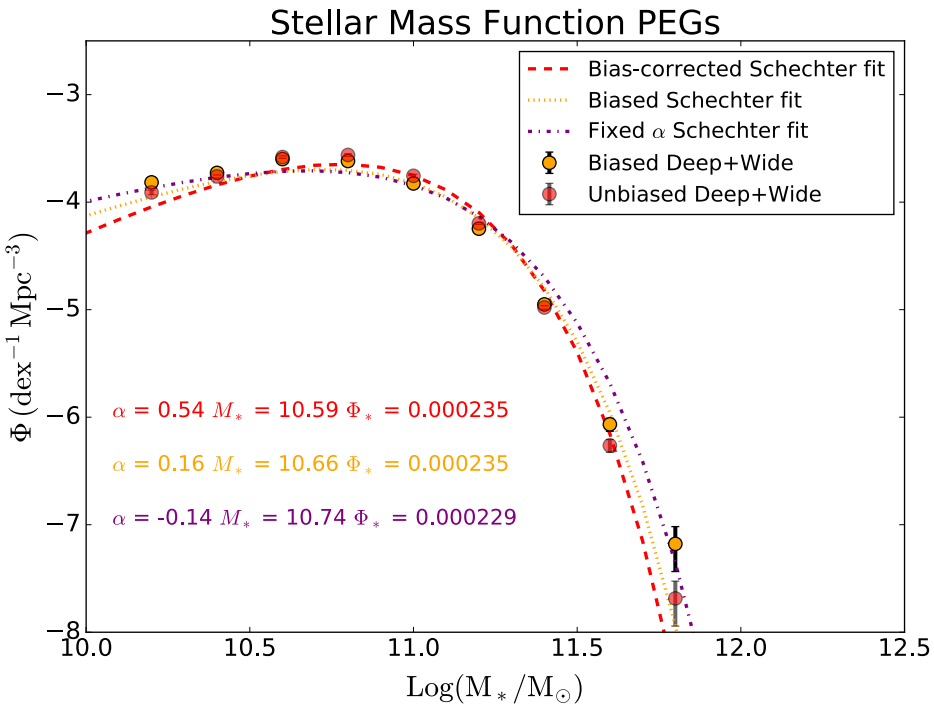

Figure 4.9: Best-fit Schechter function for our passive gzK$_s$ galaxies. A red dashed line represents the best-fit Schechter function once it has been corrected for Eddington Bias. For comparison, using a dotted orange line we show the best-fit Schechter function when this effect is not taken into account. Using the fractional change between the biased and bias-corrected Schechter fits, we correct the binned stellar mass function: Orange represents the biased SMF while red represent the Eddington-bias corrected SMF. Finally, we show a best-fit Schechter function when using a fixed faint end slope, $\alpha = -0.14$.

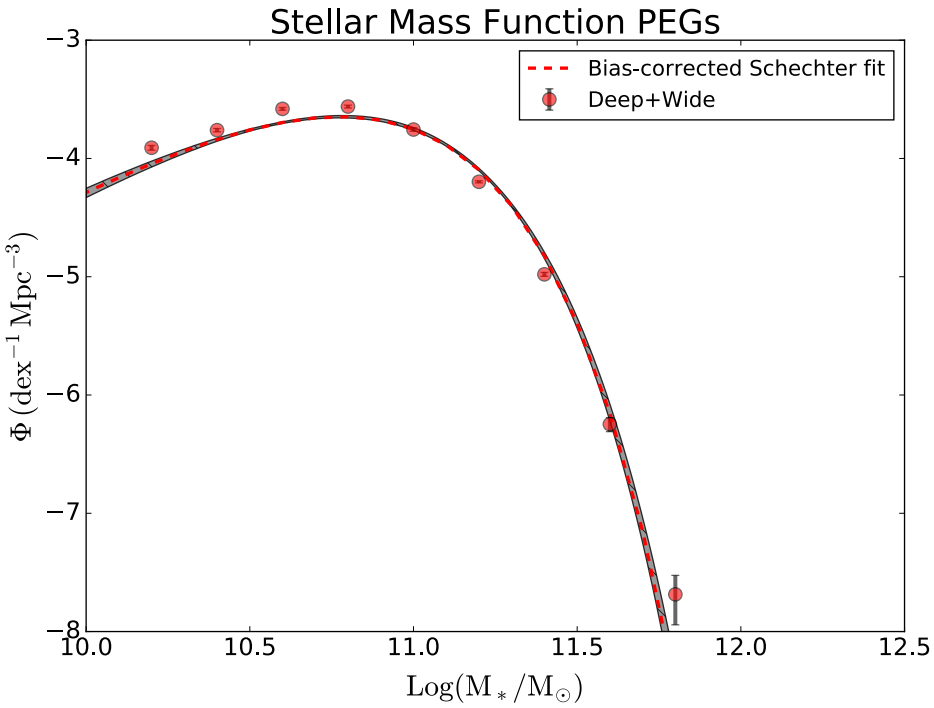

Figure 4.10: Stellar mass function of the Deep and Wide fields is shown in red filled circles. The shaded area represents the 16$^{\text{th}}$ and 84$^{\text{th}}$ percentile for the best-fit models in the bootstrapped data (10000 re-samplings).

mass function can be over estimated by as much as $\sim$ 0.5 dex. From this point onward, our binned data will be corrected for Eddington Bias.

Figure 4.10 shows the same best-fit results as Figure 4.9 and additionally shows the 16^{th} and 84^{th} percentile from the best-fit Schechter functions of the re-sampled data.

Table 4.1 shows a comparison of our results with those of previous authors at a similar redshift range. As can be seen from this Table, even though our results for Φ^* seem to be within the range of previously found results, our results for α are higher and M_* are lower, given that these two parameters are correlated, the fit is driven by the small error bars around M^*. Finally, Figure 4.11 shows the one sigma confidence levels for M^*, α and

Survey	Sample	$\log(M^*)[M_\odot]$	$\Phi^*[10^{-4}Mpc^{-3}]$	α
Muzzin et al. 2013	Quiescent	10.67 ± 0.03	$4.15^{+0.06}_{-0.08}$	0.03±0.11
Muzzin et al. 2013	Quiescent	10.80 ± 0.01	$3.61^{+0.02}_{-0.04}$	-0.4
Ilbert et al. 2013	Quiescent	$10.73^{+0.03}_{-0.04}$	$2.20^{+0.01}_{-0.01}$	$0.10^{+0.09}_{-0.09}$
Tomczak et al. 2014	Quiescent	10.76 ± 0.05	3.29 ± 0.05	-0.14±0.12
This work, free α	Quiescent	10.59 ± 0.02	2.35 ± 0.05	0.54 ± 0.08
This work, fixed α	Quiescent	10.74±0.01	2.29±0.03	-0.14

Table 4.1: Best fit Schechter function parameters for this work compared with multiple authors at 1.5 $\leq$z$\leq$ 2.0. Muzzin et al. employes two fitting techniques: One in which M^* and Φ^* are left as free parameters, while α is kept fixed to -0.4, and a second fit where M^*, Φ^* and α are all free parameters. Similarly, we present two results in our best-fit data: one with a free α and a fixed α (to the value given in Tomczak et al. (2014))

Φ^*, from the 10000 iterations.

As shown in table 4.1, there seems to be a large scatter of results around α, alongside with large associated uncertainties. This is not unexpected, given that in order to constrain this faint end slope, it is necessary to go deep below $log\,(^{M^*}/_{M_\odot}) < 10.5$. Currently, our fit is being driven by points with small error bars around M^*, hence showing a possible over-fit of our slope.

Given figure 4.7, Tomczak et al. (2014) is the only author whose completeness reaches $log\,(^{M^*}/_{M_\odot}) > 9.5$, hence probably being the best data to constrain the faint end slope. This is why we used Tomczak et al. best-fit α as a fixed parameter, and redid our fit (as described in this section) and obtained a second set of best fit parameters shown in the last row of table 4.1 and as a dot-dashed purple line in figure 4.9.

We perform a comparison of our best-fit parameters (both with a free and fixed α) in figure 4.12 and find that in our free α results M^* is systematically under, and α is systematically above all other authors, while our fixed α results seem to be in better agreement.

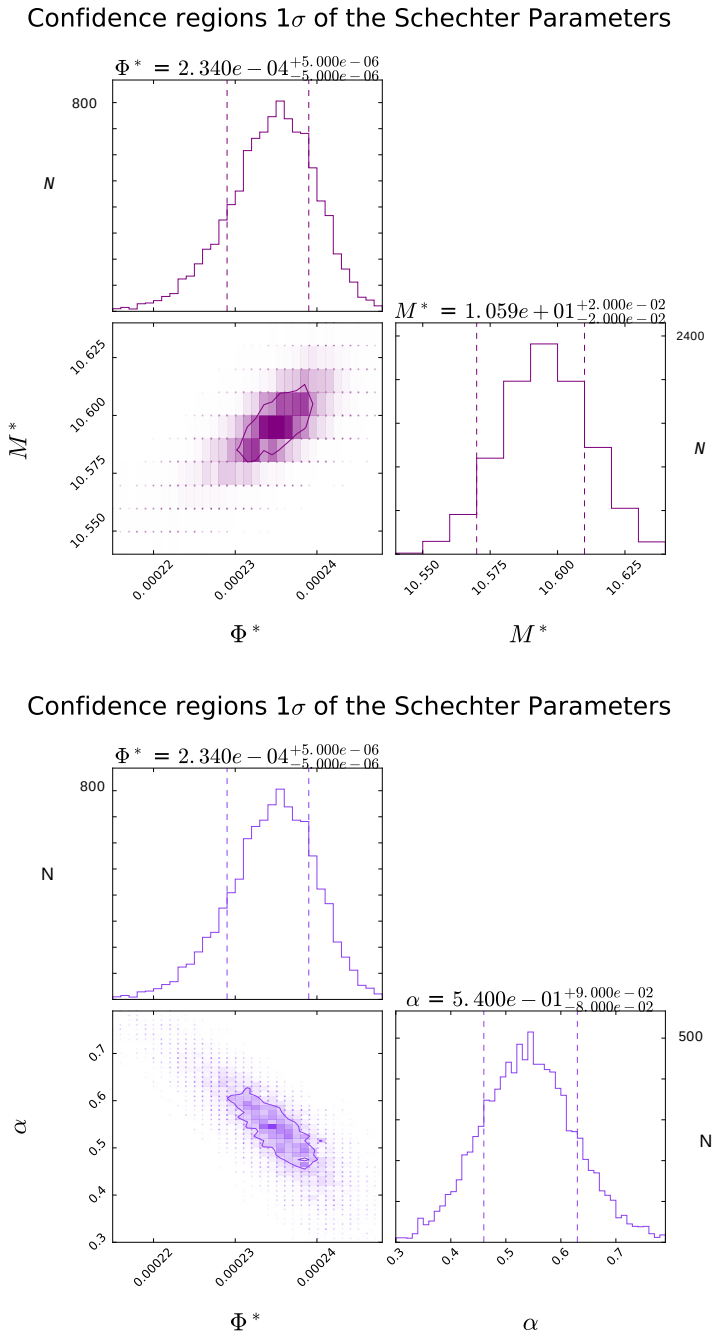

Figure 4.11: One sigma confidence regions for the best-fit Schechter parameters after 10000 bootstrap resamplings of our passively evolving gzK_s galaxies. At the top we show the confidence regions for $\Phi^*$and M^*. At the bottom for Φ^* and α. Labels at the top of each histogram show the median for each parameter.

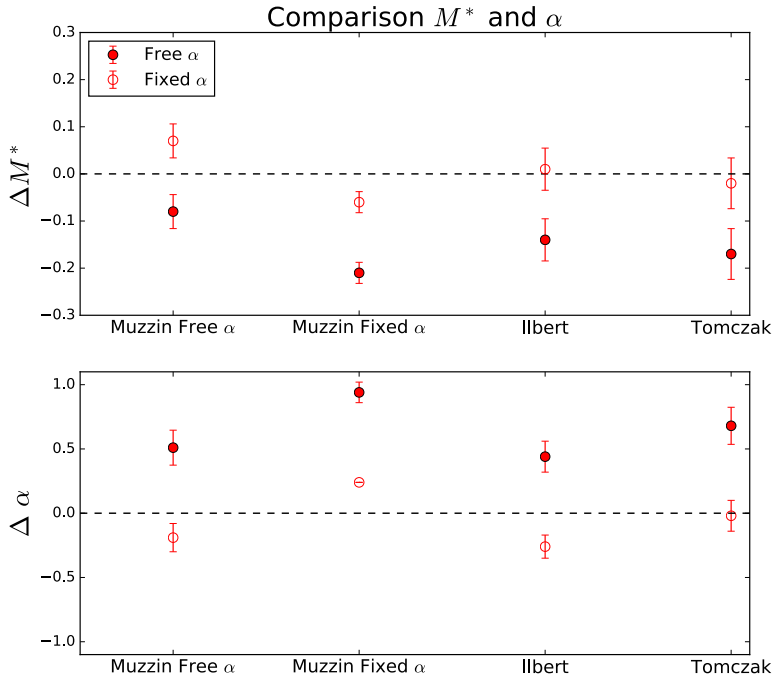

Figure 4.12: **Top panel:** Comparison of our best-fit M^* parameter for PEGs as compared with other authors (ΔM^* or $\Delta\alpha$ = This work - Other authors). As we can see, our result leaving the slope α as a free parameter is systematically lower than all authors. On the other hand, when constraining α to Tomczak's et al. best fit we find a better agreement with most authors. **Bottom panel:** Comparison of our best-fit α with other authors. Our fit is systematically higher than most authors, but a fixed value of $\alpha = -0.14$ seems in better agreement with most previous results.

As introduced in Chapter 1, Peng et al. (2010) introduced an empirical approach to explain quenching in galaxies. One of their proposed mechanisms, mass quenching, seems the dominant mechanism to explain the cessation of star-formation in massive galaxies. This mass quenching rate ($\lambda_m \sim {}^{SFR}/_{M^*} = \mu \times SFR$) is proportional to a constant $\mu = {}^{1}/_{M^*}$ (correlated to the physical mechanism behind the quenching, responsible for setting M^*) and the star-formation rate (SFR) of the galaxy. This model predicts that the SMF of passive galaxies will be well described by a Schechter function whose M^* is the same as that of the original SF population and a difference in slope of $\alpha_{PE} = \alpha_{SF} - 1.0$.

Once Eddington bias is taken into account, the stellar mass function for gzK$_s$ passive galaxies at $z \sim 1.6$ seems well described by a Schechter function, as can be seen in Figure 4.9, even at the bright end of the stellar mass function. This result is consistent with the mass quenching mechanism. Nonetheless, some authors have found that, at high redshifts ($z > 4$), the bright end of the stellar mass function in star-forming galaxies seems to deviate from a simple Schechter function (Ono et al. 2018; Bowler et al. 2014). Several solutions have been proposed to this result: Some argue that the stellar mass function is better fitted by taking into account gravitational lensing (Hildebrandt et al. 2009; Ono et al. 2018), while others postulate a double power law to fit the bright end of the stellar mass function (Bowler et al. 2014; Ono et al. 2018). However, it is possible that at these high redshifts, this mass quenching mechanism is still not in place, and the bright end of the SMF has yet to reached a critical quenching mass (Bowler et al. 2014; Peng et al. 2010). In contrast to $z \sim 4$, at $z \sim 1.6$ a SMF of quiescent galaxies well described by a Schechter function is clear evidence that the mass quenching mechanism is already in place.

Aside from predicting a Schechter function for the SMF of PEGs, Peng et al. predicts a M^*_{PE} equal to the M^*_{SF} of the SF population at the same redshift. Using best-fit M^* parameters from Ilbert et al., Muzzin et al., Tomczak et al. and our results (complemented with the best-fit parameter M^* for star-forming galaxies from Ilbert et al.) we compare in the redshift range $1.5 < z < 2.0$ how this parameter compares between these two populations. As we see on the left hand side of figure 4.13 the best fit M^* of SFGs is systematically higher by approximately ~ 0.2 dex when compared with the M^* of PEGs at $1.5 \leq z \leq 2.0$. This discrepancy between M^*_{SF} and M^*_{PE} increases to ~ 0.3 dex when we consider an under-estimation in stellar masses caused by unresolved photometry and SED fitting: Sorba & Sawicki (2018) compared the difference in stellar mass estimates when considering spatially-resolved and spatially-unresolved SED fitting. They find that unresolved fitting underestimates stellar masses by as much as a factor of five. Using an estimated $SFR \sim 10^{2.1}$ for a galaxy with $M_* = 10^{11} M_\odot$, gives $sSFR = 1.26 \times 10^{-9} yr^{-1}$ (Whitaker et al. 2014). We then use the correction formula given by Sorba et al. (their equation 6) to find the possible under-estimation in stellar masses of star-forming galaxies (shown as a blue arrow on the left panel in figure 4.13).

Even though the difference between these two parameters is not too large, if real, it would imply two things: M^*_{SF} is not constant with time, hence the physical mechanism responsible for mass quenching is also dependent on redshift (i.e., $\mu(z)$), and this mass quenching mechanism is not instantaneous but in fact has a given quenching time τ_{MQ} (consistent with a quenching mechanism with long time scales, such as kinetic AGN feedback, Moutard et al. (2016a)). These two requirements will set in place the fact that the PE

population did have the same M^* at the moment this quenching mechanism entered into play, but as M^* evolved, by the time τ_{MQ} was done, M^*_{SF} had evolved to higher masses (hence we would observe a growth of M^*_{SF} at lower redshifts).

Nonetheless, this proposed scenario is in disagreement with the top right panel in figure 4.13. The top right panel shows the evolution of M^*_{SF} and the bottom panel the evolution of M^*_{PE}. As can be seen from the two panels, both evolutions seem constant in the range $0.5 \leq z \leq 1.5$ but they starts to diverge to higher (lower) masses at higher redshifts in the SF (PE) population. The lack of evolution of M^*_{SF} below $z \leq 1.5$ is consistent with previous results (Ilbert et al. 2010; Moutard et al. 2016a) and given the large error bars in their determination at higher redshifts it is difficult to estimate if this growth is real, unconstrained (all results have high uncertainties at high redshifts) or biased (Moutard et al. 2016a finds no evolution of M^*_{SF} to $z \leq 1.5$ only when the SF population does not include transition galaxies, i.e., green galaxies).

An interesting feature is the contribution of these passive gzK$_s$ galaxies to the overall stellar mass density at redshift $z \sim 1.6$. For consistency with previous authors, we calculate the stellar mass density (SMD) by integrating the best-fit Schechter function in the range of $8 < log\left(M_*/M_\odot\right) < 13$. Uncertainties in the SMD were determined by integrating the best-fit Schechter function (with a free α) within the uncertainties in α, M^* and Φ^* given in Table 4.1.

Figure 4.14 shows the stellar mass density as a function of redshift. The work of previous authors is shown with empty symbols and for this work, passively evolving gzK$_s$ are shown as a red star. Black points represent all galaxies (selected from a rest-frame UV sam-

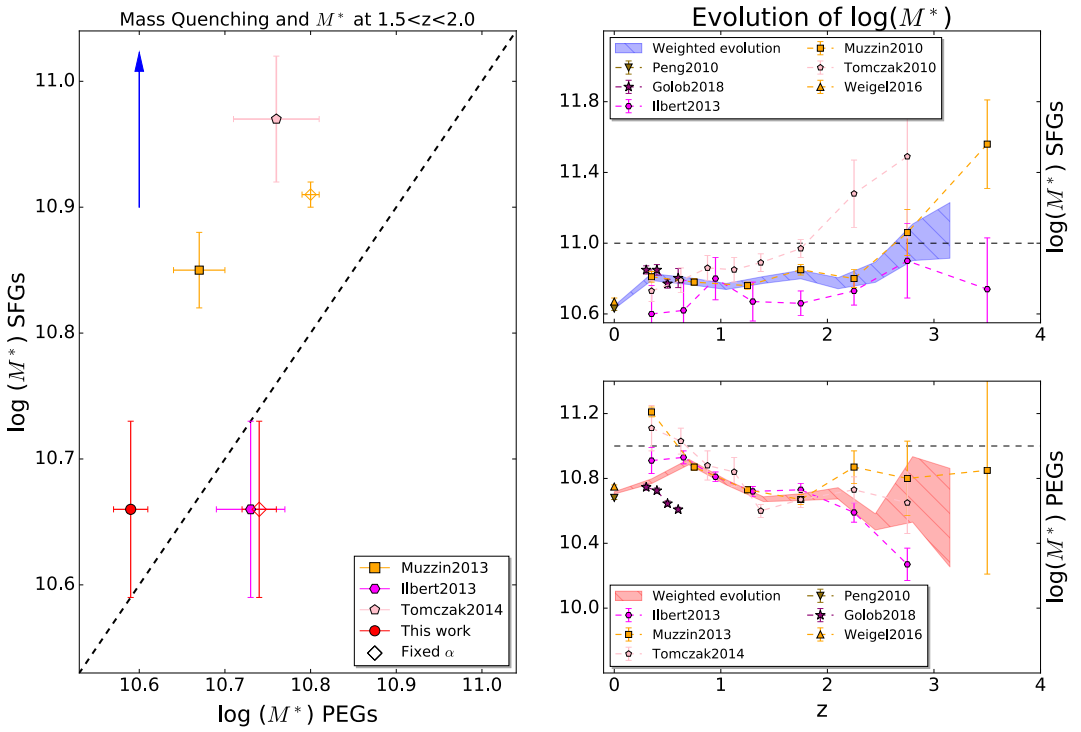

Figure 4.13: **Left panel:** Comparison of best-fit characteristic mass M* of star-forming (SFG) vs. passive galaxies (PEG) at $1.5 < z < 2.0$. As before, red symbols represent this work (our best-fit M^* for PEGs combined with Ilbert et al. best-fit M^* for SFGs) with two best fits: one with alpha as a free parameter and a second fixing alpha to Tomczak's et al. best fit slope (i.e., $\alpha = -0.14$**)**. Similarly, in orange, we show Muzzin et al. best-fit M^* with a free and fixed slope (refer to table 4.1). Finally, Ilbert et al. and Tomczak et al. are represented in magenta and pink respectively. For most of these results, we observe that the best fit M^* of SFGs is systematically higher ($\sim$ 0.2 dex mass) than the expected 1:1 correlation (shown with dashed black line) from Peng et al. Combining our results with Ilbert et al. is the only way our results would be in agreement (within uncertainties) with this 1:1 correlation. The **right panels** show the evolution of M^* for SF (**top panel**) and PEGs (**bottom panel**). Shown for each one of these evolutions, as a shaded region, is a weighted average between these authors. From this evolution, we observe a flattening of M^* for SFGs at lower redshifts, followed by a steady increase at higher redshifts ($z > 2$). In contrast, a systematic decrease of M^* for PEGs at lower redshifts, however, given the larger error bars given for each author it is difficult to assess this result.

ple for Song et al, UVJ selected by Muzzin et al., Ilbert et al. and Tomczak et al.), regardless of star-formation activity, and red represent passively evolving galaxies. For most authors the stellar mass densities have been calculated by integrating the best-fit Schechter function down to $log\,(M_*/M_\odot) = 8$, except for Tomczak et al. (2014) who calculated their stellar mass densities down to $log\,(M_*/M_\odot) = 9$. According to Tomczak et al. this would amount to a decrease in their stellar mass density of 5%. All points have been changed (when necessary) to a Chabrier initial mass function (Chabrier 2003a). Since our completeness limits are above $log\,(M_*/M_\odot) \sim 10.2$ our stellar mass density relies on a slope extrapolation at lower masses (down to $log\,(M_*/M_\odot) = 8$). As can be seen from Figure 4.14, the contribution to the stellar mass density of the passively evolving population grows with decreasing redshift and becomes almost dominant at lower redshifts.

Performing the same calculation but only for ultra-massive passive galaxies (i.e., the integral limits are $11.5 < log\,(M_*/M_\odot) < 13$) we find that this population of ultra-massive passive galaxies contribute $\sim$ 0.66% to the SMD of all passive galaxies at this redshift ($z \sim 1.6$). Assuming that the best-fit Schechter function for all galaxies at $1.5 \leq z \leq 2.0$ from Muzzin et al. (2013a) is also a good fit to describe all our gzK_s galaxies (passive and star-forming), at $z \sim 1.6$ passive galaxies contribute $\sim$ 20% to the total SMD (in good agreement with most authors) while ultra-massive passive galaxies ($11.5 < log\,(M_*/M_\odot) < 13$) contribute $\sim$ 0.13% to the SMD of all galaxies, and $\sim$ 13% to the SMD of all massive galaxies ($11.5 < log\,(M_*/M_\odot) < 13$).

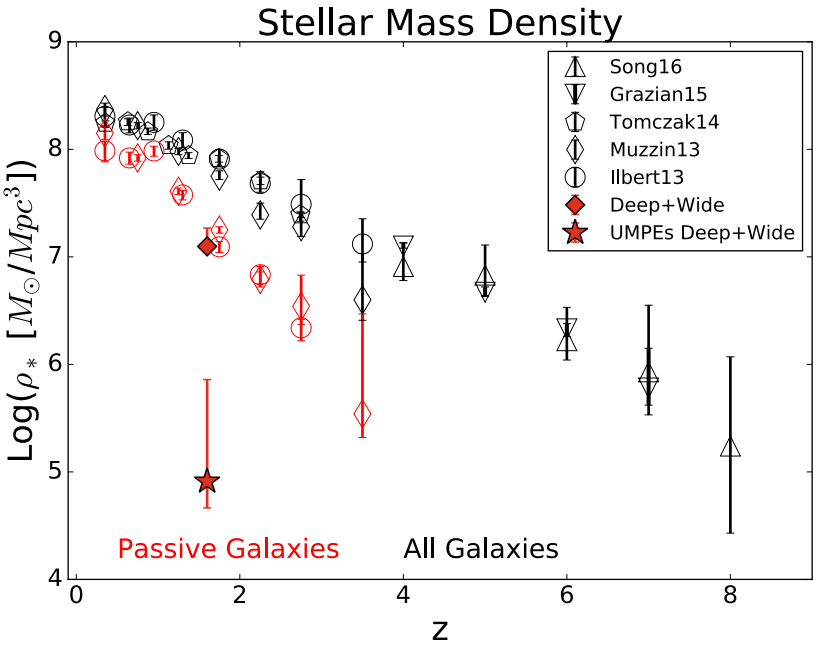

Figure 4.14: Stellar Mass Density as a function of redshift. Previous results from multiple authors are shown in open symbols, while our result for passively evolving gzK$_s$ galaxies in the range $8 < log\,(M_*/M_\odot) < 13$ is shown as a red filled diamond, while ultra massive passive galaxies ($11.5 < log\,(M_*/M_\odot) < 13$) are represented with a filled star. The stellar mass density was calculated by integrating the best-fit Schechter function (using the previously mentioned limits) assuming a Chabrier IMF.

4.4 Evolution of the Stellar Mass Function of Passively Evolving Galaxies

To get a glimpse of what happens to these massive passive galaxies once they are quenched and how they evolve up to the present time, we compared our results with those of other authors at lower redshifts: From Moutard et al. (2016b) passive galaxies at redshifts $0.8<z<1.1$ and from Peng et al. (2010) the same population of galaxies but at redshifts $0.02<z<0.085$. This comparison is shown in Figure 4.15.

The top panel shows the SMFs for this work (red filled points) alongside the SMF of Moutard et al. (orange pentagons) and Peng et al. (yellow diamonds). The bottom panel shows the fractional change of the number density from $z\sim1.6$ to $z\sim1$ and to $z\sim0$ relative to $z\sim1.6$: The ratio between Moutard et al. and our SMF is represented as orange pentagons, similarly, the ratio between and Peng et al. and our SMF is represented using yellow diamonds. Both of these ratios were calculated by interpolating between the points (and uncertainties) from each survey to the same log masses. Finally, also shown in this bottom panel is the ratio between the best-fit Schechter functions, of Peng et al. and Moutard et al. with respect to our best-fit Schechter function. These are represented as an orange dotted line for Moutard et al. and yellow dot-dash line for Peng et al.

As can be seen from the bottom panel, even though the relative evolution between the two fits is homogeneous for intermediate masses, it is dissimilar from a simple number evolution for the faint and bright end of the stellar mass function (the evolution is not simply modeled by a change in normalization, i.e., by simply quenching more galaxies

with the same stellar-mass distribution). For the low-mass end, this can be understood as the contribution of environmental quenching (mass-independent quenching process, presumably associated with satellite quenching) which only seems to make a significant contribution in the number of low-mass passive galaxies at lower redshifts. This effect can be seen as a flattening of the stellar mass function at the low-mass end, a flattening that becomes more evident at $z \sim 0$ than at $z \sim 1$.

On the other hand, at the massive end, it is hard to assess the discrepancy between these samples given the large associated uncertainties. However, if this discrepancy is true, it seems to be set in place between $z \sim 1.6$ and $z \sim 1$. It can represent the fact that during this time, quenched galaxies are significantly more massive than those quenched at higher redshifts or that there is significant growth via mergers.

Figure 4.16 shows a comparison of our passive galaxies at z $\sim$ 1.6 (filled red circles, re-scaled in Φ^*) with those of Peng et al. at z $\sim$ 0 split into environments: Filled yellow diamonds represent passive galaxies at $z \sim 0$ that reside in high density environments while open orange squares represent those galaxies at $z \sim 0$ residing in low-density environments. A corresponding colour for each population represents their best-fit Schechter function.

The bottom panel in Figure 4.16 shows a comparison of the fractional change between our results and the two environments at $z \sim 0$: The yellow dot-dashed line represents the ratio between the best-fit Schechter function from Peng et al. high-density quartile at $z \sim 0$ and our best-fit Schechter function at $z \sim 1.6$. Correspondingly, the orange dotted line represents the ratio of the best-fit Schechter function between galaxies that reside in their

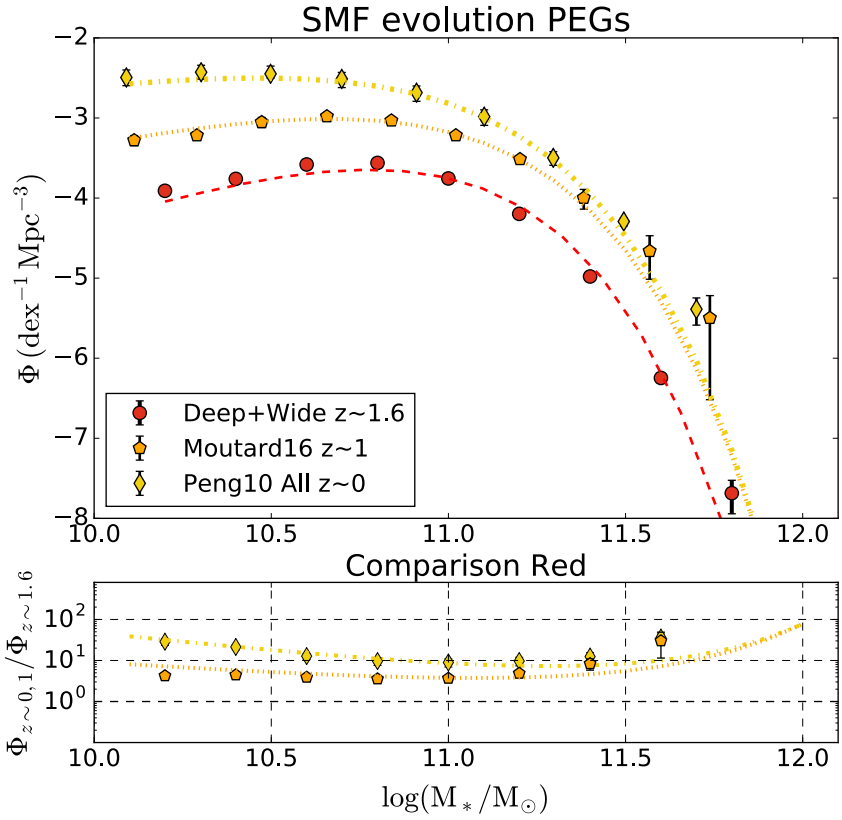

Figure 4.15: **Top panel:** Stellar Mass Function of passive galaxies (in all environments) and their best-fit Schechter models. Red points represent our sample at z∼1.6, orange pentagons represent passive BzK$_s$ galaxies at z∼1 from Moutard et al. (2016b) and yellow diamonds passive galaxies at z ∼0 from Peng et al. (2010). **Bottom panel:** Comparison between the best-fit Schechter functions between our sample and Peng et al. (yellow line), and between our sample and Moutard et al. (orange line). The points in this bottom panel represent the ratio between the SMF of Peng et al. (yellow) or Moutard et al. (orange) and our sample. As can be seen from this panel, the evolution of these z∼1.6 galaxies compared to z∼1 and z∼0 is relatively smooth for intermediate masses. Nevertheless at the faint end, where environmental quenching starts to become more important at lower redshifts, we see a divergence in the relative numbers between high redshifts and lower redshift counterparts.

low-density quartile at $z \sim 0$ from Peng et al. and our best-fit function at $z \sim 1.6$. Similarly, open orange squares were obtained by finding the ratio between an interpolated SMF from Peng et al. low-density quartile and our $z \sim 1.6$ SMF, while filled diamonds represent the same results but for Peng et al. high-density quartile.

From Figure 4.16 we can observe several different effects: At the faint end, both SMFs (low and high density environments) are shallower than our SMF at higher redshift. This can represent a build up of the faint passive population due to environmental quenching (Peng et al. 2010, Peng et al. 2012). Even though, we would expect to see the contribution of environmental quenching to be more pronounced in dense environments (by comparing both environments in Peng et al.), there is no significant change. This is possibly due to the fact that our sample is limited to $log\,(M_*/M_\odot) > 10.2$, hence our analysis is limited at fainter magnitudes.

On the other hand, at the massive end, there is a significant difference when comparing our SMF at $z \sim 1.6$ and those at lower redshifts in different environments. If we assume our massive passive galaxies to reside in truly low-density environments then we will not expect considerable evolution in mass in the SMF (if we assume low star-formation rates and no future interactions), it will only evolve in number as a re-normalization of the SMF as more galaxies are quenched up to $z \sim 0$. On the other hand, there seems to be an evolution in mass from redshift $z \sim 1.6$ to $z \sim 0$ when galaxies reside in dense environments, implying more massive SF galaxies that quench at later times or a growth of passive galaxies in mass driven by future interactions.

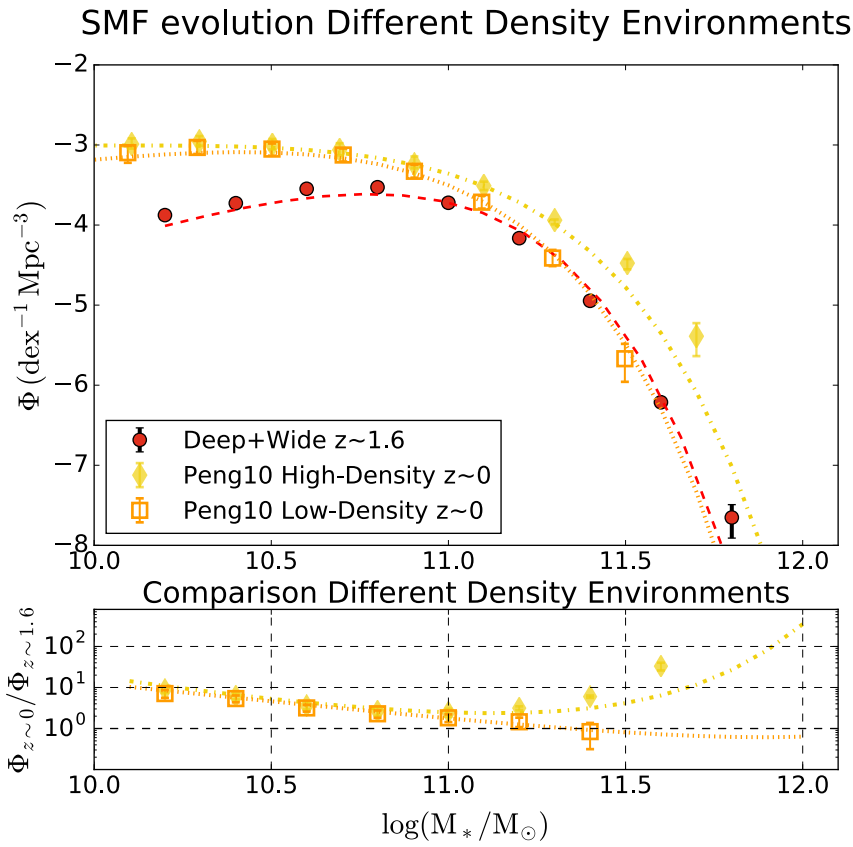

Figure 4.16: **Top panel:** Stellar mass function of passive galaxies and their best-fit Schechter model from this work at z∼1.6 (filled red circles and red dashed lines) as compared with z∼0 passive galaxies from SDSS (Peng et al. 2010) in high and low density environments: Filled yellow diamonds represent passive galaxies at $z \sim 0$ residing in high density environments, while open orange squares represent passive galaxies at $z \sim 0$ that reside in low-density environments. **Bottom panel:** Comparison between the best-fit Schechter functions from low and high-density quartiles from Peng et al. at z∼0 and our best-fit Schechter function at $z \sim 1.6$ (yellow and orange lines respectively). Also shown for comparison in the bottom panel is the ratio between an interpolated SMF from Peng et al. and our SMF of passive galaxies at $z \sim 1.6$. Orange squares and yellow diamonds represent the ratio between the SMF in the low and high density quartiles of Peng et al. and our SMF. As can be seen from the inset, the relative growth is dependent on mass (see text).

Summary

In this Chapter, we determined a magnitude-dependent redshift distribution of our sample and used this redshift distribution along with a K_s to $log(M_*/M_\odot)$ conversion to build our stellar mass function for passive gzK_s galaxies. The best-fit Schechter function to represent our data was calculated by taking into account Eddington Bias using a convolved χ^2 Schechter fit. The SMF our passive gzK_s galaxies at $z \sim 1.6$ seems well represented by a Schechter function, once Eddington Bias has been taken into account. Given our relatively bright completeness limit ($log\,(M_*/M_\odot) > 10.2$), we performed a second fit with a fixed slope, for which we find a better agreement in M^* with previous results at these redshifts. A stellar mass function that is well described by a Schechter fit can be explained by a mass quenching mechanism already in place at $z \sim 1.6$ for which we expect an exponential cutoff at high masses, with a M^* equal to that of the SF population at the moment of quenching.

By analyzing the correlation between M^*_{SF} and M^*_{PE} we find that M^*_{SF} is systematically higher than M^*_{PE} by $\sim 0.2 - 0.3$ dex, this implies a mass quenching mechanism that is redshift dependent hence setting a redshift dependent M^*_{PE} ($\mu(z) = 1/M^*(z)$). If this is true, both characteristic masses (for SF and PE galaxies) are the same at the moment the quenching mechanism has started, but if this is not an instantaneous mechanism (τ_{MQ}) M^*_{SF} continues to evolve to higher masses, while M^*_{PE} remains representative of the moment the mechanism started (Peng et al. 2010). Nonetheless, this expected evolution of M^*_{SF} to higher masses seems in disagreement with the best-fit parameters found for differ-

ent authors from $0 < z < 3.5$ (albeit large error bars at higher redshifts).

Finally, we analyzed the evolution of number density for passive galaxies between our $z \sim 1.6$ population and those at lower redshifts. From this analysis, we can see how the different quenching mechanisms and environment affects the evolution of this population: At lower redshifts a substantial growth of lower-mass passive galaxies could be due to a more efficient environmental quenching (satellite quenching) while the most likely way for massive passive galaxies, to significantly evolve to higher masses, is defined by the probability of mergers.

Chapter 5

Environments of Ultra-Massive Passive Galaxies

5.1 Nurture of Ultra-Massive Passive Galaxies

Galaxies mainly grow through two redshift-dependent mechanisms: star-formation and mergers (Vulcani et al. 2016). Specifically for massive early type galaxies, a two phase formation model has been proposed (Naab et al. 2009, Hilz et al. 2013): First, the core of the galaxy is formed through star-formation (efficient mass build-up) followed by ex-situ growth driven by a series of random encounters (minor mergers) with neighbouring galaxies. Star-formation is highly efficient at high redshifts but starting from intermediate redshifts, i.e., $z<1.5$, the main channel of growth is through minor mergers. This evolution by minor mergers can also explain the subsequent growth of massive galaxies in physical size from high to low-redshifts. (Hill et al. 2017, Hilz et al. 2013, McLure et al. 2013, Naab

et al. 2009).

Given the large area of our survey, we are able to identify the most massive passive galaxies at z$\sim$1.6 and we concern ourselves with trying to understand, now that they are passive systems (assuming their mass will not increase through re-ignited star-formation), how will they evolve to the present based on their companion galaxies and the probability of minor or major mergers.

To identify the most massive passive galaxies in our catalog (UMPEGs, for ultra-massive passive galaxies), we select all passive galaxies brighter than K_s= 19.5 (i.e., $log(M_*/M_\odot) \sim$ 11.49), leaving us with 61 UMPEGs. Two of these UMPEGs have spectroscopic redshifts: one in D2 (COSMOS field) with a redshift of $z = 1.48$ (Comparat et al. 2015) and another in W4 with $z = 0.84$.

By studying their environments, we are able to estimate their ex-situ growth phase as they evolve to lower redshifts. Similar to Tal et al. (2012) ($z \sim 0.34$ and $z \sim 0.65$), we analyzed the environments of ultra-massive galaxies at $z \sim 1.6$ based on a statistical surface density.

5.2 Environments of UMPEGs

Once we have identified our UMPEGs, following Tal et al. (2012) and Vulcani et al. (2013), we established a radius of search of 0.5 physical Mpc around each UMPEG and identified all gzK_s galaxies (i.e., star-forming and passive gzK_s galaxies) within this projected distance to this central UMPEG. Each UMPEG is the most massive passive galaxy in this

radius of search. Progenitors of present day ultra-massive galaxies are expected to reside in dark matter halos with virial masses $\sim 10^{13} M_{\odot}$ at $z \sim 1.7$ (Vulcani et al. 2016), and assuming a dark matter sphere, and a density defined as ρ_{200}, we expect a virial radius of 0.5 Mpc (Munoz-Cuartas et al. 2011). Using a simple merger time calculation (see Section 5.3), we estimate that every galaxy gravitationally bound within 0.5 Mpc will merge with the central UMPEG within 5 Gyrs in the Deep Fields and within 1.5-3 Gyrs in the Wide Fields.

Figure 5.1 shows two examples of the 0.5 physical Mpc radius of search around a central UMPEG, along with gzK_s-selected SF and PE companions in a gzK_s colour image. The UMPEG is shown in the center of the image, along with its corresponding K_s magnitude. Shown in red and cyan circles are passive and star-forming gzK_s companions to this central and, in the lower right corner, a K_s colour image of the central UMPEG. In total, we identified 6 UMPEGs in the Deep Fields, and 55 in the Wide Fields. All 61 gzK_s colour images can be found in Appendix A.

In order to obtain the relative luminosities of each companion relative to the central UMPEG, we determined rest-frame *i* magnitudes assuming the redshifts of the companion galaxies to be the same as their corresponding central UMPEG at $z \sim 1.6$ (given that we do not have a simple conversion between magnitudes and mass for SFGs). With SED fits and filter transmission curves, we use galaxy models from Bruzual & Charlot (2003) of Single Stellar Population (SSP) with extinction (E(B-V)) of zero, solar metallicities and ages of 1 Gyr for passive galaxies and Constant Star-Formation (CSF) models with an extinction E(B-V) = 0.3 (the median value given by the original Daddi et al. 2004 models), solar metallicities and ages of 0.2 Gyr for star-forming galaxies to determine a rest-frame model *i*

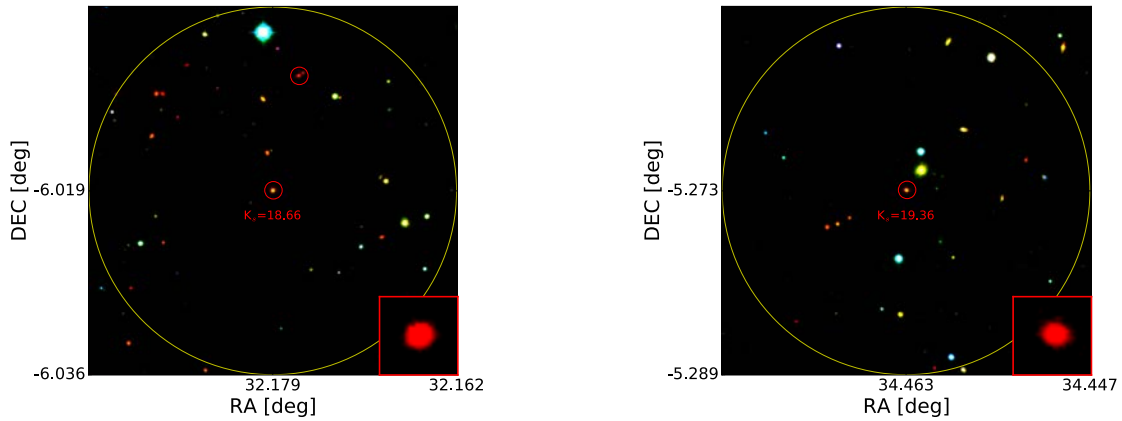

Figure 5.1: gzK_s colour images of two example UMPEGs. Each UMPEG is shown in the center of the image with its corresponding K_s magnitude (offset below the central UMPEG). Also shown, its companions within a radius of search of 0.5 physical Mpc (yellow circle): Red circles represents passively evolving companions and in blue (not present in these UMPEGs), star-forming companions. The inset in the lower right corner shows a $\sim$ 31.5 $\times$ 31.5 physical kpc K_s colour image of the central UMPEG.

magnitude (if instead we use E(B-V) = 0, this represents a change in the correction between observed to rest-frame magnitudes of $\sim$ 0.08). This provided us with a correction from observed K_s magnitudes to rest-frame i magnitudes (if we assume that the most probable redshift for our gzK_s sample is indeed 1.6, K-correction between K_s mags and rest-frame i is minimal). The ratio between these rest-frame magnitudes reflects a mass ratio.

Figure 5.2 displays the relation between the luminosity of the central UMPEGs with that of their corresponding companion satellites as a function of the rest-frame i magnitude of each central. The top figure shows the Deep Fields, and the bottom figure the Wide fields. Shown as a shaded yellow area is the magnitude range of our central UMPEGs which are shown as magenta circles. Out of those magenta circles, some are filled, to highlight the fact that those UMPEGs had no companions within the radius of search. Shown in a gray

shaded area is the 50% zone, i.e., where companions would be if they are at least half the luminosity of the central. Each neighbour is represented as either a blue or red symbol, depending on whether or not they were classified as SF or PE gzK$_s$ galaxies.

Due to the different completeness of our samples (refer to Section 3.3), the relative luminosity of the detectable companion compared with the central UMPEG will be different for the Deep and Wide Fields. This limiting completeness can be seen in Figure 5.2 as a dot-dashed line boundary (complemented by an orange shaded region) that represents the completeness of our sample.

From this figure, we can see an absence of companions at least half as bright as the central UMPEG, and only start to see a significant contribution of companions that are approximately $30-40\%$ the luminosity of the central UMPEG, however, most of these companions are approximately only 10% the luminosity of the central UMPEG. Results from this scatter figure also display background/foreground galaxies, but this contamination does not affect the conclusion of a lack of bright companions. Background/foreground contamination is completely removed in the surface density results (refer to Figure 5.4).

To correct for foreground/background contamination, we chose random locations in our fields (ensuring that after masking stars and spurious regions, the minimum area at these random locations is at least as big as the smallest area of search for the real UMPEGs) and assumed our UMPEGs to be at the center of those locations. We sampled 300 random environments to estimate an average surface density of foreground/background contamination of gzK$_s$ galaxies.

The left-hand side of Figure 5.3 shows the relative position of each neighbour around

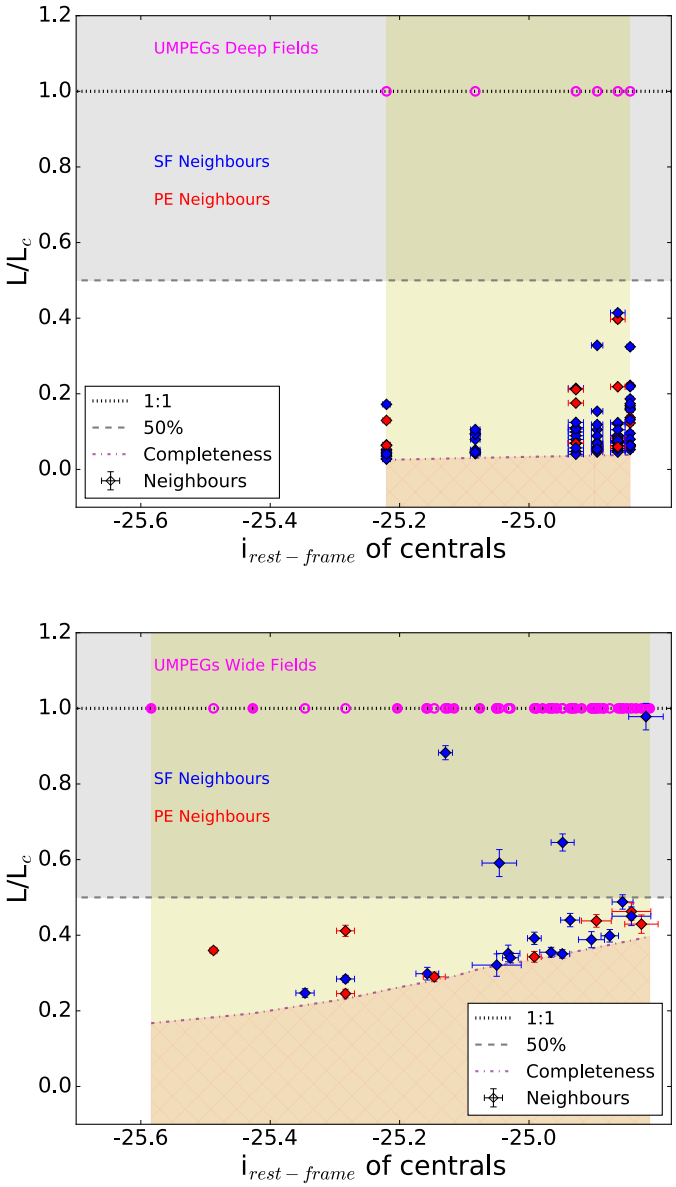

Figure 5.2: Scatter plots of companion galaxies with respect to the rest-frame i luminosity of the central UMPEG. Shown as a shaded yellow area is the magnitude range of our UMPEGs, empty magenta symbols are all identified UMPEGs, whereas filled magenta symbols represent those UMPEGs for which no companion was found. A gray shaded area represents the positions these companions would occupy if they were at least 50% as bright as the central UMPEG. As can be seen, there is a gap in this 50% region, showing the lack of companions with similar luminosities to the central UMPEG. This is no longer the case around $30-40\%$ which represents the presence of companions that are approximately $30-40\%$ the total luminosity of the central UMPEG. Finally, our completeness limit for each sample is shown in a crossed shaded orange region at the bottom of each figure.

their given UMPEG. In these plots which represent the Deep (6 UMPEGs, top figure) and Wide (55 UMPEGs, bottom figure) fields, we have overlapped all UMPEGs and their corresponding neighbours into one scatter plot (in this kind of plot, without specific redshift information, it is not possible to identify which of these companions are in fact foreground/background interlopers).

The central UMPEG is shown as a magenta circle in the center with a radius of search of 0.5 Mpc (also in magenta). Each companion has been represented with a symbol whose size scales accordingly to the mass of its central (the colour identifies these companions either as star-forming -blue- or passive -red- galaxies).

The right-hand side of this Figure shows a sample distribution of foreground/ background contamination by recovering neighbouring gzK_s when the central position within the 0.5 Mpc search radius is any random position in the sky (and not our UMPEGs). From this sample distribution of foreground/background contamination, we estimate that, for a 0.5 Mpc radius of search, each UMPEG has, on average (after correcting for this foreground/ background contamination), 15.5 and 0.89 companion galaxies in the Deep and Wide fields respectively.

Considering the redshift distribution of our passive galaxies presented in Figure 4.3, if our central happens to be found at the most probable redshift (the peak of our redshift distribution in the magnitude bin 19.5, where most of our UMPEGs will reside), then we will be able to recover within completeness limits all of its companions since they will be at the same redshift. However, if our central happens to be in the wings of this redshift distribution, it is possible we will miss some (or many) of its companions. To correct for

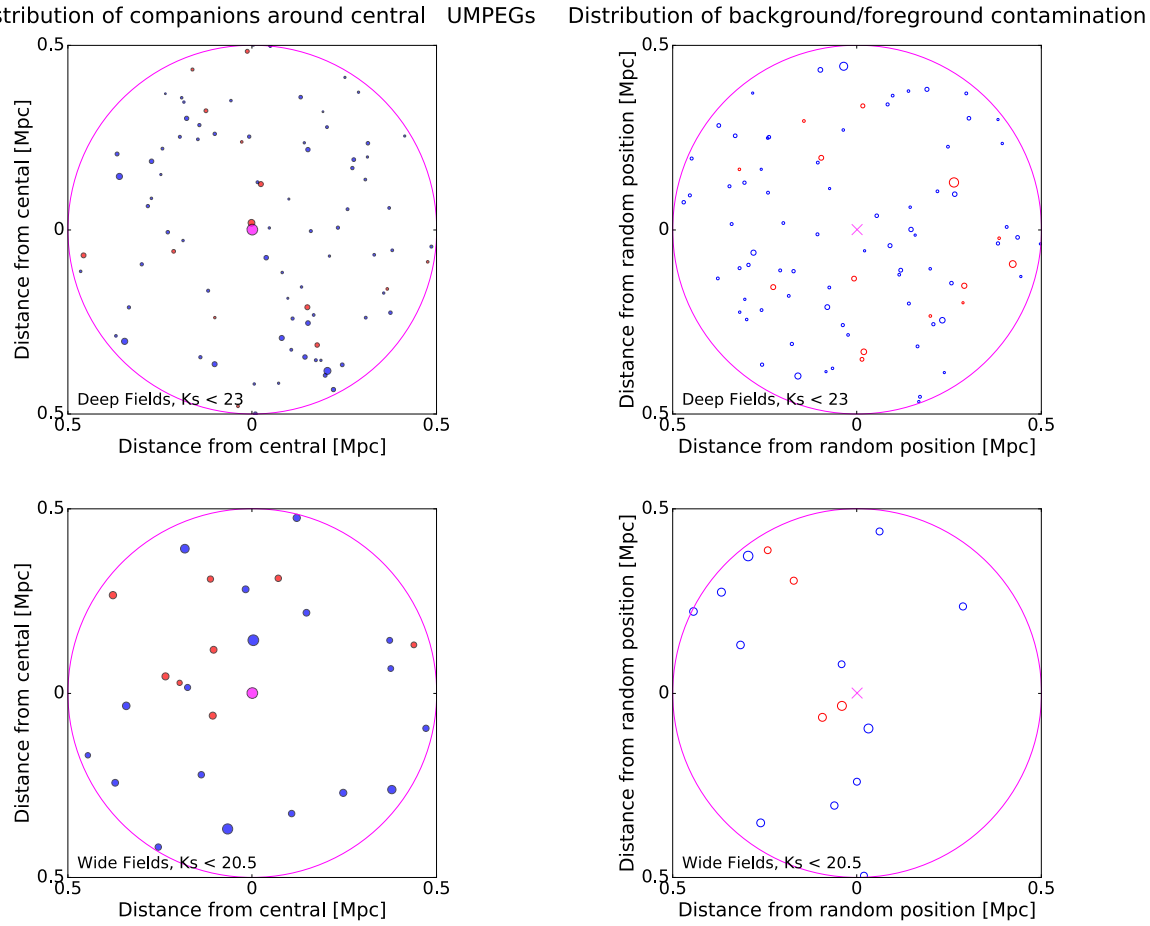

Figure 5.3: Sample of all combined neighborhoods: Central magenta points represent the position of the UMPEG in each group and the magenta outer circle represents a radius of search of 0.5Mpc. Also shown as blue and red points are a superposition of all the relative positions for all neighbours surrounding their 6 central UMPEGs in the Deep (top left plot) and 55 in the Wide (bottom left plot) fields. The size of the symbol for each companion represents how their mass scales with that of their central. Shown in black is the completeness in K_s magnitudes for each field. Shown on the right hand side are similar results when using random positions in our fields and recovering surrounding gzK_s in the same radius of search and for the same number of random positions as centrals.

this effect, we have corrected our companion counts using Equation 5.1:

$$\sum_{corrected} = \sum_{original} \times \frac{\int n_{umpeg}(z)\, dz}{\int n_{umpeg}(z) \times n_{companion}(z)\, dz}, \tag{5.1}$$

where $n(z)$ is the redshift probability distribution (as shown in Section 4.1) of either the central UMPEG or its companions (even though we assume the satellite to be a companion, their probability density distribution is different given their different magnitudes). Using this formula, we calculate the probability of finding the central UMPEG combined with the probability of finding the companion galaxies based on the redshift distribution that most likely represents the population.

In Figure 5.4, we show the surface density of companion galaxies (corrected for foreground/background interlopers) as a function of their relative luminosities compared to their central UMPEG. The Deep Fields are shown as filled circles and Wide Fields as open diamonds. An interesting feature in Figure 5.4 is the apparent scarceness of companions that are half or more than half the luminosity of their central UMPEG. This would imply, that these ultra-massive objects are not likely to experience major mergers and are destined to evolve mainly through minor mergers (starting from 1:4) to the present, in accordance with several studies on the evolution of the most massive passive galaxies in the local universe (Hill et al. 2017, Vulcani et al. 2016, Tal et al. 2012, Naab et al. 2009). As seen in approximately eight of the colour images in Appendix A, some of our UMPEGs seem to have small companions (or tidal features) indicative of minor mergers.

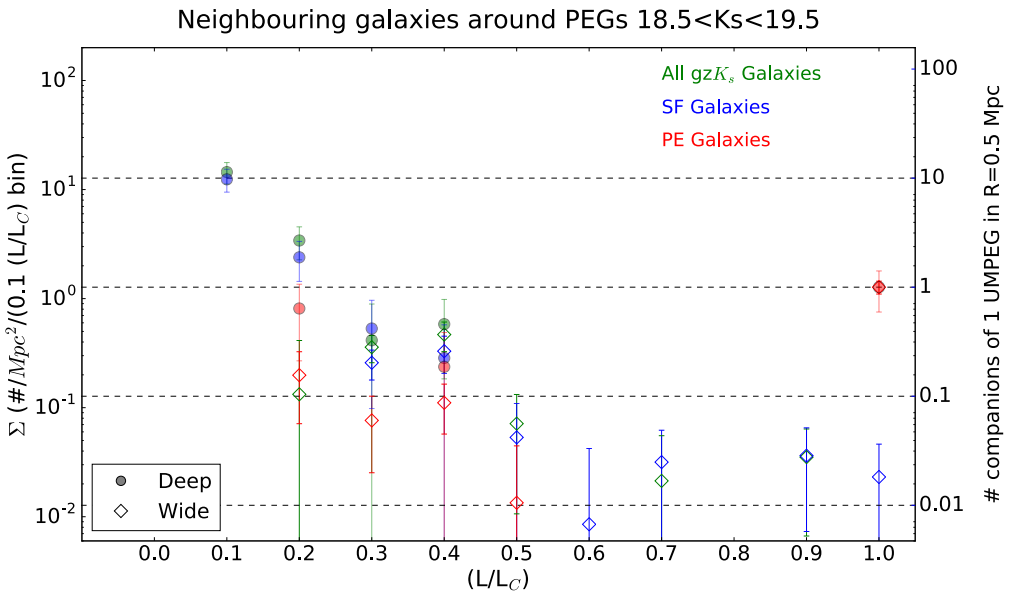

Figure 5.4: Shown in this plot is the surface area density of companion gzK$_s$ galaxies around UMPEGs in the Deep (filled circles) and Wide (empty diamonds) fields, as a function of their fractional luminosity compared with that of their central UMPEGs. This surface density plot has been corrected for foreground and background correction. Blue and red symbols represent star-forming and passive galaxies respectively. Green symbols represent all gzK$_s$ galaxies. Horizontal dashed lines represent the number of companions (0.01, 0.1, 1 or 10) an UMPEG would have in a radius of 0.5 Mpc. As can be seen, in both surveys, there is a scarceness of companions brighter than half the luminosity of the UMPEG, suggesting that companions of these UMPEGs are more likely to be at most half the luminosity of the central UMPEG. Most of the companions of these UMPEGs appear to be relatively small satellites.

5.3 Evolution of UMPEGs

Once we have identified the closest neighbours to our ultra-massive galaxies, and determined that most of these companions appear to be at most half as massive as their central UMPEG, we concern ourselves with trying to understand the evolution of these systems.

Since these UMPEGs are the most massive gzK_s galaxies in a given neighbourhood, it is not unreasonable to suggest that through dynamical relaxation, most of these companions will become satellites to this massive halo and eventually merge with it. Eventually an important follow up question is to wonder if, assuming all of these companions could merge with our central, how long this will take and how much the mass of our central UMPEG will increase.

In order to estimate how long it would take these companions to merge with their central UMPEG, we used two recipes: a revised dynamical friction timescale from Jiang et al. (2008) and a calibrated merger time based on the Millennium Simulation from Kitzbichler & White (2008).

For the first estimate, starting from the derived equation of dynamical friction from Lacey & Cole (1993), Jiang et al. compared these theoretical merger time -scales with timescales obtained from a theoretical N-body simulation[1]. They developed a revised merger time scale formula, shown in Equation 5.2, defined as the time starting the moment the satellite crosses the virial radius of the central galaxy and ending in a final coalescence of central and satellite galaxy (Jiang et al. 2008):

[1]GADGET-2 is an N-body cosmological simulation freely available at http://wwwmpa.mpa-garching.mpg.de/gadget/.

$$T_{merge} = \frac{0.94\varepsilon^{0.60} + 0.60}{0.86} \frac{M_{cent}}{M_{sat}} \frac{1}{ln\,(\Lambda)} \frac{r}{v}, \tag{5.2}$$

where

$$ln\,(\Lambda) = ln\left\{1 + \frac{M_{cent}}{M_{sat}}\right\}, \tag{5.3}$$

and ε measures how eccentric the orbit is (defined as the ratio of the angular momentum of a circular orbit to that of an orbit with the same energy, Lacey & Cole 1993). This means that a value of $\varepsilon = 1$ will represent a circular orbit. As expected, merger times will be systematically larger for more circular orbits. M_{cent} and M_{sat} are the masses of the central UMPEG and of its corresponding satellite at the beginning of the interaction, r is the radius of the orbit in kpc, and v is the circular velocity of the satellite at the start of the interaction.

For our sample, we can estimate values for the masses and distances but we will assume a value of $\varepsilon = 0.5$, which is independent on the masses of the interacting galaxies (Jiang et al. 2008) and a circular velocity $v \sim$860 km/s (A velocity that relates to a high likelihood of interaction for close pairs: Patton et al. 2000). Finally, the Coulomb logarithm ($log\,(\Lambda)$) correlates the efficiency of the collision with the masses of the central and satellite galaxies.

Kitzbichler & White (2008) proposed a fitting formula to determine the merger time -scales for close pairs based on results from an N-body simulation (Millennium simulation, Springel et al. 2005) and the identification of candidate merger pairs based on their projected separation, radial velocity difference and redshift difference. Equation 5.4 shows the calibrated formula to estimate the average merger timescales in close pairs with $r_p <$

$50h^{-1}kpc$ and $\triangle v < 3000km/s$.

$$T_{merge} = 3.2Gyr\frac{r_p}{50kpc}\left[\frac{M_*}{4\times10^{10}h^{-1}M_\odot}\right]^{-0.3}\left(1+\frac{z}{20}\right), \tag{5.4}$$

where M_* is the stellar mass of the companion at the observed redshift (Groenewald et al. 2017). Given that Kitzbichler et al. formula is calibrated for close pairs, equation 5.4 could represent an under-estimate in merger times for the companions of our UMPEGs, which reside at much larger radii (up to 500 kpc).

Both estimates for merger times are uncertain and make several assumptions. For instance, Jiang et al. concluded that even though their proposed Coulomb logarithm was a better estimate than the one originally proposed in Lacey et al. $\left(i.e.,\ log(\Lambda) = \frac{M_{cent}}{M_{sat}}\right)$ it still underestimates the merger timescale by a factor of two when the total mass of the satellite (at its initial crossing) is used. On the other hand, Kitzbichler et al. also observed a discrepancy (the timescales they find are larger by a factor of two) between their simulation results and most published determinations of merger rates.

Figure 5.5 shows the resulting radii for which (shown in three different colours) neighbouring satellites will merge with the central galaxy if the systems are bound. Since the merger timescales are dependent on the masses of the central UMPEG and the satellites, we have assumed $log\left(M_*/M_\odot\right) = 11.49$ as the mass of the central (since in our binned distribution of galaxies, the faintest bin, i.e., 19.5, equivalent to $log\left(M_*/M_\odot\right) = 11.49$, is the bin with the most number of UMPEGs). For the mass of the satellite a similar assumption was made down to the completeness of the sample and their corresponding mass at

that limit (i.e, $log\,(M_*/M_\odot) = 10.27$ for the Deep fields and $log\,(M_*/M_\odot) = 11.14$ for the Wide). Also shown in magenta text are the calculated merging times for any bound satellite galaxy within our 0.5 Mpc search radius. It is important to point out that, most of these galaxies are in fact foreground and background contaminants. Nevertheless, when calculating the possible growth of the central UMPEGs we correct for this effect by using the background/foreground corrected surface density numbers presented in section 5.2.

It is interesting to observe in Figure 5.5 how the merger timescales given by the two equations differ, especially when the mass of the satellite is significantly larger, as is the case for the Wide Fields. This could represent the importance of taking into account the changing mass of the satellite as it mergers with its central (For the Wide Fields, where the mass of the satellites are assumed to be 7.4 times larger than in the Deep Fields, the merger timescales between Jiang et al. and Kitzbichler et al. differ approximately by a factor of two). Hence, as concluded by Jiang et al. assuming the mass of the satellite as being that at the start of the interaction can underestimate merger timescales by a factor of two, this discrepancy being more evident at larger satellite masses.

To begin with, there is a probability that none of these companions (after subtracting foreground/background interlopers) are bound to the central and will never merge (e.g., satellite galaxies in hyperbolic orbits), in this case our central UMPEG will most likely remain the same mass. On the other hand, if given enough time, dynamical friction could eventually cause real companion satellite galaxies to merge. Some of these companions could also represent projection over-densities close to our R=0.5 Mpc in redshift, hence our merger calculations represent a likely over-estimate of real interactions, specially when we

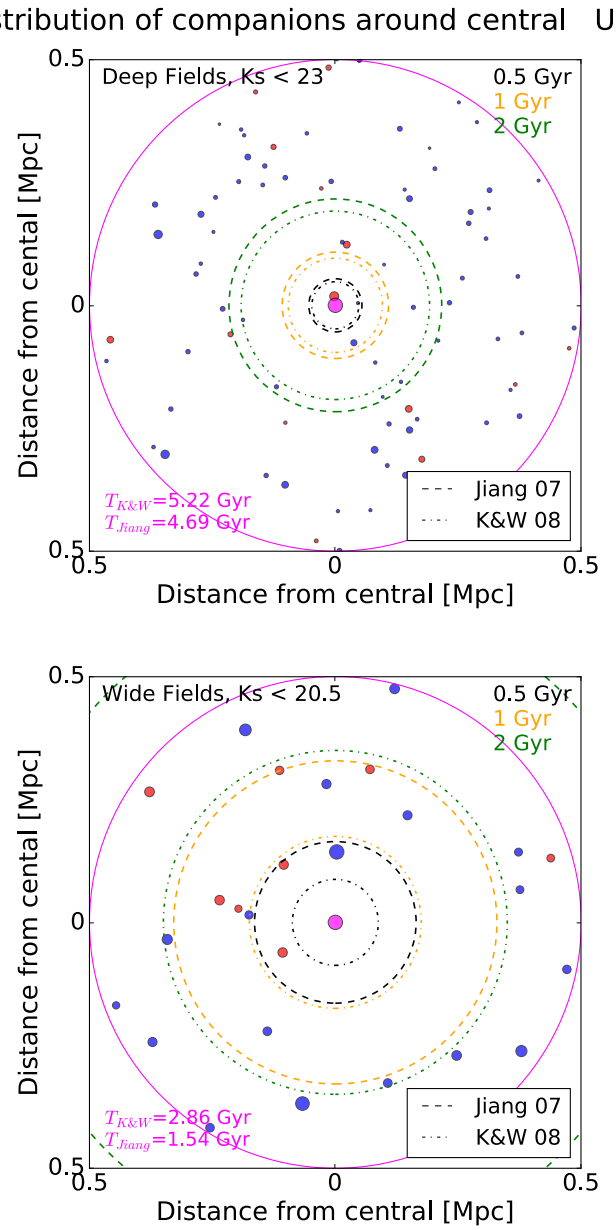

Figure 5.5: Distribution of neighbouring galaxies around the central UMPEGs as shown in Figure 5.3. Aside from showing in magenta the radius of search, we have added concentric circles that show, assuming central and satellites will merge, how long this will take according to the dynamical friction timescales calculated in Equations 5.2 and 5.4. For both fields, the mass of the central galaxy was assumed to be $log\,(M_*/M_\odot) = 11.49$ but the mass of the satellites are smaller for the Deep ($log\,(M_*/M_\odot) = 10.27$) than for the Wide ($log\,(M_*/M_\odot) = 11.14$), which explains the difference in sizes of convergence for the same timescales. Magenta numbers at the bottom of the figure show merger timescales for 0.5 Mpc. Most of these companion galaxies are in fact background interlopers, nevertheless, we correct for this effect when calculating the growth of the central UMPEGs.

consider the fact that masses for SFG from i-band rest-frame magnitudes are likely to be over-estimated by a factor of two and are also model dependent (when using a different extinction, e.g., E(B-V)=0, our SFG masses can also be overestimated by a factor of two). Finally, very few of these companions ($\sim$ 0.01 companions per UMPEG) will be massive SFGs, leading to a 'wet' merger, causing enhanced star-formation, hence increasing the stellar mass (given the low number of massive SF companions this contribution will be very low).

We can estimate, using Equations 5.2 and 5.4, a foreground/background corrected growth of these UMPEGs from $z \sim 1.6$ to $z \sim 1$ (trying to estimate the growth evolution below $z \sim 1$ involves making an assumption on the distribution of neighbouring galaxies significantly past our established 0.5 Mpc^2 radius of search).

Figure 5.6 shows our stellar mass function (SMF) for passive galaxies at $z \sim 1.6$ (red circles) compared to the stellar mass function of passive galaxies at redshift $z \sim 1$ from Moutard et al. (2016a) (yellow shaded area). Using an average between equations 5.2 and 5.4 we calculate, given the merging time between $z = 1.6$ and $z = 1$ ($\sim$ 1.78 Gyr), the growth of UMPEGs by adding the contribution from their companion satellites (and their individual masses). This final growth (for the combined SMF) is mainly driven by the growth of UMPEGs in the Wide fields (since 90% of our UMPEGs were found in the Wide fields). Based on these results, as an example, an UMPEG with an initial mass of $log\left(M_*/M_\odot\right) \sim 11.60$ will grow a factor of 1.25 times (i.e., $\left(M_{final}/M_{initial}\right) \sim 1.25$) between redshifts $z = 1.6$ and $z = 1$ (equivalent to a growth of $\sim$ 14% per Gyr). Using this result, we could follow the evolution of these $log\left(M_*/M_\odot\right) \sim 11.60$ UMPEGs (assuming the distri-

bution of satellite companions remains consistent to larger radii), down to $z \sim 0$, resulting in them having masses of $log\,(M_*/M_\odot) \sim 11.97$ in the local universe. This mass is consistent with NGC 4874 ($log\,(M_*/M_\odot) \sim 11.98$; Veale et al. 2017), one of the main central galaxies in the Coma cluster (Coma A); this result, combined with an estimated dark matter halo mass of $13.9 < log(M_{200}[M_\odot/h]) < 14.2$ (Cheema et al. in prep), makes UMPEGs likely progenitors of some of the present-day central galaxies in clusters.

This predicted evolution, due to mergers, of the bright end of the SMF is presented with black arrows in figure 5.6. For comparison, we also show as red triangles our SMF at $z \sim 1.6$ re-normalized 3.5 times to match the yellow $z \sim 1$ SMF, to represent the evolution of the SMF driven by newly quenched galaxies (shown as a red arrow).

Even though there is not a good constraint on the bright end of passive galaxies at $z \sim 1$, it seems that while mergers contribute a mass growth of $\sim$ 25%, neither pure quenching nor pure merging can explain the evolution of UMPEGs between $z \sim 1.6$ and $z \sim 1.0$. Consequently, it is likely that their evolution is a combination of both processes. Nevertheless, it is important to remember that these results are a simple extrapolation and do not include the dependency in the masses at lower redshifts of recently-quenched galaxies, nor the loss of some the merged material to the intracluster medium ($\leq$ 10%, Sinha & Holley-Bockelmann 2009).

As previously mentioned, our choice for velocity separation is such that close pairs (i.e., $r < 50\,kpc$) are more likely to exhibit signs of interactions (Patton et al. 2000). Since most of our companions lie at distances beyond the definition of a close pair, we added an additional estimate to the expected evolution of UMPEGs: Dashed vertical lines at the

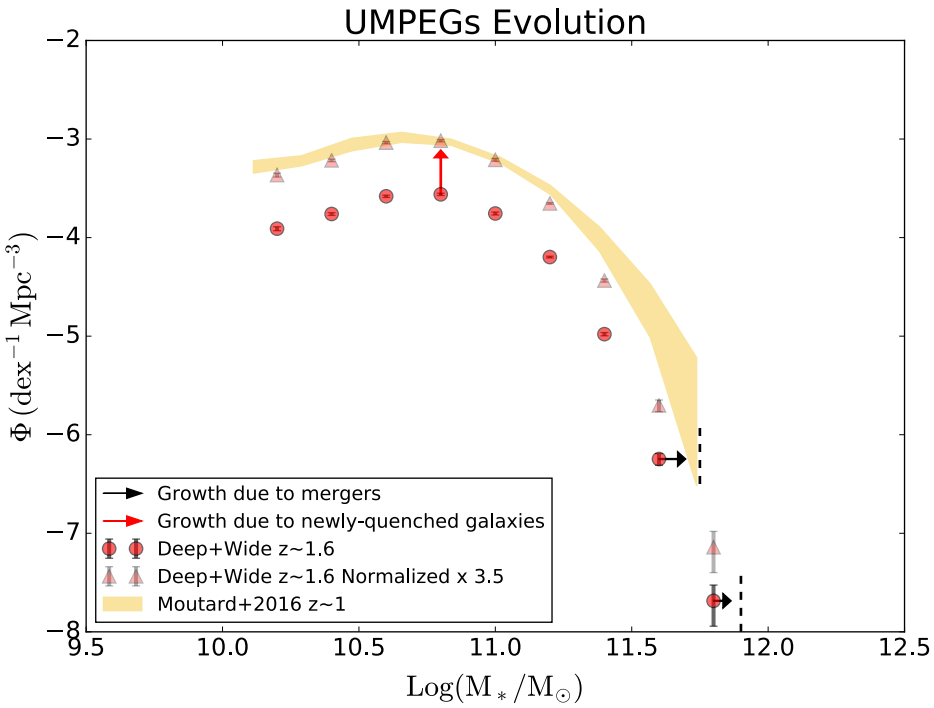

Figure 5.6: Stellar mass function of passive galaxies at $z \sim 1.6$ and the expected evolution of UMPEGs down to $z \sim 1$. Shown in red circles is our stellar mass function of passive galaxies as shown in Chapter 3. Red triangles show a re-normalized version of this stellar mass function ($\times$ 3.5) to match the $z \sim 1$ SMF of passive galaxies shown as a yellow shaded area (that encompasses their uncertainties) from Moutard et al. (2016a). Shown as black arrows is the possible growth of UMPEGs from $z = 1.6$ to $z = 1$ from mergers, calculated using an average between equations 5.2 and 5.4, and as a red arrow the growth of the SMF due to newly-quenched galaxies (i.e., the previously mentioned $\times$3.5 re-normalization). Finally, to estimate the dependency on the assumed velocity we show, as dashed lines, the final length of the arrow if we assume a velocity twice what is estimated to correspond to close pairs as stated by Patton et al. As can be seen, individually, neither mergers nor simple mass quenching is enough to explain the evolution of the bright end of the SMF, it is however likely that the evolution is driven by a combination of both processes.

end of the each arrow in Figure 5.6 show the expected length of each arrow if we were to consider a velocity that is twice that of our initial assumption. As can be seen, and as expected from the inverse proportionality between T_{merge} and v in equation 5.2, a larger velocity will result in faster interactions which can generate an extra growth of $\sim$0.05 dex in the bright end of the SMF.

Finally, since Kitzbichler et al. is a formula fine-tuned for close pairs, we reproduce figure 5.6 and separate the contributions of growth of the two given formulas (i.e., equations 5.2 and 5.4) in figure 5.7, using a green arrow to represent Jiang et al. and a blue arrow to represent Kitzbichler et al. As can be seen, the growth is driven mainly by the dynamical friction equation of Jiang et al. For comparison, an UMPEG with an initial mass of $log\left(M_*/M_\odot\right) \sim 11.60$ has a growth of $\sim$ 25% using an average of the two formulas, resulting in an UMPEG with mass $log\left(M_*/M_\odot\right) \sim 11.70$ at $z \sim 1$, while using only a growth predicted by Jiang et al. this growth changes to $\sim$ 32% (and a final mass $log\left(M_*/M_\odot\right) \sim 11.72$) and a growth of $\sim$ 19% when using only the predicted growth of Kitzbichler et al. (with a final mass of $log\left(M_*/M_\odot\right) \sim 11.67$). Hence, if we only consider a growth by Jiang et al. (assuming Kitzbichler et al. formulation is not correct for our satellites, being at larger separations) we obtain an upper limit growth of $\sim$ 32%.

5.4 Summary

In this Chapter, we have studied the environments surrounding Ultra Massive Passive Galaxies (or UMPEGs for short), defined to be passively evolving gzK$_s$ selected galaxies

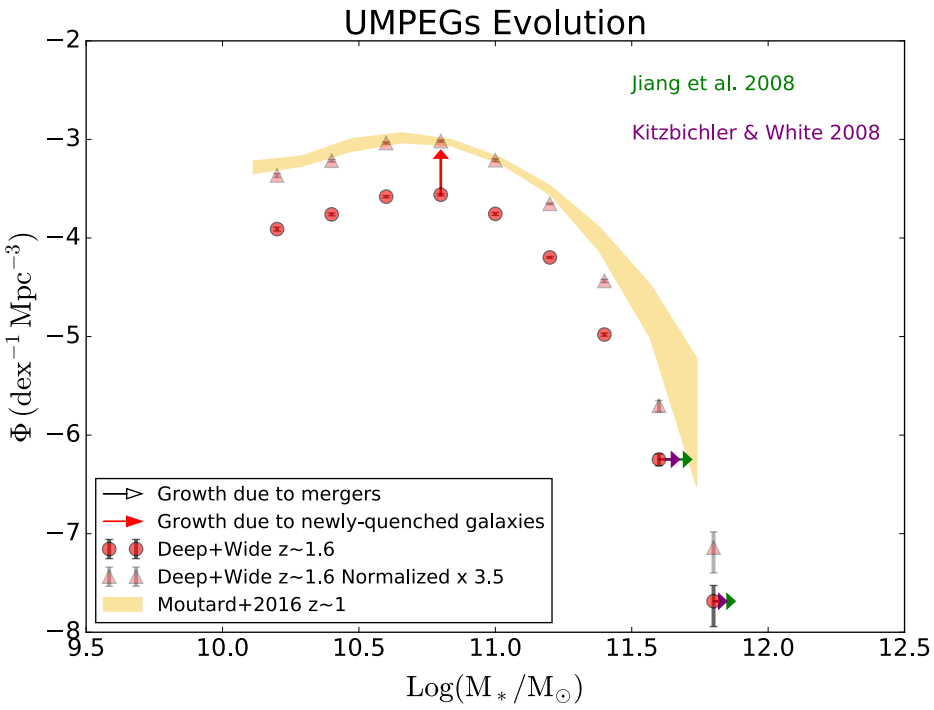

Figure 5.7: As in figure 5.6, we show the stellar mass function of passive galaxies at $z \sim 1.6$ (red points) and $z \sim 1$ (yellow shaded area, Moutard et al. 2016a). Instead of showing a combined growth for Jiang et al. (2008) and Kitzbichler & White (2008) as a black arrow, we separate both contributions using a green (Jiang et al.) and blue arrow (Kitzbichler et al.). As can be seen, the growth is driven by the Jiang et al. dynamical friction formula, for which, when used independently, we expect a growth of $\sim 32\%$ of our UMPEGs between $z = 1.6$ and $z = 1$.

at $z \sim 1.6$ with masses larger than $log\,(M_*/M_\odot) \sim 11.49$. We found that most of these UMPEGs do not have massive companions (with masses that are $\sim 50\%$ or more the mass of the central UMPEG), whereas there is a relative low abundance of low mass companions (with masses $\sim 30\%$ or less the mass of the UMPEG).

Calculating merger times we estimated the evolution of the bright end of the SMF from $z = 1.6$ to $z = 1$ and compared these results with Moutard et al. (2016a) SMF at $z \sim 1$. Based on this comparison, we estimate that their evolution is driven by a combination of both mergers (which can account to a growth of up to $\sim 25\%$ to 32%) and mass quenching.

Finally, by separating the growth by mass of the satellites, we estimate that 88% of the contribution to this growth comes from smaller companions (with masses corresponding to 40% or less the mass of the central UMPEG). This result seems to be in agreement with growth estimates from the progenitors of present-day massive galaxies ($log\,(M_*/M_\odot) \sim 11.5 - 11.8$ from Hill et al. 2017; Marchesini et al. 2014).

Chapter 6

Groups of massive passive galaxies

Is the environment in which a galaxy resides important to understand its evolution? Or is a galaxy more likely to be dominated by internal effects? Ongoing research shows that, in clusters of galaxies, the importance of different effects is most likely redshift-dependent, driven mainly by the time needed to reach relaxation (Peng et al. 2010; Vulcani et al. 2016; Nantais et al. 2016).

In terms of environmental effects, several external mechanisms can shape the general characteristics of galaxies (e.g., mergers, galaxy harassment, starvation). Major and minor mergers, not only modify the mass of the galaxy but also affect its general structure and star-formation activity within its member galaxies. Interestingly, at intermediate redshifts ($1.3<z<2$) is when we should start discerning the effects of environmental quenching (Nantais et al. 2016, Peng et al. 2010).

Even though there is evidence of significant star-formation in central cluster regions at $z \geq 1.5$ (Daddi et al. 2017, Chiang et al. 2017, Webb et al. 2015), there is also evidence of a

characteristic population of passively-evolving galaxies (Lee-Brown et al. 2017: $z \sim 1.62$, Nantais et al. 2016: $1.37 < z < 1.63$, Strazzullo et al. 2015: $z \sim 2$, Newman et al. 2014: $z \sim 1.8$). Hence leading to believe that these evolved passive galaxies can be used to trace proto-clusters (Strazzullo et al. 2015).

In this chapter we identify dense environments based on over-densities of ultra-massive passive galaxies (i.e., passive galaxies with $K_s < 20.5$, which represents a mass of $log\left(M_*/M_\odot\right) \sim 11.14$, see section 4.2) and identify 37 evolved proto-cluster candidates at $z \sim 1.6$ in the Deep and Wide fields. Once identified, we study the stellar mass function of passive galaxies and the fractional numbers of passive and star-forming galaxies residing in these proto-cluster candidates

6.1 Finding groups of massive passive galaxies

We used a 2D density field to identify rich environments. This 2D density field was constructed by assigning a Gaussian distribution at the position of each one of our passive $K_s < 20.5$ galaxies. The peak of each Gaussian is normalized to one and for pixels where multiple Gaussians overlap, their final value will be the total additive contribution from all overlapping Gaussians.

To check for model dependence, we repeated this procedure using several options for a full width at half maximum (FWHM) : 1, 1.5, 2.3 and 3 physical Mpc and levels (a level is defined as the pixel value above which we consider a connected net of pixels to be a dense environment). We chose these FWHM values based on the virial radius of previously

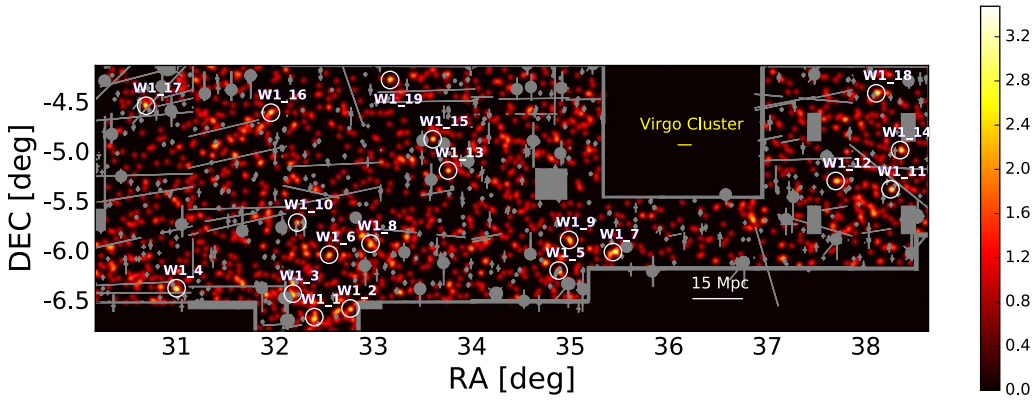

Figure 6.1: Gaussian density map for W1. The density map was constructed only taking into account passive gzK$_s$ galaxies with $K_s < 20.5$. In this map, we sample a FWHM of 1.5 Mpc. Regions that have been identified as dense environments are enclosed with white circles. Also shown in gray are flagged pixels for this field. For comparison, we show the size of the Virgo Cluster in yellow and 15 Mpc in white. Color bar represents the additive contribution of overlapping gaussians at each pixel.

identified clusters at similar redshifts (Newman et al. 2014; Andreon et al. 2009; Hilton et al. 2010).

After constructing a Gaussian density map for each field, we identified as dense environments a net of connected pixels (pixel scale is 0.186 arcseconds, or at $z \sim 1.6$, ~ 1.6 physical kpc) with density values of 2.7 or more. Figures 6.1, 6.2 and 6.3 show Gaussian density maps for W1, W4 and Deep fields, with a FWHM of 1.5 physical Mpc.

6.2 Groups

After several FWHM and levels have been tested to model and recover dense environments of massive passive galaxies, we selected our groups based on three conditions:

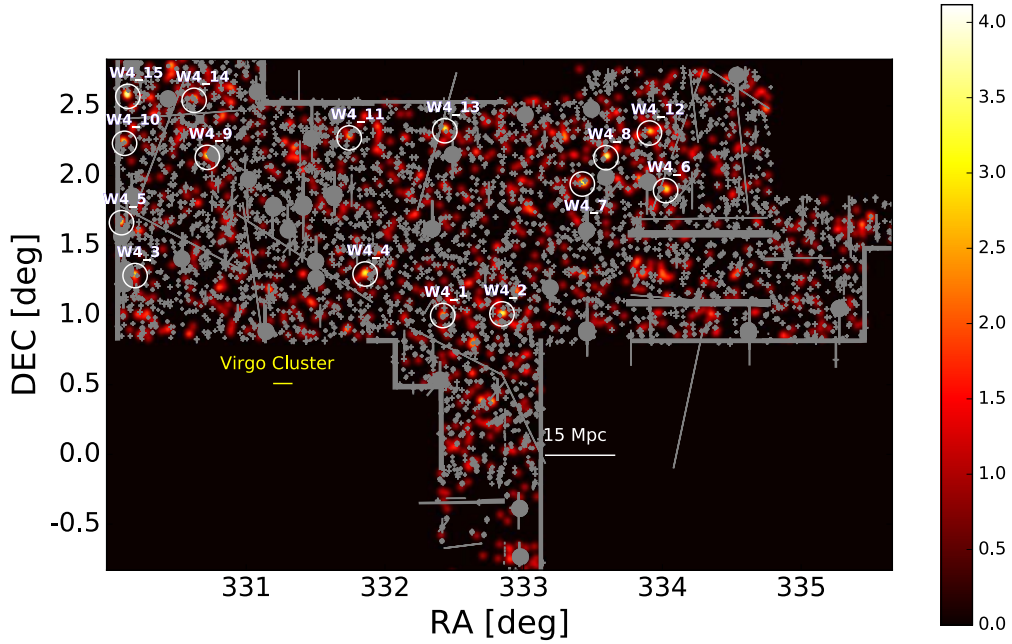

Figure 6.2: Gaussian density map for W4. Similar to W1, the density map was constructed only taking into account passive gzK$_s$ galaxies with $K_s < 20.5$. In this map, we sample a FWHM of 1.5 Mpc. Regions that have been identified as dense environments are enclosed with white circles. Also shown in gray are flagged pixels for this field.

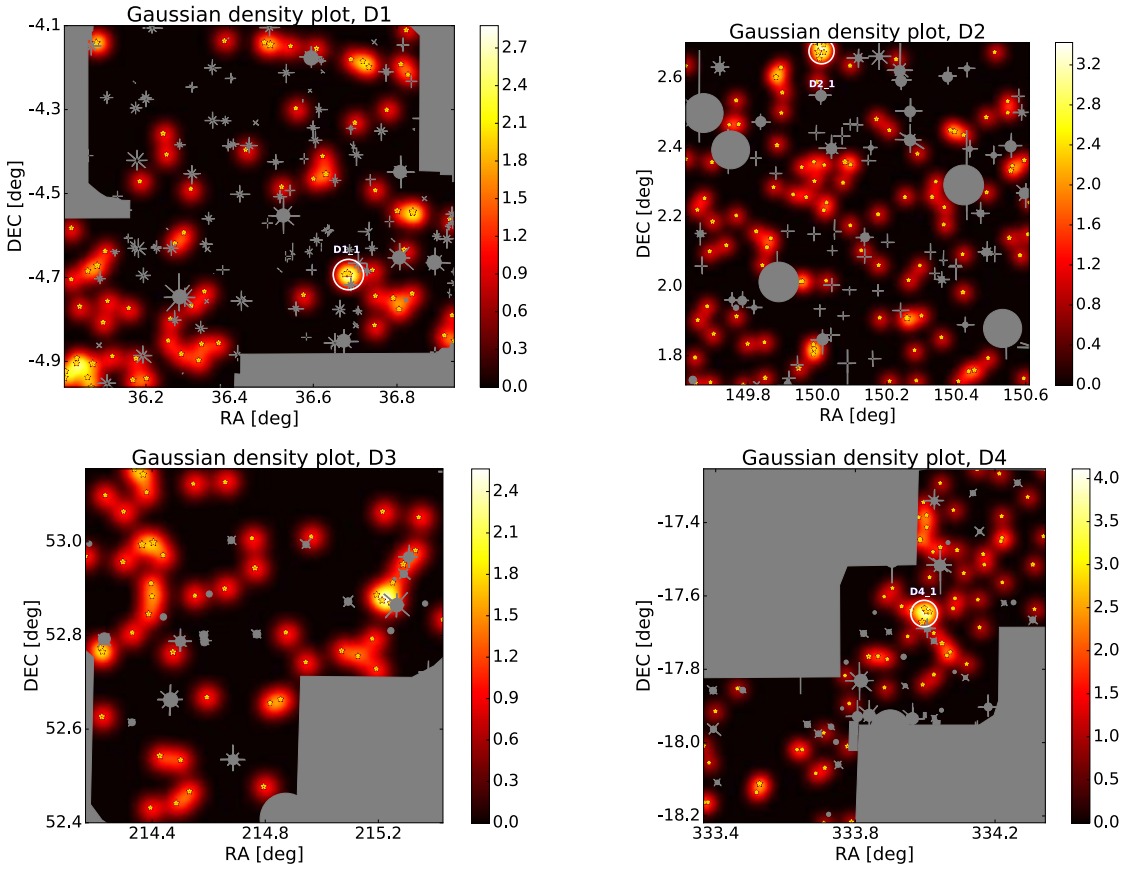

Figure 6.3: Gaussian density map for the Deep Fields. The density map was constructed only taking into account passive gzK$_s$ galaxies with $K_s < 20.5$ (shown as yellow stars). In this map, we sample a FWHM of 1.5 Mpc. Regions that have been identified as dense environments are enclosed with white circles. Also shown in gray are flagged pixels for each field.

1. First, we identified an over-density of massive passive galaxies as a region in the Gaussian density map of connected pixels above a certain level. These are also referred to as 'hot spots' (seen as bright yellow in Figures 6.3, 6.1 and 6.2).

2. Next, we defined a equi-level contour around hot spots with a value of 70% of the selected level (e.g., if a hot spot is identified as connected pixels above a value of 2.7, the 70% equi-level contour will be defined by a connected path of pixels with a value of 1.89 around this hot spot. These equi-level paths are shown as white contours in Figures 6.4, 6.5, 6.6,6.7,6.8). This level selected to ensure a minimum recovery of galaxies in the group, based on decreasing surface density.

3. Finally, if there are at least three bright ($K_s < 20.5$) passive galaxies inside the 70% equi-level contour, that group is identified as a potential proto-cluster (Given their similar magnitudes, $K_s \sim 20.5$ we assume them to have the same peak redshift distribution, however, this might not always be the case).

Figure 6.4 shows three groups identified in the Deep fields. These dense environments have been selected using a FWHM of 1.5 Mpc, a level of 2.7 and a completeness equi-level of 70% (This means that a hot spot is identified, as explained before, as connected pixels above 2.7 and the full group is recovered with an equi-level path of 1.89 around the hot-spot). Shown as a white contour is the final recovered group, i.e., the 70% equi-level path. Star symbols represent the position of bright galaxies ($K_s < 20.5$), circles are used to represent fainter passive galaxies (down to the completeness limit of each field). Finally, yellow symbols are used for passive galaxies and blue for star-forming ones.

Figures 6.5, 6.6, 6.7 and 6.8 show groups identified within the Wide fields, using the same parameters as those in the Deep Fields. Since the completeness for passive galaxies in the Wide fields is $K_s < 20.5$ only star symbols are used to represent their location within the groups. Groups D1-1 and D4-1 have been previously reported as high-redshift proto-clusters (Newman et al. 2014; Hilton et al. 2009) as shown in Section 6.3.2.

In order to understand the general characteristics of each group, we have taken the 70% equi-level contour (i.e., pixels that are equal or above than 70% of 2.7) and modeled it as an ellipse. Shown in Figure 6.9 is a sample of this fit to two groups, on the right one of our worst case scenarios (when the group's contour is distorted) and on the left an average case. From this ellipse we estimated the minor and major axis of our group and assumed that, the third axis length is the average of the minor and major axis. Calculating an estimated volume from these three axis, we can recover a number density of galaxies for each group.

A summary of most of the characteristics for these groups is shown in Table 6.1. Number densities include the number of SF and PEGs in each group per Mpc^3, however, due to our lack of a suitable estimate for the masses of star-forming galaxies, the total mass of the proto-cluster is only estimated using passive galaxies. We note, however, that as shown in Figures 6.16 and 6.17, the groups contain few bright star-forming galaxies ($K_s < 20.5$), hence the masses in Table 6.1 are not likely to be severely under-estimated. To correct for foreground/background contamination, we calculated the same characteristics (e.g., number density) for the corresponding field, then subtracted them from the group characteristics.

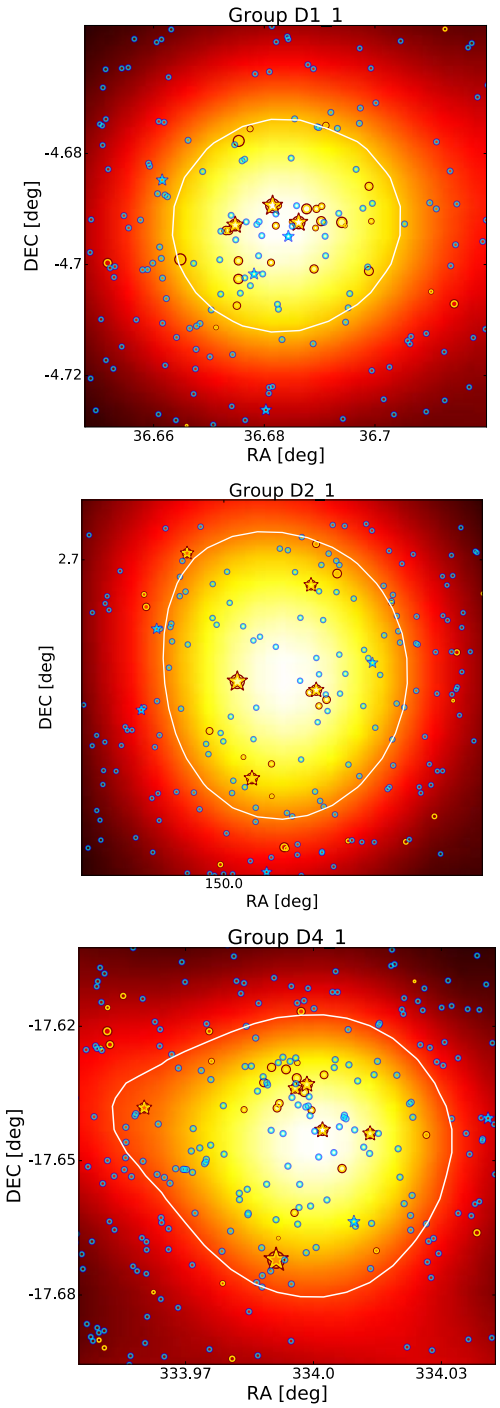

Figure 6.4: Groups recovered in the Deep fields. Groups were identified as those having a contour value of 2.7 or higher and least having three objects with K_s <20.5. To recover the full group, another contour level was defined around the initial 2.7 level with a value of 1.89 (or 70% of 2.7). This final 1.89 contour level is shown in white. Orange points define the positions of our passive gzK_s galaxies, while blue points represent the position of star-forming galaxies within these groups. Circles in any colour, represent galaxies down to the completeness limits of the field, while stars represent galaxies (either SF or PE) with $K_s < 20.5$. On average, these groups have an area of ~ 2 physical Mpc^2.

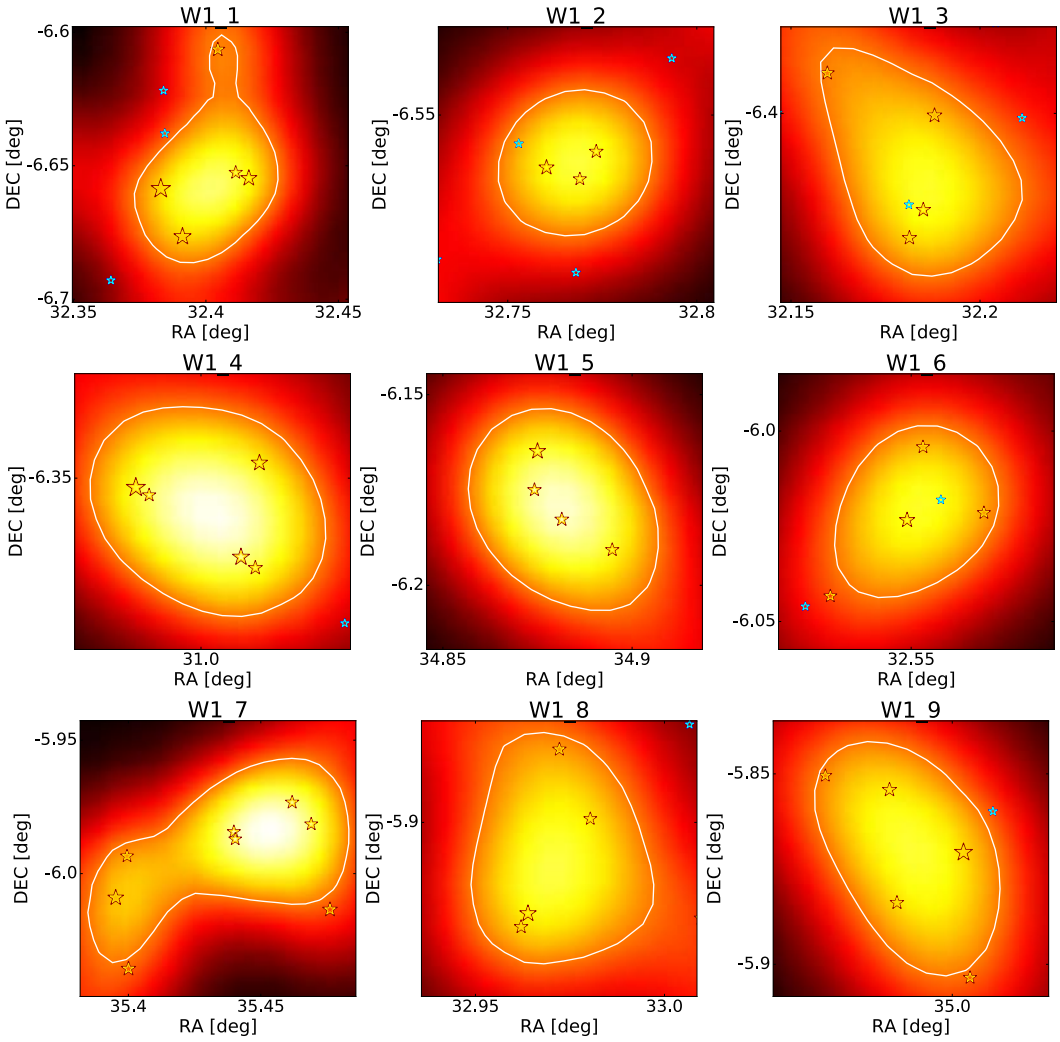

Figure 6.5: Groups recovered in the Wide 1 field. Groups were identified as those having a contour value of 2.7 or higher and least having three objects with K_s <20.5. To recover the full group, another contour level was defined around the initial 2.7 level with a value of 1.89 (or 70% of 2.7). This final 1.89 contour level is shown in white. Orange stars define the positions of our passive gzK_s galaxies, while blue stars represent the position of star-forming galaxies within these groups.

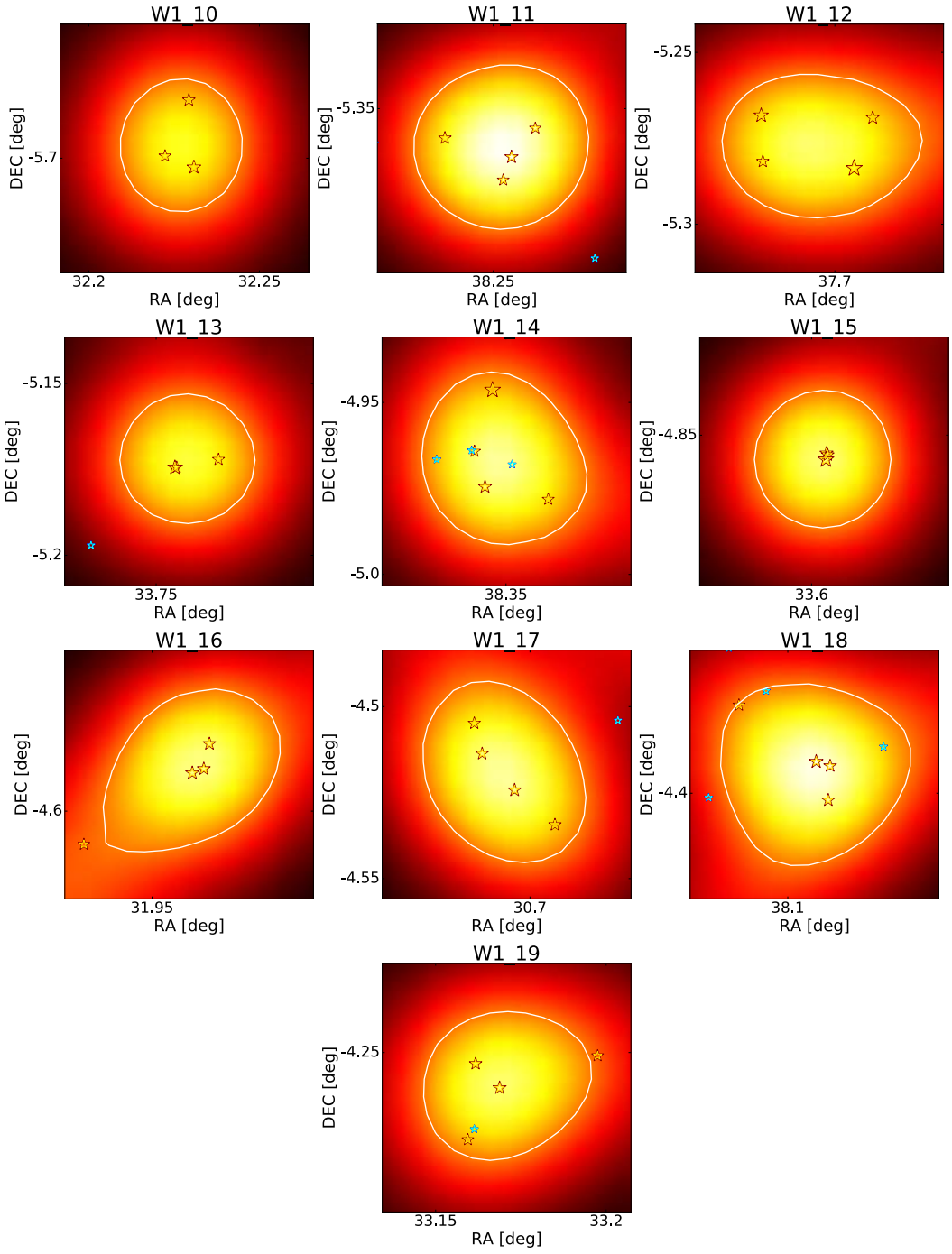

Figure 6.6: Cont: Groups recovered in the Wide 1 field. Groups were identified as those having a contour value of 2.7 or higher and least having three objects with K_s <20.5. To recover the full group, another contour level was defined around the initial 2.7 level with a value of 1.89 (or 70% of 2.7). This final 1.89 contour level is shown in white. Orange stars define the positions of our passive gzK_s galaxies, while blue stars represent the position of star-forming galaxies within these groups.

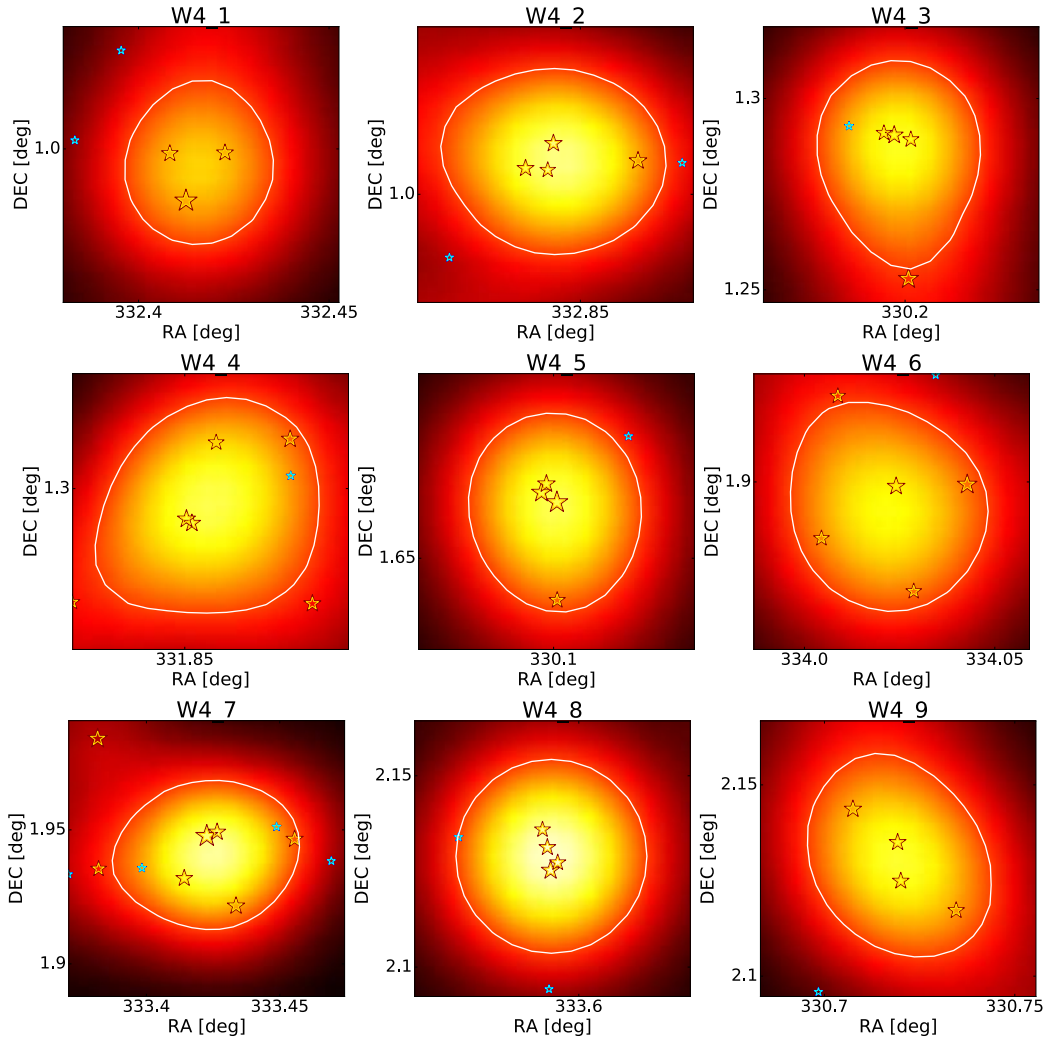

Figure 6.7: Groups recovered in the Wide 4 field. Groups were identified as those having a contour value of 2.7 or higher and least having three objects with K_s <20.5. To recover the full group, another contour level was defined around the initial 2.7 level with a value of 1.89 (or 70% of 2.7). This final 1.89 contour level is shown in white. Orange stars define the positions of our passive gzK_s galaxies, while blue stars represent the position of star-forming galaxies within these groups.

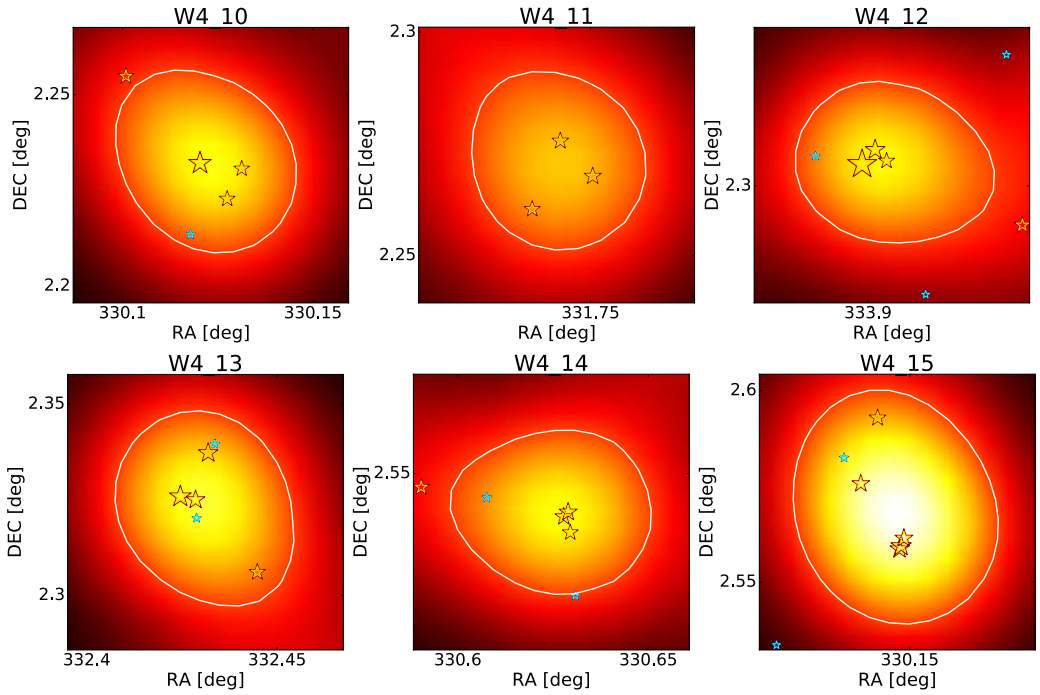

Figure 6.8: Cont: Groups recovered in the Wide 4 field. Groups were identified as those having a contour value of 2.7 or higher and least having three objects with K_s <20.5. To recover the full group, another contour level was defined around the initial 2.7 level with a value of 1.89 (or 70% of 2.7). This final 1.89 contour level is shown in white. Orange stars define the positions of our passive gzK_s galaxies, while blue stars represent the position of star-forming galaxies within these groups.

Field and group number	Num. of PE-gzK_s	Num of SF-gzK_s	RA [deg]	DEC [deg]	Number Density [#PE-gzK_s/Mpc^3]	Mass PE-gzK_s[log ($M_*/M_\odot$)]
D1_1	3(23)[1]	2(8)	36.682	-4.689	3.05(24.63)	11.71(12.28)
D2_1	4(8)	0(12)	150.002	2.674	1.47(3.29)	11.93(12.10)
D4_1	5(14)	0(18)	333.992	-17.672	1.12(3.12)	12.08(12.33)
W1_1	5	0	32.385	-6.661	1.48	12.03
W1_2	3	1	32.762	-6.566	3.08	11.68
W1_3	4	1	32.190	-6.403	1.75	11.82
W1_4	5	0	30.984	-6.354	1.60	12.03
W1_5	4	0	34.876	-6.167	1.93	11.82
W1_6	3	1	32.551	-6.025	2.29	11.67
W1_7	6	0	35.397	-6.011	0.86	11.93
W1_8	4	0	32.965	-5.926	1.61	11.81
W1_9	4	0	35.006	-5.873	1.74	11.85
W1_10	3	0	32.234	-5.705	3.75	11.69
W1_11	4	0	38.258	-5.366	2.10	11.78
W1_12	4	0	37.707	-5.286	2.10	11.90
W1_13	3	0	33.757	-5.177	3.36	11.70
W1_14	4	2	38.348	-4.949	2.20	11.85
W1_15	3	0	33.606	-4.859	3.01	11.78
W1_16	3	0	31.962	-4.591	1.62	11.71
W1_17	4	0	30.697	-4.526	2.08	11.80
W1_18	4	1	38.111	-4.393	1.60	11.82
W1_19	3	1	33.173	-4.262	1.95	11.67
W4_1	3	0	332.415	0.980	2.82	11.77
W4_2	4	0	332.867	1.003	1.64	11.80
W4_3	3	1	330.200	1.285	1.71	11.65
W4_4	4	0	331.853	1.287	1.22	11.80
W4_5	4	0	330.104	1.661	2.19	11.91
W4_6	4	0	334.045	1.897	1.64	11.82
W4_7	5	1	334.425	1.945	1.30	11.96
W4_8	4	1	333.595	2.123	1.95	11.80
W4_9	4	0	330.709	2.142	1.99	11.80
W4_10	3	1	330.122	2.231	1.75	11.74
W4_11	3	0	331.753	2.267	3.01	11.66
W4_12	3	1	331.901	2.305	1.82	11.93
W4_13	4	2	332.427	2.325	2.15	11.92
W4_14	3	1	330.631	2.540	1.74	11.68
W4_15	5	0	330.149	2.559	1.68	11.98

Table 6.1: Summary table of all the groups found in the Deep and Wide fields and their respective characteristics. Characteristics in table: Field in which the group was found and assigned group number, number of passive and star-forming gzK_s in group, right ascension and declination of the brightest member in group, total mass of passive gzK_s in group, number of passive gzK_s per physical Mpc^3 and total mass of passive gzK_s per physical Mpc^3. Characteristics in this table for the Deep fields report both down to the completeness of the field (in parenthesis) and down to $K_s < 20.5$ ($log\,(M_*/M_\odot) \sim 11.14$) for direct comparison with the Wide fields. All of these numbers are background/foreground corrected.

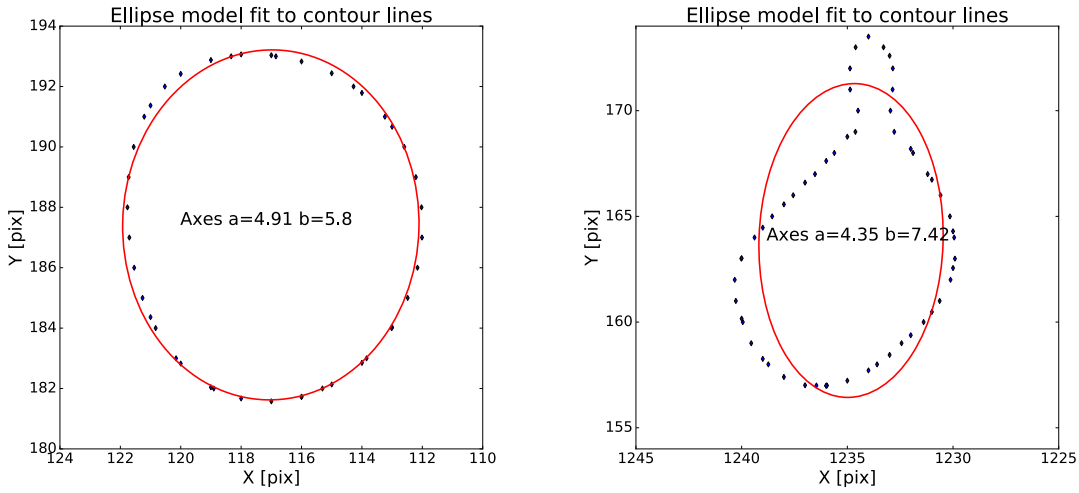

Figure 6.9: Sample of two ellipse fits using the 70% contour lines. Shown are two sample cases, on the left the fit for the group found in Deep field 2, an average shape to most of our groups, and on the right the fit for a group found in W1, this is one of the groups with most skewed profiles. As can be seen, even in a highly asymmetrical group, an ellipse fit will recover an approximate value to the axes that define the group.

6.3 Are these groups real?

6.3.1 Random Projections

To assess the probability that these dense environments could be chance associations, we randomized 100 times the positions of our catalog of passive galaxies in W1 (taking into account bad pixels, just as it was done for our real catalog) and identified dense groups of massive passive galaxies by chance associations using the same technique discussed in Section 6.2. We found that up to 34% of our groups could be formed by simply having an over-density of random galaxies (if we consider only groups with four or more galaxies, the probability changes to 24%) . However, this estimate does not take into account small scale clustering: i.e., the fact that we might have a pair (or triplet, etc.) of galaxies that are

gravitationally bound and that one or more galaxies could be a random projection in our redshift distribution hence, appearing on the whole as a dense environment.

To estimate an upper-limit scenario that includes small scale clustering, we used our largest field, W1, to perform a KD-Tree search around each galaxy, using as a radius of search the average radius of the previously identified groups, and assumed that all galaxies inside the defined radius of search are gravitationally bound. Hence we refer to this radius as linking length. After we identified galaxies at distances less or equal than this linking length, we performed a friends-of-friends link (FoF), so that if a galaxy or a small-scale structure (i.e., pair, triplet, etc) lies inside the linking length of search of another small-scale structure, this extra galaxy/structure is appended to the original one, hence forming small scale clustering groups of 3 or more objects.

Using this catalog of linked small scale structures and single galaxies (galaxies with no companion galaxies within the linking length), we randomize their positions 100 times, maintaining linked small-scale structures together, and find that we can form as many groups as we find in our data.

This result is highly dependent, as expected, on the chosen linking length. If instead of using the average radius of our identified groups we use ten times the expected distance between close pairs (i.e., 300 kpc, Bluck et al. 2009, Patton et al. 2000) and use the same FoF linking process and randomization, we can form half the number of groups ($\sim 55\%$). This result should be taken as an upper limit, since we do not have an estimate of how many of these small scale associations are real and which are in fact random associations.

Even though groups were selected in the deep fields as an association of over-dense

passive galaxies at $K_s < 20.5$, once we include the total number of members, down to the completeness of the field, we can observe in Figures 6.4 that these associations also correlate with a high number density of less massive passive galaxies. Moreover, two of the groups in the Deep fields have been previously identified as high-redshift proto-clusters by Newman et al. (2014) and Stanford et al. (2006); Hilton et al. (2007) (see Section 6.3.2 for their spectroscopic results).

6.3.2 Comparison with previously identified proto-clusters

A different approach to verify our selection of over-dense regions is to cross-correlate these groups with the literature to see if they have been previously identified. For the Deep fields, we identified our group in D1 as being the same group presented in Newman et al. (2014) where, using Hubble Space Telescope's (HST) Wide Field Camera 3, they present the spectroscopic confirmation of a rich galaxy cluster designated JKCS 041, at redshift 1.8 with a total of 22 members (of which 19 are spectroscopically confirmed), 18 of those quiescent (15 spectroscopically confirmed). Their HST pointing covers a radius of 60 arc seconds or 0.51 physical mega parsecs at z$\sim$1.8. This pointing matches the virial radius of 0.52 Mpc found based on their best fit spectral model temperature for the X-ray emission of the cluster (Andreon et al. 2009). Cluster members are distributed non-uniformly within the radius of 0.51 Mpc. Similar to other high redshift clusters, JKCS 041 does not have a single dominant galaxy located at its center which reflects the possibility that dynamical relaxation has not yet been achieved.

Newman et al. find that the mean ages of passive galaxies in the group do not dif-

fer from similar redshift passive galaxies in the field, although there is a higher fraction of passive galaxies in the cluster than in the field at a given stellar mass. Therefore, even though high-density environments are responsible for quenching a higher fraction of massive galaxies, the mode of quenching does not affect when star formation is quenched.

Even though D1_1 is identified as JKCS 041, our sample is not directly comparable to that of Newman et al. due to different completeness limits: we found 13 common passive galaxies between the two surveys ($\sim$ 56% of our PE sample, after taking into account background and foreground correction), and one Newman star-forming galaxy was also identified as one of our passive gzK$_s$, as can be seen in Figure 6.10. This source, identified as 387 in their work, lacks any detectable emission lines, but was classified as SF based on its position on the (U-V) vs. (V-J) colour-colour diagram.

When comparing the masses of these common 13 passive galaxies, Newman et al. found a total mass of $log(M_*/M_\odot) = 12.08$, whereas for the same 13 PE-gzK$_s$ in D1_1 we find a total stellar mass of $log(M_*/M_\odot) = 12.09$. Newman et al. uses a custom code to find best-fit stellar parameters developed to jointly make use of the spectroscopic and photometric data. Given that the total stellar mass of D1_1 is in reasonable agreement with that of JKCS 041, we can corroborate our K$_s$ to mass conversion.

On the other hand, the group in D4 has been identified (using a position match) as possibly being the galaxy cluster J221538.9-1738 (J2215 from now on). J2215 was initially reported in Stanford et al. (2006), found in archival XMM data as an extended X-ray source. Follow-up observations of this galaxy cluster (Hilton et al. 2007, 2009, 2010) have identified it as being at redshift z = 1.46, with a radius of 2 Mpc. Initially, Hilton et al. (2009)

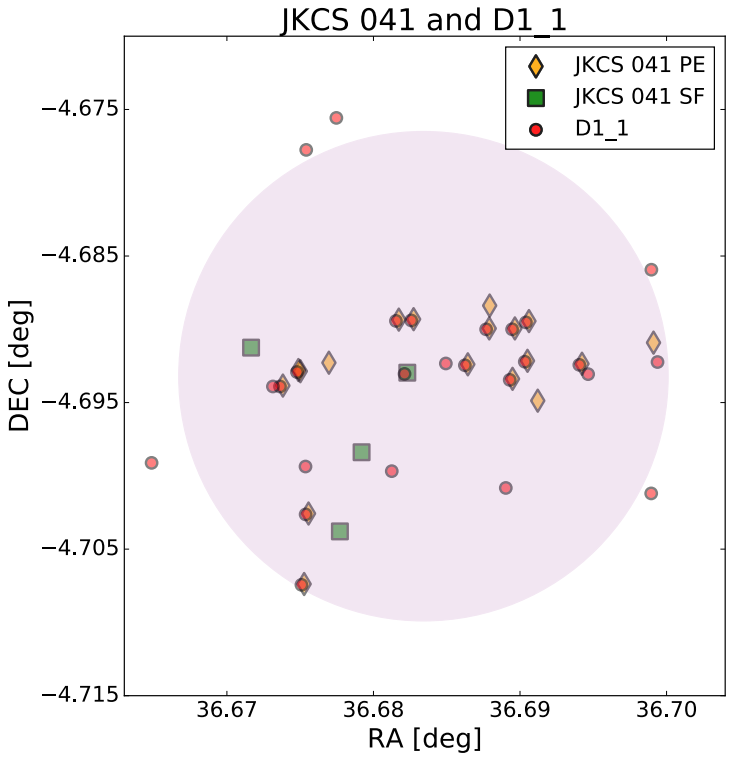

Figure 6.10: Comparison of JKCS 041 with D1_1. As can be seen thirteen of our members are also found in Newman et al. and identified as passive galaxies. One of our passive gzK$_s$ galaxies in the group is identified as a star-forming in Newman et al. based on their colours in the UVJ colour-colour diagram. Also shown is a gray circle with a radius of 0.51 Mpc at z$\sim$1.8, which represents the virial radius of the group.

presented a morphological study of 63 members (based on photometric redshifts) of J2215, afterwards, Hilton et al. (2010) explored star-formation and AGN activity, for 44 sources belonging to J2215 based on spectroscopic redshifts and recessional velocities. Even though they were unable to obtain good spectroscopic redshifts for all of the 63 originally presented sources, they identified 14 previously not detected members.

In Figure 6.11 we compared galaxies identified as belonging to the group D4_1 as red and blue symbols (for passive, and star-forming) and galaxies identified by Hilton et al. as belonging to J2215 in green diamonds, yellow squares and purple triangles. Green diamonds represent those galaxies for which Hilton et al. detected [OII] emission whereas yellow squares represent those where no emission was detected, and purple triangles represent photometrically identified galaxies for which there is no available spectroscopic follow up.

After performing a cross-match between both catalogs (i.e., Hilton et al. initial photometrically selected sample and extended spectroscopical follow-up) and our passive and star-forming galaxies identified in D4_1, a total of 10 passive and 18 star-forming common galaxies were identified ($\sim$ 70% and 100%. of our full PE and SF population, after taking into account foreground and background contamination).

Galaxies that were not matched between these catalogs could be background or foreground contamination as a result from the technique we use to identify dense environments, or additionally, the gzK_s selection technique could miss some population of high-redshift galaxies. Finally, three unmatched sources in Hilton et al. are beyond our completeness limit.

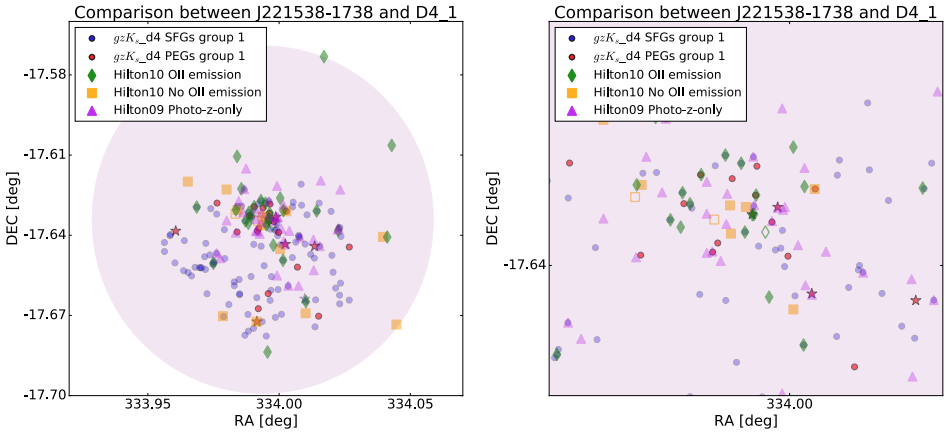

Figure 6.11: **Left panel:** Comparison between identified group in D4 and J221538.9-1738. Galaxies identified as PE-gzK_s in this group are represented in red symbols (stars represent, as before the brightest galaxies in these groups with $K_s < 20.5$. Galaxies identified as belonging to J2215.9-1738 based on spectroscopic redshifts and recessional velocities are identified as either green diamonds or yellow squares based on the presence or absence of [OII] emission respectively. **Right panel:** Zoom in the center of the cluster. The data for J221538.9-1738 was obtained from Hilton et al. (2009) and Hilton et al. (2010).

Additionally, Wen & Han (2011) identified a total of 1644 galaxy clusters from a merging of the CFHTLS Wide, Deep Fields, the Cosmic Evolution Survey (COSMOS) and the Spitzer Wide-area InfraRed Extragalactic Survey (SWIRE). Most of these clusters were found at lower redshifts although the full sample covers a redshift distribution of $0.1 \leq z \leq 1.6$ (approximately 13% of their sample are at $z > 1$, out of those, 11 clusters are at $z \sim 1.6$). These clusters are identified as an over density of galaxies within a radius of 0.5 Mpc and a given photometric redshift range. For W1, even though their analysis does not overlap entirely with our sample, we are able to identify group W1_9 as possibly being the cluster SWIRE J022005.5-055232, a rich cluster with 16 member candidates at redshift 0.75. If in fact this is consistent with being the same cluster, it is at a lower redshift than previously identified objects, but still within the expected redshift distribution of our gzK_s sample (Figure 4.3).

Similarly to W1, W4 overlaps only partially with Wen's full sample, nevertheless, and none of our groups in W4 were matched with those in Wen et al. Finally, the groups identified in D1 and D4 were found to be within 10 arcseconds of two of Wen et al. proto-clusters, one at redshift 0.98 and another at redshift 1.18.

In contrast, there are seven high-redshift ($z \geq 1.5$) clusters in W1, from Wen et al. 2011 that are not identified in our sample (Wen et al. does not report any high-redshift clusters in W4 and our K_s selected sample does not overlap with their recovered clusters in the Deep fields, i.e., they are in parts of the sky for which we had no available K_s information). Similarly, high-redshift cluster XMM-LSS J02182-05102 (also known as IRC 0218), a relatively low mass, not virialized cluster at z=1.62 (Papovich et al. 2010, Tanaka et al. 2010, Lee-Brown et al. 2017) was not recovered by our technique.

The reason why our technique does not recover all previously identified clusters at high redshifts could be because we define dense environments as environments with an over density of $K_s < 20.5$ (i.e., $log_{10}\left(M_*/M_\odot\right) > 11.14$) passive galaxies, hence these dense environments are a special kind of environments, dominated by bright passive galaxies, as described by Strazzullo et al. (2015) these dense environments are biased toward proto-clusters with more evolved structures (refer to Chapter 1).

6.3.3 Clustering

Finally, Cheema et al. in prep, calculated correlation functions for the over-densities of massive passive galaxies presented in this work. This correlation function describes the excess probability of finding a galaxy at a distance r from a given galaxy over what would

be expected in a random uniform distribution. Figure 6.12 shows this correlation function for groups with an over-density of massive passive galaxies (black points). For comparison, Cheema et al. also presents the correlation functions for passive galaxies at different magnitude ranges.

From figure 6.12 we can see that over-densities of these groups seem to be more clustered than any magnitude interval of passive galaxies, confirming the fact that we are recovering a sample of clustered over-densities with an evolved population. Using an equivalence between the correlation function of dark matter (DM) halos from the MXXL simulation (Millennium XXL Simulation; Angulo et al. 2012) and the correlation function of these over-densities, Cheema et al. established a DM halo mass of $\sim log(M_{200}) < 14.6$, hence, confirming the fact that these are massive structures.

6.4 Stellar Mass Function of Passive Galaxies Residing in Dense Environments

In this section, we built a stellar mass function (SMF) of passive galaxies that reside in environments with an over-density of passive galaxies.

First, to assess how each parameter influences the outcome, we constructed a SMF (not corrected for Eddington Bias) of passive galaxies that reside in dense environments using different parameters. To build the SMF, we used the volume of the groups as estimated by the model ellipse shown in Figure 6.9 as an approximation for the normalization. Figure 6.13 shows, as red points, the SMF of all passive galaxies in the field and a comparison

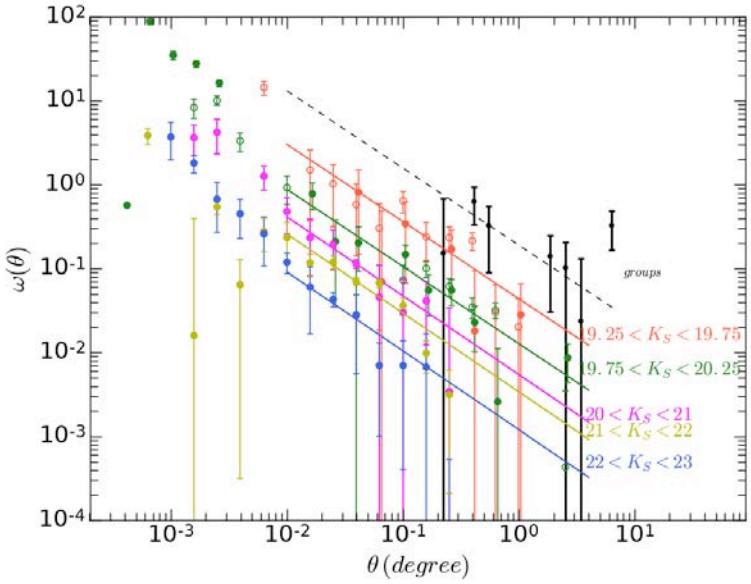

Figure 6.12: Angular correlation function as a function of angular separation for groups with an over-density of massive passive gzKs (black points) compared with passive gzKs at different magnitude ranges. Magnitude intervals are $19.25 < K_s < 19.75$, and $19.75 < K_s < 20.25$ for the Wide fields (filled symbols for W1, open symbols for W4). For the Deep fields, the magnitude intervals are $20 < K_s < 21$, $21 < K_s < 22$ and $22 < K_s < 23$. The black dashed line shows the best-fit line to the correlation function. As can be seen, these over-densities seem to be a more clustered population than passive galaxies at all magnitudes. Figure taken from Cheema et al. in prep.

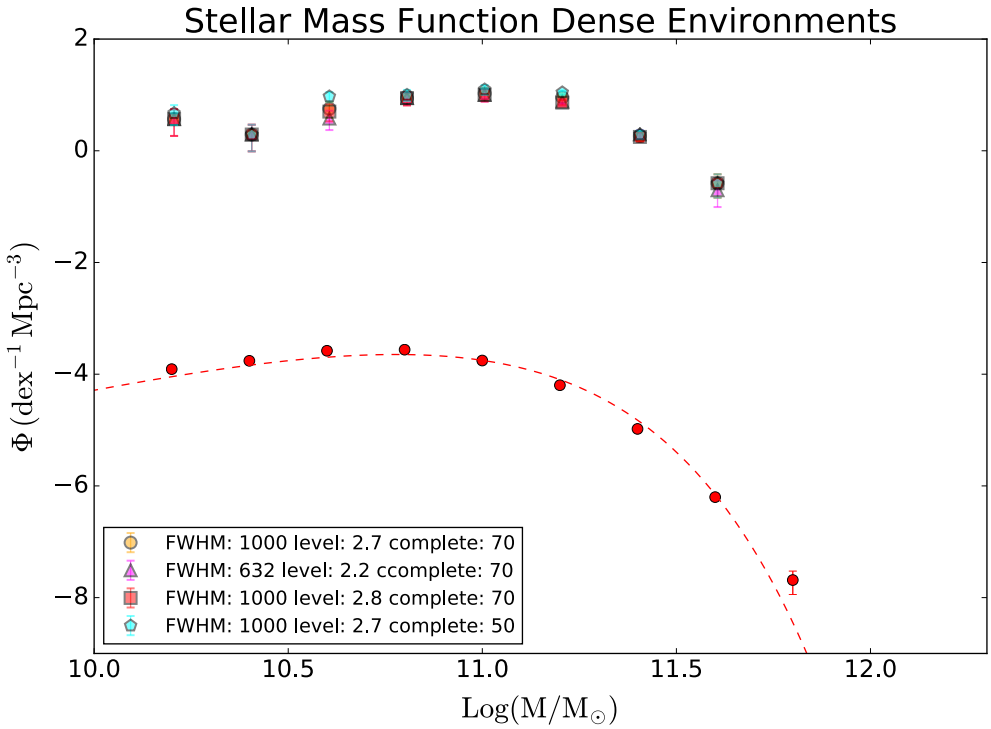

Figure 6.13: To assess the dependency on our initial FWHM, levels (to determine what is considered as a dense environment) and equi-level paths (to determine what constitutes a complete group). We built a stellar mass function of all galaxies in the field (red points) compared with the stellar mass function of galaxies residing in dense environments as defined by a choice of different FWHM, level and completeness (orange circles, magenta triangles, red squares and cyan pentagons). As can be seen, the general shape of the stellar mass function remains unchanged, although there is small scatter between some models.

between the SMF of passive galaxies that reside in dense environments selected with different FWHM, different levels (which determines what constitutes a dense environment), and different equi-level paths (which determines the extent of each group). As can be seen from this figure, the general shape of our SMF remains relatively unchanged except for a small scatter, most visible when choosing a smaller equi-level path to choose which galaxies belong to the same group.

Using the orange model presented in Figure 6.13 as our fiducial model, Figure 6.14 shows, as before, a comparison between the SMF of all field passive galaxies (shown as red circles) compared with passive galaxies that reside in environments with an over-density of massive passive galaxies (orange circles) as defined in Section 6.2. In comparison with the SMF of the field, we observe a lack of UMPEGs (or data above $log\,(M_*/M_\odot) \sim 11.6$ showing a lack of these ultra-massive passive galaxies in dense environments. As presented in Chapter 5, UMPEGs have companions that are preferentially 30% or less their mass, hence these proto-clusters with an over-density less-massive passive galaxies are unlikely environments where they reside. For the SMF of passive galaxies that reside in dense environments, at intermediate and faint masses ($log\,(M_*/M_\odot) < 11.14$), the SMF is composed of only the three groups found in the Deep fields.

Each SMF has been fitted with a convolved Schechter function, following the same procedure described in Section 4.3, hence the fit and points are corrected for Eddington Bias. In addition, shown as an inset in this figure, is the ratio per mass between these two SMFs (orange diamonds) and the ratio between the two best-fit Schechter functions (dashed orange lines).

An interesting feature in the SMF of dense environments is the apparent increase in number per volume in the least massive bin of our sample (our completeness level for this graph was taken into account when setting bin boundaries). To address if this is an effect of cosmic variance, or a systematic effect (these bins are populated only by galaxies residing in the three groups in the Deep fields: D1, D2 and D4), we performed a Jackknife resampling on our catalog and analyzed its results in Figure 6.15: As before, we show the SMF

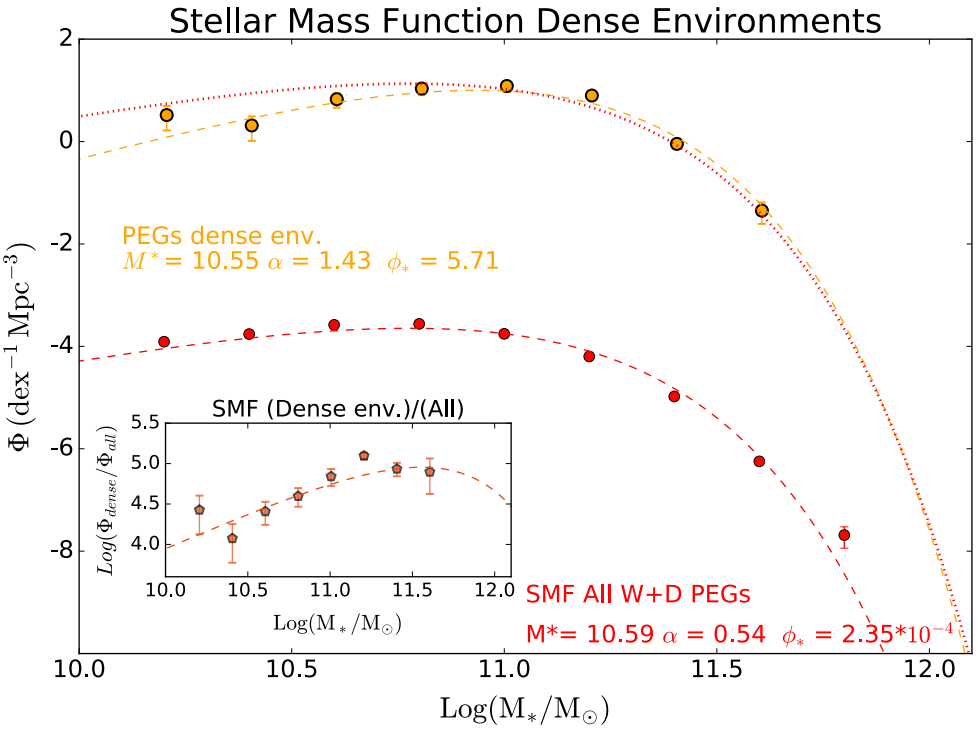

Figure 6.14: Stellar mass function of all galaxies in the field compared with the stellar mass function of passive galaxies residing in environments with an over-density of massive passive galaxies. Red circles represent the stellar mass function of all passive galaxies (field galaxies), while orange circles represent the stellar mass function of galaxies residing in a massive-passive galaxy overdense group. Also shown for both populations is their best-fit Schechter function corrected for Eddington Bias (a dashed red line for field galaxies and a dashed orange line for dense environments). Additionally, the best-fit Schechter function for field galaxies (red-dashed line) has been re-normalized to match the data in dense environments (red dotted line). The inset at the bottom shows the ratio of both stellar mass functions (points) and the ratio between both best fit lines (dashed line).

of passive galaxies in the field, as red points, and the SMF of passive galaxies residing in environments with an over-density of massive passive galaxies as orange points (shifted horizontally for clarity). Alongside the SMF of dense environments we show in three different colours the result of each Jackknife resampling, where each resampling leaves one field out of the calculation: Purple empty circles represent our SMF of dense environments when the group in D1 was removed from the sample, magenta when the group in D2 was removed and pink when the group in D4 was removed.

Also shown in this figure as an inset, a comparison between the three Jackknife resamplings (with the same colours as mentioned before). From this figure we can see that the effect on the less massive bin of our SMF does not change with each resampling.

As can be seen from Figure 6.14, at the low-mass end, there seems to be an absence of low-mass galaxies in these groups, contrary with what would be expected from environmental quenching. This could either be due to a bias in our results due to the fact that the low-mass end is only constrained by three groups in the Deep fields (which can be appreciated by the fact that the pink resampling matches more closely the shape of the field SMF, as seen in Figure 6.15), or due to the fact that these are young proto-clusters where environmental quenching is still to manifest a flattening of the SMF, or because we need to probe lower masses in order to observe the environmentally quenched population. Compared with low-redshift ($z \sim 0$) SMF from Peng et al. (refer to Figure 4.16), galaxies residing in dense environments exhibit a flattening of the SMF at low masses, as environmental quenching becomes efficient at z$\sim$1 (Peng et al. 2010; Peng et al. 2012).

There seems to be an over-density of massive passive galaxies ($log\left(M_*/M_\odot\right) \sim 11.5$),

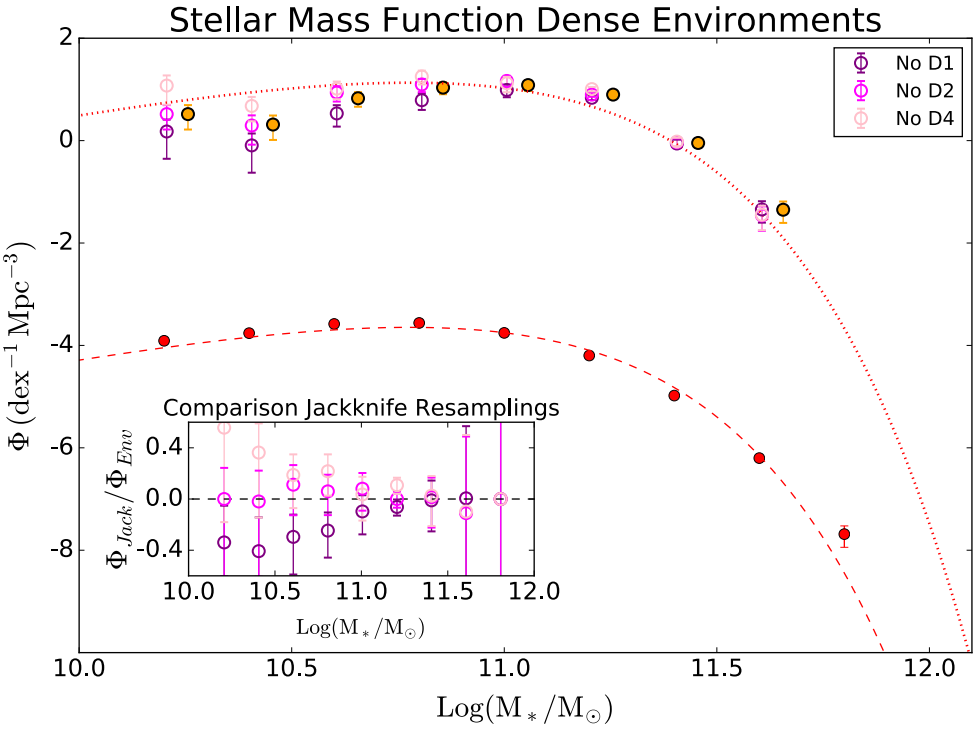

Figure 6.15: Stellar mass function of field galaxies (red points) and galaxies residing in dense environments (orange points, horizontally shifted for comparison purposes). Additionally, we show three alternative stellar mass functions for objects in dense environments, where for each iteration, we removed one of the Deep fields to account for cosmic variance. As in Figure 6.14, the red dashed line represents the best-fit Schechter function for field galaxies. Additionally, the best-fit function for field galaxies has been re-normalized to match the data in dense environments (shown as a red dotted line). The inset of the graph shows a comparison for each jackknife resampling and the combined stellar-mass function in dense environments.

this could represent the fact that these environments are populated mainly with massive passive galaxies due to: A selection bias (in the way we selected our environments), or due to the effect of mass quenching being more efficient at higher redshifts (Peng et al. 2010), or due to the fact that these environments do play a role in quenching galaxies at high masses (Newman et al. 2014).

6.5 Star-forming Galaxies in Passive Dense Environments

Up until now we have characterized passive galaxies that reside in massive dense environments, but we have not yet analyzed if these environments also posses an over-density of star-forming galaxies. Figures 6.4, 6.5, 6.6, 6.7 and 6.8 show the position of SFGs in each group using blue symbols. Starting from environments with an over-density of massive passive galaxies, (defined in Sections 6.1 and 6.2) we identify SF galaxies that reside in those environments. Equivalently to the criteria we employed in the passive population, we define a SFGs as residing in one if these environments if it lies inside the 70% level contour (white contour) surrounding a hot spot. GzK_s colour figures of these groups are shown in Appendix B.

Figure 6.16 shows the number counts, per unit area, in one magnitude bins for galaxies in the field (represented as open square symbols) and galaxies that reside in dense environments (filled circles) corrected for foreground/background contamination. Populations have been divided as star forming and passive galaxies (blue and red colours respectively). In bins where no counts have been detected (i.e., brightest two bins in the SF population)

we included, using Poisson statistics, 90% upper confidence limits as blue downward arrows. This means that in repeated measurements, 90% of the time we will obtain a value below this limit.

Compared to the field number density, there is a distinct over density of passive galaxies in dense environments, (similar to results reported by Newman et al. 2014), except at the faint end, where there seems to be a slight under-density. This result is not unexpected, given the way we defined a dense environment, nevertheless, when we compare these over densities with the star-forming population, we observe what seems to be an under-density of star-forming galaxies in these environments, (specially at bright magnitudes) compared with their field number density.

Figure 6.17 shows the fraction of passive galaxies (corrected for background/foreground contamination) in dense environments; i.e., the number of passive galaxies compared to the total number of gzK_s galaxies (star-forming and passive). As shown in Figure 4.3, the peak redshift distribution per magnitude of the star-forming and passive population is not the same (and we do not have a good estimate for the stellar mass of star-forming galaxies), so in order to present a comparison we plot this ratio in terms of their absolute i magnitudes. Even though we have small number of passive galaxies in the brightest magnitude bins, we find no K-selected star-forming galaxies of comparable brightness (although according to the 90% upper confidence level in Figure 6.16, we could simply be missing these objects). In general, it seems that the brightest K-selected sources in dense environments are in fact passive, and that star-forming galaxies only start to make a significant contribution towards fainter magnitudes. However, using these K-selected SF galaxies, we could be

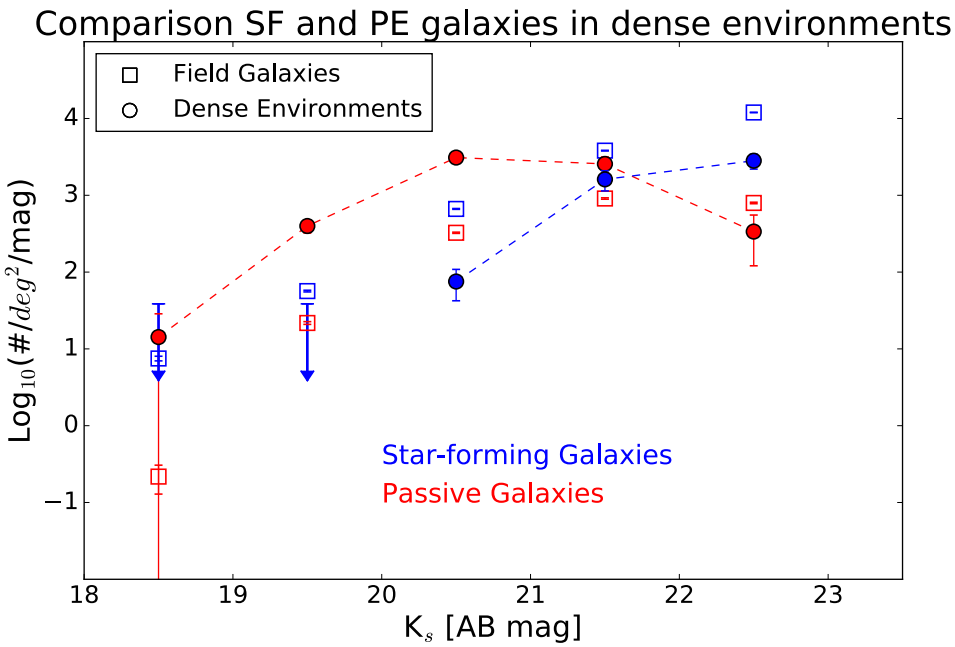

Figure 6.16: Number counts of star-forming and passive galaxies residing in the field and in dense-environments. Shown in open squares are the number counts per area of galaxies in the field whereas galaxies in dense environments are represented with filled circles. Red circles are used to represent passive galaxies, and blue circles for star-forming ones. 90% upper confidence levels in bins with no detections are represented as downward arrows. Areas for dense environments were calculated based on the area of the model ellipse shown in Figure 6.9.As can be seen, compared to the field number density, there is a higher fraction of passive galaxies residing in dense environments compared to star-forming objects.

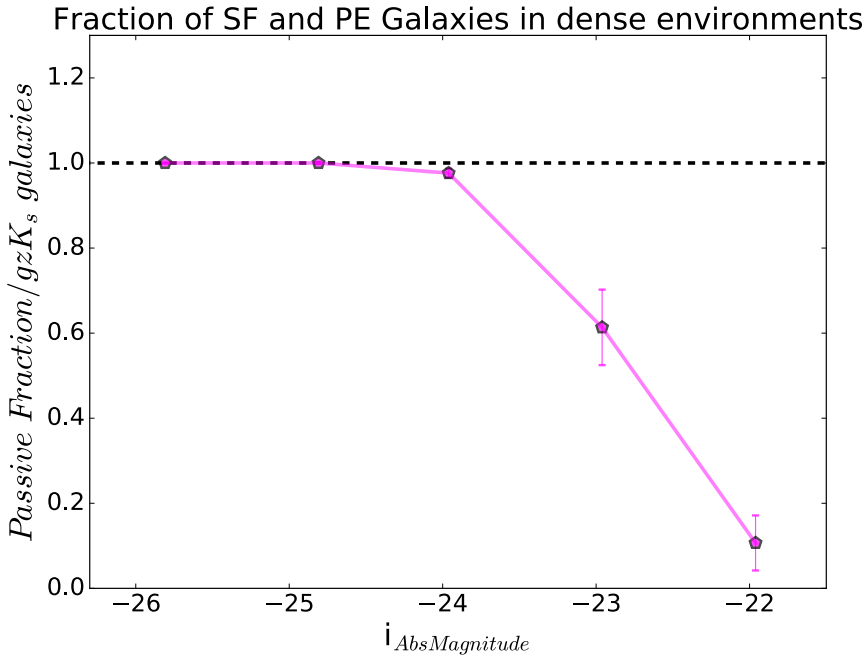

Figure 6.17: Number of total gzK$_s$ selected galaxies (passive and star-forming) in dense groups, compared with the total number of only passive galaxies in those groups. As can be seen, these dense environments are dominated by passive galaxies at the brighter magnitudes. On the other hand, as we start to consider fainter magnitudes, there is a significant contribution of star-forming galaxies in these groups.

missing the presence of dusty SF, faint in K-band but with high levels of star-formation. These kind of dusty-SF galaxies have previously been identified in proto-clusters (Chapman et al. 2001; Daddi et al. 2009; Casey et al. 2014; Kato et al. 2016).

Nantais et al. (2016) performed a similar analysis, using four proto-clusters at $1.37 < z < 1.63$ from the SpARCS (Spitzer Adaptation of the Red-sequence Cluster) Survey (Wilson et al. 2009). By comparing them with a field SMF, they find that the SMF of cluster galaxies resembles that of field galaxies and that the passive and star-forming fractions are close to $\sim 50\%$ for all masses. There are several factors to take into account when compar-

ing their results to ours. First, their selection recovers a population of clusters with an over-density of red galaxies at masses down to their completeness limit ($log\,(M_*/M_\odot) \sim 10.1$), while we recover over-densities of passive galaxies down to $log\,(M^*/M_\odot) \sim 11.14$. In addition, their highest-mass bin is $log\,(M^*/M_\odot) \sim 11.4$ for which there is only a single star-forming galaxy in their sample (an unconfirmed photometric cluster member), hence not allowing them to draw a reliable conclusion at the high-mass end.

We estimated the environmental quenching efficiency in our groups using Nantais et al. (2016) equation 1:

$$Efficiency = \frac{f_{pe-group} - f_{pe-field}}{1 - f_{pe-field}}, \tag{6.1}$$

where $f_{pe-group}$ is the fraction of passive galaxies in our groups and $f_{pe-field}$ is the fraction of passive galaxies in the field. The results for our environmental quenching efficiency are shown in Figure 6.18, where we assumed that mass is proportional to rest-frame i band flux. As can be seen from this plot, in these groups, we find a mass-dependent quenching efficiency, where massive galaxies are more likely to be quenched than less massive galaxies. This result is in agreement with Papovich et al. (2018) who find that the evolution of the quiescent SMF from high-redshfits to low redshifts, specifically, a rapid grow of low-mass galaxies at low redshifts, requires that at high redshifts ($z > 1$), the environmental quenching efficiency decreases with decreasing stellar mass. They claim that this effect has not been recovered in previous works (Balogh et al. 2016 at $0.8 < z < 1$ and van der Burg et al.

2013 at $1 < z < 1.5$), because their efficiency is calculated with respect to the field instead of truly low density environments. However, it is possible that we still recover the same results albeit using field estimates, due to our groups being part of an evolved population of proto-clusters.

Proposed mass-dependent environmental quenching mechanisms (that can produce a mass-dependent quenching efficiency) include gas stripping (McCarthy et al. 2008; Tonnesen & Bryan 2009), tidal interactions or mergers (Dekel & Woo 2003; Deason et al. 2014) and "overconsumption" (McGee et al. 2014) a process in which star-formation-driven outflows leads to the rapid quenching of a satellite galaxy if the halo of the central prevents the accretion of more gas (more efficient in more massive systems because they deplete their gas reservoir faster).

The evolution in the SMF from high to low redshifts found by Papovich et al. is similar to our findings in Chapter 4, Papovich et al. also finds that M^* for PE and SF changes with time (increasing and decreasing at low redshifts respectively, by as much as ~ 0.4 dex), but they find that this effect is dependent on density: galaxies in the lowest density quartile show no evolution in their M^* parameters for both PE and SF populations.

6.6 UMPEGs and dense environments

Following our results from the previous chapter, it is important to understand where UM PEGs (Ultra-Massive Passive Galaxies, $log\,(^{M_*}/_{M_\odot}) > 11.49$) reside with respect to massive dense environments. Figures 6.19 and 6.20 show the position of UMPEGs with respect to

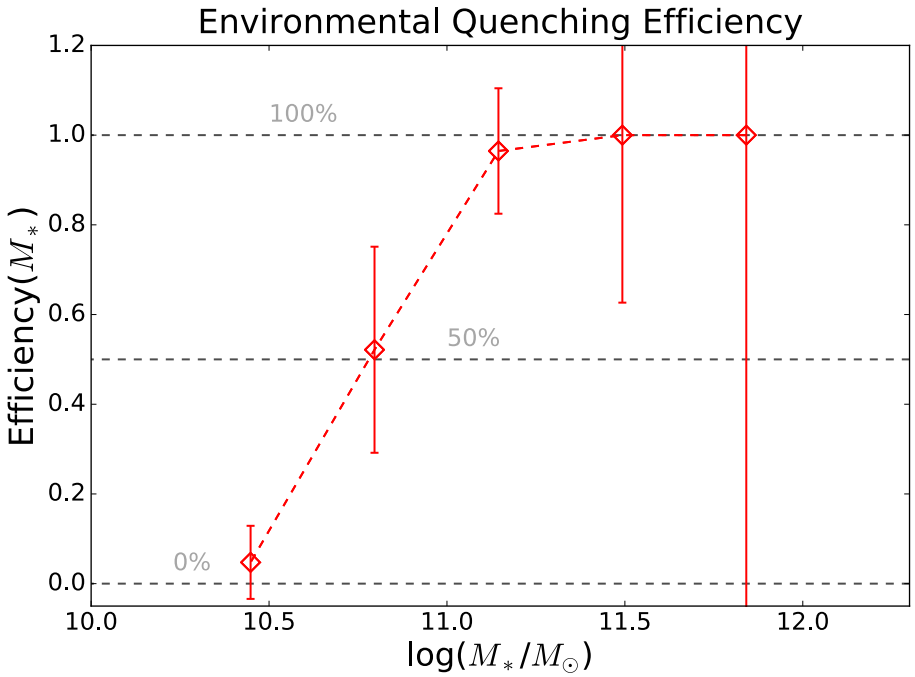

Figure 6.18: Environmental quenching efficiency. Calculated using equation 6.1, and our binned foreground and background corrected counts form Figure 6.16, it shows a mass-dependent quenching efficiency: more massive galaxies are more likely to be quenched in our groups than less-massive galaxies.

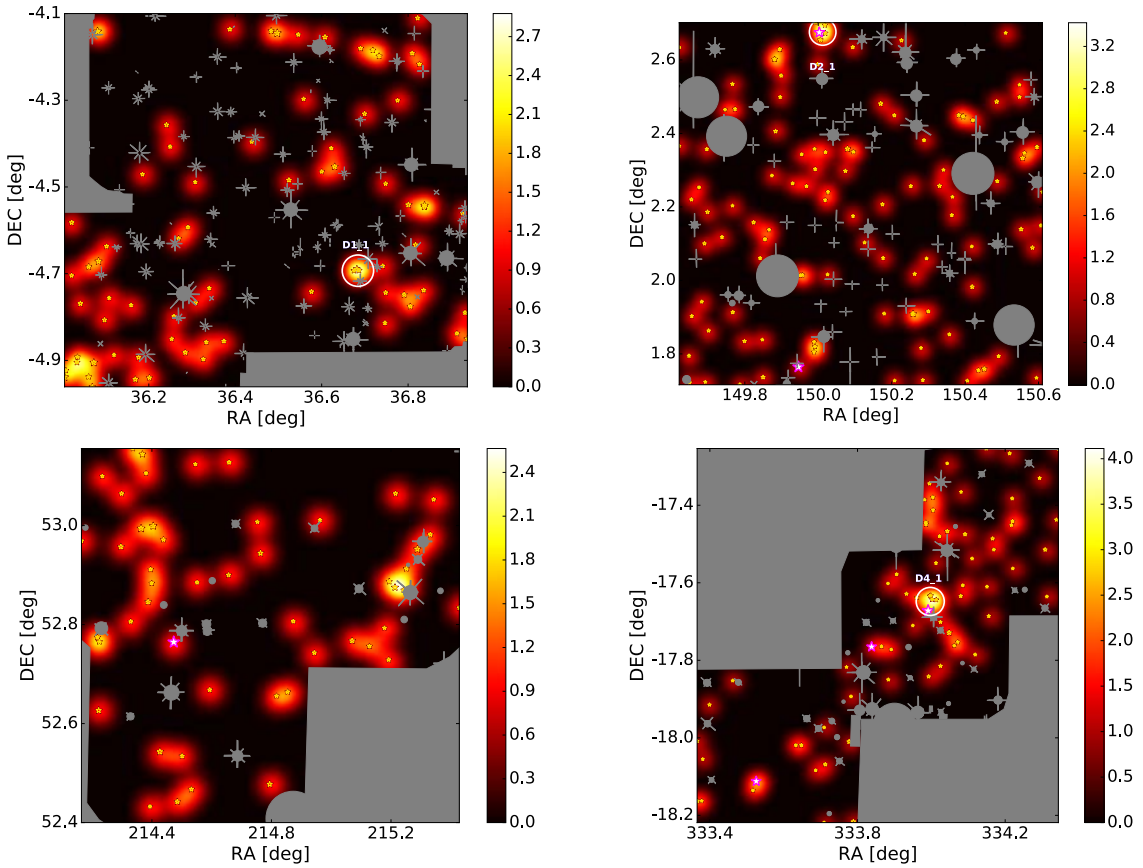

Figure 6.19: Gaussian density maps for the Deep Fields. Dense environments are highlighted by a white circle and a label. Shown as stars are $K_s < 20.5$ passive galaxies. Additionally, UMPEGs are shown in magenta-white. As can be seen from these plots, out of the six UMPEGs present in the Deep fields, two lie in what we consider a dense environment.

identified dense environments. As can be seen from these figures, approximately 8% (5 out of 61) of UMPEGs reside in what we consider a dense environment (recall that these dense environments are characterized by an over-density of $K_s < 20.5$ passive galaxies, hence ignoring the faintest galaxies). Given the effective area of our sample ($\sim 27.6\, deg^2$) we would expect to find ~ 2.2 UMPEGs per deg^2, hence, given the total area of our groups ($\sim 0.07\, deg^2$) , we only expect 0.15 UMPEGs by random association in groups.

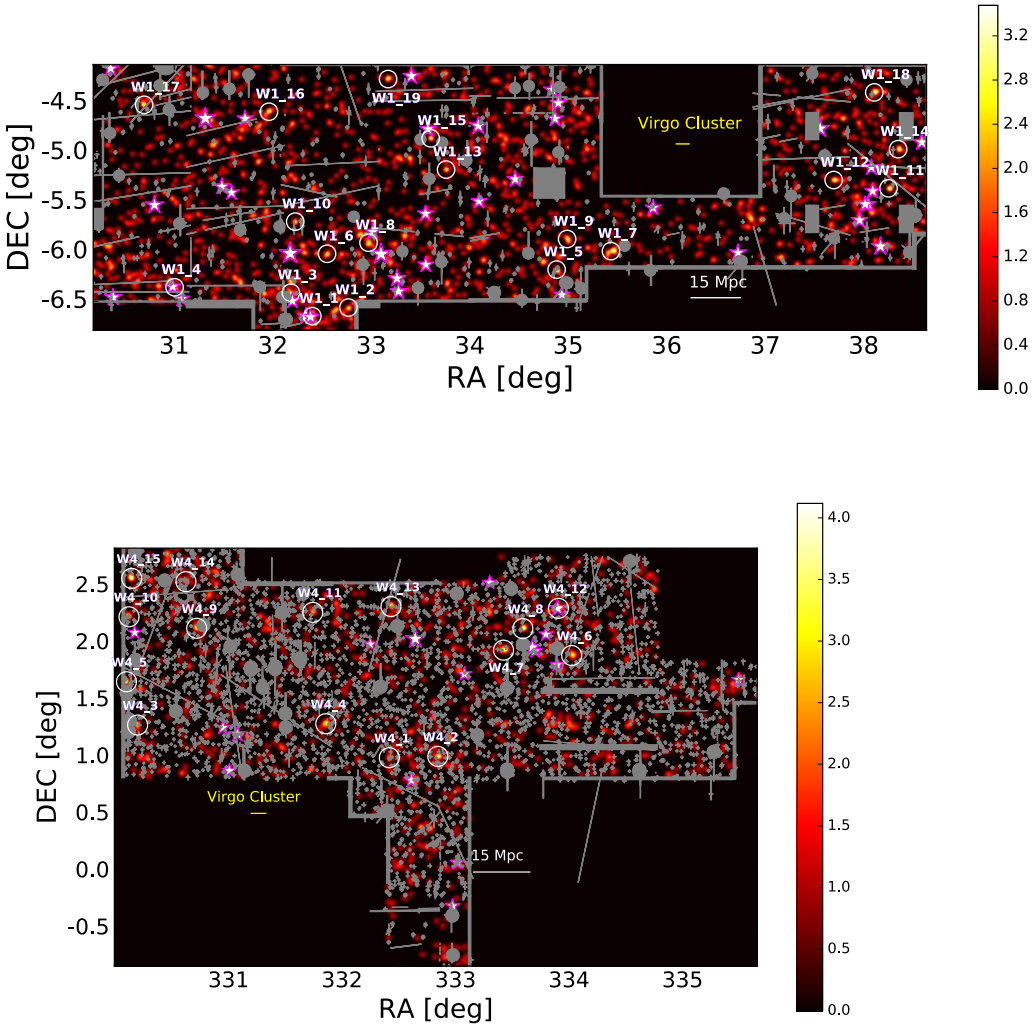

Figure 6.20: Gaussian density maps for the Wide Fields. Dense environments are highlighted by a white circle and a label. UMPEGs are shown as magenta-white stars. As can be seen from these plots, out of the 55 UMPEGs present in W1 and W4, three lie in what we consider a dense environment.

The lack of UMPEGs in these dense environments is not surprising, given that in Chapter 5 we found an absence of bright companions to these UMPEGs (if we consider 19.5 as the most likely magnitude for UMPEGs, companions that are $40-50\%$ fainter lie in magnitudes fainter than $K_s \sim 20.5$). Regarding the five UMPEGs that reside in dense environments, these galaxies are not found at the center of their proto-groups, they are mainly found in the outskirts. Assuming UMPEGs are the central galaxy of their dark matter halos, this could mean that these groups are not yet virialized.

Summary

In this chapter, we have identified dense environments as an over-density of massive ($log_{10}\left(M_*/M_\odot\right) > 11.14$) passive galaxies. Some of these dense environments have previously been identified as high-redshift clusters from previous authors, but others have not, confirming our selection process but also highlighting the fact that we are in fact, recovering a special subset of high-redshift proto-clusters.

When analyzing the populations that inhabit these proto-clusters, we find an underdensity of bright star-forming galaxies residing in these dense environments, hinting at the influence of dense environments in the quenching of star-formation. This observation matches the scenario presented by Chiang et al. (2017), who propose a three stage cluster formation: First, an inside-out growth phase ($10 \leq z \leq 5$), followed by an extended star-formation phase ($5 \leq z \leq 1.5$) and ending in a violent infalling and quenching phase ($z \leq 1.5$). It is possible that PE gzK_s selected clusters are in transition between these last two

phases, where galaxy quenching is enhanced. This environmental quenching efficiency is mass dependent, i.e., more massive systems are more likely to be quenched in these proto-clusters.

Research has shown that galaxy proto-clusters with redshifts $z > 2$ tend to be dominated by young, star-forming galaxies (Steidel et al. 1998; Venemans et al. 2007, Toshikawa et al. 2016), and multiple techniques are fine-tuned to find clusters based on that population (e.g., u, g, r, i-dropout technique: Toshikawa et al. 2016, 2018, and radio-selected technique: Daddi et al. 2017). It is only below z$\sim$2 that passive galaxies start to become a dominant population in proto-clusters (Chiang et al. 2017, Lemaux et al. 2014). If our $z \sim 1.6$ selected clusters are in fact lacking a population of bright star-forming galaxies (and are not in fact dust obscured SF-galaxies missed by our K-selected sample), this could represent either the fact that our groups are not a representative population of proto-clusters, but instead a specific case of over-densities with multiple massive passive galaxies whose evolution is somewhat different from more commonly found proto-clusters, or we are in fact witnessing a quenching downsizing effect in over-dense regions where more massive star-forming galaxies tend to quench earlier than less massive ones.

Finally, galaxy clusters in the local universe tend to be dominated by a passive population of galaxies with similar morphologies which are significantly different from field galaxies, and are characterized by having a dominant cluster member (Brightest Cluster Galaxy or BCG). Nevertheless, we find that only 8% of our UMPEGs reside in these dense environments. Hence, we would expect environmental quenching and dynamical relaxation to play important role in these high-redshift proto-clusters as they evolve to a distri-

bution that more closely resembles present-day clusters (i.e., as these massive PEGs merge and potentially become BCGs for these groups in the local universe). This result is consistent with Cheema et al. in prep for which they find that at $z \sim 1.6$, there are more halos that will become present-day massive clusters than UMPEGs (at $z \sim 1.6$, approximately1 in 8 UMPEGs reside in the progenitor halos of massive clusters, such as Coma or Virgo). If this is indeed the case, most of the present-day massive clusters were probably not populated by a single BCG at $z \sim 1.6$, but instead of several less massive PEGs that will eventually become, by mergers, the brightest galaxy in their clusters.

Chapter 7

Conclusions and Future Work

7.1 Conclusions

In this thesis, we have used an adaptation of the BzK_s colour-colour technique (the gzK_s or $gzHK_s$ technique) to build a combined catalog of star-forming and passive galaxies at $z \sim 1.6$. In order to do this, we used optical information (g and z) from the Canada-France-Hawaii Telescope Legacy Survey (CFHTLS, Hudelot et al. 2012, Goranova 2012), and near-infrared infrared data (H and K_s) from WIRDS (Bielby et al. 2012) and VIPERS-MLS (Moutard et al. 2016b) in four and two of the CFHTLS Deep and Wide fields. Our final combined catalog has a total effective area of 27.6 deg^2, from which we extracted $\sim 700,000$ sources.

Due to our lack of intermediate near-infrared filters, in order to obtain an estimate of photometric redshifts and stellar masses, we cross-matched our catalog of passive galaxies with that of Muzzin et al. (2013b) and determined that our passively evolving gzK_s galaxies

(PEGs) have a magnitude-dependent redshift distribution. Brighter galaxies tend to be found at lower redshifts than fainter ones. As an example, a PEG with $K_s \sim 19.5$ is more likely to be found at $z \sim 1.6$, while the faintest galaxies in our sample, at $K_s \sim 23.5$, are more likely to be found at $z \sim 1.75$. Moreover, using an empirical K_s to $log\,(M_*/M_\odot)$ conversion, we built a stellar mass function (SMF) for these passive galaxies. Due to the wide areas of our sample we were able to recover a significant sample of rare ultra-massive passive galaxies $(log\,(M_*/M_\odot) > 11.49)$. Allowing us to constrain the exponential cut-off at the massive end of the SMF, and study this population in more detail. Key points from this analysis are:

- After taking into account Eddington bias (due to uncertainties in the mass conversion and fewer galaxies at the massive end, galaxies are more likely to scatter into bins of higher mass, causing a steepening of the SMF), we found our SMF of PEGs is well described by a Schechter function characterized by a normalization factor $\Phi^* = 2.35 \times 10^{-4}\, Mpc^{-3}$, a characteristic mass $M^* = 10.59\, M_\odot$ and a faint end slope $\alpha = 0.54$. The fact that the shape of the number density of PEGs is well described by a Schechter function was proposed by Peng et al. (2010), who suggest that once massive galaxies quench through a mass quenching mechanism, their distribution will be a Schechter function with the same characteristic mass as the original star-forming population.

- A comparison between best-fit M^* parameters between PEGs and SFGs at $1.5 < z < 2.0$ shows that the M^* of SFGs (M^*_{SF}) is higher than the M^* of PEGs (M^*_{PE}). This

would imply an evolution to higher masses of M^*_{SF} to lower redshifts and a quenching mechanism that is not instantaneous, but requires long timescales to stop the star-formation in the galaxy (enough to allow the evolution of M^*). However, when studying the evolution of M^*_{SF} we observe no evolution up to $z \sim 2$ after which (i.e., $z > 2$) we observe an increase in M^*_{SF}. For M^*_{PE}, due to large error bars, it is difficult to assess its evolution at $z > 2$ but for $z < 1.5$ there seems to be a systematic increase. According to Papovich et al. (2018) this effect is dependent on environment: they observe the same behaviour in dense environments (an evolution of M^* for both PE and SFGs), but no evolution in low-density environments. Moreover, the evolution in M^* for the total SMF tracks the same evolution in dense environments. This implies that an universal quenching process it at play in all environments, for which, in isolated systems we observe the same non-evolving M^*_{PE}, while in higher regions, there seems to be an enhanced growth of PEGs due to interactions, though not yet in place at $1.5 < z < 2.0$.

- Following the number density evolution of passive galaxies to $z \sim 0$, we find first a flattening of the SMF at the low-mass end, most likely driven by environmental quenching. Second, depending on the environment in which massive passive galaxies at $z \sim 0$ reside, they will evolve by either a simple re-normalization as more galaxies are 'mass-quenched' when living in low density environments, or an evolution in mass for galaxies that live in dense environments, most likely the result of galaxy interactions (such as galaxy mergers).

- We defined Ultra-Massive Passive Galaxies (UMPEGs) as PE gzK_s -selected galaxies with masses $log\,(M_*/M_\odot) > 11.49$. Starting from these UMPEGs, we studied their environments and found that most of them do not exhibit companions of similar mass (50% or more of the mass of the UMPEG), but there is a relative abundance of low mass companions ($\sim$ 30% or less the mass of the UMPEG).

- Using the companions to these UMPEGs, and a simple dynamical friction timescale, we estimated the merger times of these satellite galaxies and determined the possible growth of UMPEGs from $z = 1.6$ to $z = 1$. For an UMPEG of mass $log\,(M_*/M_\odot) \sim 11.60$ we find a grow of $25 - 32\%$ in mass down to $z = 1$. These values are upper limits, as the masses of our SF satellites are likely overestimated.

- Comparing the expected evolution of UMPEGs with the observed SMF at $z \sim 1$, we estimated that UMPEGs will evolve based on a combination of both mergers and mass quenching, where most of the merger growth will be driven by smaller companions (those with masses 50% or less the mass of the UMPEG).

- Finally, we analyzed regions with an over-density of massive passive galaxies, $log\,(M_*/M_\odot) \geq 11.14$. This allowed us to select a special subset of high-redshift proto-clusters in which significant quenching has already occurred. These over-densities seem to have an under-density of bright K-selected star-forming galaxies. If this is not due to a selection effect (where we are missing dusty, star-forming galaxies) it is consistent with proto-cluster formation theory, where following an extended star-formation phase proto-clusters start to transition to a quenching phase at $z \sim 1.5$,

possibly quenching first the most massive galaxies.

- The quenching efficiency in these proto-clusters seems to be dependent on mass: more massive galaxies are more likely to be quenched than less massive ones. This leads to a physical quenching process that is mass dependent at least at these redshifts (Papovich et al. 2018).

- We find that most of our UMPEGs do not reside in these over-dense environments, regardless, we expect these over-densities to evolve into a distribution that more closely resembles present-day clusters. This result is consistent with Cheema et al. in prep, who find that at $z \sim 1.6$ there are more dark matter halos that will become present-day massive clusters than UMPEGs (at $z \sim 1.6$, approximately 1 in 8 of these halos are occupied by UMPEGs). Most of these dark-matter halos still do not display a dominant BCG at high redshifts, but possibly a combination of passive galaxies that due to mergers will become one (or may still be star-forming galaxies in proto-clusters).

- A proposed growth of local ultra-massive galaxies (UMGs, $log\,(M_*/M_\odot) \sim 11.8$) by Marchesini et al. (2014) suggest that UMGs start by having dusty, intense star- formation rates at high redshifts and by $z \sim 1.6$, $\sim 60\%$ are already quenched. Their evolution, after quenching, is followed by dry minor mergers and aging, with an expected growth of $\sim 40\%$ between $0 < z < 1.6$, hence our UMPEGs could be the progenitors of local UMGs. However, as previously mentioned, Cheema et al. find that only 1 in 8 of local UMGs halos are occupied by UMPEGs, leading to the conclusion that while some of these halos will be occupied by newly quenched SFGs

(for which 40% of progenitors will come from this population), some of these UMGs would have to be descendants of major merger events that will result in galaxies with $log\left(M_*/M_\odot\right) \sim 11.8$ today, which is in disagreement with the expected minor merger evolution.

7.2 Future Work

- It is important to study the evolution in the environments of UMPEG progenitors to higher redshifts: has the lack of massive companions been in place at high redshifts? and how does it relate with the growth in mass of the UMPEG?

- It is also important to obtain spectroscopic information of our UMPEGs and its companions in a given merger radius. This will allow us, first to confirm the redshift (and constrain a low-redshift interloper rate), determine how many of the companions are chance projections, mass (and confirm their position in the SMF) and star-formation activity (or lack of) of the central UMPEG and relate its companion in three-dimensions, allowing us to estimate a better growth due to mergers (GEMINI proposal submitted).

- Two of our three proto-clusters candidates in the Deep fields have been identified by previous authors (Newman et al. 2014; Hilton et al. 2009, 2010), hence the remaining proto-cluster (in COSMOS) is a good candidate for spectroscopic follow up, alongside with all the available proto clusters in the Wide fields ($\sim$ 34 proto-clusters). This would allow us to confirm the presence of a proto-cluster, its real associated mem-

bers, their nature (passive or star-forming) and total mass of the proto-cluster.

Appendix A

The following Figures show gzK_s colour images of the environments in a radius of 0.5 Mpc around six ultra-massive passive galaxies in the Deep and 55 in the Wide fields. The yellow circle represents the radius of search and enclosed in blue and red circles are star-forming and passive galaxies respectively. Any star-forming or passive galaxy inside this radius of search is considered as part of the environment of its central UMPEG. Also shown as a small inset is a zoom-in of the central ultra-massive galaxy.

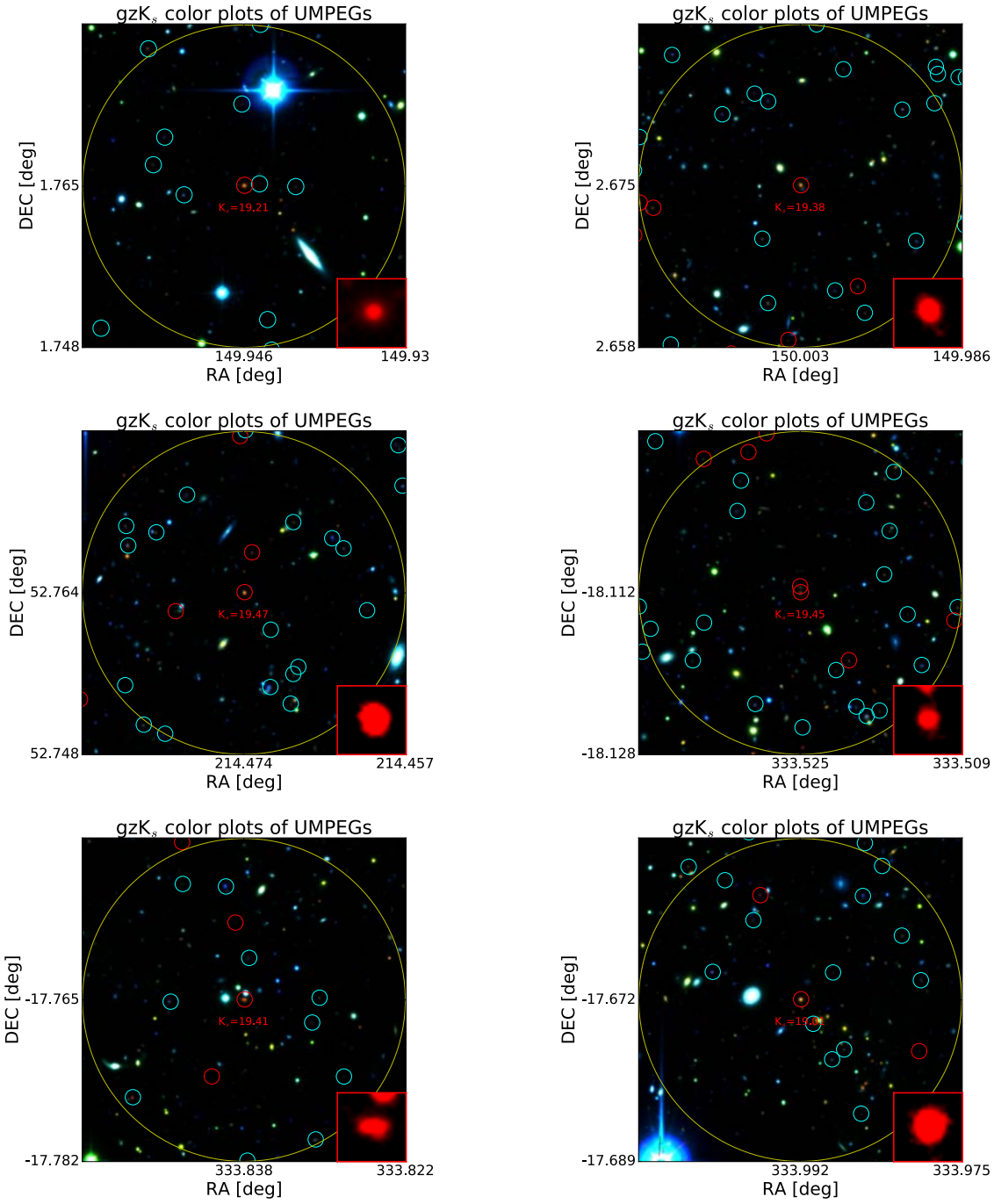

Figure 7.1: Deep Fields, UMPEGs and their environments: UMPEGs 1 through 6

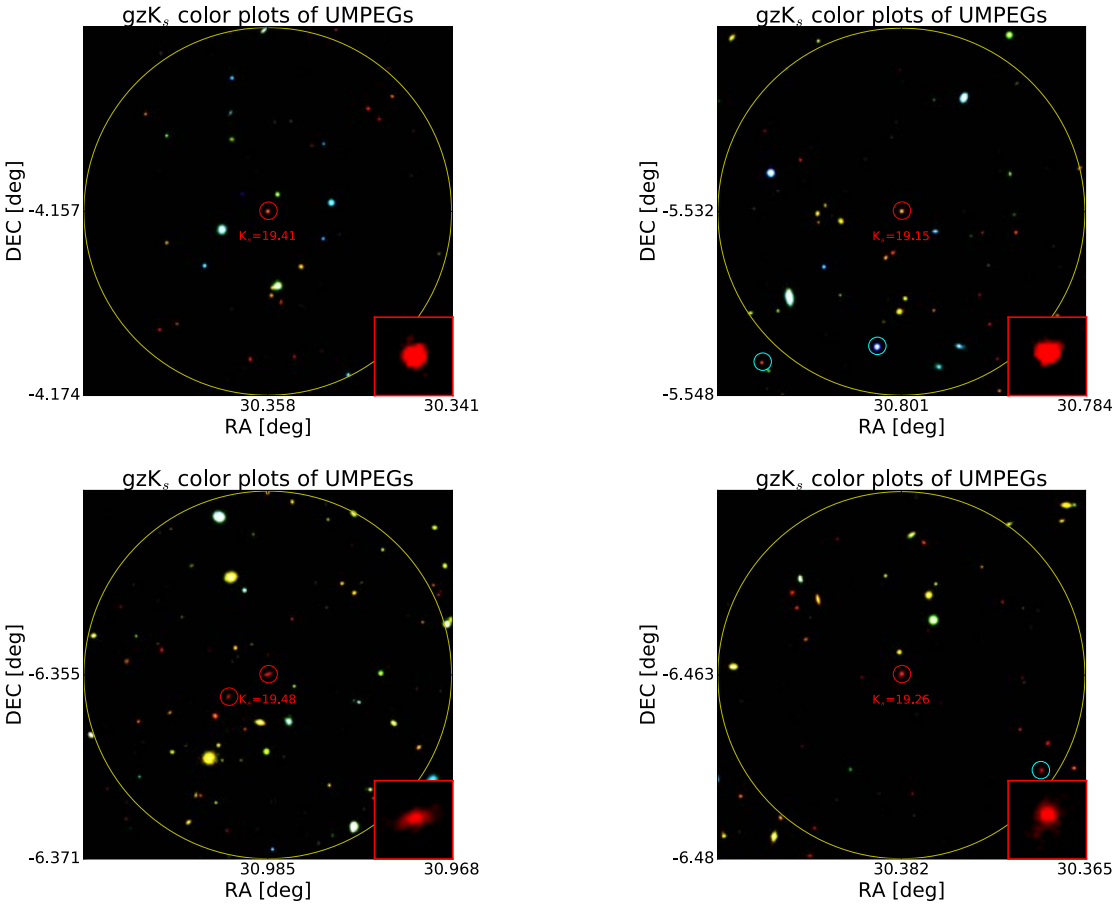

Figure 7.2: Wide Fields, UMPEGs and their environments: UMPEGs 1-4.

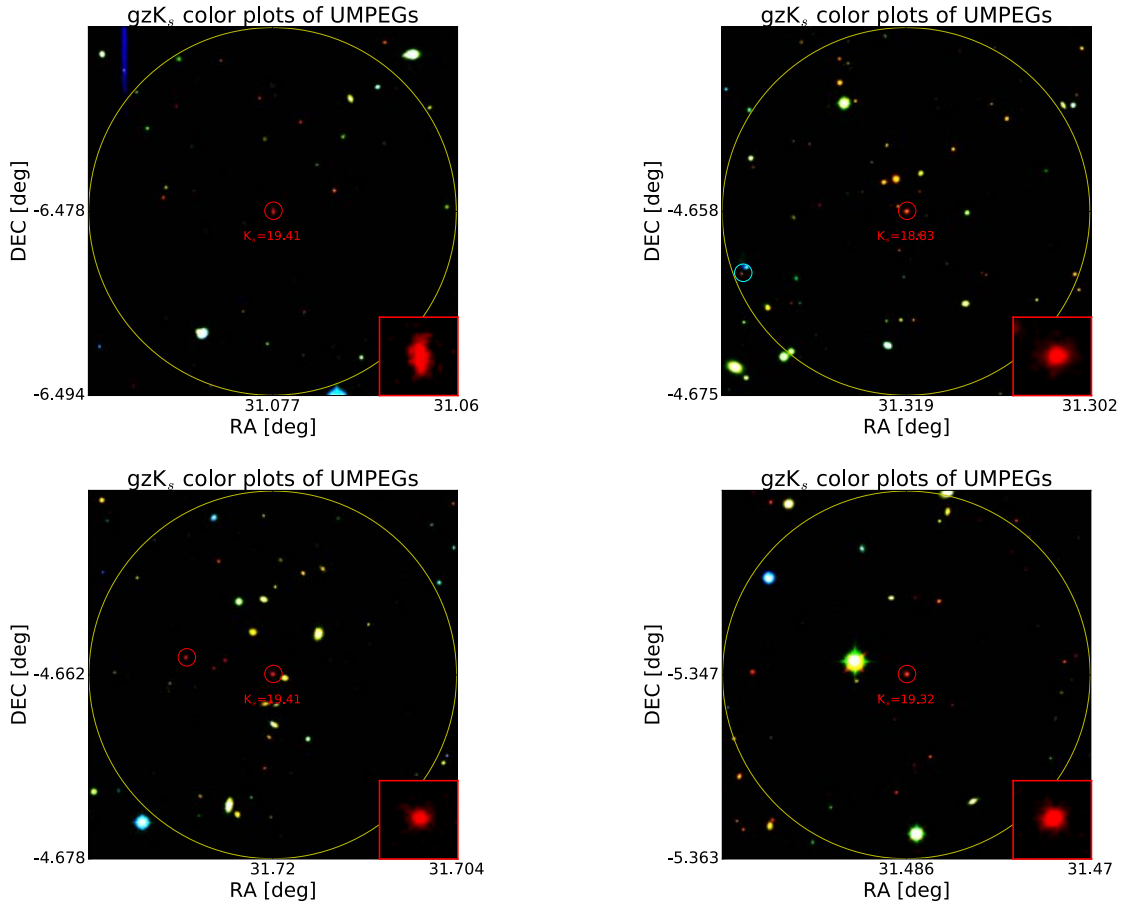

Figure 7.3: Wide Fields, UMPEGs and their environments: UMPEGs 5-8.

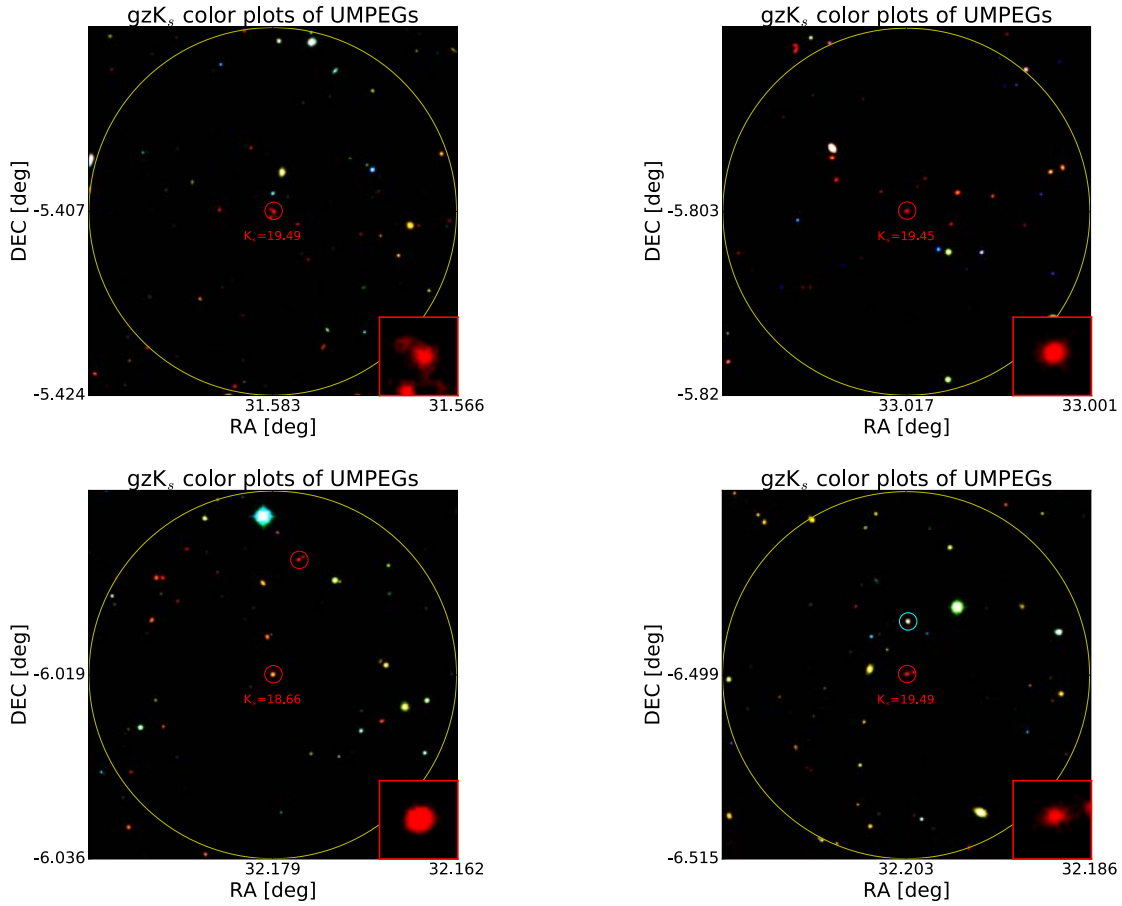

Figure 7.4: Wide Fields, UMPEGs and their environments: UMPEGs 9-12.

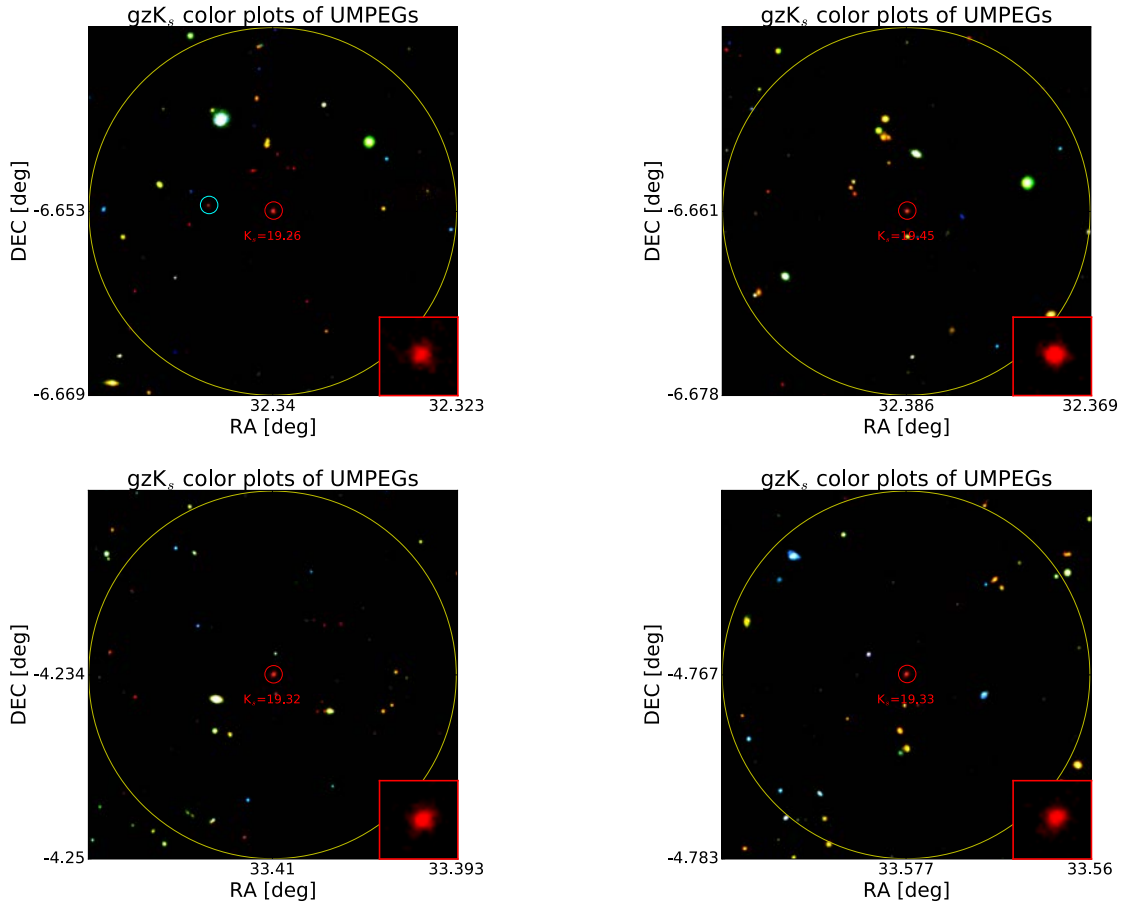

Figure 7.5: Wide Fields, UMPEGs and their environments: UMPEGs 13-16.

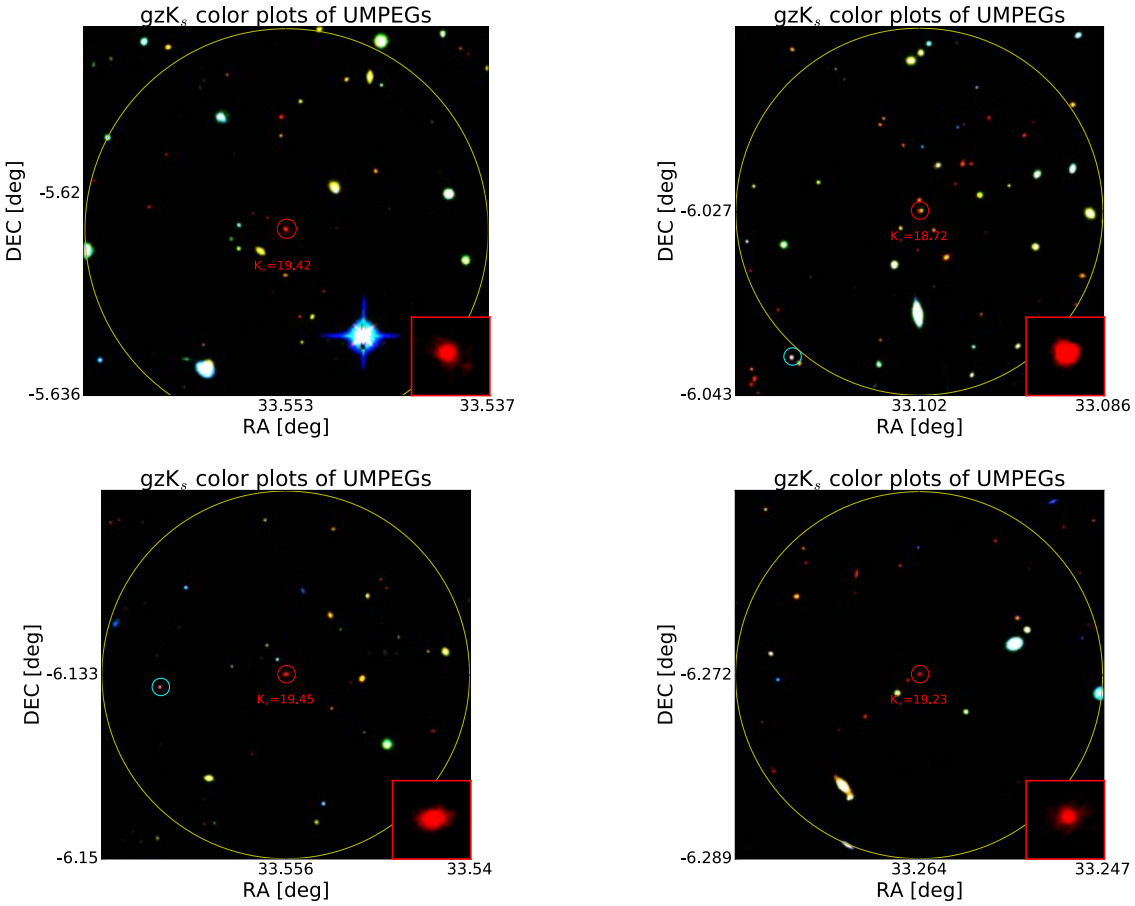

Figure 7.6: Wide Fields, UMPEGs and their environments: UMPEGs 17-20.

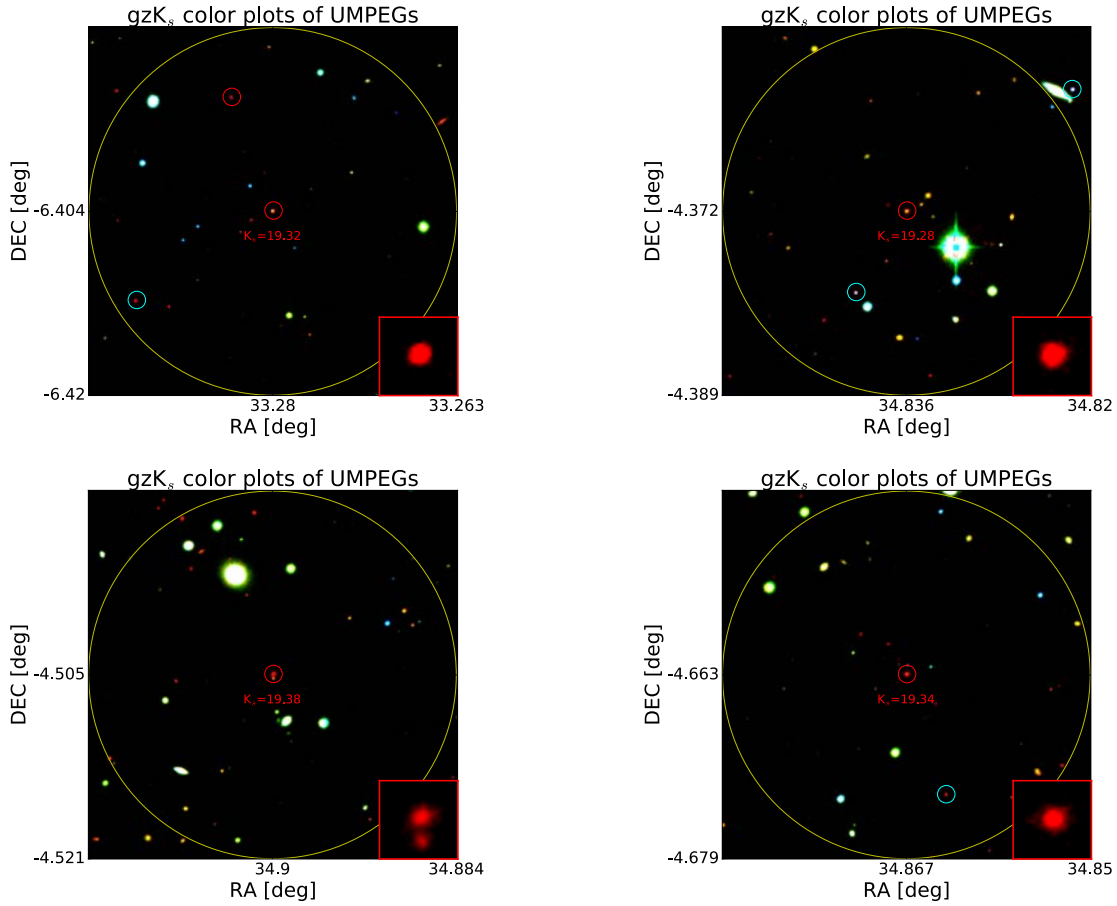

Figure 7.7: Wide Fields, UMPEGs and their environments: UMPEGs 21-24.

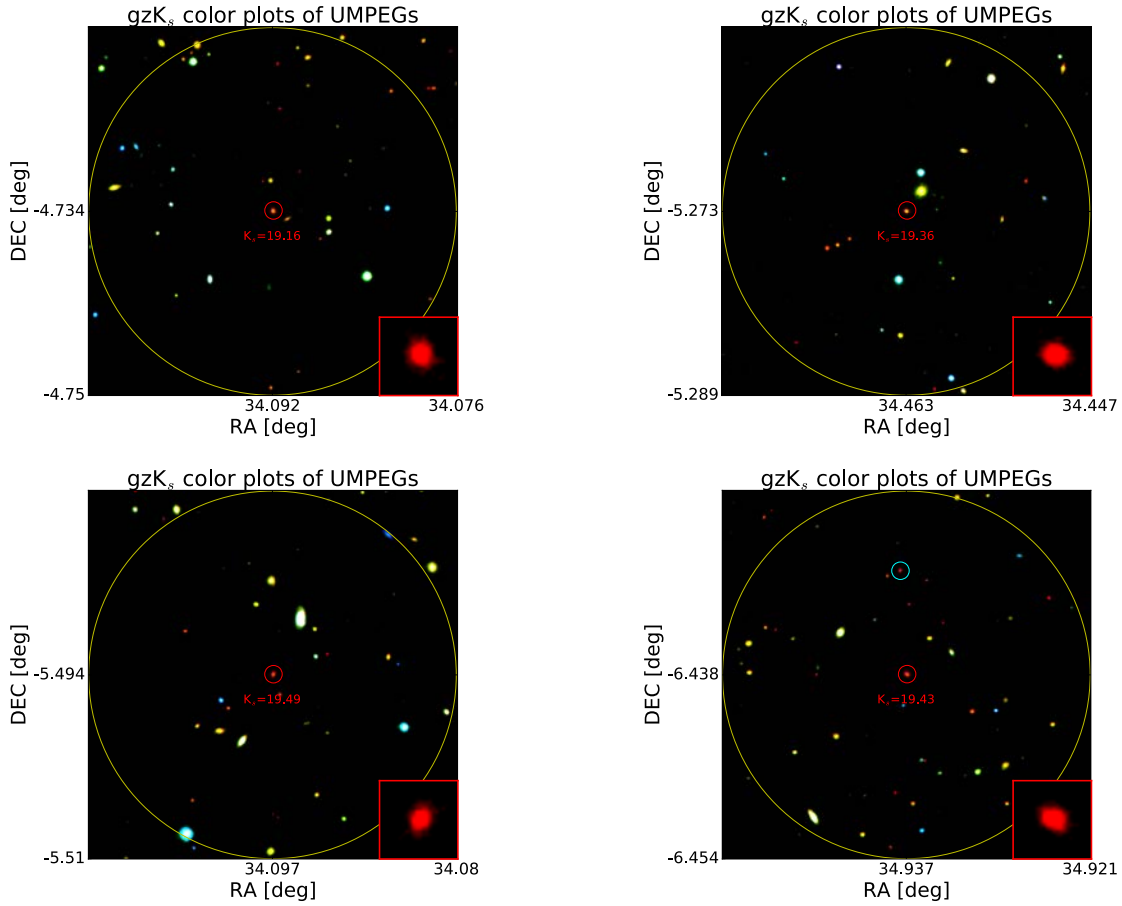

Figure 7.8: Wide Fields, UMPEGs and their environments: UMPEGs 25-28.

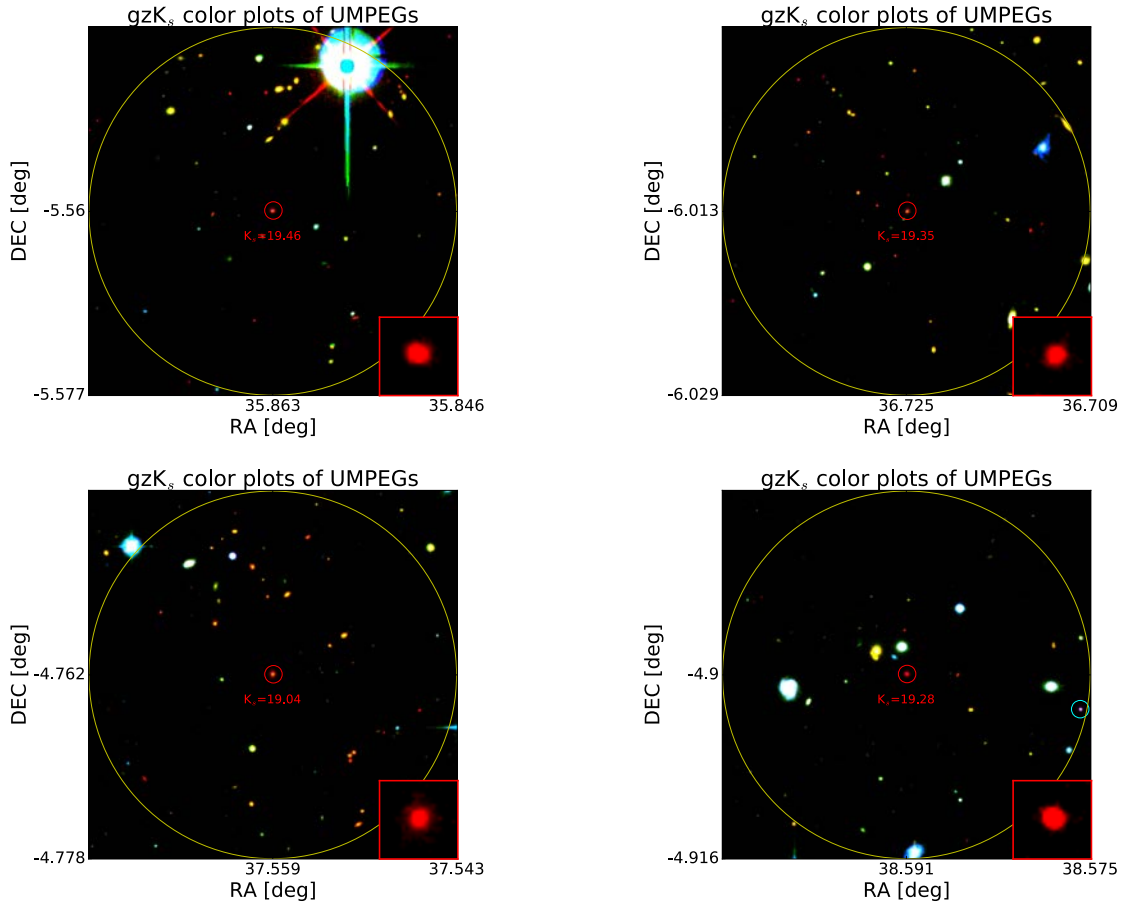

Figure 7.9: Wide Fields, UMPEGs and their environments: UMPEGs 29-32.

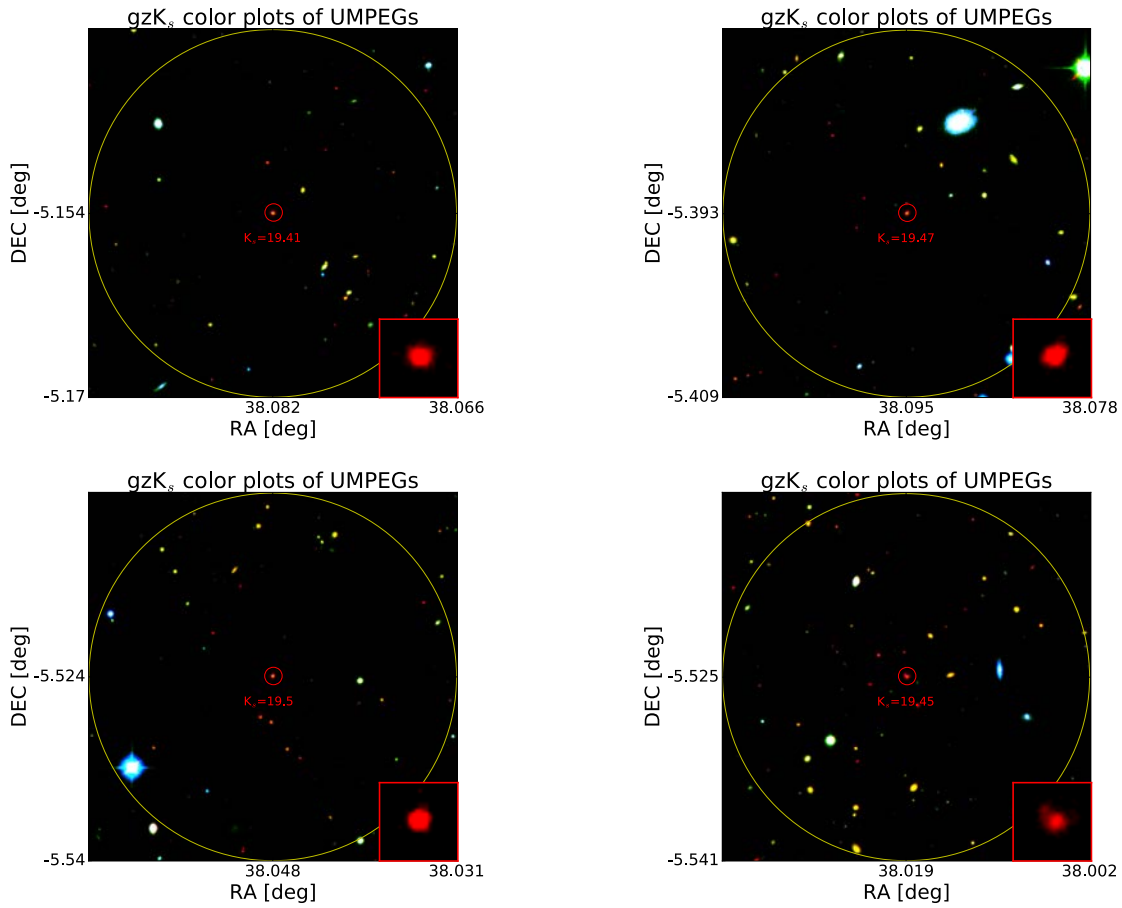

Figure 7.10: Wide Fields, UMPEGs and their environments: UMPEGs 33-36.

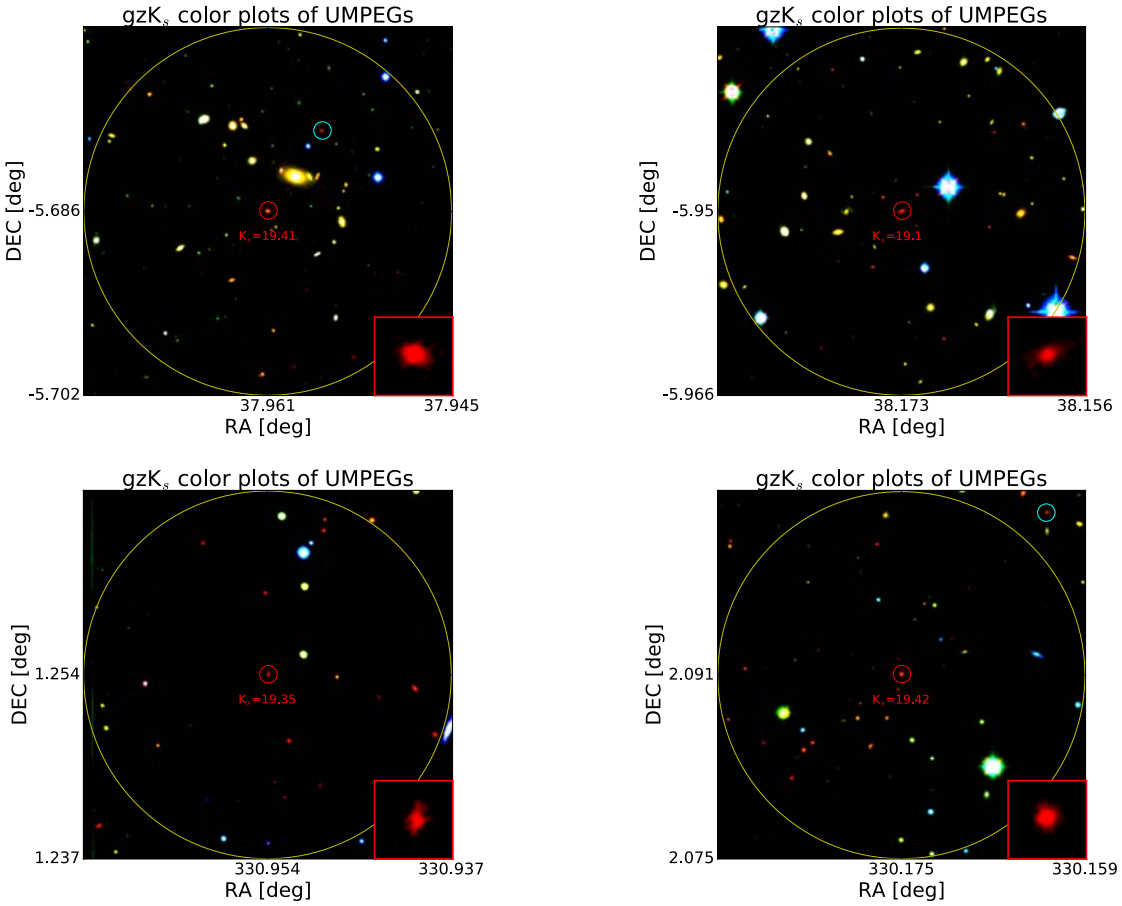

Figure 7.11: Wide Fields, UMPEGs and their environments: UMPEGs 37-40.

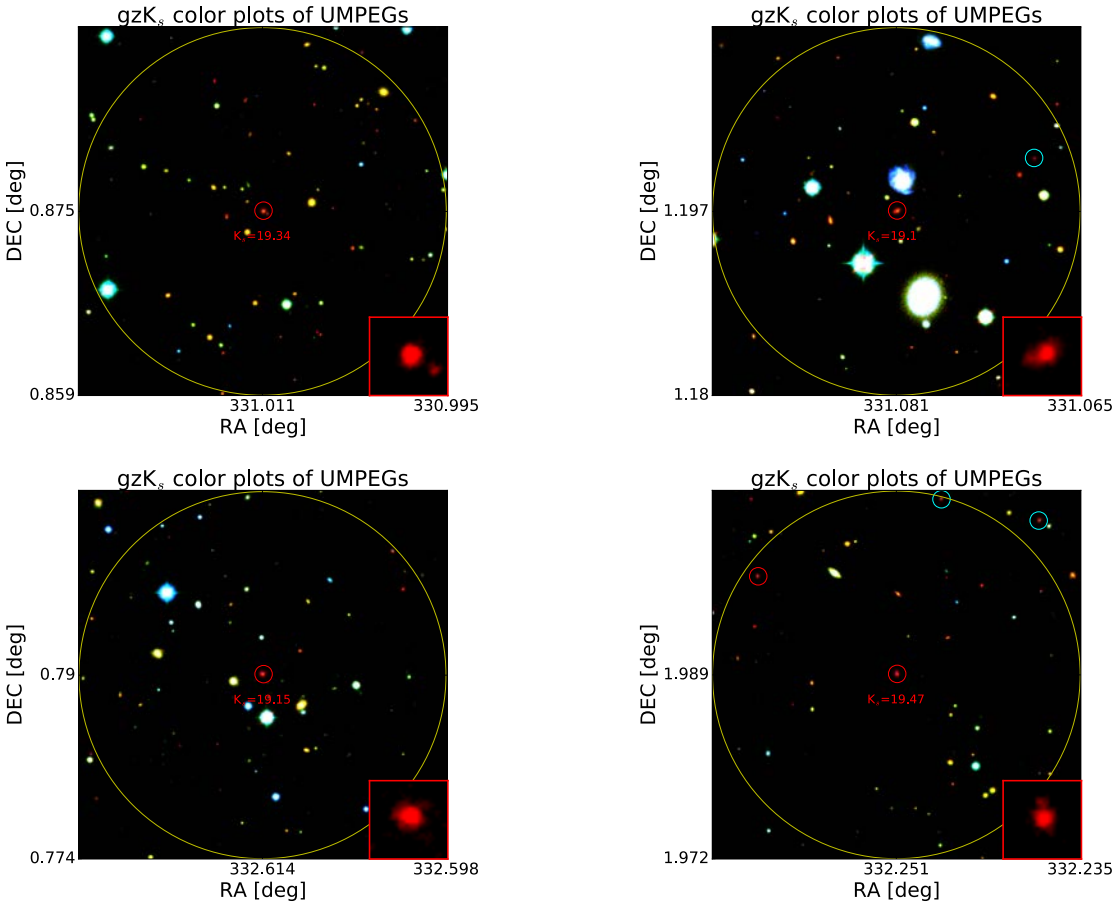

Figure 7.12: Wide Fields, UMPEGs and their environments: UMPEGs 41-44.

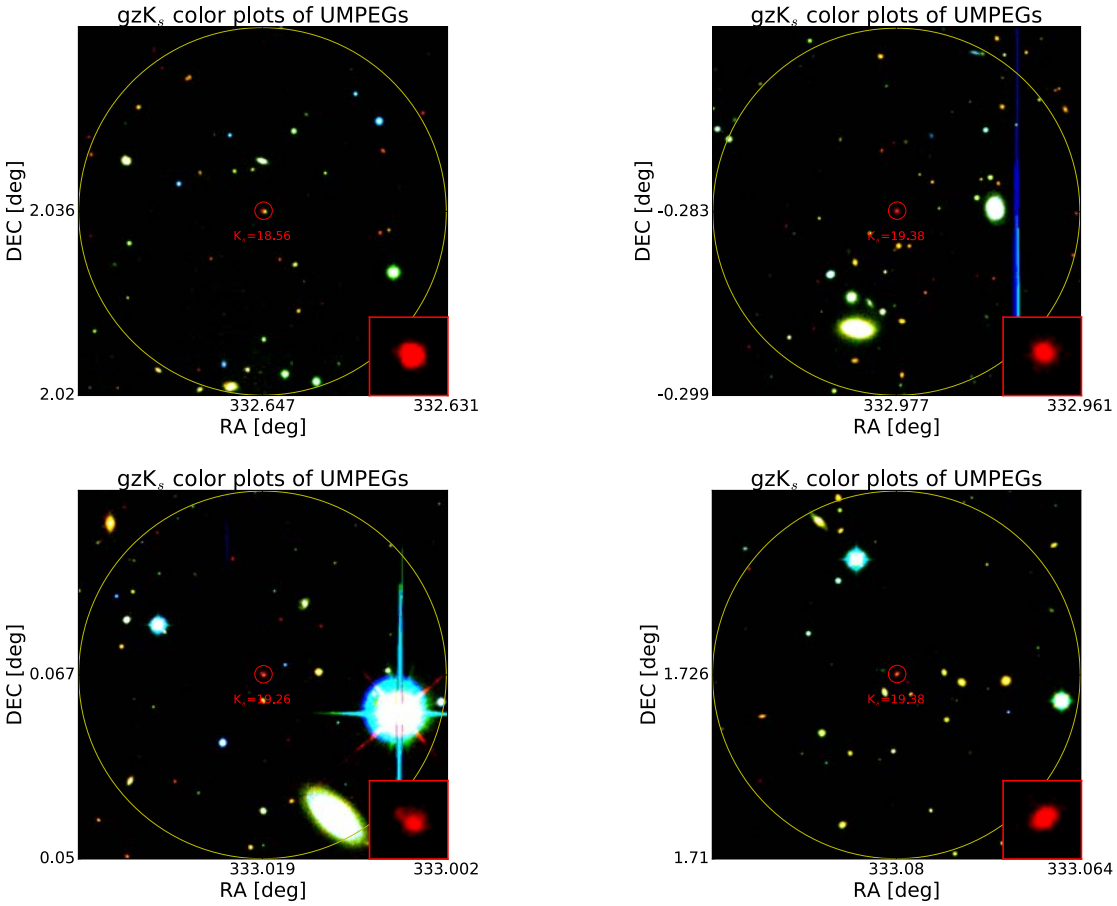

Figure 7.13: Wide Fields, UMPEGs and their environments: UMPEGs 45-48.

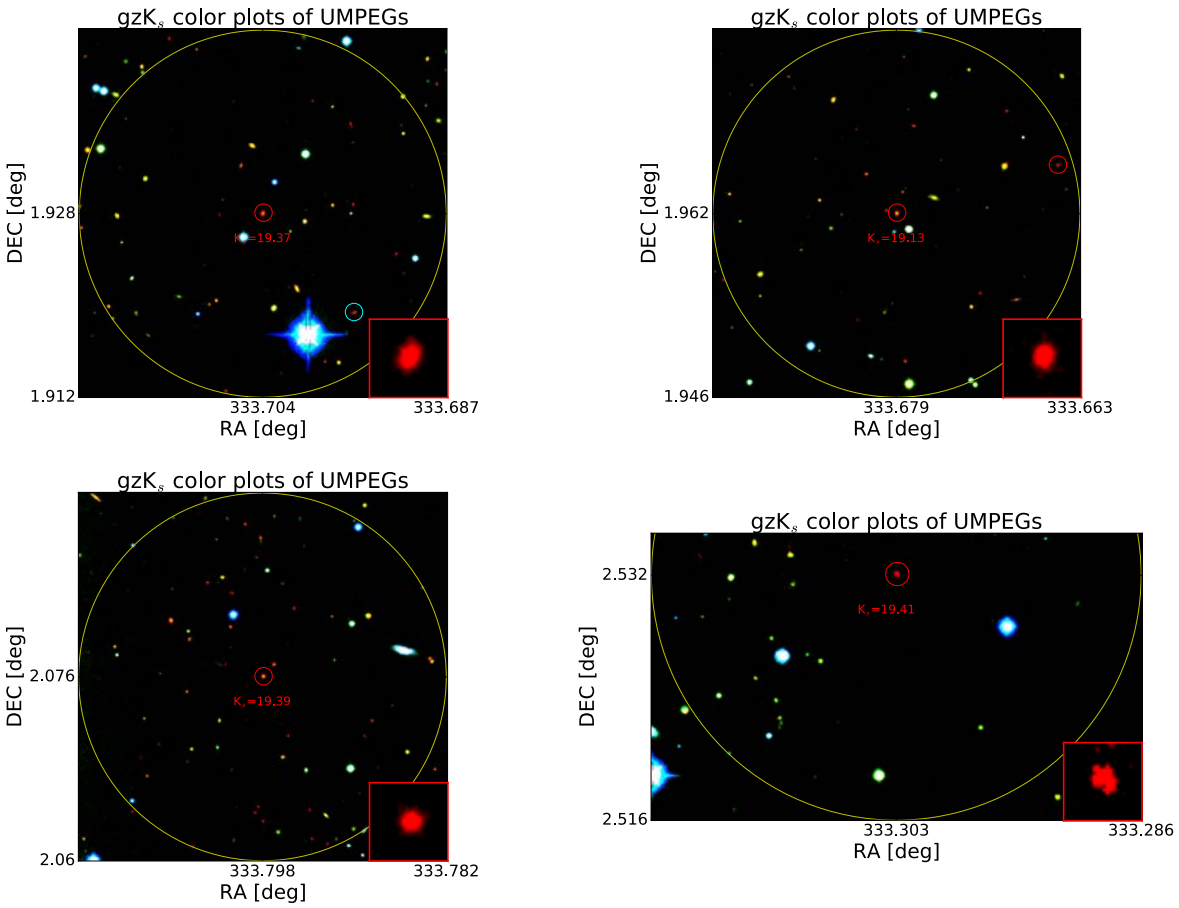

Figure 7.14: Wide Fields, UMPEGs and their environments: UMPEGs 49-52.

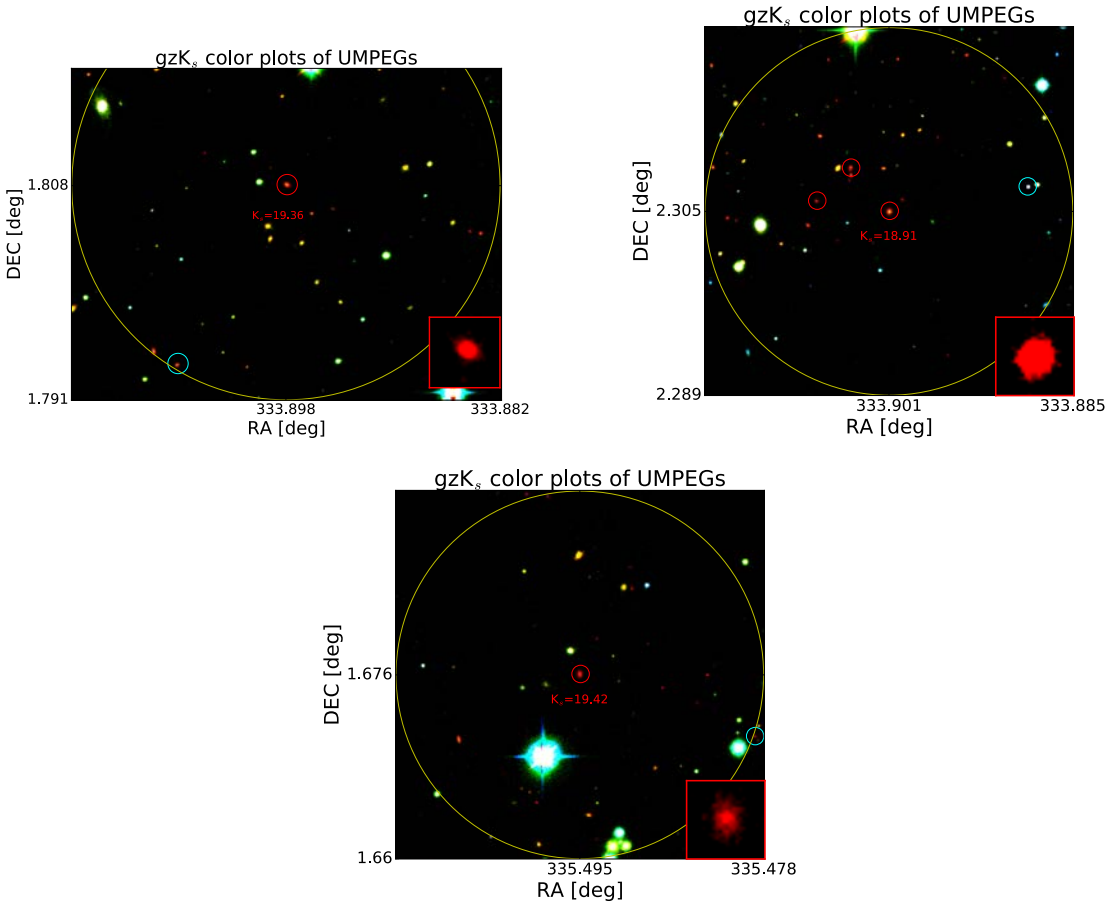

Figure 7.15: Wide Fields, UMPEGs and their environments: UMPEGs 53-55.

Appendix B

The following Figures show gzK_s colour images of dense environments in the Deep and Wide Fields.

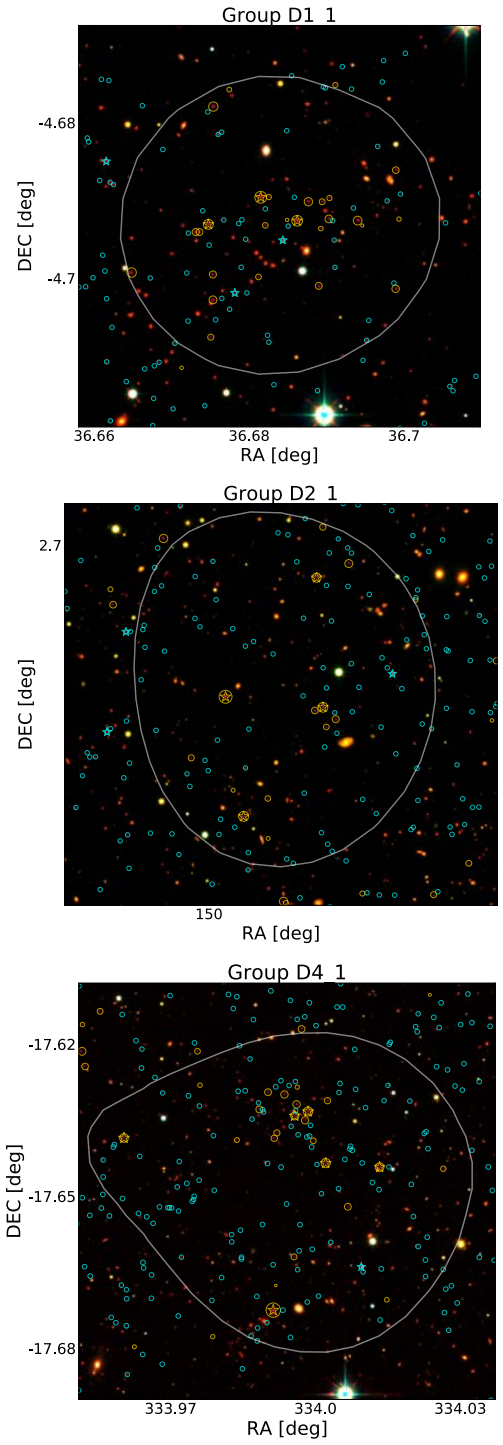

Figure 7.16: gzK_s colour images of dense environments in the Deep fields. As before, orange points define the positions of our passive gzK_s galaxies, while blue points represent the position of star-forming galaxies within these groups. Circles in any colour, represent galaxies down to the completeness of the field, while stars represent galaxies with $K_s < 20.5$. Dense environments are defined based on an over density of massive (K_s<20.5) passive galaxies as defined in 6.2.

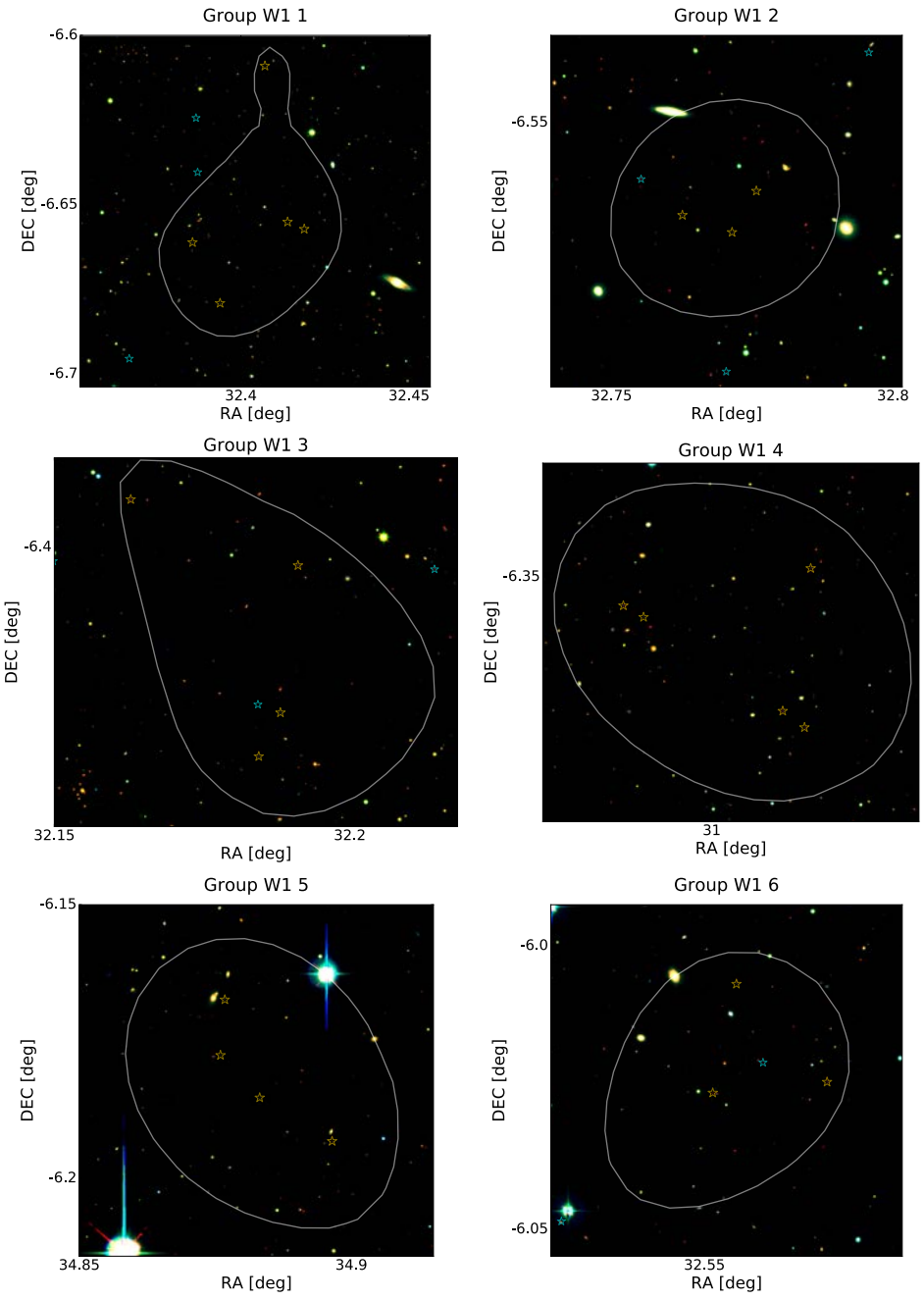

Figure 7.17: gzK$_s$ colour images of dense environments in the Wide fields

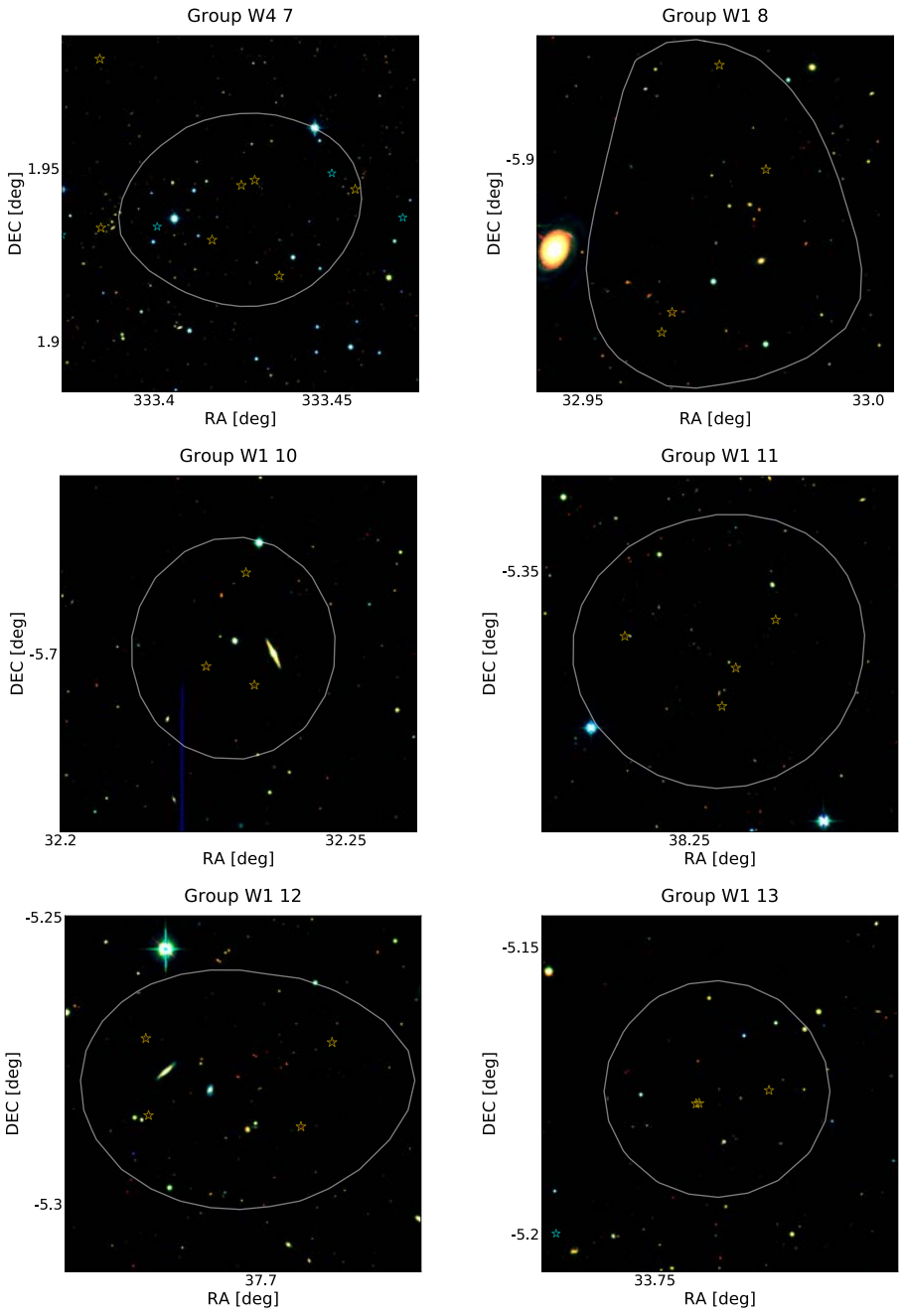

Figure 7.18: gzK$_s$ colour images of dense environments in the Wide fields

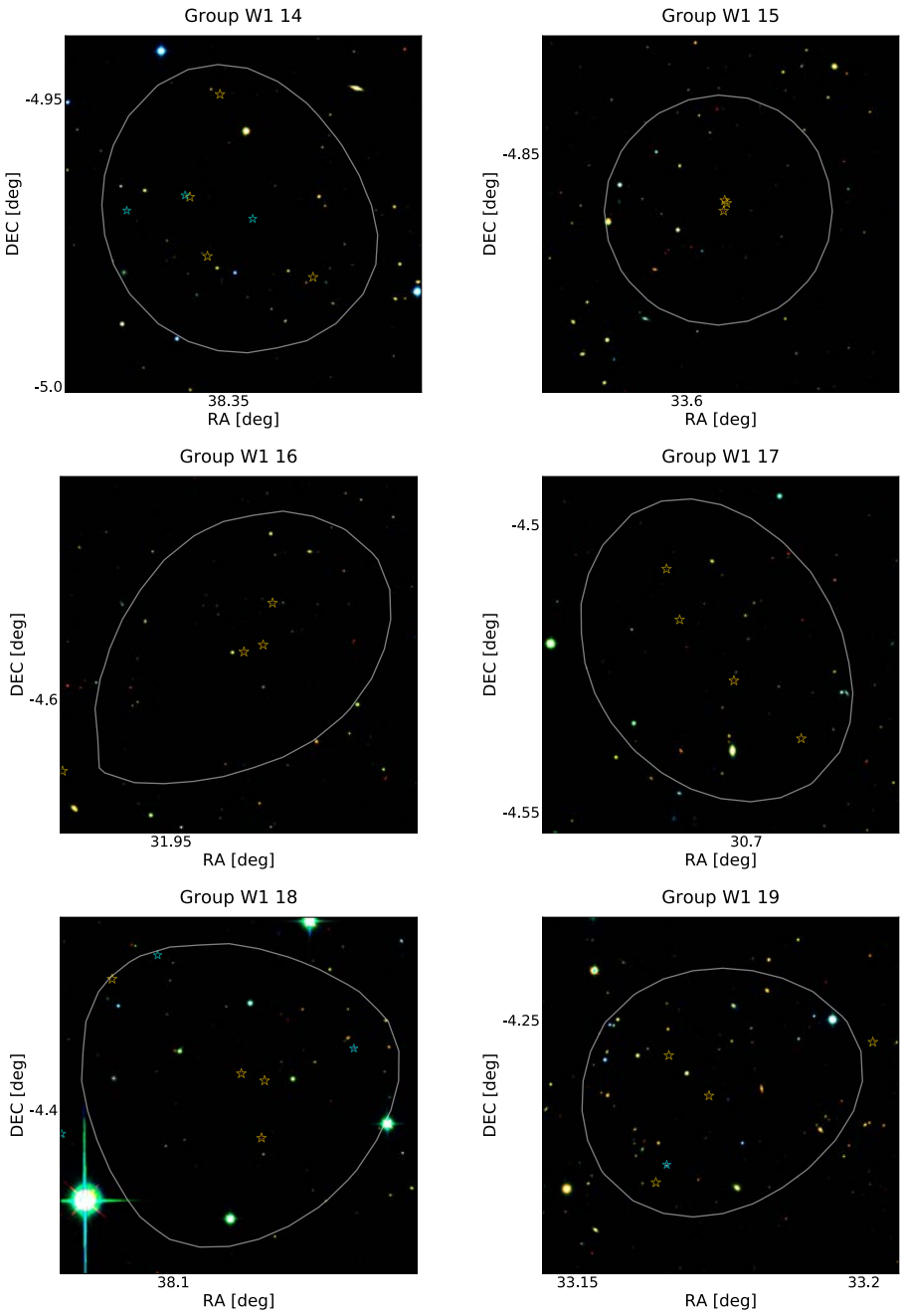

Figure 7.19: gzK$_s$ colour images of dense environments in the Wide fields

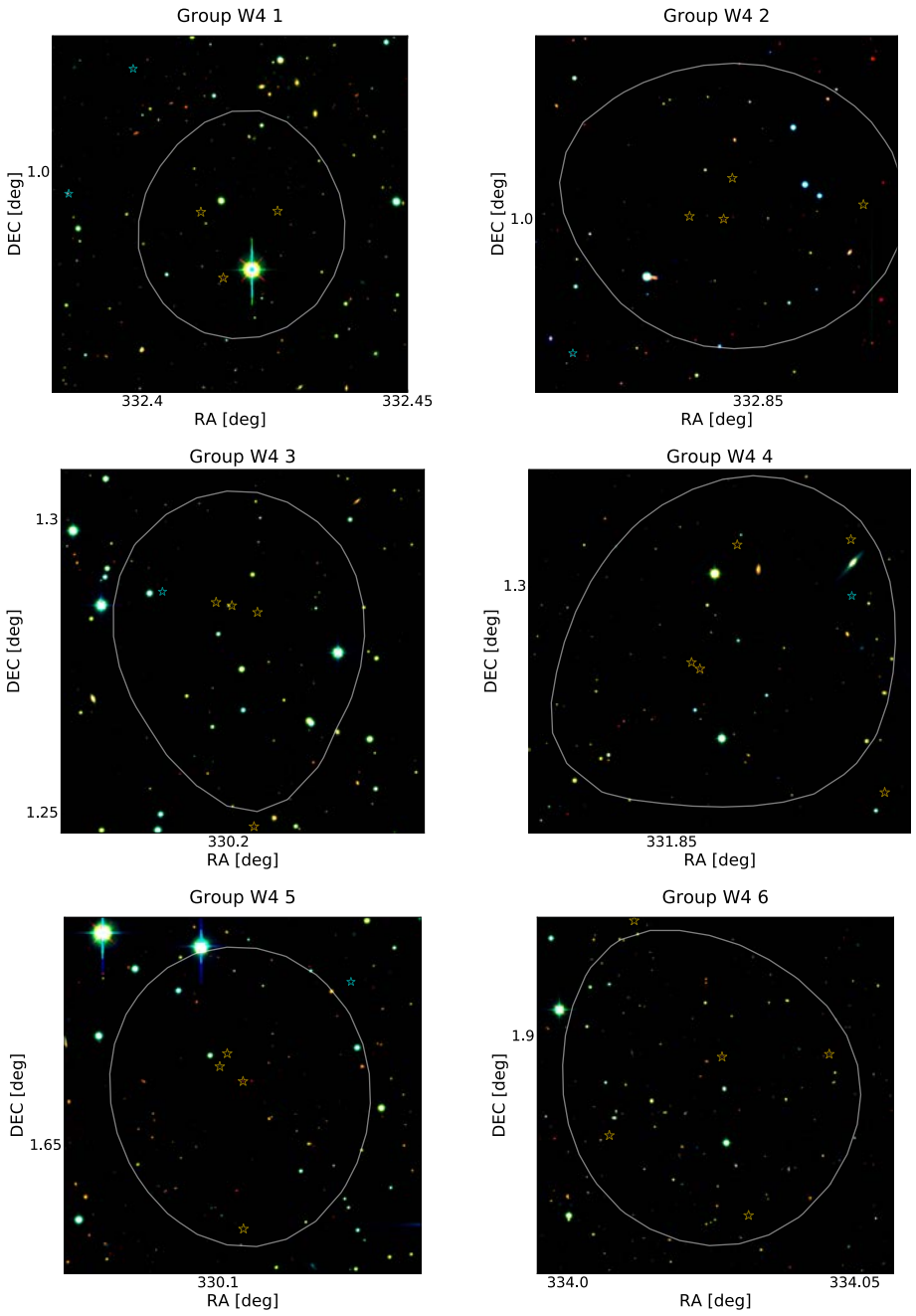

Figure 7.20: gzK$_s$ colour images of dense environments in the Wide fields

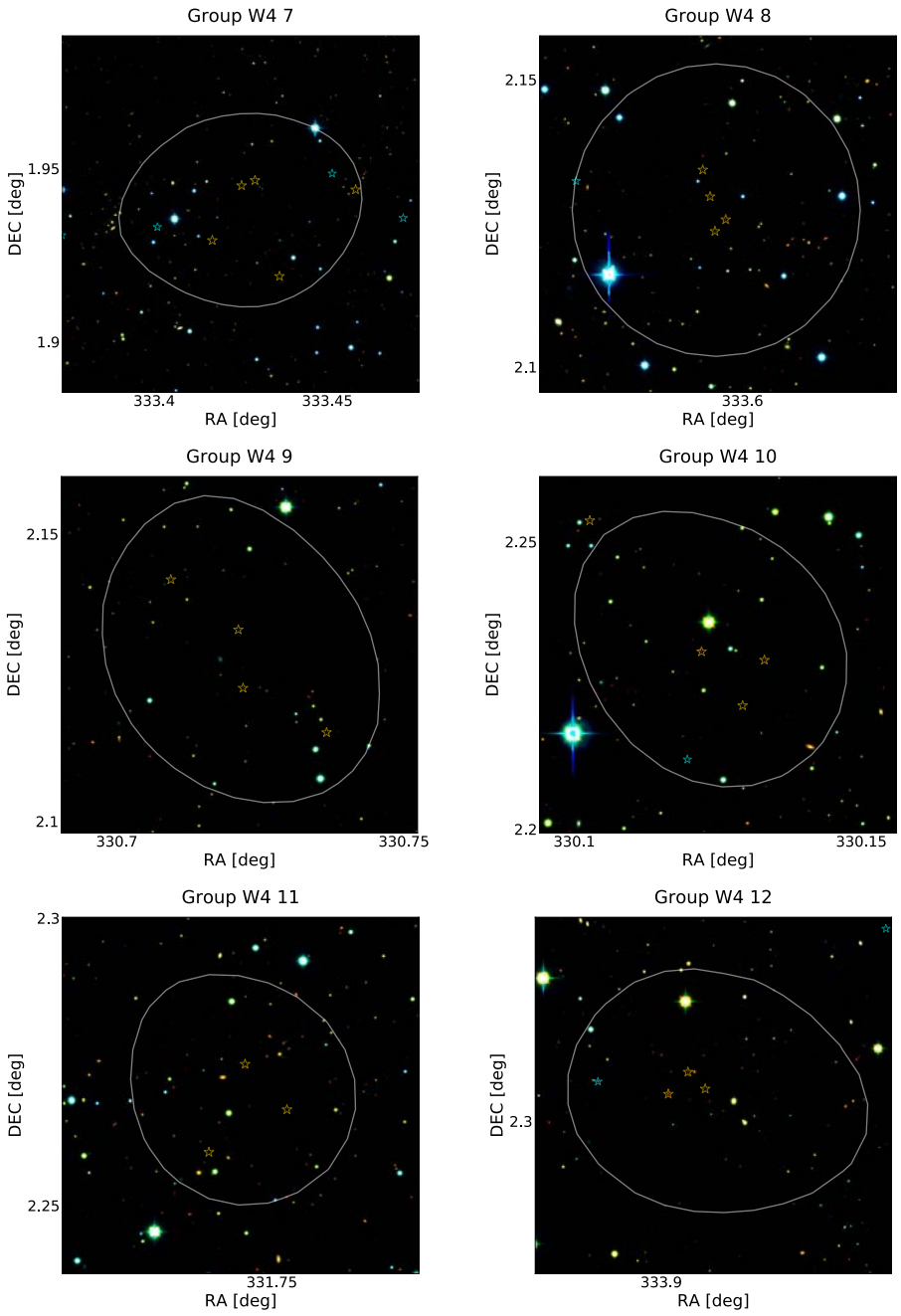

Figure 7.21: gzK$_s$ colour images of dense environments in the Wide fields

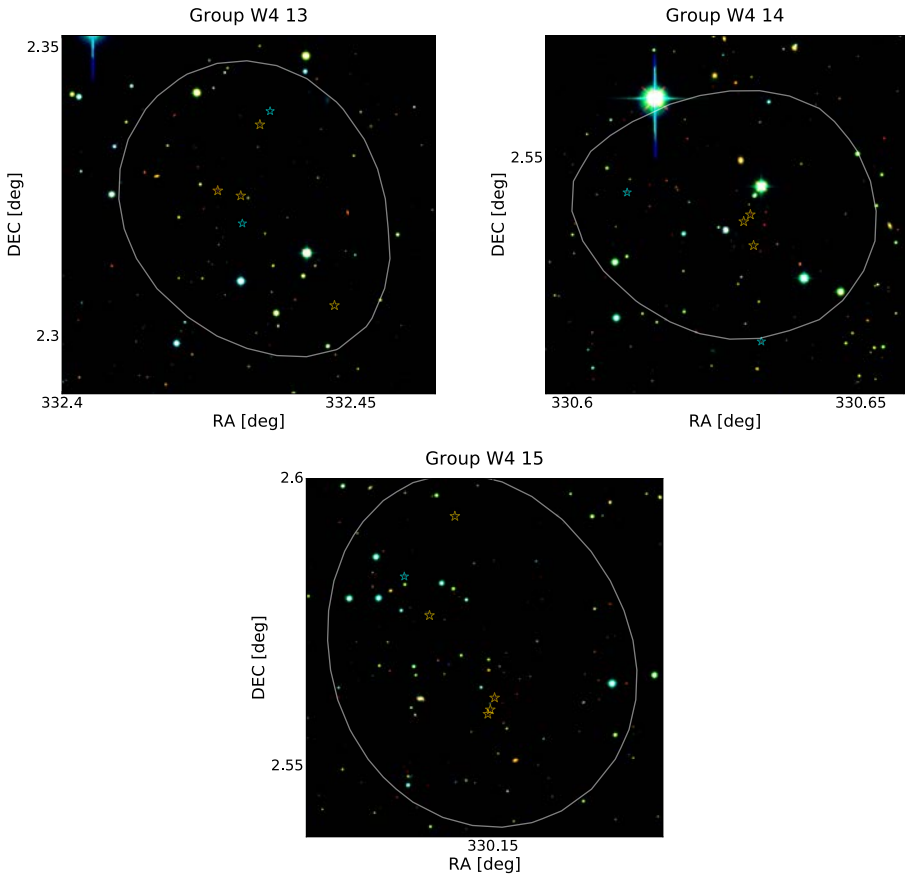

Figure 7.22: gzK_s colour images of dense environments in the Wide fields

Bibliography

Andreon, S., Maughan, B., Trinchieri, G., & Kurk, J. 2009, Astronomy & Astrophysics, 507, 147

Andreon, S., Newman, A. B., Trinchieri, G., et al. 2014, Astronomy and Astrophysics, 565, A120

Angulo, R. E., Springel, V., White, S. D. M., et al. 2012, Montly Notices of the Royal Astronomical Society, 426, 2046

Arcila-Osejo, L. 2011, Master's thesis, Saint Mary's University, 923 Robie Street, Halifax, NS.

Arcila-Osejo, L. & Sawicki, M. 2013, Monthly Notices of the Royal Astronomical Society, 435, 845

Arnouts, S., Moscardini, L., Vanzella, E., et al. 2002, Monthly Notices of the Royal Astronomical Society, 329, 355

Balogh, M. L., McGee, S. L., Mok, A., et al. 2016, Montly Notices of the Royal Astronomical Society, 456, 4364

Bastian, N., Covey, K. R., & Meyer, M. R. 2010, Annual Review of Astronomy and Astrophysics, 48, 339

Bertin, E. & Arnouts, S. 1996, Astronomy and Astrophysics Supplement Series, 117, 393

Bielby, R., Hudelot, P., Mccracken, H. J., et al. 2012, Astronomy & Astrophysics, 23

Bielby, R. M., Finoguenov, A., Tanaka, M., et al. 2010, Astronomy and Astrophysics, 523, A66

Blanton, M. R., Schlegel, D. J., Strauss, M. a., et al. 2005, The Astrophysical Journal, 129, 2562

Bleem, L. E., Stalder, B., de Haan, T., et al. 2015, The Astrophysical Journal, Supplement, 216, 27

Bluck, A. F. L., Conselice, C. J., Bouwens, R. J., et al. 2009, Monthly Notices of the Royal Astronomical Society, 394, L51

Bower, R. G., Benson, A. J., Malbon, R., et al. 2006, Monthly Notices of the Royal Astronomical Society, 370, 645

Bower, R. G., Morris, S. L., Bacon, R., et al. 2004, Monthly Notices of the Royal Astronomical Society, 351, 63

Bowler, R. A. A., Dunlop, J. S., McLure, R. J., et al. 2014, Monthly Notices of the Royal Astronomical Society, 440, 2810

Boylan-Kolchin, M. & Ma, C.-P. 2007, Monthly Notices of the Royal Astronomical Society, 374, 1227

Brammer, G. B., van Dokkum, P. G., & Coppi, P. 2008, The Astrophysical Journal, 686, 1503

Bruzual, G. & Charlot, S. 2003, Monthly Notices of the Royal Astronomical Society, 344, 1000

Calzetti, D., Armus, L., Bohlin, R. C., et al. 2000, The Astrophysical Journal, 533, 682

Cappellari, M., Emsellem, E., Krajnović, D., et al. 2011, The Monthly Notices of the Royal Astronomical Society, 416, 1680

Casey, C. M., Narayanan, D., & Cooray, A. 2014, Physics Reports, 541, 45

Chabrier, G. 2003a, Publications of the Astronomical Society of the Pacific, 115, 763

Chabrier, G. 2003b, The Astrophysical Journal, 586, L133

Chandrasekhar, S. 1943, The Astrophysical Journal, 97, 255

Chapman, S. C., Richards, E. A., Lewis, G. F., Wilson, G., & Barger, A. J. 2001, The Astrophysical Journal, Letters, 548, L147

Chiang, Y., Overzier, R., & Gebhardt, K. 2014, The Astrophysical Journal, Letters, 782, L3

Chiang, Y., Overzier, R. A., Gebhardt, K., & Henriques, B. 2017, The Astrophysical Journal, 844, L23

Cohen, M., Wheaton, W. A., & Megeath, S. T. 2003, The Astronomical Journal, 126, 1090

Collet, C., Nesvadba, N. P. H., De Breuck, C., et al. 2015, Astronomy & Astrophysics, 579, A89

Comparat, J., Richard, J., Kneib, J.-P., et al. 2015, Astronomy and Astrophysics, 575, A40

Coupon, J., Ilbert, O., Kilbinger, M., et al. 2009, Astronomy and Astrophysics, 500, 981

Cowie, L. L., Songaila, A., & Barger, A. J. 1999, Astronomical Journal, 118, 603

Daddi, E., Cimatti, A., Renzini, A., et al. 2004, The Astrophysical Journal, 617, 746

Daddi, E., Dannerbauer, H., Stern, D., et al. 2009, The Astrophysical Journal, 694, 1517

Daddi, E., Dickinson, M., Morrison, G., et al. 2007, The Astrophysical Journal, 670, 156

Daddi, E., Jin, S., Strazzullo, V., et al. 2017, The Astrophysical Journal, 846, L31

Daddi, E., Renzini, A., Pirzkal, N., et al. 2005, The Astrophysical Journal, 626, 680

Damjanov, I., Zahid, H. J., Geller, M. J., & Hwang, H. S. 2015, The Astrophysical Journal, 815, 104

de Jong, J. T. A., Verdoes Kleijn, G. A., Boxhoorn, D. R., et al. 2015, Astronomy and Astrophysics, 582, A62

Deason, A., Wetzel, A., & Garrison-Kimmel, S. 2014, The Astrophysical Journal, 794, 115

Dekel, A. & Birnboim, Y. 2006, Montly Notices of the Royal Astronomical Society, 368, 2

Dekel, A. & Woo, J. 2003, Montly Notices of the Royal Astronomical Society, 344, 1131

Diener, C., Lilly, S. J., Knobel, C., et al. 2013, The Astrophysical Journal, 765, 109

Dressler, A. 1980, The Astrophysical Journal, 236, 351

Edge, A., Sutherland, W., Kuijken, K., et al. 2013, The Messenger, 154, 32

Erben, T., Hildebrandt, H., Miller, L., et al. 2012, Monthly Notices of the Royal Astronomical Society, 14, 1

Fabian, A. C. 2012, Annual Review of Astronomy & Astrophysics, 50, 455

Feldmann, R., Hopkins, P. F., Quataert, E., Faucher-Giguere, C. A., & Keres, D. 2016, Monthly Notices of the Royal Astronomical Society: Letters, 458, L14

Ferreras, I., Hopkins, A. M., Gunawardhana, M. L. P., et al. 2016, Monthly Notices of the Royal Astronomical Society, 14, 1

Franck, J. R. & McGaugh, S. S. 2017, The Astrophysical Journal, 836, 136

Franx, M., Labbé, I., Rudnick, G., et al. 2003, The Astrophysical Journal, Letters, 587, L79

Golob, A. 2018, PhD thesis, Saint Mary's University

Goranova. 2012, The CFHTLS T0006 Release, Terapix

Goranova, Y., Hudelot, P., Mccracken, H. J., & Mellier, Y. 2010, The CFHTLS T0006 release

Goulding, A. D., Forman, W. R., Hickox, R. C., et al. 2012, The Astrophysical Journal, Supplement, 202, 6

Groenewald, D. N., Skelton, R. E., Gilbank, D. G., & Loubser, S. I. 2017, Monthly Notices of the Royal Astronomical Society, 467, 4101

Gunn, J. E. & Gott, III, J. R. 1972, The Astrophysical Journal, 176, 1

Gutcke, T. A., Macciò, A. V., Dutton, A. A., & Stinson, G. S. 2017, Monthly Notices of the Royal Astronomical Society: Letters, 466, 4614

Hildebrandt, H., van Waerbeke, L., & Erben, T. 2009, Astronomy and Astrophysics, 507, 683

Hill, A. R., Muzzin, A., Franx, M., et al. 2017, The Astrophysical Journal, 837, 147

Hilton, M., Collins, C. A., Stanford, S. A., et al. 2007, The Astrophysical Jounal, 670, 1000

Hilton, M., Lloyd-Davies, E., Stanford, S. A., et al. 2010, The Astrophysical Journal, 718, 133

Hilton, M., Stanford, S. A., Stott, J. P., et al. 2009, The Astrophysical Journal, 697, 436

Hilz, M., Naab, T., & Ostriker, J. P. 2013, Monthly Notices of the Royal Astronomical Society, 429, 2924

Hudelot, P., Goranova, Y., Mellier, Y., et al. 2012, Proceedings of the SPIE, 8448

Huertas-Company, M., Bernardi, M., Pérez-González, P. G., et al. 2016, Monthly Notices of the Royal Astronomical Society, 462, 4495

Ilbert, O., Arnouts, S., McCracken, H. J., et al. 2006, Astronomy and Astrophysics, 457, 841

Ilbert, O., McCracken, H. J., Le Fèvre, O., et al. 2013, Astronomy & Astrophysics, 556, A55

Ilbert, O., Salvato, M., Le Floc'h, E., et al. 2010, The Astrophysical Journal, 709, 644

Jiang, C. Y., Jing, Y. P., Faltenbacher, A., Lin, W. P., & Li, C. 2008, The Astrophysical Journal, 675, 1095

Kado-Fong, E., Marchesini, D., Marsan, Z. C., et al. 2017, The Astrophysical Journal, 838, 57

Kato, Y., Matsuda, Y., Smail, I., et al. 2016, The Monthly Notices of the Royal Astronomical Society, 460, 3861

Katz, N., Keres, D., Dave, R., & Weinberg, D. H. 2003, in Astrophysics and Space Science Library, Vol. 281, The IGM/Galaxy Connection. The Distribution of Baryons at z=0, ed. J. L. Rosenberg & M. E. Putman, 185

Kauffmann, G. & Charlot, S. 1998, Monthly Notices of the Royal Astronomical Society, 297, L23

Kitzbichler, M. G. & White, S. D. M. 2007, Monthly Notices of the Royal Astronomical Society, 376, 2

Kitzbichler, M. G. & White, S. D. M. 2008, Monthly Notices of the Royal Astronomical Society, 391, 1489

Kong, X., Daddi, E., Arimoto, N., et al. 2006, The Astrophysical Journal, 638, 72

Kriek, M., van Dokkum, P. G., Labbé, I., et al. 2009, The Astrophysical Journal, 700, 221

Labbé, I., Franx, M., Rudnick, G., et al. 2003, Astronomical Journal, 125, 1107

Lacey, C. & Cole, S. 1993, Monthly Notices of the Royal Astronomical Society, 262, 627

Lane, K. P., Almaini, O., Foucaud, S., et al. 2007, Monthly Notices of the Royal Astronomical Society: Letters, 379, L25

Lani, C., Almaini, O., Hartley, W. G., et al. 2013, Monthly Notices of the Royal Astronomical Society, 435, 207

Lawrence, A., Warren, S. J., Almaini, O., et al. 2007, Monthly Notices of the Royal Astronomical Society, 379, 1599

Lee, J. & Yi, S. K. 2017, The Astrophysical Journal, 836, 161

Lee-Brown, D. B., Rudnick, G. H., Momcheva, I. G., et al. 2017, The Astrophysical Journal, 844, 43

Lemaux, B. C., Cucciati, O., Tasca, L. A. M., et al. 2014, Astronomy and Astrophysics, 572, A41

Lidman, C., Suherli, J., Muzzin, A., et al. 2012, Monthly Notices of the Royal Astronomical Society, 427, 550

Lin, H., Kirshner, R. P., Shectman, S. A., et al. 1996, The Astrophysical Journal, 464, 60

Longhetti, M. & Saracco, P. 2009, Monthly Notices of the Royal Astronomical Society, 394, 774

López-Corredoira, M., Vazdekis, A., Gutiérrez, C. M., & Castro-Rodríguez, N. 2017, Astronomy & Astrophysics, 600, A91

Mancini, C., Daddi, E., Renzini, A., et al. 2010, Monthly Notices of the Royal Astronomical Society, 401, 933

Marchesini, D., Muzzin, A., Stefanon, M., et al. 2014, The Astrophysical Journal, 794, 65

Marchesini, D., van Dokkum, P. G., Förster Schreiber, N. M., et al. 2009, The Astrophysical Journal, 701, 1765

Matthews, T. A., Morgan, W. W., & Schmidt, M. 1964, The Astrophysical Journal, 140, 35

McCarthy, I. G., Babul, A., Bower, R. G., & Balogh, M. L. 2008, Montly Notices of the Royal Astronomical Society, 386, 1309

McCracken, H. J., Capak, P., Salvato, M., et al. 2010, The Astrophysical Journal, 708, 202

McCracken, H. J., Milvang-Jensen, B., Dunlop, J., et al. 2012, Astronomy and Astrophysics, 544, A156

McGee, S. L., Bower, R. G., & Balogh, M. L. 2014, Montly Notices of the Royal Astronomical Society, 442, L105

McLure, R. J., Pearce, H. J., Dunlop, J. S., et al. 2013, Monthly Notices of the Royal Astronomical Society, 428, 1088

Merson, A. I., Baugh, C. M., John, H. H., et al. 2013, Monthly Notices of the Royal Astronomical Society, 429, 556

Miyatake, H., More, S., Takada, M., et al. 2016, Physical Review Letters, 116, 041301

Moore, B., Katz, N., Lake, G., Dressler, A., & Oemler, A. 1996, Nature, 379, 613

Moutard, T., Arnouts, S., Ilbert, O., et al. 2016a, Astronomy & Astrophysics, 590, A103

Moutard, T., Arnouts, S., Ilbert, O., et al. 2016b, Astronomy & Astrophysics, 590, A102

Moutard, T., Sawicki, M., Arnouts, S., et al. 2018, ArXiv e-prints

Munoz-Cuartas, J. C., Maccio, A. V., Gottlober, S., & Dutton, A. A. 2011, Monthly Notices of the Royal Astronomical Society, 411, 584

Muzzin, A., Marchesini, D., Stefanon, M., et al. 2013a, The Astrophysical Journal, 777, 18

Muzzin, A., Marchesini, D., Stefanon, M., et al. 2013b, The Astrophysical Journal Supplement Series, 206, 8

Muzzin, A., Wilson, G., Yee, H. K. C., et al. 2009, The Astronomical Journal, 698, 1934

Naab, T., Johansson, P. H., & Ostriker, J. P. 2009, The Astrophysical Journal, 699, L178

Nantais, J. B., Rettura, A., Lidman, C., et al. 2013, Astronomy and Astrophysics, 556, A112

Nantais, J. B., van der Burg, R. F. J., Lidman, C., et al. 2016, Astronomy & Astrophysics, 592, A161

Nelson, E., van Dokkum, P., Franx, M., et al. 2014, Nature, 513, 394

Newman, A. B., Ellis, R. S., Andreon, S., et al. 2014, The Astrophysical Journal, 788, 51

Noeske, K. G., Weiner, B. J., Faber, S. M., et al. 2007, The Astrophysical Journal, Letters, 660, L43

Noirot, G., Stern, D., Mei, S., et al. 2018, ArXiv e-prints

Noirot, G., Vernet, J., De Breuck, C., et al. 2016, The Astrophysical Journal, 830, 90

Oemler, Jr., A. 1974, The Astrophysical Journal, 194, 1

Ono, Y., Ouchi, M., Harikane, Y., et al. 2018, Publications of the Astronomical Society of Japan, 70, S10

Onodera, M., Arimoto, N., Daddi, E., et al. 2010, The Astrophysical Journal, 715, 385

Overzier, R. A. 2016, Astronomy & Astrophysics Reviews, 24, 14

Pacifici, C., Kassin, S. A., Weiner, B. J., et al. 2016, The Astrophysical Journal, 832, 79

Pandya, V., Brennan, R., Somerville, R. S., et al. 2017, The Monthly Notices of the Royal Astronomical Society, 472, 2054

Papovich, C., Kawinwanichakij, L., Quadri, R. F., et al. 2018, The Astrophysical Journal, 854, 30

Papovich, C., Momcheva, I., Willmer, C. N. A., et al. 2010, The Astrophysical Journal, 716, 1503

Partridge, R. B. & Peebles, P. J. E. 1967, The Astrophysical Journal, 147, 868

Patton, D. R., Carlberg, R. G., Marzke, R. O., et al. 2000, The Astrophysical Journal, 536, 153

Peng, Y., Maiolino, R., & Cochrane, R. 2015, Nature, 521, 192

Peng, Y.-j., Lilly, S. J., Kovač, K., et al. 2010, The Astrophysical Journal, 721, 193

Peng, Y.-j., Lilly, S. J., Renzini, A., & Carollo, M. 2012, The Astrophysical Journal, 757, 4

Pope, A., Chary, R.-R., Alexander, D. M., et al. 2008, The Astrophysical Journal, 675, 1171

Quadri, R., Marchesini, D., van Dokkum, P., et al. 2007, Astronomical Journal, 134, 1103

Ravindranath, S., Daddi, E., Giavalisco, M., Ferguson, H. C., & Dickinson, M. E. 2007, Proceedings of the International Astronomical Union, 3, 407

Reddy, N. a., Erb, D. K., Steidel, C. C., et al. 2005, The Astrophysical Journal, 633, 748

Regnault, N., Conley, A., Guy, J., et al. 2009, Astronomy and Astrophysics, 506, 999

Salim, S., Rich, R. M., Charlot, S., et al. 2007, The Astrophysical Journal, Supplement, 173, 267

Salpeter, E. E. 1955, Astrophysical Journal, 121, 161

Santini, P., Fontana, A., Castellano, M., et al. 2017, The Astrophysical Journal, 847, 76

Santini, P., Fontana, A., Grazian, A., et al. 2009, Astronomy and Astrophysics, 504, 751

Sato, T., Sawicki, M., & Arcila-Osejo, L. 2014, Monthly Notices of the Royal Astronomical Society, 443, 2661

Sawicki, M. 2012, Publications of the Astronomical Society of the Pacific, 124, 1208

Schawinski, K., Urry, C. M., Simmons, B. D., et al. 2014, Monthly Notices of the Royal Astronomical Society, 440, 889

Schechter, P. 1976, The Astrophysical Journal, 203, 297

Schlafly, E. F. & Finkbeiner, D. P. 2011, The Astrophysical Journal, 737, 103

Schlegel, D. J., Finkbeiner, D. P., & Davis, M. 1998, The Astrophysical Journal, 500, 525

Scoville, N., Aussel, H., Brusa, M., et al. 2007, The Astrophysical Journal, Supplement, 172, 1

Shimizu, I. & Inoue, A. K. 2013, Publications of the Astronomical Society of Japan, 65, 96

Sinha, M. & Holley-Bockelmann, K. 2009, in Astronomical Society of the Pacific Conference Series, Vol. 419, Galaxy Evolution: Emerging Insights and Future Challenges, ed. S. Jogee, I. Marinova, L. Hao, & G. A. Blanc, 263

Somerville, R. S., Gilmore, R. C., Primack, J. R., & Domínguez, A. 2012, Monthly Notices of the Royal Astronomical Society, 423, 1992

Sommariva, V., Fontana, A., Lamastra, A., et al. 2014, Astronomy & Astrophysics, 571, A99

Sorba, R. & Sawicki, M. 2018, Montly Notices of the Royal Astronomical Society, 476, 1532

Speagle, J. S., Steinhardt, C. L., Capak, P. L., & Silverman, J. D. 2014, The Astrophysical Journal, Supplement, 214, 15

Springel, V., White, S. D. M., Jenkins, A., et al. 2005, Nature, 435, 629

Stanford, S. A., Brodwin, M., Gonzalez, A. H., et al. 2012, The Astrophysical Journal, 753, 164

Stanford, S. A., Romer, A. K., Sabirli, K., et al. 2006, The Astrophysical Journal, 646, L13

Steidel, C. C., Adelberger, K. L., Dickinson, M., et al. 1998, The Astrophysical Journal, 492, 428

Steidel, C. C. & Hamilton, D. 1993, The Astronomical Journal, 105, 2017

Strazzullo, V., Daddi, E., Gobat, R., et al. 2015, Astronomy & Astrophysics, 576, L6

Strazzullo, V., Rosati, P., Pannella, M., et al. 2010, Astronomy and Astrophysics, 524, A17

Tal, T., Dekel, A., Oesch, P., et al. 2014, The Astrophysical Journal, 789, 164

Tal, T., van Dokkum, P. G., Franx, M., et al. 2013, The Astrophysical Journal, 769, 31

Tal, T., Wake, D. A., van Dokkum, P. G., et al. 2012, The Astrophysical Journal, 746, 138

Tanaka, M., Finoguenov, A., & Ueda, Y. 2010, The Astrophysical Journal, 716, L152

Terrazas, B. A., Bell, E. F., Henriques, B. M. B., et al. 2016, The Astrophysical Journal, Letters, 830, L12

Thomas, D., Maraston, C., Bender, R., & Mendes de Oliveira, C. 2005, The Astrophysical Journal, 621, 673

Tomczak, A., Quadri, R., Tran, K.-V., et al. 2014, The Astrophysical Journal, 783, 85

Tonnesen, S. & Bryan, G. L. 2009, The Astrophysical Journal, 694, 789

Toshikawa, J., Kashikawa, N., Overzier, R., et al. 2016, The Astrophysical Journal, 826, 114

Toshikawa, J., Uchiyama, H., Kashikawa, N., et al. 2018, Publications of the Astronomical Society of Japan, 70, S12

Van der Burg, R. F. J., Muzzin, a., Hoekstra, H., et al. 2013, Astronomy & Astrophysics, 557, A15

van der Burg, R. F. J., Muzzin, A., Hoekstra, H., et al. 2013, Astronomy and Astrophysics, 557, A15

van Dokkum, P. G. & Franx, M. 2001, The Astrophysical Journal, 553, 90

van Dokkum, P. G., Labbé, I., Marchesini, D., et al. 2009, Publications of the Astronomical Society of the Pacific, 121, 2

van Dokkum, P. G., Quadri, R., Marchesini, D., et al. 2006, The Astrophysical Journal, Leters, 638, L59

Veale, M., Ma, C.-P., Greene, J. E., et al. 2017, The Monthly Notices of the Royal Astronomical Society, 471, 1428

Venemans, B. P., Röttgering, H. J. A., Miley, G. K., et al. 2007, Astronomy and Astrophysics, 461, 823

Visvanathan, N. & Sandage, A. 1977, The Astrophysical Journal, 216, 214

Vulcani, B., Marchesini, D., Lucia, G. D., et al. 2016, The Astrophysical Journal, 816, 86

Vulcani, B., Poggianti, B. M., Oemler, A., et al. 2013, Astronomy & Astrophysics, 550, A58

Webb, T., Noble, A., DeGroot, A., et al. 2015, The Astrophysical Journal, 809, 173

Weigel, A. K., Schawinski, K., & Bruderer, C. 2016, Monthly Notices of the Royal Astronomical Society, 459, 2150

Weinzirl, T., Jogee, S., Neistein, E., et al. 2014, Monthly Notices of the Royal Astronomical Society, 441, 3083

Wellons, S., Torrey, P., Ma, C. P., et al. 2016, Monthly Notices of the Royal Astronomical Society, 456, 1030

Wen, Z. & Han, J. 2011, The Astrophysical Journal, 734, 68

Wen, Z. L. & Han, J. L. 2015, Monthly Notices of the Royal Astronomical Society, 448, 2

Whitaker, K. E., Franx, M., Leja, J., et al. 2014, The Astrophysical Journal, 795, 104

Whitaker, K. E., van Dokkum, P. G., Brammer, G., & Franx, M. 2012, The Astrophysical Journal, Letters, 754, L29

Whitaker, K. E., van Dokkum, P. G., Brammer, G., et al. 2013, The Astrophysical Journal, 770, L39

Wilson, G., Muzzin, A., Yee, H. K. C., et al. 2009, The Astrophysical Journal, 698, 1943

Wuyts, S., Labbé, I., Förster Schreiber, N. M., et al. 2008, The Astrophysical Journal, 682, 985

Yang, X., Mo, H. J., & van den Bosch, F. C. 2008, The Astrophysical Journal, 695, 900